



UNIVERSITY OF
BIRMINGHAM

SCHOOL OF CHEMISTRY

Synthesis of electrolyte and electrode materials for solid oxide fuel cells

Philip J Keenan

2016

PROJECT SUPERVISOR: *Prof P Slater*

UNIVERSITY OF
BIRMINGHAM

University of Birmingham Research Archive

e-theses repository

This unpublished thesis/dissertation is copyright of the author and/or third parties. The intellectual property rights of the author or third parties in respect of this work are as defined by The Copyright Designs and Patents Act 1988 or as modified by any successor legislation.

Any use made of information contained in this thesis/dissertation must be in accordance with that legislation and must be properly acknowledged. Further distribution or reproduction in any format is prohibited without the permission of the copyright holder.

Acknowledgements

Firstly, I would like to acknowledge and thank Peter Raymond Slater, my supervisor, for his instruction, guidance and help through-out my PhD as well as for the opportunity. I would further like to thank the EPSRC and the School of Chemistry for funding it. In addition to the chemistry that Peter has taught me over the years he has also educated me on metal music and real ales, which he would say is sometimes more important than the science; from attending gigs in dubious areas of Birmingham to the beer festivals and brewery tours.

I would also like to show my appreciation to all of the past and present members of the Slater group; including Cathryn Hancock who helped me from the very beginning as a lowly masters student (even if she was forced to). To Laura Driscoll who has gone through a PhD in the Slater group at the same time, sharing the highs and lows. In addition, I would like to thank other group members; Alaric Smith, Ben Corrie and Felix Shin for their help and numerous pub trips. Outside of my research group, I would like to thank other members of the School of Chemistry for sharing an office with me for the past three years as well as Dr Jackie Dean for training me on the equipment.

Outside of chemistry, I would like to thank previous housemates - Adam Ramli and Naomi Dixon for keeping me grounded with continuous abuse about my fading hairline and cheeky Nandos/cinema trips. - Matthew Howard, Geoffrey Laurence Cutts and George Day for fantastic house nights out and never knowing who would be in our lounge the next day. - Evin Chen, my fake wife, who cooked and cleaned, as well as the numerous residents of 118 Quinton Road.

Internationally I would like to acknowledge the University of Malaga, and Dr Jose Porras for his help in the testing of my materials and looking after me during in my time there, as well as helping me learn some pigeon Spanish. To my German contingent Dr Oliver Clemens at KIT, I would like to show my appreciation for his help with neutron data analysis and the use of his high temperature X-ray diffractometer. Finally, I would like to thank my family for their support and continuous abuse about begin a life-long student.

Abstract

In this PhD thesis, new materials for solid oxide fuel cells have been researched. It focuses on both the cathode and electrolyte components. Two general systems, the perovskite-type ABO_3 and apatite-type $M_{10-x}(XO_4)_6O_{2+y}$ structures, have been investigated. The structural characteristics, conductivity and stability have been examined.

The perovskite work for the cathode uses doping strategies to introduce disorder into the system and change the conduction characteristics through a structure change to cubic. It has been shown that only small amounts of dopants are required to cause this structural change and effect the conductivity. In addition, thermal and chemical compatibility tests, along with ASR tests with known fluorite and apatite electrolytes, have been investigated. Their stability in a CO_2 containing environment was tested and a full-scale production of a fuel cell was attempted (Chapters 3 and 4).

The electrolyte investigations focussed on doping the $Ba_2Sc_2O_5$ sample to form a perovskite structure that possesses both oxide ion and protonic conductivity. The doping has decreased the amount of scandium present with cheaper elements such as rare earth Yb^{3+} , or transition metals Fe^{4+} and Ti^{4+} , all in an attempt to form the cubic structure that results in high oxide ion/proton conductivity and increased stability in CO_2 environments (Chapter 5). The final chapter focuses on phosphate and rare earth doping of $BaPrO_3$, to form the cubic perovskite structure. These samples were seen to have increased water incorporation and stability in CO_2 . However, this was at the expense of the ionic conductivity due to vacancy trapping.

Collaborations

This PhD has allowed me to collaborate internally at the University of Birmingham, UK nationally and internationally with institutions below:-



UNIVERSITY OF
BIRMINGHAM



WARWICK
THE UNIVERSITY OF WARWICK



Science & Technology Facilities Council
ISIS



NANYANG
TECHNOLOGICAL
UNIVERSITY

Table of Content

1	Introduction	1
1.1.1	History of fuel cells	2
1.1.2	How a fuel cell works.....	3
1.1.3	Fuel cell efficiency vs. fossil fuels.....	4
1.1.4	Types of fuel cell.....	6
1.1.5	Solid Oxide fuel cells	8
1.2	Conventional materials for SOFCs	12
1.2.1	Oxide ion conducting electrolytes	12
1.2.1.1	Fluorite electrolytes.....	12
1.2.1.2	Apatite electrolytes	14
1.2.1.3	Perovskite materials	16
1.2.2	Proton conducting electrolyte	18
1.2.2.1	Perovskite-type proton conducting electrolytes.....	19
1.2.2.2	Lanthanum phosphate.....	20
1.2.2.3	Lanthanum niobate	20
1.2.2.4	Lanthanum barium gallate.....	21
1.3	Electrodes.....	21
1.3.1	Cathode materials	22
1.3.1.1	Platinum	22
1.3.1.2	Perovskite cathodes.....	23
1.3.1.3	Ln_2NiO_4	25
1.3.2	Anode materials	27
1.3.2.1	Nickel.....	27
1.3.2.2	Alternative anodes.....	28
1.4	Project overview.....	29
1.4.1	Cathode materials	29
1.4.2	Electrolyte materials.....	30
2	Experimental	31
2.1	Synthesis techniques	31
2.1.1	Solid state synthesis	31
2.2	Structural Characterisation.....	33

2.2.1	Crystallography.....	33
2.2.2	X-ray diffraction.....	36
2.2.2.1	Scattering.....	37
2.2.2.2	Generation of X-rays.....	39
2.2.2.3	Bragg's Law	41
2.2.2.4	Instrumentation.....	43
2.2.2.5	Powder diffraction data	44
2.2.3	Rietveld analysis	45
2.2.3.1	General structure analysis software	46
2.3	Raman Spectroscopy	49
2.4	Thermal analysis.....	52
2.4.1	TGA coupled with DTA and GA-MS.....	52
2.4.2	Dilatometry.....	54
2.5	DC Conductivity	55
2.5.1	Van de Pauw technique	56
2.5.2	Standard 4 probe DC technique.....	56
2.6	AC Impedance conductivity measurements	57
2.6.1	Electrical impedance theory	58
2.6.2	Analysis of impedance data	64
2.6.2.1	Equivalent circuit elements	64
2.6.2.2	Bulk and grain electrolyte analysis and fitting model	67
2.6.2.3	Area specific resistance (ASR) analysis and fitting model	69
2.6.2.4	Reporting of conductivity	70
2.6.3	Instrumentation.....	71
2.7	Fuel Cell Test	71
2.8	Scanning electron microscope.....	73
3	Evaluation of $\text{Sr}_{0.8}\text{Ca}_{0.2}\text{Mn}_{0.9}\text{Si}_{0.1}\text{O}_{3-6}$ composite cathode material with apatite and fluorite electrolytes	75
3.1	Introduction.....	75
3.2	Experimental	77
3.3	Structural studies - $\text{Sr}_{0.8}\text{Ca}_{0.2}\text{Mn}_{1-x}\text{Si}_x\text{O}_{3-6}$	80
3.4	Conductivity measurements.....	83
3.5	Chemical compatibility results.....	84

3.6	Area specific resistance results.....	90
3.7	Fuel cell test	94
3.8	Conclusion	95
4	Evaluation of $\text{Ba}(\text{Co/Fe})_{0.9}\text{Bi}_{0.1}\text{O}_{3-\delta}$ perovskite as a fuel cell cathode	97
4.1	Introduction.....	97
4.2	Experimental	99
4.3	Synthesis and X-ray Diffraction analysis of $\text{BaCo}_{0.9-x}\text{Fe}_x\text{Bi}_{0.1}\text{O}_{3-\delta}$	103
4.4	Thermal analysis	109
4.4.1	Dilatometry.....	109
4.4.2	Water contents.....	112
4.4.3	CO_2 Stability results	114
4.5	Conductivity	116
4.6	Chemical Compatibility.....	117
4.6.1	$\text{Ba}_2\text{In}_{1.6}\text{Zr}_{0.2}\text{Si}_{0.2}\text{O}_{5.2} + \text{BaCo}_{0.9-x}\text{Fe}_x\text{Bi}_{0.1}\text{O}_{3-\delta}$	117
4.6.2	Chemical Compatibility CGO + $\text{BaCo}_{0.9-x}\text{Fe}_x\text{Bi}_{0.1}\text{O}_{3-\delta}$	120
4.7	Area specific resistance on $\text{Ba}_2\text{In}_{1.6}\text{Zr}_{0.2}\text{Si}_{0.2}\text{O}$ and $\text{Ce}_{0.9}\text{Gd}_{0.1}\text{O}_{1.95}$ pellet in wet N_2 and O_2	123
4.8	Fuel Cell Test	129
4.9	Cross sectional structure of the fuel cell	131
4.10	Conclusion	133
5	Doping in $\text{Ba}_2\text{Sc}_2\text{O}_5$ to reduce costs and increase stability	135
5.1	Introduction.....	135
5.2	Experimental	137
5.3	Synthesis results	139
5.4	Scanning electron microscopy studies.....	142
5.5	Thermogravimetric analysis (TGA).....	143
5.5.1	Hydration	143
5.5.2	CO_2 stability	145
5.6	Conductivity measurements.....	146
5.7	Synthesis and characterisation of $\text{BaYb}_{0.6-z}\text{Fe}_2\text{B}_{0.05}\text{Ti}_{0.3}\text{O}_{3-\delta}$ ($z = 0.05, 0.1, 0.2$)	151
5.7.1	XRD analysis of $\text{BaYb}_{0.6-z}\text{Fe}_2\text{B}_{0.05}\text{Ti}_{0.3}\text{O}_{3-\delta}$ ($z = 0.05, 0.1, 0.2$)	152
5.7.2	Conductivity measurements.....	153
5.8	Conclusion	156

6	Synthesis and characterization of phosphate doped $\text{Ba}(\text{Y}/\text{Yb}/\text{Tm})_y\text{O}_{3-\delta}$	157
6.1	Introduction.....	157
6.2	Experimental	158
6.3	Structural studies	161
6.4	Conductivity measurements.....	166
6.5	Thermogravimetric analysis	171
6.6	Conclusions	173
7	Conclusions	174
7.1	Silicon doped $\text{Sr}_{0.8}\text{Ca}_{0.2}\text{MnO}_{3-\delta}$ perovskite as a fuel cell cathode with apatite and fluorite electrolytes.....	174
7.2	$\text{Ba}(\text{Co}/\text{Fe})_{0.9}\text{Bi}_{0.1}\text{O}_{3-\delta}$ perovskite as a fuel cell cathode for proton and oxide ion conductors.	175
7.3	Doping $\text{Ba}_2\text{Sc}_2\text{O}_5$ to reduce costs and increase stability.	175
7.4	Synthesis and characterization of phosphate doped $\text{BaPr}_{1-y}(\text{Y}/\text{Yb}/\text{Tm})_y\text{O}_{3-\delta}$	176
8	Further work	177
9	Publication list	178
10	Conference list	179
11	References.....	180

Abbreviations

AC Alternating Current

AFC Alkaline Fuel Cell

ASR Area Specific Resistance

BIZS $\text{Ba}_2\text{In}_{1.6}\text{Zr}_{0.2}\text{Si}_{0.2}\text{O}_{5.2}$

CGO $\text{Ce}_{0.9}\text{Gd}_{0.1}\text{O}_{1.95}$

DC Direct Current

DTA Differential Thermal Analysis

GA-MS Gas Analysis – Mass Spectrometry

GSAS General Structure Analysis System

HOR Hydrogen Oxidation Reaction

HT-XRD High Temperature X-ray Diffraction

ICSD International Crystallographic Structural Database

LCO LaCoO_3

LGSO $\text{La}_{10}\text{GaSi}_5\text{O}_{26.5}$

LSCF $\text{La}_{0.6}\text{Sr}_{0.4}\text{Co}_{0.2}\text{Fe}_{0.8}\text{O}_{3-\delta}$

LSGM $\text{La}_{0.8}\text{Sr}_{0.2}\text{Ga}_{0.8}\text{Mg}_{0.2}\text{O}_3$

LSM $\text{La}_{1-x}\text{Sr}_x\text{MnO}_{3-\delta}$

LSSO $\text{La}_9\text{SrSi}_6\text{O}_{26.5}$

MCFC Molten Carbonate Fuel Cell

MIEC Mixed Ionic Electronic Conductor

NMR Nuclear magnetic Resonance

OCV Open Circuit Voltage

ORR - Oxygen Reduction Reaction

PAFC Phosphoric Acid Fuel Cell

PC-SOFC Proton Conducting Solid Oxide Fuel cell

PEMFC Polymer Electrolyte Membrane Fuel Cell

SCM $\text{Sr}_{0.8}\text{Ca}_{0.2}\text{MnO}_{3-\delta}$

SCMS $\text{Sr}_{0.8}\text{Ca}_{0.2}\text{Mn}_{1-x}\text{Si}_x\text{O}_{3-\delta}$

SEM Scanning Electron Microscopy

SOFC - Solid Oxide Fuel Cell

TEC Thermal Expansion Coefficient

TGA-MS Thermogravimetric Analysis – Mass Spectrometry

TPB Triple Phase Boundary

XRD X-Ray Diffraction

YSZ $\text{Zr}_{1-x}\text{Y}_x\text{O}_2$

Chapter 1

1 Introduction

There is a serious need to find a more efficient energy source to burning conventional fossil fuels, (coal, oil, gas) which we have been dependent on since the industrial revolution.¹ We have become so reliant on fossil fuels as they are convenient for energy production. Their use in power generation is especially a problem, since currently most of our electrical energy is produced through the burning of these fuels (in 2014 over 60% was produced in this way (Figure 1-1).² However the depletion of these fossil fuels, coupled with our increase in energy demands, due to population growth and higher living standards around the world, have caused an

instability in price and supply.³ Furthermore the rise in the production of greenhouse gases is having devastating effects on the planet e.g. CO₂. These gases are known to contributes to the global warming.⁴⁻⁶

Therefore the need to develop cleaner low

carbon energy sources or renewable energy sources, are vital to our energy supply,

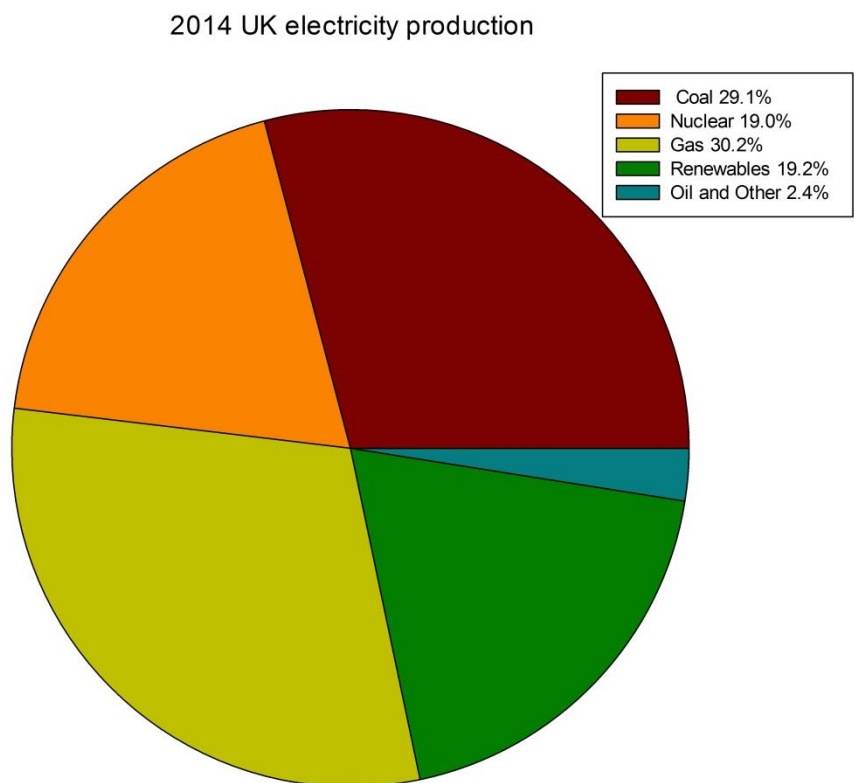


Figure 1-1 the generation of UK electricity in 2014

economy and environment.^{3, 6-9} Current main stream renewable energy sources such as solar, hydroelectric or wind power have great interest but require huge areas of land being available, and have an intermittent supply chain that cannot be relied upon to generate the total amount of energy required indefinitely. Therefore there is the need to make our electricity production more efficient and reliable, one example being the use of fuel cells.¹⁰



**Figure 1-2 Birmingham University
Hydrogen powered car.**

1.1.1 History of fuel cells

A fuel cell is a device that directly converts chemical energy into electrical energy, ideally with no heat loss involved.¹¹⁻¹³ This technology is not a new technology and has been around for over 150 years.^{14, 15} The earliest work on fuel cells was begun in 1839 by William Grove,¹⁶ when he observed an electrical output from the combination of H_2 and O_2 . His experiments produced electrical energy by submerging two platinum electrodes in a sulphuric acid solution, with each end sealed in either oxygen or hydrogen atmospheres.¹⁶ He theorised that there was a contact area between electrode, electrolyte and gas similar to what we know as the triple phase boundary.¹⁷ Continuing on from this, Thomas Francis Bacon produced the first fuel cell that used H_2 and air directly to produce energy in 1933.

His research into fuel cells was used in the war effort for the Royal Navy's submarines in 1939, 100 years after fuel cells were first discovered.¹⁷ The development of fuel cells continued and further practical uses were found late into the last century for the Apollo space missions.^{14, 18} Even today research on fuel cells and their application is of great interest, and in the last 10-15 years public opinion and knowledge of fuel cells and renewables has increased.^{19, 20} Both portable and stationary applications are commercially available, with automobiles fitted with fuel cells, and household natural gas fuel cell systems replacing the current gas boilers.^{9, 21}

1.1.2 How a fuel cell works

In principle all fuel cells operate in much the same way and consist of a similar structure and components; two electrodes (cathode and an anode) placed either side of an electrolyte material.^{12, 22}

They operate in a similar way to our mobile phone batteries

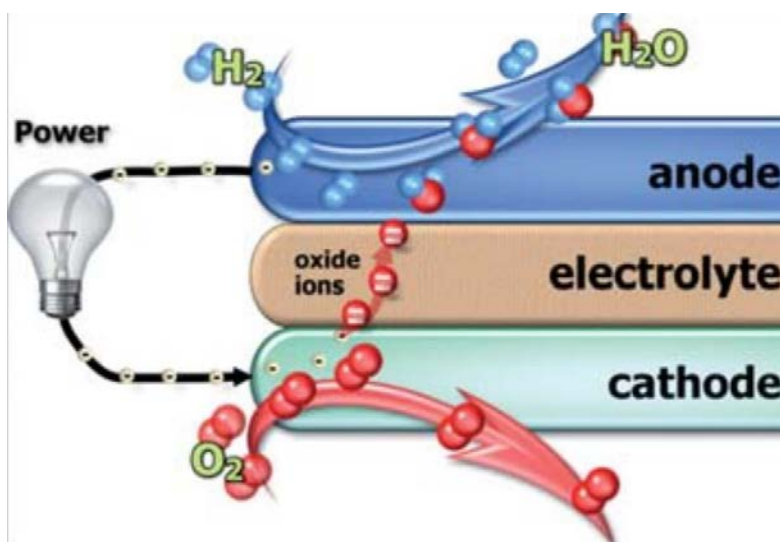


Figure 1-3 Diagram showing the simple operation of a fuel cell Taken from Energy & Environmental science with permission from the RSC.

in that a chemical process takes place to produce electricity. However, a key difference compared with a battery, where the reactants are stored in limited amounts in the electrodes, is that a fuel cell will provide continuous power for as long as external fuel and oxidants are supplied.

The electrolyte usually conducts oxide ions or protons, and the chemical reactions occur at each of the respective electrodes to combine molecules of the fuel and oxidant to produce external electrical energy.^{12, 16, 23} The fuel used and the type of cell used will have an effect on the half reactions and the overall chemical reactions. For simplicity, the solid oxide fuel cell (SOFC) electrode processes for a pure hydrogen fuel cell are shown below¹²:-



The oxidant, usually air, is supplied to the cathode; this undergoes the oxygen reduction reaction forming two oxide ions. The oxide ions move through the electrolyte towards the anode. Once at the anode the oxide ions and hydrogen fuel meet and combine to produce water and four electrons. The electrons pass through the external circuit from the anode to the cathode producing the power (Figure 1-3).²⁴ The performance of the fuel cell depends on the properties of the component materials.²⁵

1.1.3 Fuel cell efficiency vs. fossil fuels

The fuel cell has the potential to have a significantly improved efficiency over the burning of fossil fuels to produce electricity. In a fuel cell the efficiency is generally higher due to the direct energy conversion from chemical to electrical energy.²⁶

The fuel cell efficiency is given by the thermodynamic efficiency η , which is the change in Gibbs function (electrical work done) in relation to the change in enthalpy (heating value of the fuel i.e. hydrogen) Equation 1-4.^{12, 27}

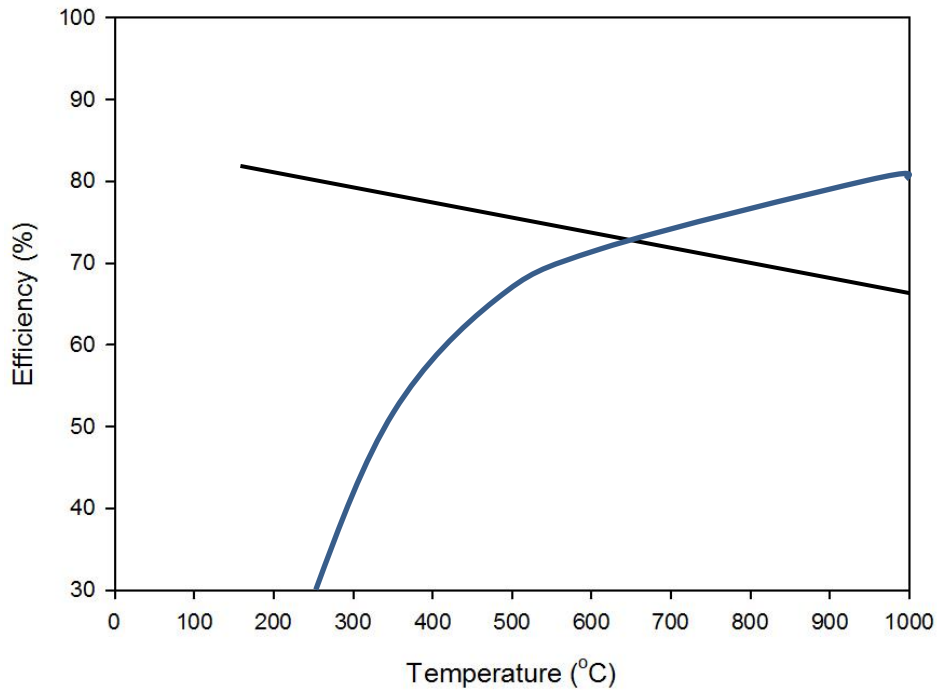


Figure 1-4 Schematic trend of the maximum Efficiency of H₂ fuel cell at standard pressure (steam as a product = Black line), Carnot limit with 50°C exhaust temperature (blue line)

$$\eta = \frac{\Delta G}{\Delta H} \quad \text{Equation 1-4}$$

Consequently, the efficiency of a fuel cell decreases with temperature as the Gibbs function become less negative due to increased entropy at higher temperatures.²⁸ In addition to the higher efficiency at lower temperatures, fuel cells typically produce lower harmful emissions than conventional electrical power generation. Moreover if H₂ is used as the fuel, the only by-product is H₂O.¹⁶ There are also fewer moving parts than in a conventional combustion system reducing noise and vibrations, leading to a quieter system and lower maintenance requirements.¹³ These advantages allow for applications ranging from local power generation, to transport and even small portable devices.⁷ Furthermore the fuel

flexibility of some fuel cells (e.g. solid oxide fuel cells) has meant that they have been proposed as a bridging gap between the current fossil fuel hydrocarbon (previous experiments reporting CH₄ oxidation in to CO₂ and H₂)²⁹ and the hydrogen based economy proposed for the future.³⁰

1.1.4 Types of fuel cell

Different types of fuel cells are available, normally categorised into high and low temperature fuel cells, and named according to the electrolytes used (solid or liquid based).

There are five common fuel cell types, each with their own positive and negative features, summarised in Table 1-1 and Figure 1-5.^{12, 26, 27, 31,32, 33,34}

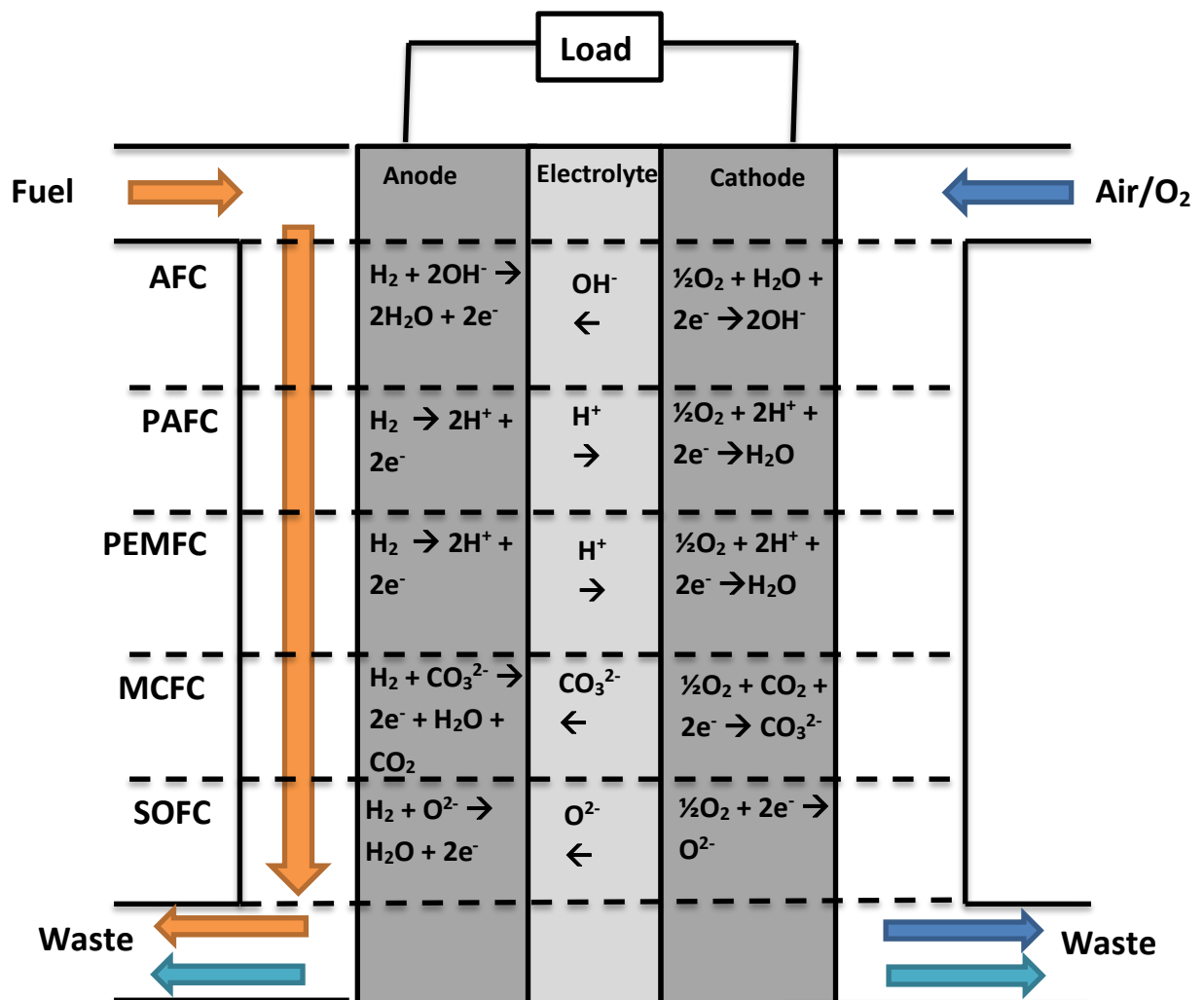


Figure 1-5 Types of Fuel Cells

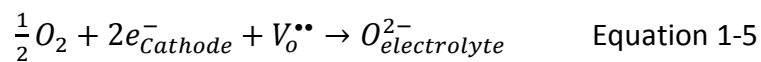
Table 1-1 Operating temperature, electrolyte employed, advantages and disadvantages, and applications of the various fuel cell systems.

Fuel Cell type	Operating Temp °C	Electrolyte	Advantages	Disadvantages	Application
Alkali (AFC)	50-100 <i>Low</i>	Concentrated Potassium Hydroxide (liquid)	-Cheapest fuel cells to produce. - Fast kinetics for the oxygen reduction reaction	-Susceptible to CO ₂ from the air. Leading to Performance degradation	Speciality transport to medium CHP (combined heat and power)
Phosphoric acid (PAFC)	150-200 <i>High</i>	Phosphoric acid (liquid)	-Higher temperature operation allows the use of impure fuels as the cell is CO ₂ and CO tolerant even at high levels.	-Highly corrosive nature of hot phosphoric acid. -Long start up time.	Medium to large scale CHP
Polymer (H⁺/OH) (PEMFC)	50-100 <i>Low</i>	Sulfonated fluoro polymer membrane (solid)	-Low temperature allows fast start up time	-Expensive catalyst materials. -Sensitive to fuel impurities due to low temperature operation.	Portable devices to medium CHP
Molten Carbonate Fuel Cell (MCFC)	600-650 <i>High</i>	Alkali metal carbonates (liquid)	-High temperature operation allows the use of impure hydrogen fuels, and cell is not susceptible to poisoning by CO and CO ₂ . - can use a variety of catalysts.	-High temperatures and the corrosive electrolyte corrodes the cell, decreasing cell life. -Long start up time. -feeding of CO ₂ to cathode required	Medium to Large CHP
Solid Oxide Fuel Cells (SOFC)	500-1000 <i>High</i>	Ceramic (solid)	-High Efficiency. -Fuel Flexibility -All solid state systems -Cheaper electrodes -CO no longer poisons the catalyst, but rather can be a fuel. High temperature exhaust can be used to generate further electricity (co-generation)	-High operating temperature. -Long start up time. -Thermal compatibility and expansion issues -Cell sealing issues	Small to large CHP

1.1.5 Solid Oxide fuel cells

The focus of this project is the development of new materials for solid oxide fuel cells (SOFCs) for operation at intermediate temperatures (500°C-700°C). SOFCs use a solid ceramic electrolyte, which conducts via either oxide ions or protons. The solid electrolyte removes the problems of liquid based systems (PAFC, MCFC), such as the leakage issues and high corrosion.¹⁶ The higher temperature operation of the system allows the use of cheaper electrodes, avoiding the need for expensive metal catalysts e.g. platinum.³⁵ Even though the high temperature lowers the theoretical maximum thermodynamic efficiency of the fuel cell, the higher temperatures increases the reaction kinetics at the triple phase boundaries (TPB) and so improves the overall achievable performance.

A TPB is the point at which the three different phases meet i.e. electrolyte (conducting ions), electrode (conducting electrons) and the gas (either the fuel (anode) or oxidant (cathode)). It is at these points that the electrochemical reaction occurs; for example, the oxygen from the air is reduced at the boundary to form oxide ions which move to the electrolyte (Equation 1-5).



The amount of TPB points are limited in a conventional set up as shown in Figure 1-6a²⁴ and the kinetics would only increase when more energy is available (even higher temperatures). Therefore, in order to increase the kinetics of the chemical reactions involved in a fuel cell at the same temperature, more TPB points must be introduced. A method to do this is to employ electrode/electrolyte composites, which ensures the electrode has both ionic and electronic conductivity Figure 1-6b.²⁴ This allows the oxide

ions to pass through to the electrolyte meet the component of the composite, in this case an anode electrolyte composite. The additional reaction sites cause an increase in the electrochemical reactions and therefore improve performance.^{24, 36} However in Figure 1-6b the highlighted regions 1 and 2 illustrate the possible deactivation areas of the TPB composite where there is not an oxide ion pathway (1) or an electronic pathway (2).²⁴

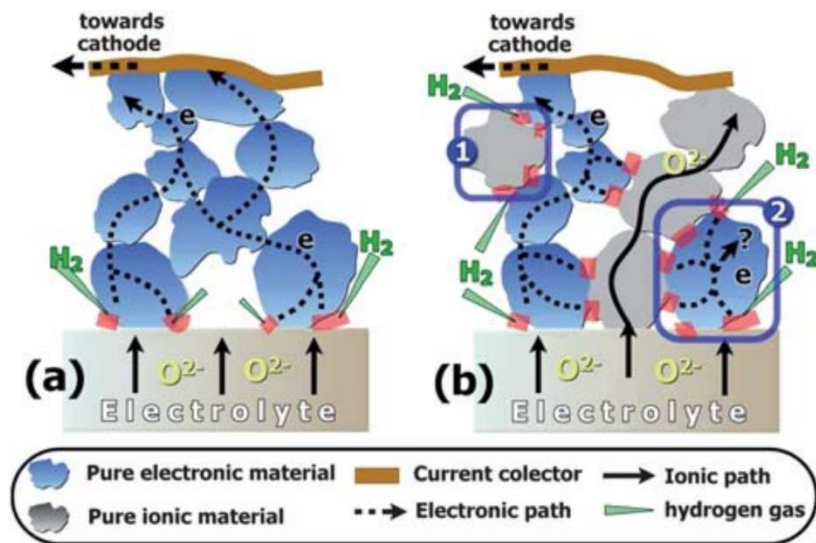


Figure 1-6 Illustration of a) pure anode in contact with an electrolyte b) Composite material of anode and electrolyte in contact with an electrolyte. (red sites are the triple phase boundary points showing the meeting of O²⁻, e⁻ and H₂). Taken from Energy & Environmental science with permission from the RSC.

The total voltage output of the SOFC is equal to the predicted thermodynamic potential, minus the voltage associated with the activation losses, the ohmic losses and mass transport losses (Equation 1-6).

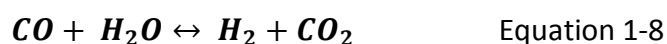
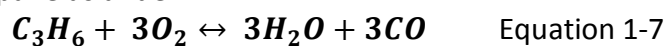
$$V_{output} = E_{thermo} - V_{activation} - V_{ohmic} - V_{mass\ transport} \quad \text{Equation 1-6}$$

Table 1-2 Explanation of the thermodynamic potential and the losses occurred to a fuel cells output voltage

V_{output}	Total voltage output under operation of the fuel cell
V_{activation}	These are the losses due to the kinetic limitation of the reactions of the TPB at the electrodes.
V_{ohmic}	These are the losses associated with movement of the charge carriers through the fuel cell.
V_{mass transport}	These are the losses associated with the removal of waste materials and the supply of fuel /oxidant at the TPB, which becomes most significant at high current densities
E_{thermo}	Thermodynamically predicted potential

Taking Equation 1-6 and its factors into account, the lower theoretical thermodynamic efficiency caused by the higher temperature can be overcome. The total performance output of the cell can be maximised by operating at elevated temperatures as this minimises the losses. In addition, using a high temperature allows a wide range of fuels (hydrogen-hydrocarbon) to be used, thus removing the need to purify the fuel and allowing internal reforming in the cell.^{16, 35, 37} Internal reforming can be achieved in a SOFC to allow the use of smaller hydrocarbons as fuels. For example if propane was supplied as the fuel to the anode it would undergo reactions to produce hydrogen and CO, with CO further reacting with H₂O to give H₂ and CO₂ (Equation 1-7 and Equation 1-8).²¹ Further gains in efficiency can be achieved making use of waste heat to deliver a combined heat and power system (CHP).

Reactions with propane as a fuel:



However, there are critical disadvantages to using hydrocarbons and the high temperature operation of fuel cells. Hydrocarbon fuels added to the anodes side usually contain impurities such as sulphur which can poison the anode. The high temperature operation, (800°C-1000°C for traditional systems) has also limited the commercial applications, due to issues with the long term stability of the materials used and the sealing of the cell.^{38, 39} Lowering the operational temperatures to around 500°C would help to solve many of these disadvantages whilst keeping the advantages. However with the current materials such as yttria stabilised zirconia electrolyte, this can severely limit the cells performance and so there is a key need to develop new materials with improved properties.^{40, 41}

The anodes in the SOFCs must have high electrocatalytic activity for the hydrogen oxidation reaction (HOR) while the cathode must have high activity for the oxygen reduction reaction (ORR). Both electrodes require high electronic conductivity to transport the electrons to/from an external circuit and they must also be stable in the harsh oxidising (cathode) and reducing environments (anode).⁴² Together they must also show compatible chemical stability and thermal expansions with the electrolyte that they sandwich. The production of an intermediate temperature fuel cell would be beneficial not only in terms of stability and sealing of the cell, but also for the overall production and maintenance costs.⁴³ Therefore new electrode and electrolyte materials are necessary to operate SOFCs successfully at intermediate temperatures (500°C-700°C).

1.2 Conventional materials for SOFCs

1.2.1 Oxide ion conducting electrolytes

SOFC electrolytes need high ionic conductivity, negligible electronic conductivity, good densification and chemical/thermal stability at both the operating temperature and in reducing/oxidising conditions.^{4,38} Conventional electrolytes conduct through the migration of oxide ions and in this respect, the traditional SOFC electrolyte materials are the fluorite-type oxide ion conductors, which conduct through the migration of oxide ions via a vacancy hopping mechanism.^{38,44,45} In general the ionic conductivity of these vacancy conducting electrolytes can be improved by; increasing the fraction of vacancies available, having an open framework to allow the movement of ions, and having full and vacant sites of comparable energy.⁴⁶ An alternative conduction mechanism is displayed by the more recently developed apatite electrolytes. They have been shown to conduct via an interstitial oxide ion conduction mechanism, with the flexibility of the structure allowing the accommodation of extra oxide ions in interstitial sites within the structure.

1.2.1.1 Fluorite electrolytes

The most common SOFC electrolyte is based on zirconia ZrO_2 which has the fluorite structure, and below 2300°C is a poor conductor. Above this temperature a phase change from monoclinic to cubic occurs and the conductivity increases significantly.^{46, 47} In this structure the Zr^{4+} cation forms a face centred cubic lattice with O^{2-} anions in the tetrahedral sites.²⁵ In order to stabilise this cubic structure to lower temperatures various doping strategies have been employed. This involves lower valent dopants (Y^{3+} , Yb^{3+} , Gd^{3+} , Ca^{2+} , Mg^{2+}) on the Zr^{4+} site, which have two beneficial effects; namely they stabilise the cubic structure (favouring disorder) and at the same time produce oxygen vacancies.³⁵ Doping

with Y^{3+} to give yttria stabilised zirconia (YSZ) has proven to be the most widely used electrolyte, due to its low cost and its good mechanical and electrical properties.⁴⁸ However this electrolyte requires high operating temperatures (800-1000°C) to provide the acceptable oxide ion conductivity. This is a major disadvantage in the operation of the cell, causing problems in terms of stability and sealing of the overall cell.^{38, 49} Further doping studies with scandium have provided stabilised zirconia with higher oxide ion conductivity, and machine processes to produce thin films have been attempted but both these strategies are at the expense of increasing costs.

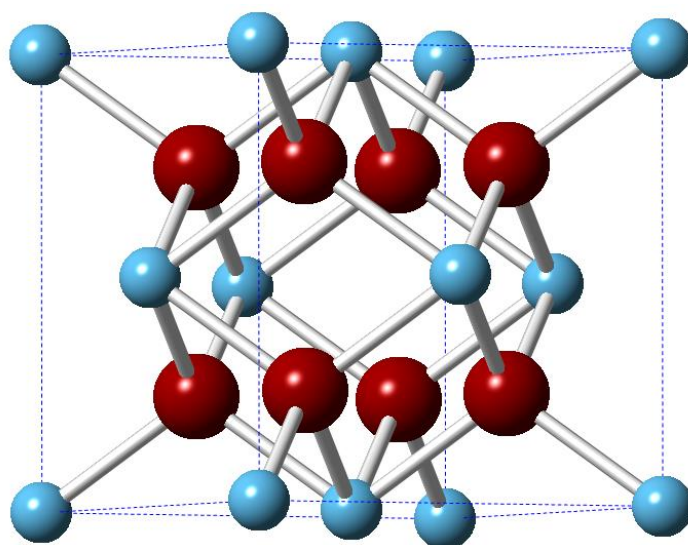


Figure 1-7 Fluorite structure XO_2 ; cations are blue and oxide anions are red $\text{X} = \text{Zr}, \text{Ce}$.

Another fluorite electrolyte material is doped CeO_2 , which has a better ionic conductivity than YSZ at lower temperatures. The dopants (e.g. Sm^{3+} , Gd^{3+}) produce oxide ion vacancies which increase the ionic conductivity and allow a lower operating temperature to be used (500-700°C).^{38, 43, 50} The disadvantage of stabilised ceria is that at temperatures above 600°C in low partial pressure of O_2 , partial reduction of the ceria takes place converting some Ce^{4+} to Ce^{3+} . This leads to a reduction in the overall voltage of the cell as the electronic

conductivity is no longer negligible (some electrons flow through the electrolyte) leading to partial cell short circuiting.⁵¹⁻⁵³

1.2.1.2 Apatite electrolytes

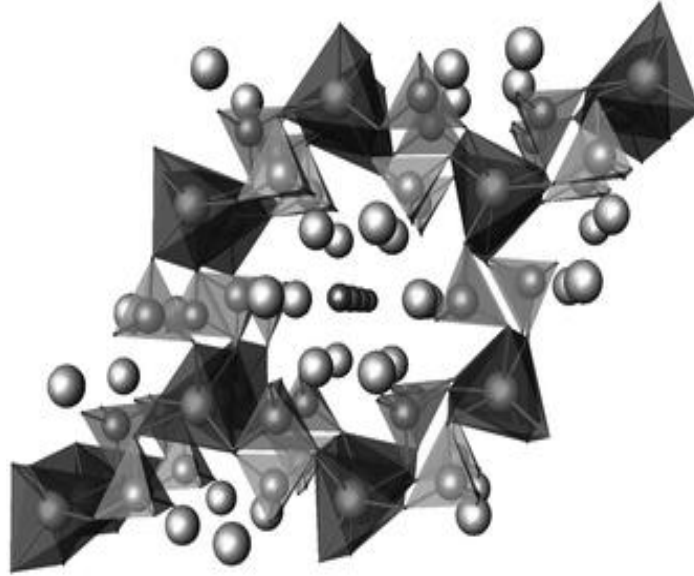


Figure 1-8 Apatite structure (tetrahedral (XO₄), Large sphere = M small sphere = O

Apatite electrolytes have been widely researched due to reports of high oxide ion conductivity and lower activation energies for oxide ion conduction than the conventional YSZ electrolytes.^{38,54} The high conductivity of this system was first reported in 1995, and they have the general formula $M_{10-x}(XO_4)_6O_{2+y}$, (M = alkaline or rare earth metal and X = Si, Ge, P).^{38,44,55} The apatite structure consists of $(M_4)(XO_4)_6$ framework with the remaining M_6O_2 occupying the channels (shown in Figure 1-8).⁴⁴ The silicate and germanate apatite systems have been shown to have the highest oxide ion conductivity, and have a great flexibility to dope on either the M or X site to introduce oxide ion excess.^{4, 45, 55} Apatite silicate and germanate systems, in particular, are reported to conduct by an interstitial oxide ion mechanism, with the structure having the capability to accommodate excess O^{2-}

ions. In contrast, the inability to accommodate these excess oxide ions accounts for the poor conductivity seen in apatite phosphate systems.

The high conductivity of the silicate apatites has attracted major research for SOFCs due to the lower activation energy and lower cost of the raw materials compared to the germanate systems. The fully (cation and oxygen) stoichiometric systems $\text{La}_8\text{A}_2\text{Si}_6\text{O}_{26}$ ($\text{A} = \text{Ca}, \text{Sr}, \text{Ba}$), however, show extremely poor conductivity (e.g. for $\text{La}_8\text{Sr}_2\text{Si}_6\text{O}_{26}$ $\sigma = 5.6 \times 10^{-4} \text{ S cm}^{-1}$ at 800°C).^{56, 57} Computer modelling studies suggest the stoichiometric systems have no interstitial oxide ions and that the poor conductivity seen is due to a vacancy conduction mechanism only (with such vacancies present due to low levels of Schottky defects).⁵⁶ Further studies of apatite silicate systems have shown a major improvement in the conductivity, provided by either the incorporation of oxygen excess or by the presence of cation vacancies, the latter are believed to create interstitial oxide ions by enhancing Frenkel defect formation.^{38, 58, 59} However the location of the interstitial sites that mediate the conduction mechanism has proven difficult to conclusively identify, and the conduction is seen to be anisotropic, with much higher conductivity seen parallel to the c direction than perpendicular.^{58, 60} The introduction of oxygen excess systems in particular leads to higher conductivity. The extra oxygen is believed to be located within the channels for the silicate apatites, allowing oxide ion migration through the structure, with a maximum of 0.5 excess oxygen per formula unit being accommodated in the channels for the silicate apatites.⁶¹ The doping on the Si^{4+} site with Al^{3+} , Mg^{2+} , or Ga^{3+} with concomitant charge balancing by increasing the lanthanum content has also provided higher conductivity results, especially if oxide ion excess is present e.g. $\text{La}_{9.8}\text{Si}_{5.7}\text{Mg}_{0.3}\text{O}_{26.4}$ $\sigma_{800^\circ\text{C}} = 0.074 \text{ S cm}^{-1}$.⁶¹ The added advantage of these apatite materials is that their thermal expansion is compatible with

known electrode materials.³⁸ The disadvantage of these apatite systems is the high temperature (>1600°C) required to produce dense membranes and large grain sizes, required for a SOFC electrolyte.⁶² In addition other researchers have suggested problems with the chemical compatibility of silicon containing materials with conventional perovskites.⁴⁹ So far fuel cell testing containing $\text{La}_{9.8}\text{Si}_{5.7}\text{Mg}_{0.3}\text{O}_{26.4}$ electrolyte, $\text{La}_{0.8}\text{Sr}_{0.2}\text{CoO}_3$ cathode and Ni-Sm doped ceria anode has achieved a power density of 120 mW cm^{-2} at 800°C, which is much lower than current YSZ based systems, showing the need for further development work.⁶¹

1.2.1.3 Perovskite materials

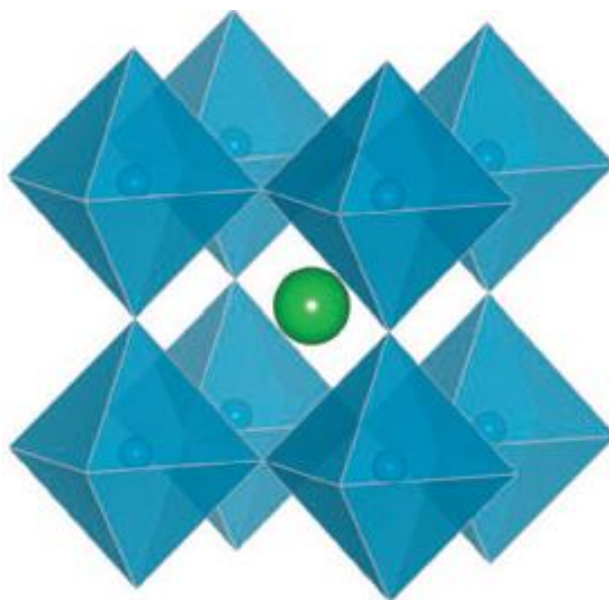


Figure 1-9 :- Perovskite structure showing corner-shared BO_6 octahedra with A centred on 12-coordinate sites.

Perovskite (CaTiO_3) is a mineral found in nature, however, it is now more used as general description for a material with the same type of crystal structure. The ideal formula for a perovskite oxide is ABO_3 . The structure of a cubic perovskite is shown above in Figure 1-9, and it consists of an A cation in the centre with 12 anions coordinated around it.²⁵ The B cations are on the corners of the cell with octahedral co-ordination to the anions. The

perovskite structure has great flexibility in the cations it can contain, although the A cation is required to be larger in comparison to the B cation. The crystal class that the structure forms i.e. cubic, hexagonal, tetragonal, and so forth, can be predicted by the Goldschmidt tolerance factor. This factor is calculated from the ionic radii (Equation 1-9)

$$\text{tolerance factor} = \frac{(R_a + R_o)}{\sqrt{2}(R_b + R_o)} \quad \text{Equation 1-9}$$

For an ideal cubic perovskite, the tolerance factor will be equal to one. However, the many combinations of cations on both A and B sites result in a non-ideal structure and a tolerance factor that deviates from one.⁶³⁻⁶⁵ If the B cation is too large, a tolerance factor lower than 1 is obtained. This causes strain in the structure, which is compensated by tilting of the octahedra to remove the strain, resulting typically in a unit cell of lower symmetry. If the factor is greater than 1 the B cation is too small, so there will either be displacement of the B cation off centre, as in BaTiO₃, or a change in the structure where there will be some face sharing of the BO₆ octahedra leading to a hexagonal perovskite system. The cation is not the only ion that can affect the tolerance factor, as the change in stoichiometry of the structure (usually oxygen) can also allow deviations from the ideal value of 1. Oxygen vacancies can cause or relieve the strain on the structure, e.g. by altering the B cation oxidation state (hence its size). Perovskite electrolytes are usually formed through doping of the A and B sites with aliovalent cations. These cause oxide ion vacancies and give rise to the high oxide ion conductivity seen in some perovskite electrolytes e.g. Sr and Mg doped LaGaO₃ (LSGM). However, producing too many oxide ion vacancies will result in a structure change e.g. for the highly deficient SrFeO_{2.5} the brownmillerite structure is formed. The brownmillerite structure is an oxide ion vacancy ordered perovskite structure

consisting of alternating octahedral and tetrahedral B cation layers. This ordering of the oxide ions significantly decreases the oxide ion conductivity.

1.2.2 Proton conducting electrolyte

Traditionally the electrolyte used in SOFCs consists of an oxide ion conductor, e.g. Gd doped CeO₂ or YSZ. However it was reported that high temperature proton conductivity was possible in some systems containing no structural proton, such as Gd doped BaCeO₃ ($\sigma_{600^\circ\text{C}} = 0.05 \text{ S cm}^{-1}$).^{66, 67} Further research into proton conductivity was conducted and oxides that were originally thought to show only oxide ion conduction, were shown to display proton conduction in a wet atmosphere.^{38, 68, 69} The proton conduction is provided by the adsorption of water molecules from the gas phase into oxide ion vacancies. The water dissociates to produce hydroxide defects at the cost of an oxide ion vacancy.^{25, 38, 68-71}



The proton conduction mechanism in perovskite electrolytes involves the transfer of protons between the OH⁻ ions and the O²⁻ ions in the structure (Grotthus mechanism),^{69, 71-73} rather than the vehicle mechanism of hydroxide ion transport.^{38, 73} The neighbouring environments of the oxygen atoms and the hydroxide ion have a major effect on the proton conduction, with the rate limiting step being the proton transfer between the OH⁻ and O²⁻, as the reorientation step involved is predicted to be faster, due to a lower activation energy.^{25, 71}

The advantage of SOFCs utilising a proton conducting electrolyte is that a lower operating temperature can be used due to the lower activation energy for proton conduction, which is typically 2/3 that of oxide ion conduction. Furthermore the transport

of protons removes potential water management issues on the anode side, as the fuel is no longer diluted since the water exhaust is now produced on the cathode side of the cell.⁶⁹ There are a number of high temperature protonic conductors suitable for proton conducting solid oxide fuel cell (PC-SOFC) electrolytes, with the most promising having the perovskite structure.

1.2.2.1 Perovskite-type proton conducting electrolytes

The most promising ceramic oxide proton conductors, discovered first in the 1980s and since then extensively studied, are the perovskite-type cerates and zirconates. Both the cerate systems, BaCeO₃ and SrCeO₃ doped with a trivalent cation (e.g. Gd³⁺/Y³⁺), are shown to have high protonic conductivity, with the BaCeO₃ based systems having the highest.⁷⁴ However both BaCeO₃ and SrCeO₃ have poor mechanical and chemical stability, being susceptible to CO₂ below 800°C which can result in decomposition and the formation of non-conducting carbonates e.g. BaCO₃.⁷⁴⁻⁷⁶ Zirconate perovskite-type systems such as BaZrO₃ have been shown to have the higher mechanical and chemical stability required for commercial applications, but a much lower protonic conductivity due to a high grain boundary resistance.^{69, 74, 75} Further research has been conducted on these two systems whereby Zr⁴⁺ doping into the BaCeO₃ system can provide both improved stability along with comparable proton conductivity of the pure cerates.^{69, 70, 74} A number of lanthanum containing systems have also been shown to display protonic conduction despite no structural protons, with lanthanum phosphates, lanthanum niobate and lanthanum barium gallate being the most researched systems.

1.2.2.2 Lanthanum phosphate

Lanthanum orthophosphate (LaPO_4) came under intense research in the 1990s due to its high chemical stability and unexpected protonic conduction (albeit of relatively low magnitude).^{73, 77-80} The proton conductivity is introduced through alkaline earth doping to introduce oxide ion vacancies. The oxide ion vacancies are accommodated as $\text{P}_2\text{O}_7^{4-}$ units that are capable of adsorbing water from a wet atmosphere, breaking up the $\text{P}_2\text{O}_7^{4-}$ units to give hydrogen phosphate ions (HPO_4^{2-}).^{6,45,49} The larger sized Sr^{2+} doping provides a higher conductivity than the Ca^{2+} doped system, with negligible electronic conductivity at intermediate temperatures.^{77, 79} However excess doping in the LaPO_4 system causes impurities to form at the grain boundaries e.g. $\text{Sr}_2\text{P}_2\text{O}_7$, which decreases the conductivity.⁷⁸ Further disruption to the conductivity is seen at high sintering temperature (above 1350°C), due to the appearance of impurity phases in both the Sr^{2+} and Ca^{2+} doped LaPO_4 .⁷⁷ The proton conductivity at 900°C in a wet atmosphere is $3 \times 10^{-4} \text{ S cm}^{-1}$ and $2 \times 10^{-4} \text{ S cm}^{-1}$ for Sr^{2+} and Ca^{2+} doped LaPO_4 respectively.⁷⁷ These low levels suggest that it is not viable material for commercial SOFCs.

1.2.2.3 Lanthanum niobate

Lanthanum niobate has attracted the most recent interest, for which alkaline earth doping leads to significant proton conductivity^{69, 76} On Sr^{2+} or Ca^{2+} doping, oxide ion vacancies are accommodated as defect clusters e.g. $\text{Nb}_3\text{O}_{11}^{7-}$. The highest conductivity is seen for the Ca^{2+} doped LaNbO_4 (0.001 S cm^{-1} at 800°C).^{81, 82} However problems are seen with these system in terms of the thermal expansion co-efficients and chemical reactions of doped LaNbO_4 with potential cathodes e.g. LaCoO_3 . On the other hand good chemical compatibility can be seen between LaNbO_4 and LaMnO_3 based cathodes, with high stability towards a CO_2

environment.^{25, 76} Therefore to achieve a successful SOFC with doped LaNbO_4 further work is required to either increase the protonic conduction, which is much too low for commercial application at the moment, or to produce thinner electrolyte layers with the mechanical strength and stability required.⁸²

1.2.2.4 Lanthanum barium gallate

The lanthanum barium gallate system ($\text{La}_{1-x}\text{Ba}_{1+x}\text{GaO}_{4-x/2}$) displays both oxide and proton conductivity, in this structure, the Ga^{3+} is tetrahedrally co-ordinated.⁸³ The addition of extra Ba^{2+} or Sr^{2+} in place of La^{3+} increases the conductivity by forming oxide ion vacancies, which are available for H_2O incorporation. These oxide ion vacancies are accommodated by the formation of $\text{Ga}_2\text{O}_7^{8-}$ units. The $\text{La}_{0.8}\text{Ba}_{1.2}\text{GaO}_{3.9}$ system has the highest conductivity of $1 \times 10^{-4} \text{ S cm}^{-1}$ at 800°C ⁸³⁻⁸⁵ Further research is required to improve the performance of such systems as well as examine the chemical and mechanical compatibility with commercially used electrodes.

Overall proton conducting electrolyte research is dominated by barium based perovskite type systems, but the doped lanthanum based systems do provide alternative avenues of research for proton conducting electrolytes, which have improved CO_2 stability.

1.3 Electrodes

SOFCS requires two electrodes, a cathode and an anode, and these have attracted considerable research effort over the last 60 years. The greatest problem for the traditional cathode material at intermediate temperature ($500\text{-}700^\circ\text{C}$) is the poor kinetics of the ORR. This is the limiting factor for most cathode materials and therefore solid oxide fuel cells; “The overall reaction cannot move faster than the slowest step”.⁸⁶ Limitations for the

anode is its toxicity with nickel based materials used and its chemical stability due to either sulphur poisoning or the hydrogen reducing atmospheres.

1.3.1 Cathode materials

As previously mentioned the cathode in SOFCs is supplied with air and the O_2 adsorbs to the surface of the cathode and is reduced to form two oxide ions by accepting electrons, with this reaction usually occurring on what is known as a TPB. In the case of an oxide ion conducting electrolytes, the oxide ions are then transported through the remaining cathode to the dense electrolyte and through to the other side of the cell combining with hydrogen at the anode forming water. For this all to occur the cathode must possess certain properties a

- High electronic conductivity in an oxidizing environment.
- High oxide ion conductivity.
- Good chemical compatibility and thermal stability with the electrolytes and interconnector materials.
- High catalytic activity towards the oxygen reduction reaction (ORR).
- Sufficient TPB and porosity to allow for O_2 diffusion.
- Low cost.

1.3.1.1 Platinum

Platinum was the first cathode material used successfully in SOFCs and is still scientifically one of the best today. Generally, platinum now is used in small amounts as a paste or on a supported material, so that the cathode contains small Pt particles on a larger substrate. This provides a high surface area for the Pt and defined particle sizes, this results in an

increased efficiency of the Pt cathode. Problems do still exist with Pt cathode, mostly associated with its cost which has limited its use commercially. In addition Pt cathodes can be poisoned at low temperatures by CO, if this enters the cell and absorbs to the surface it can block the active sites and reduces the efficiency. Mixed cathode alloys containing Pt and Ru have been investigated to solve this problem however this increases costs even further and is not commercially viable. In the 1960s it was discovered that low cost transition metal oxides with the perovskite structure could be used as an alternative to Pt based cathodes.

1.3.1.2 Perovskite cathodes

The highly flexible perovskite structure allows for its potential use as not only a electrolyte but also a cathode.⁸⁷ The traditional perovskite oxide ABO_3 , consists of a metal oxide containing a large alkaline or rare earth cation (A) and the smaller transition metal cation (B) such as $SrCoO_3$ (SCO), $LaCoO_3$ (LCO) and $LaMnO_3$ (LMO). Perovskites can alter their symmetry when heated for example SCO can have three structure types depending on the temperature orthorhombic $>653^\circ\text{C}$ hexagonal $>920^\circ\text{C}$ cubic Figure 1-10.⁸⁸ At each structure change there is an increase in the electronic conductivity, however extremely high temperatures are required to give conductivity values which are required for a successful SOFC cathode.

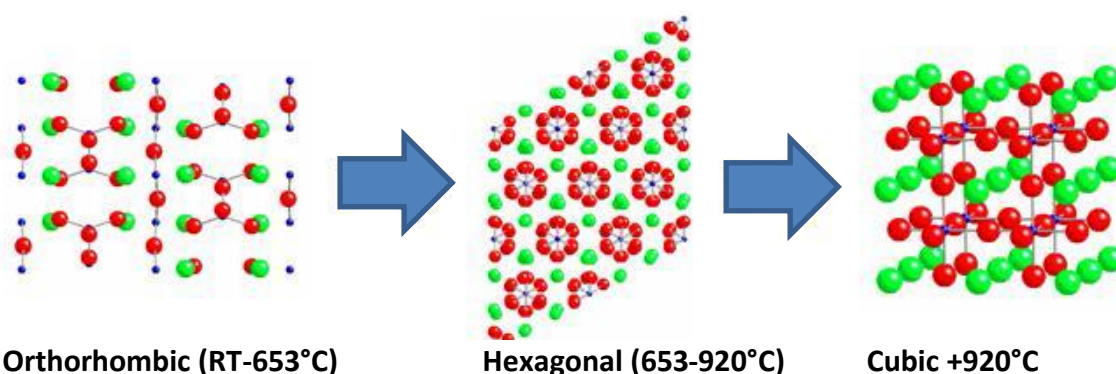


Figure 1-10 $SrCoO_3$ perovskite structure showing the change of structure as the temperature is increased (strontium = green, cobalt = blue, oxygen = red)

The majority of undoped perovskite materials at intermediate fuel cell temperatures are poor conductors in air, and therefore also poor cathode materials. Consequently, doping of these materials with lower valent dopants Ca^{2+} or Sr^{2+} on to La^{3+} site is typically performed, which introduces mixed valency. The size and charge of each dopant affects the perovskite system. $\text{La}_{1-x}\text{Sr}_x\text{CoO}_{3-\delta}$ (LSC) was reported as a cathode for SOFCs in 1966 and is an oxygen deficient perovskite, with the oxygen vacancies allowing for increased oxide ion conduction.⁸⁹ $\text{La}_{1-x}\text{Sr}_x\text{CoO}_{3-\delta}$ (LSC) provides better catalytic performance than other perovskites but when used in conjunction with commercial electrolytes, for example YSZ or CGO, there are problems due to its larger thermal expansion co-efficient in comparison. This can lead to the cell undergoing thermal cracking and degradation under operation. A composite of LSC and the electrolyte can be used to lower the differences in the thermal expansion of the cathode and electrolyte, and is also as a way to produce more reaction sites improving the performance of the electrode. However, even in these cases the high thermal expansion co-efficient is still an issue.

Following on from this perovskite $\text{La}_{1-x}\text{Sr}_x\text{MnO}_3$ (LSM) was proposed in 1975; it was found that doping the La^{3+} site with Sr^{2+} causes the oxidation of the Mn^{3+} to Mn^{4+} to charge compensate. This resulted in high electronic conductivity and high catalytic activity for the ORR. The LSM perovskite structure is stable and possesses high p-type conductivity in oxidising atmospheres ideal for cathodic conditions. However, at intermediate temperatures (<800°C) low ionic conductivity is a limiting factor, while at higher temperatures there are issues with poor chemical compatibility with YSZ, the most commercially available electrolyte. In particular at the YSZ/LSM boundary a nonconductive

layer of $\text{La}_2\text{Zr}_2\text{O}_7$ can form at elevated temperatures, which decreases the overall performance of the cell.⁹⁰

$\text{La}_{1-x}\text{Sr}_x\text{Co}_y\text{Fe}_{1-y}\text{O}_3$ (LSCF) is a perovskite type material currently under intense investigation as it is suitable for use at intermediate temperatures, having high electrocatalytically activity and a more than acceptable chemical stability and thermal expansion coefficient with commercial electrolytes. The mixing of the LSCF with commercial electrolytes forms a composite cathode.³⁶ The LSCF is utilised mainly as the electronic conductive phase and the electrolyte materials as the ionic conductive phase. The composite allows both electrons and oxide ions to move simultaneously through the cathode. However, the LSCF does have a lower electro catalytic activity when compared to LSC and LSM due to the Fe^{3+} doping, and has some potential reaction issues with chromium from the interconnectors forming SrCrO_4 which poisons the cathode affecting the ORR.⁹¹

Overall the research on doped perovskite cathode has shown many positives for the ORR and ionic conductivity, but has resulted in negatives relating to; the composition of the composite cathode, the interconnectors, the particle size and microstructure, and the chemical and thermal stability.

1.3.1.3 Ln_2NiO_4

More recently $\text{Ln}_2\text{NiO}_{4+\delta}$ materials have been proposed as a new potential cathode material. They have a variety of electrical and catalytical properties making them suitable as cathodes for SOFCs. These systems have the well-known K_2NiF_4 type structure (Figure 1-11) which consists of perovskite type LnNiO_3 layers separated by rock salt type LaO^+ layers.⁹² Each layer has advantageous properties for a cathode material; the perovskite layer can accommodate oxygen vacancies while the rock salt layer can accommodate

oxygen interstitials. Allowing them to work in conjunction with each other with additional oxide ion found in the Ln_2O_2 layer that can then be transported in the LnNiO_3 layer.

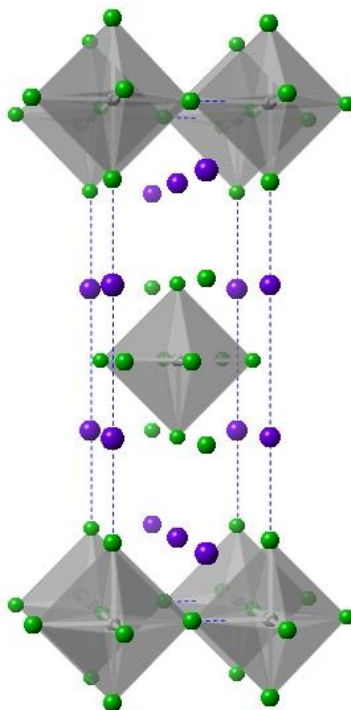


Figure 1-11 Structure of $\text{La}_2\text{NiO}_{4+\delta}$ (La = blue, Ni = Grey, O = Green)

For SOFC cathodes two $\text{Ln}_2\text{NiO}_{4+\delta}$ compositions have been principally studied, namely $\text{Ln}=\text{La}$ and Nd . Other known compositions are possible with nickel being partially substituted by cobalt or iron. However for fuel cell cathodes $\text{La}_2\text{NiO}_{4+\delta}$ and $\text{Nd}_2\text{NiO}_{4+\delta}$ are used due to the higher conductivity and lower activation energy that they possess.^{92, 93} It is the oxygen non-stoichiometry that affects the properties important to the fuel cells performance such as electronic conductivity, TEC and chemical stability. $\text{La}_2\text{NiO}_{4+\delta}$ exhibits electronic conductivity above 100 S cm^{-1} at 800°C , making it lower than some of the perovskite based cathodes, but suitable for SOFCs.⁹⁴ The main advantage of using $\text{La}_2\text{NiO}_{4+\delta}$ and $\text{Nd}_2\text{NiO}_{4+\delta}$ materials with YSZ and CGO is their comparable thermal expansion co-efficient which are considerably lower than Co containing perovskite materials Table 1-3.⁹⁴⁻⁹⁷ On the other

hand the chemical compatibility studies of these $\text{Ln}_2\text{NiO}_{4+\delta}$ compositions against YSZ and CGO showed that $\text{Nd}_2\text{NiO}_{4+\delta}$ is unreactive towards YSZ at 1000°C although reactivity is seen at 1100°C forming a $\text{Nd}_2\text{Zr}_2\text{O}_7$ phase.⁹⁸ In the case of $\text{La}_2\text{NiO}_{4+\delta}$ studies showed that even at 900°C there is a significant reactivity with both YSZ and CGO forming $\text{La}_2\text{Zr}_2\text{O}_7$ and $\text{La}_3\text{Ni}_2\text{O}_7$ respectively when heated for over two hours. This would have a detrimental effect on the long term stability of the materials at high fuel cell operating temperatures.⁹⁹

Table 1-3 The thermal expansion coefficient in air of electrolyte and electrode materials.

Thermal expansion co-efficient ($\times 10^{-6} \text{ K}^{-1}$) 300-1000°C	
YSZ (10%)	10.8
CGO (10%)	13.5
$\text{Nd}_2\text{NiO}_{4+\delta}$	12.7
$\text{La}_2\text{NiO}_{4+\delta}$	13.0
LSCF	17.5

1.3.2 Anode materials

The anode requires stability in reducing conditions and catalytic activity towards the hydrogen oxidation reaction (HOR), high electronic and ideally also ionic conductivity, with compatible chemical and thermal stability with the electrolytes and interconnector materials similar to the cathode.

1.3.2.1 Nickel

The most commercially used anode consists of a metal dispersed in a matrix of the electrolyte; these are known as cermets. Nickel metal is commonly used due to its high activity towards the HOR.¹⁰⁰ Typically it is used as part of a cermet with the electrolyte to reduce the formation of Ni clusters that would normally reduce the number of reaction sites present, as well as to enhance the triple phase boundaries. Further the use as a cermet with the electrolyte ensures similar thermal expansion co-efficient reducing any thermal

cracking problems. The disadvantage of the use of nickel cermets is that a cross reaction can occur with La based electrolytes forming a non-conducting layer between the anode and electrolyte.⁵³ Further stability problems exist with sulphur, which is a major impurity in natural gas leading to the formation of NiS and consequently poisoning of the anode. Furthermore coking can also occur when using hydrocarbon fuels, which also reduces the activity of the anode by the deposition of carbon onto the Ni particles.^{101, 102} Therefore newer alternative anode materials are under investigation, including perovskite chromates/titanates and doped CeO₂.^{40, 103}

1.3.2.2 Alternative anodes

Perovskites materials have also been studied as prospective anode materials with one material, La_{0.75}Sr_{0.25}Cr_{0.5}Mn_{0.5}O_{3-δ} (LSCM), being used as both an anode and a cathode material making a successful symmetrical fuel cell material. This material has reasonable electrochemical reactivity towards the HOR as the Ni/YSZ cermets. However, it has a lower electronic conductivity and is also unstable with sulphur forming impurities.

Another suitable perovskite is doped strontium titanate (SrTiO₃), it is usually doped with trivalent cations such as Y³⁺ or La³⁺, causing mixed valency and oxide ion vacancies. The doped titanates exhibit high electronic conductivity in a reducing atmosphere i.e. hydrogen, and they also possess high chemical stability with sulphur impurities and the coking reactions depending on the fuels used.^{40, 104} Furthermore even though adequate thermal expansion compatibility is seen with commercial electrolytes such as YSZ, the titanates do have both poor ionic conductivity and electrochemical activity for the HOR required by a fuel cell.^{104, 105}

Finally copper doped CeO_2 has shown significant electronic and ionic conductivity, and is more sulphur tolerant than Ni/YSZ cermets. Whilst nickel cermets become poisoned at below 15ppm H_2S in the fuel, the copper doped CeO_2 can function up to 450 ppm H_2S before any poisoning occurs. However, the problems with the doped ceria system is that the electronic conductivity tends to be lower than ideal, consequently the search for new anode systems is an ongoing process and something that is not examined in this project.

1.4 Project overview

In this project new materials for SOFCs have been researched, focusing on two components of the cell; the electrolyte and the cathode. These components were chosen as both tend to be limiting parts in terms of lower temperature operation. The research has focussed on involving only the perovskite structure, for both the cathode and the electrolyte given the known promise of such materials.

1.4.1 Cathode materials

Over a number of decades, the perovskite structure has been investigated for its use as a cathode material. It has previously been used as a mixed ionic and electronic conductor at high and low temperatures. Research here has involved the use of doping strategies to introduce disorder into the system and improve the conduction characteristics. The doping strategies includes a novel oxyanion (silicate) doping into SrMnO_3 (chapter 3) and pentavalent dopant strategies into BaCoO_3 (chapter 4) in an effort to alter the perovskite tolerance factor toward 1 (cubic perovskite). Successful materials which showed promising properties were studied further against both commercial electrolytes such as CGO and alternative electrolytes such as doped silicate apatites and doped barium indates.

1.4.2 Electrolyte materials

The electrolyte research involved a strategy based upon reducing costs, whilst maintaining high ionic conductivity properties. It focused on modifying scandium containing cubic perovskite systems which have previously shown high ionic conductivity but are high cost. The strategy was to try to decrease the amount of scandium in the perovskite system by the addition of cheaper rare earth elements while maintaining the high oxide ion/proton conductivity (chapter 5 and 6).

Chapter 2

2 Experimental

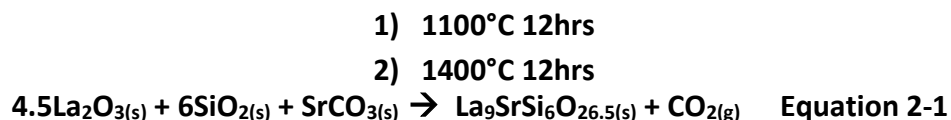
2.1 Synthesis techniques

There are a number of different synthesis techniques used in materials chemistry, these include solid state, sol gel, co-precipitation, microwave and hydrothermal. Further techniques are available, with each synthesis technique having its own advantages and disadvantages. Which technique is used usually depends upon the situation i.e. the product required, laboratory constraints, cost and time available. This project uses the solid state synthesis route, as described below in section 2.1.1.

2.1.1 Solid state synthesis

Solid state reaction synthesis, also known as the ceramic method, is the most widely used and accepted synthesis technique for the formation of inorganic solids. It involves the intimate grinding of two or more high purity solids usually carbonates or oxides, in the relevant stoichiometric ratios using an agate pestle and mortar. Carbonates and oxides are usually used as air sensitive or hygroscopic solids can lead to incorrect ratios of starting materials. The samples are usually heated at high temperature (>800°C) for over 12hrs.

Example – Preparation of lanthanum strontium silicate apatite (Equation 2-1)



High temperatures are required as the reactant must break their initial bonds, diffuse through the interfaces and form new bonds.^{106, 107} The sample is usually reground after the

first heat treatment as the product will only form at the contacted interfaces of the reactants. This regrinding process produces new interfaces between the reactants, reducing the particle sizes and increasing the surface area which means a higher reactivity. As the product grows the length of diffusion increases and the reaction rate falls. Not only grinding but varying the firing conditions e.g. temperature, time and the reaction atmosphere can increase the reaction rate.

The subsequent pure products are pressed into pellets increasing the contact between the grains, using either 10 or 13 mm dies, at a pressure of 2500-5000 kg cm⁻² and sintered. Sintering is when a material is heated to near its liquefaction temperature and causes particles separated by grain boundaries to merge together creating one solid grain.

The advantages of the solid state reaction technique are its inherent success and simple procedure. The major disadvantages to this method are the need for both high temperatures and long reaction times. This results in high costs for the technique and, in some cases, partial evaporation of volatile starting materials (for example barium in this work). To overcome the evaporation issues a sealed container can be used, and/or additional excess of the starting

material (barium carbonate) can be added before the first heat treatment, usually between 3%-10% by weight. In this work all heat treatments took place in an alumina crucible with a lid, and pressed pellets were covered with sacrificial powder where appropriate (Figure 2-1). Full synthesis details are provided in the experimental sections of each chapter.

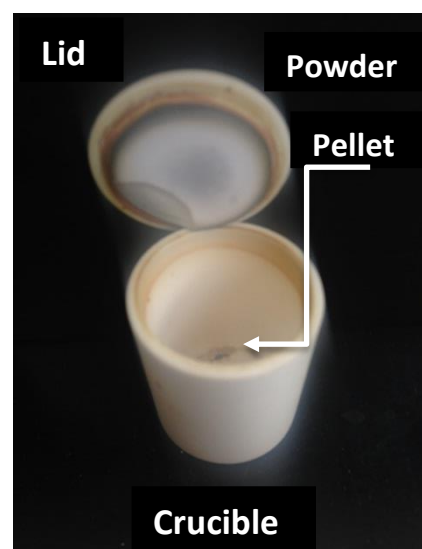
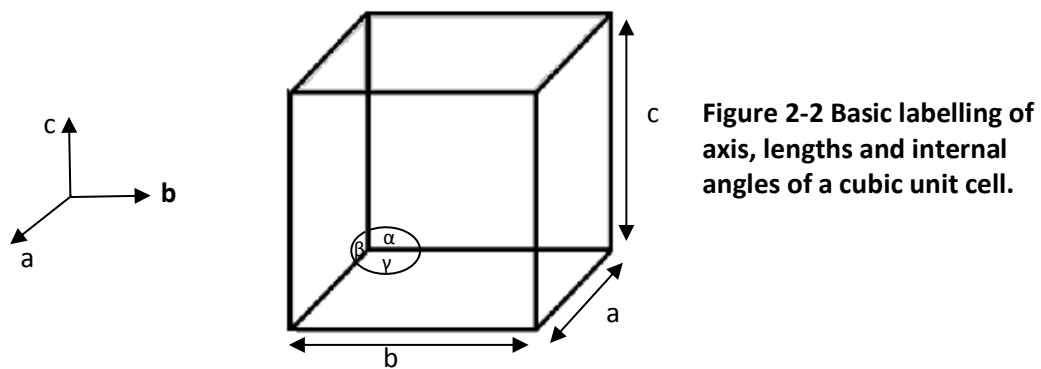


Figure 2-1 Solid State – alumina crucible, lid and sample.

2.2 Structural Characterisation

Powder diffraction is a non-destructive technique for the analysis of crystalline materials and is used to identify new phases as well as the purity of a material. In order to fully appreciate and understand powder diffraction, a basic background to crystallography is required.

2.2.1 Crystallography

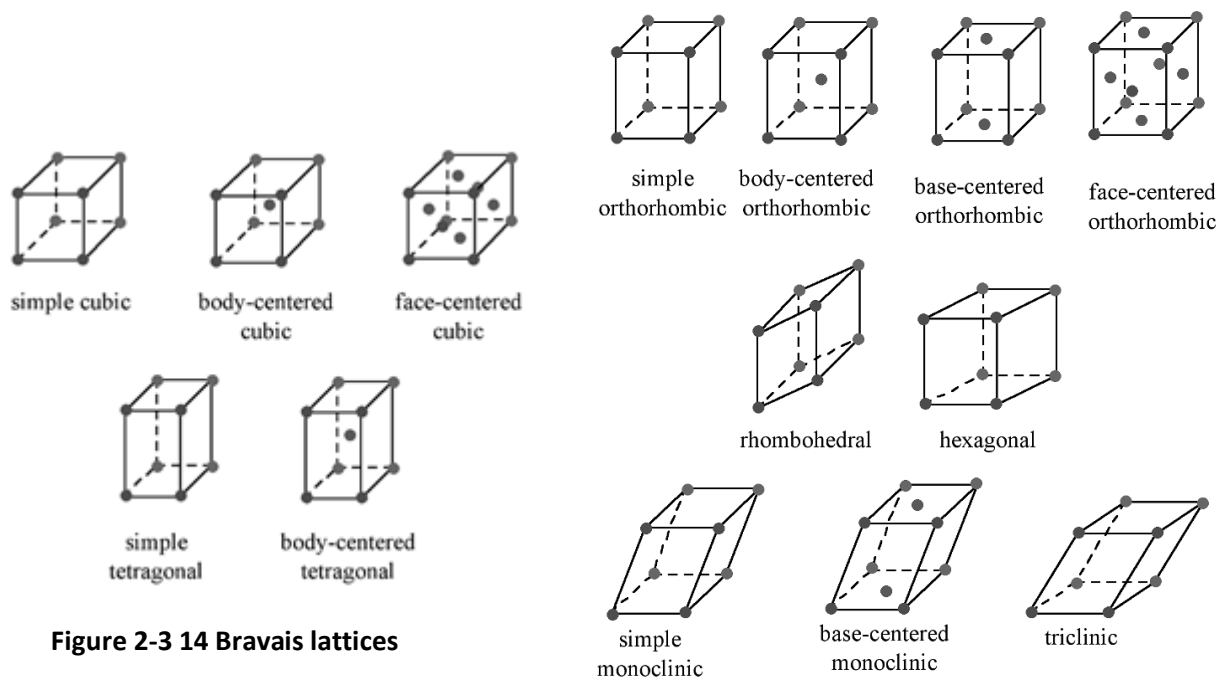


Crystalline materials comprise a 3-dimensional array of atoms, regularly arranged in an “ideal” crystal structure; the simplest repeating arrangement of the atoms is represented by the unit cell. This unit cell can be repeated by translations and shows the symmetry of the entire crystal lattice. The dimensions of the unit cell are known as its cell parameters, these are defined as the length of each axes in each of the three directions a, b, c and the internal angles between the axes α, β, γ (Figure 2-2).

Each unit cell can be classed in to one of the seven possible unit cell shapes also known as crystal classes. The crystal class of a unit cell is defined when the different angles and lengths of the cell parameters are considered. The seven different unit cell shapes are shown in Table 2-1.

Table 2-1 Seven crystal classes

Unit cell shape	Lengths	Angles
Cubic	$a=b=c$	$\alpha=\beta=\gamma=90^\circ$
Tetragonal	$a=b\neq c$	$\alpha=\beta=\gamma=90^\circ$
Orthorhombic	$a\neq b\neq c$	$\alpha=\beta=\gamma=90^\circ$
Hexagonal	$a=b\neq c$	$\alpha=\beta=90^\circ\gamma=120^\circ$
Trigonal/ Rhombohedral	$a=b=c$	$\alpha=\beta=\gamma\neq 90^\circ$
Monoclinic	$a\neq b\neq c$	$\alpha=\gamma=90^\circ\beta\neq 90^\circ$
Triclinic	$a\neq b\neq c$	$\alpha\neq\beta\neq\gamma\neq 90^\circ$



In addition to the crystal classes there are different types of unit cells, each relating to the placement of lattice points within the cells; i.e. primitive (P), body centred (I), and face centered (F) side centred (C). The use of these crystal classes, along with the allowed placement of lattice points within the cell, produce 14 lattices; these are known as the Bravais lattices, as shown in Figure 2-3.^{108, 109}

Table 2-2 Unit Cell types

Type of unit cell	Lattice point allowed placement
Primitive (P)	One lattice point at each corner
Body Centred (I)	One lattice point at each corner one in the centre
Face centred (F)	One lattice point at each corner and one in the centre of each face
Side centred (C)	One lattice point at each corner and pair of points in the centre of opposite faces

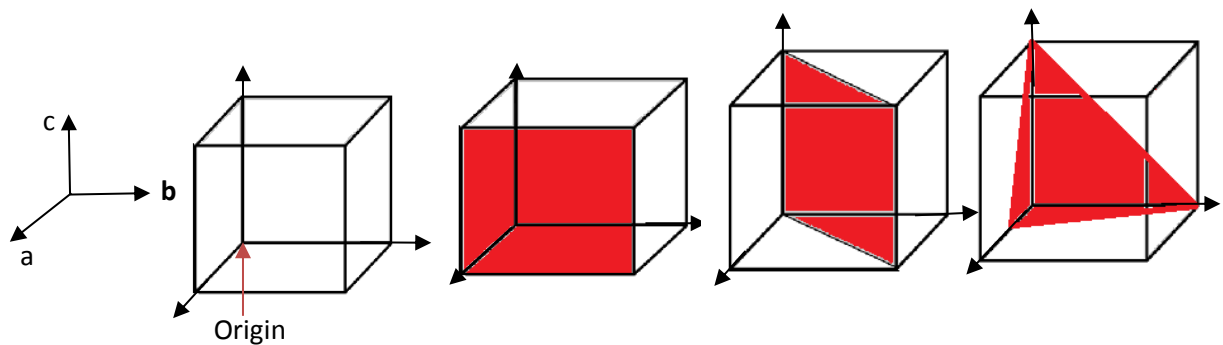
There are also additional symmetry elements to a crystal structure; these symmetry operations are known as point groups of which there are 32. They are produced through the symmetry operations: -

- Centre of inversion
- Mirror plane
- Rotation axis
- Translation vector
- Rotation followed by inversion
- Screw axis (rotation then translation)
- Glide plane (mirror plane then translation)

Combining the 32 point groups and the 14 Bravais lattices gives 230 possible crystallographic space groups. These space groups show the structures full symmetry operations.

To fully explain the diffraction elements of a crystal the concept of lattice planes are used. The lattice planes are shown in the terms of Miller indices, and they describe the planes

within the crystal. The planes intersect with the lattice points and are expressed as fractional coordinates in each direction along the unit cell lengths (a, b, c) from a defined origin. These fractions are seen as whole numbers known as the (hkl) values. They are usually defined within brackets, and a selection of fractional coordinates with their respective lattice planes are shown in Figure 2-4. The combination of the space group, the atom positions and cell parameters provides the full description of a crystal structure.



$$\frac{1}{1} \frac{1}{\infty} \frac{1}{\infty} \quad (100) \quad \frac{1}{1} \frac{1}{1} \frac{1}{\infty} \quad (\bar{1}10) \quad \frac{1}{0.5} \frac{1}{1} \frac{1}{1} \quad (211)$$

Figure 2-4 Example of Lattice Planes with fractional intercepts and hkl values for (100), (-110) and (211)

2.2.2 X-ray diffraction

X-ray diffraction can be performed on either single crystals or powders, with X-rays having a similar wavelength to the atomic spacing in crystalline structures. This is an extremely powerful technique first developed in 1913 by W.H Bragg and W.L Bragg, and it is useful

for a wide range of studies including phase purity, structure refinement, lattice strain, crystallite size and phase transitions.

2.2.2.1 Scattering

X-rays are scattered by the electrons in the atoms; thus the x-rays are scattered by the electron density distribution in the crystal structure. The scattering occurs as a beam of X-rays (incident X-rays S^0) hits an atom causing the electron to oscillate, the electrons gain and lose energy and emit radiation (giving another beam of X-rays S). When the wavelengths of the X-rays beams match, it is known as elastic scattering. The interaction of X-rays is different in every element due to the number of electrons present, this gives rise to the form factor of an atom f (equation 2-2).

$$f \propto \text{number of electron possessed by the atom} \quad \text{Equation 2-2}$$

Consequently, the form factor will increase as the atomic number (Z) increases. The form factor for each element has a dependence on $\sin \theta/\lambda$ (θ = angle of incidence and λ = X-ray wavelength). The consequence of this dependency on both $\sin \theta/\lambda$ and Z is that at zero θ the scattering of the X-rays = the number of electrons within the electron cloud. As θ increases to a higher angle the scattering is weaker as there is an increase in destructive interference between the X-rays scattered by different parts of the electron cloud so the form factor decreases. Studying lighter elements such as oxygen or fluorine in the presence of heavier elements such as the lanthanides causes the X-rays to scatter less with lighter elements than with heavier ones due to the number of electrons. This results in the position

of the lighter elements being harder to determine, Figure 2-5 shows the form factors of different numbered electrons in atoms and ions.¹¹⁰

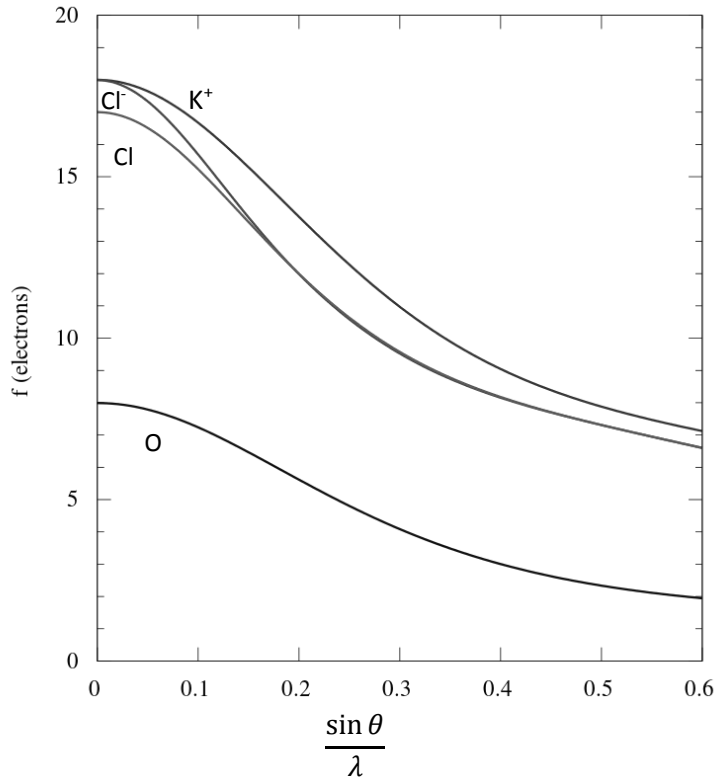


Figure 2-5 Form factors for different number electrons atoms and ion.

The structure factor F_{hkl} is the collective scattering power of the atoms in the unit cell. It is calculated through the atom scattering factor and the crystal structure (the unit cell atomic position/coordinates of each atom (equation 2-3)).

$$F_{hkl} = \sum_1^N f_n e^{2\pi i(hx_n + ky_n + lz_n)} \quad \text{Equation 2-3}$$

2.2.2.2 Generation of X-rays

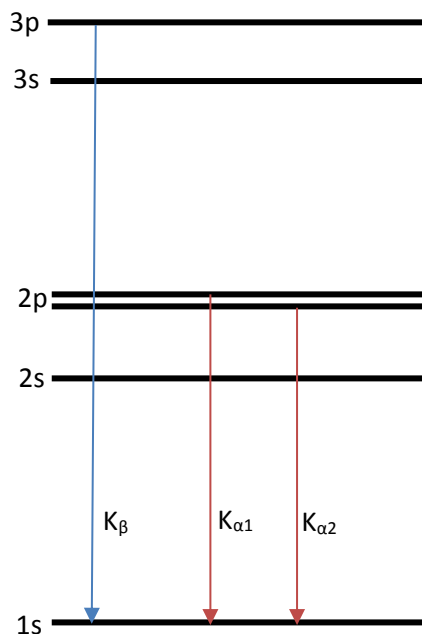


Figure 2-6 Energy level diagram of copper

X-rays are high energy electromagnetic radiation (200eV – 1 MeV); the typical X-ray source used in solid state chemistry produced X-ray wavelengths between 0.5 – 2.5 Å matching the interatomic distances of materials. X-rays are generated through accelerating high energy electrons from a cathode over a large negative potential to a metal anode. The metal anode, usually copper in most university lab based diffractometers, is bombarded by electrons leading to the ejection of metal core orbitals resulting in electron holes. The electron holes are then filled by electrons in a high energy state decaying to the electron holes. The electron transition from higher states to core releases energy; this corresponds to the X-rays wavelength. Figure 2-6 shows the decay of the outer states in electron levels 2 and 3. Each of the outer states have sub levels (2s, 2p, 3s and 3p). It is the sublevels that

result in the different wavelengths of X-ray observed, for example decay from 2p to 1s produces $K_{\alpha 1/\alpha 2}$ and 3p to 1s produces K_{β} .

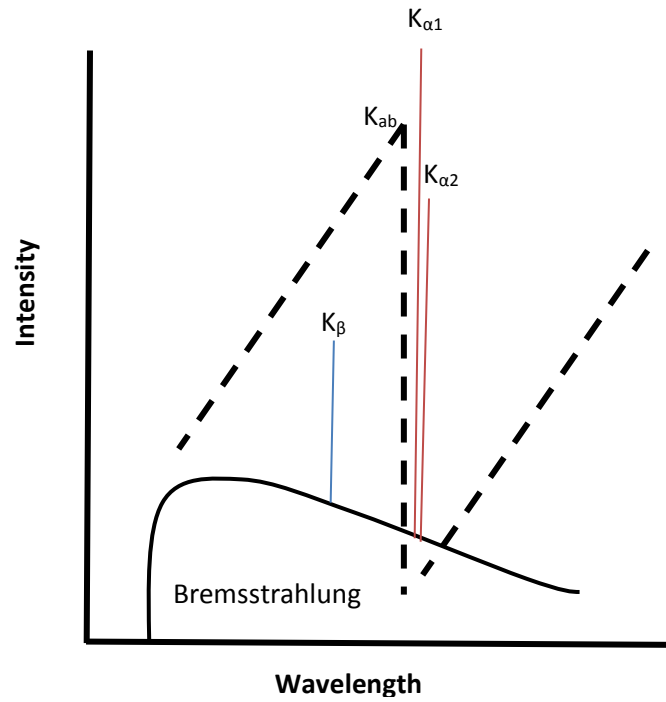


Figure 2-7 X-ray spectrum of copper

A copper X-ray spectrum is shown in Figure 2-7; the sharp peak corresponds to electrons decaying, producing X-ray radiation.¹¹¹ The spectrum shows two sets of peaks K_{α} and K_{β} , while in a lab based x-ray diffraction experiment a single wavelength of X-ray radiation is used, and most diffractometers use $K_{\alpha 1}$ radiation due to its higher intensity. The use of a crystal monochromator or filter is employed to remove the additional unwanted wavelengths. The crystal monochromator commonly used is a germanium single crystal orientated so that only $K_{\alpha 1}$ radiation is reflected and focussed on to the sample. The filter option passes the X-ray beam through a metal foil filter whose absorption edge lies between the K_{α} and K_{β} radiation; for this to occur it must have a lower atomic number than the copper source, and so nickel foil filters are usually used. This filter absorbs the energy

of the K_{β} ($\lambda = 1.392 \text{ \AA}$) as it has an absorption edge of (K_{ab}) $\lambda = 1.488$. However, the filter does not remove the $K_{\alpha 2}$ radiation, and so a combination of the $K_{\alpha 1}$ and $K_{\alpha 2}$ is obtained.

2.2.2.3 Bragg's Law

W.H Bragg and W.L Bragg understood that a crystal structure is a 3-dimensional array of atoms, and proposed that a crystal was composed of aligned lattice planes on which individual lattice points sat. In order to observe diffraction peaks, constructive interference must occur between the X-rays and each lattice plane. Therefore, observed diffraction is heavily dependent on the X-rays scattering angles on each plane and the distance between the lattice planes. As the spacing between the planes provides a path difference for the X-rays, if this path difference (d) is equal to an integer (n) of the X-ray wavelength (λ) constructive interference will occur as build-up of intensity maxima (peaks) is observed. If, however the path difference does not equal an integer (n) of the X-ray wavelength, then destructive interference occurs, by which the X-ray beams scattering angle for the different planes will be different to one another, and therefore the intensity will cancel out and no peaks will be observed (background).

Consider Figure 2-8 for constructive interference, as two parallel X-ray beams are diffracted from different lattice planes, the lower beam that travels adjacent and parallel to the first beam, will also travel a further diffraction distance ($AB + BC$) to the detectors, leading to a phase shift. The distances AB and BC are equivalent and therefore it is equal to $2AB$. This all states that $AB + BC = 2AB = \text{path difference} = n \lambda$.¹¹² Therefore the path difference can be given in terms of the plane spacing (d_{hkl}) and the angle of radiation (θ).

$$\sin \theta = \frac{AB}{BD} \quad BD = d_{hkl}$$

$$d_{hkl} \sin \theta = AB$$

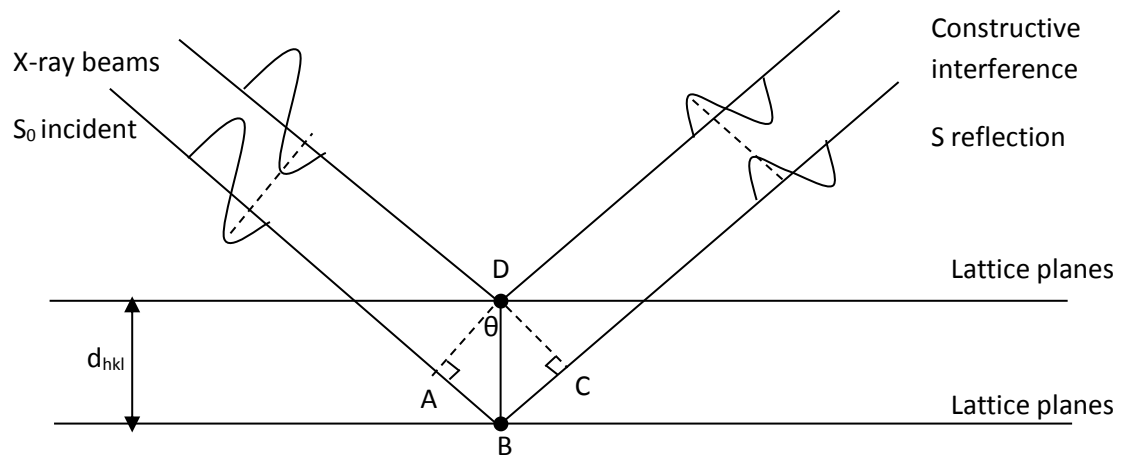


Figure 2-8 Depiction of Bragg's law from two incident beams

$$2AB = 2d_{hkl}\sin\theta$$

$$n\lambda = 2d_{hkl}\sin\theta \quad \text{Equation 2-4}$$

It is possible to relate the d-spacing in crystals to the unit cell parameters. The practical application is that either from known unit cell parameters, one can predict the diffraction pattern i.e. peak positions, or from experimental observed peaks positions you can determine the unit cell parameters. Each of the crystal classes has a different expression for d_{hkl} in terms of lattice parameters and Miller indices (some of the crystal systems investigated are shown in Table 2-3).

Table 2-3 Expression of d-spacing in 4 crystal classes

Crystal systems	Relation of Lattice parameters / Miller indices
Cubic	$\frac{1}{d^2} = \frac{h^2 + k^2 + l^2}{a^2}$
Tetragonal	$\frac{1}{d^2} = \frac{h^2 + k^2}{a^2} + \frac{l^2}{c^2}$
Orthorhombic	$\frac{1}{d^2} = \frac{h^2}{a^2} + \frac{k^2}{b^2} + \frac{l^2}{c^2}$
Hexagonal	$\frac{1}{d^2} = \frac{4}{3} \left(\frac{h^2 + hk + k^2}{a^2} \right) + \frac{l^2}{c^2}$

2.2.2.4 Instrumentation

The general arrangement of an X-ray diffractometer is fairly standard due the requirements needed to satisfy Bragg's law and the commercial aspects of mass production. In this work the Bruker D8 X-ray diffractometers are used and are operated in both transmission and reflection geometry using Cu $K_{\alpha 1}$ radiation (Figure 2-9).^{112, 113} The transmission D8 is equipped with a 9 cassette auto sampler and uses a germanium monochromator. The reflection D8 has a nickel foil filter and is single sample only.

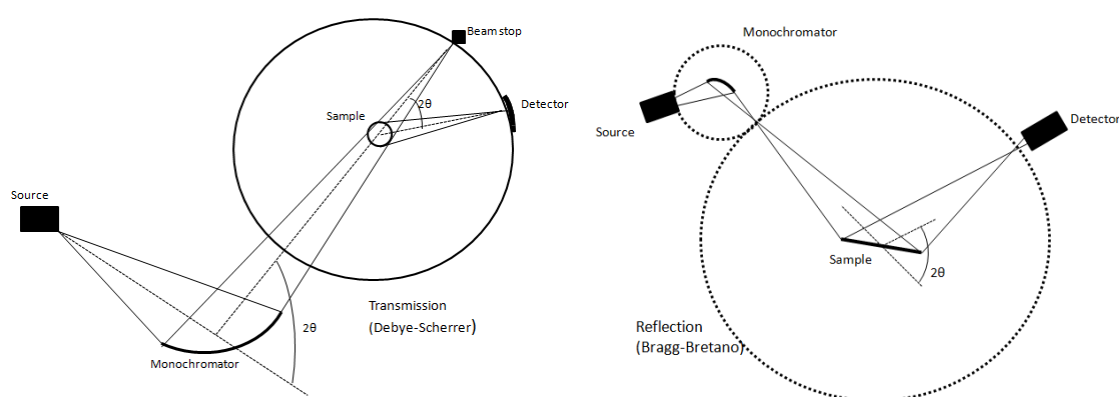


Figure 2-9 D8 Transmission and reflection geometries for X-ray diffraction.

2.2.2.5 Powder diffraction data

Each polycrystalline material will have a characteristic diffraction pattern that allows for phase identification. Figure 2-10 shows the simple information in a X-ray diffraction powder pattern; including the background, peak intensity, peak position and peak shape.

- The background contains information about short range ordering.
- Peak intensities provide information about the atoms i.e. their position, occupancy and thermal motion.
- Peak positions are determined by the unit cell size and shape (lattice parameters).
- Peak shape is determined by the crystallinity and micro strains of the crystallites.

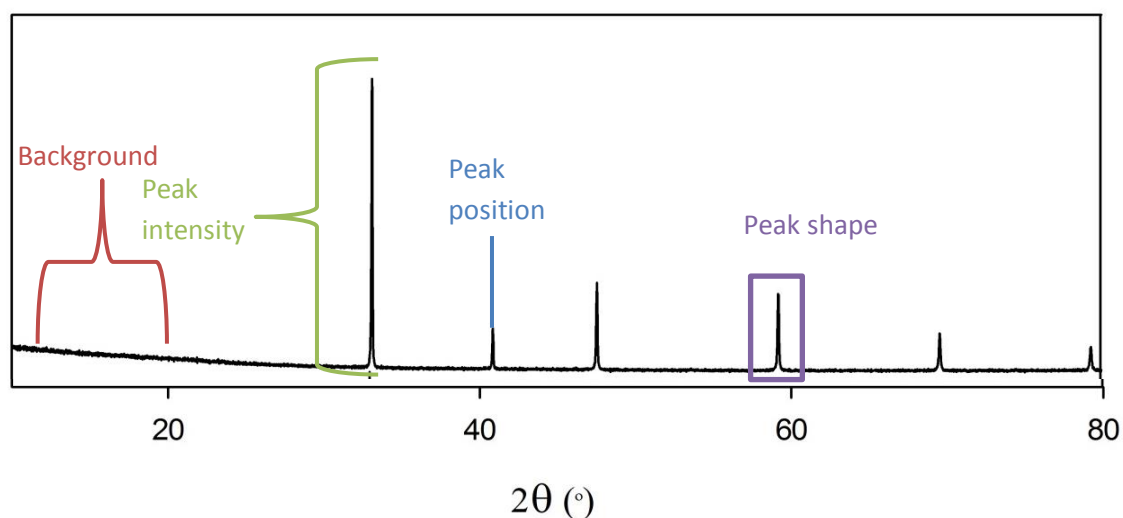


Figure 2-10 Main components of a powder XRD pattern

Powder diffraction is affected by both the instrument and the sample; this can include the sample holders, the detector, the beam intensity and the samples; fluorescence, crystallinity and crystallite orientation. Overall powder diffraction can give you a wide range of information from crystal structure, particle size/strain, phase transitions, thermal expansion.

2.2.3 Rietveld analysis

Before the Rietveld method the structural determination of a crystalline material was firstly performed on single crystals of an appropriate size. However, the production of large single crystal is not always possible for some materials. Consequently, structural determination of X-ray powder diffraction was developed but it was only initially performed on powder diffraction materials that were of high symmetry. This was due to peaks at high symmetry being well resolved (not overlapping with each other), so an integrated intensity method was possible. However, most structures are not such high symmetry and so, recognising this, Hugo Rietveld in the 1960s produced a method now known as the Rietveld refinement method.¹¹⁴⁻¹¹⁶ It allows powder diffraction data to be used for complex structural determination. Rather than using the intensity of each peak the data is collected in thousands of individual 2θ steps. Every data point (background included) is then used and applied to a least square refinement model until the observed experimental data and calculated model fit.¹¹⁷ To fit the observed data model, the calculated base model must be created and requires information such as the symmetry information (space group and cell parameters) and the approximate atomic structure (starting atomic positions) which can all be gained from the crystallographic information files (CIF) of related materials. These data files are available for a wide range of materials from the International Crystallographic Structural Database (ICSD). In addition the Rietveld refinement requires the instrumental parameter file of the X-ray diffractometer used, which includes information such as the source of radiation wavelength used and whether a monochromator or filter was used to select the wavelength.

There are a variety of computer programs that can be used for Rietveld refinement. They include GSAS (General Structure Analysis Software), TOPAS (Total Pattern Analysis Solution) and Fullprof.^{118, 119} Each system works on the same principles, but each has its own advantages and disadvantages to the user. They all allow for single or multiple phase refinements and for several atoms to be added on to the same position so that the partial replacement of atoms through doping can be studied. For this work the GSAS suites programmes was only used and the quality of the Rietveld refinement is assessed both visually and mathematically.^{117, 120}

2.2.3.1 General structure analysis software

The GSAS Rietveld refinement programme uses a least squares model to minimise the difference between the calculated and observed patterns on a point by point basis. The minimisation during the least square model is equal to the residual S_y (equation 2-5).

$$S_y = \sum_i w_i [y_i(obs) - y_i(calc)]^2 \text{ Equation 2-5}$$

$y_i(obs)$ = observed intensity at the i^{th} step

$y_i(calc)$ = calculated intensity at the i^{th} step

w_i = weighting of each point ($1/y_i$)

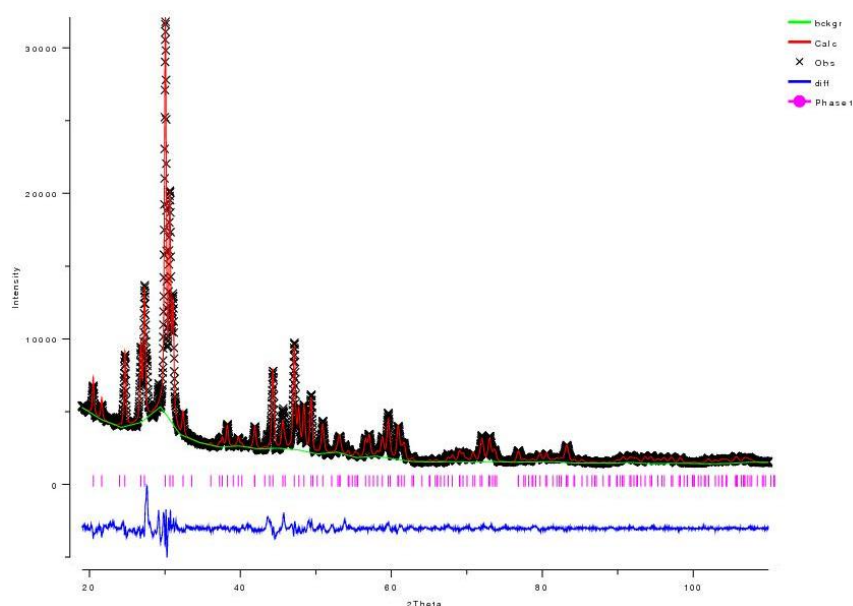


Figure 2-11 GSAS live plot view refinement profile; background (green), Calculated (red), observed (X), difference between the observed and calculated (blue) and phase (pink tick marks)

In order to determine the best fit of the calculated data to the observed data, certain parameters can be refined; these include the unit cell parameters, zero-point error, background, scale factors, profile parameters, atomic co-ordinates, site occupancies and thermal parameters.^{117, 120} The approach is to refine the parameters of the initial calculated data incrementally in order to fit the experimental data. The refinements to the parameters are applied to the initial data over a continual cycle process, with each cycle producing a new fit. A visual sign of the fit between the calculated and the observed is possible with live plot view (Figure 2-11). The difference line, shown here in blue, is used to determine the refinements success.^{117, 120}

$$\chi^2 = \left[\frac{R_{wp}}{R_{exp}} \right]^2 \quad \text{Equation 2-6}$$

For a “perfect refinement chi squared” χ^2 should be equal to 1 with R_{wp} and R_{exp} being the same (equation 2-6). It is known as the goodness of fit parameter and a value lower than 4 in a refinement is seen as a success. However, it can also be misleading and is only an

indication of the refinement, as it is heavily dependent on the R_{exp} . Also χ^2 values <1 are impossible and is not an indication of a good fit, but more an over analysis of the parameters used on poor quality data. Successful refinement uses both numerical methods (R factors/chi) and visual plots to evaluate whether the structural model is a good one.^{117,}

120

The R factors of each cycle that are used to validate the fit are

$$\text{R profile - } \mathbf{R_p} = \frac{\sum y_i(obs) - y_i(calc)}{\sum y_i(obs)} \quad \text{Equation 2-7}$$

$$\text{R weighted - } \mathbf{R_{wp}} = \left[\frac{\sum w_i((y_i(obs) - y_i(calc))^2)}{\sum w_i(y_i(obs))^2} \right]^{1/2} \quad \text{Equation 2-8}$$

$$\text{R expected } \mathbf{R_{exp}} = \left[\frac{(N - P - C)}{\sum w_i(y_i(obs))^2} \right]^{1/2} \quad \text{Equation 2-9}$$

N = diffraction patterns total number of data points

P = number of refined parameters

C = number of constraints

The R factors can sometimes give misleading results though with

- R_{wp} being over and under estimated for example; an unknown impurity present will change the calculated and observed scan difference, causing a much larger R_{wp} value. On the other hand if the background is incorrectly refined and accounts for some of the intensity of a peak then a lower R_{wp} is seen.

- R_{exp} the results can give errors related to the length of scan, a too short scan will give poor quality of data and a large R_{exp} . A too long scan will cause a too small R_{exp} due to the errors.

2.3 Raman Spectroscopy

Raman spectroscopy is used to study the bonding in materials through analysis of the vibrational and rotational modes in a molecule.¹²¹ It was first discovered in 1928 by C.V. Raman and K.S. Krishnan, and named after Raman. For the modes to be observed (i.e. be Raman active) the molecules must have a change in polarizability; this is the affinity of a molecule to have a dipole moment. Raman spectroscopy uses monochromatic light (single wavelength) over a possible range of infrared to ultraviolet light. The radiation of specific wavelength interacts with the molecules electron cloud and raises its vibrational energy level to what is known as an excited or virtual state.¹²¹

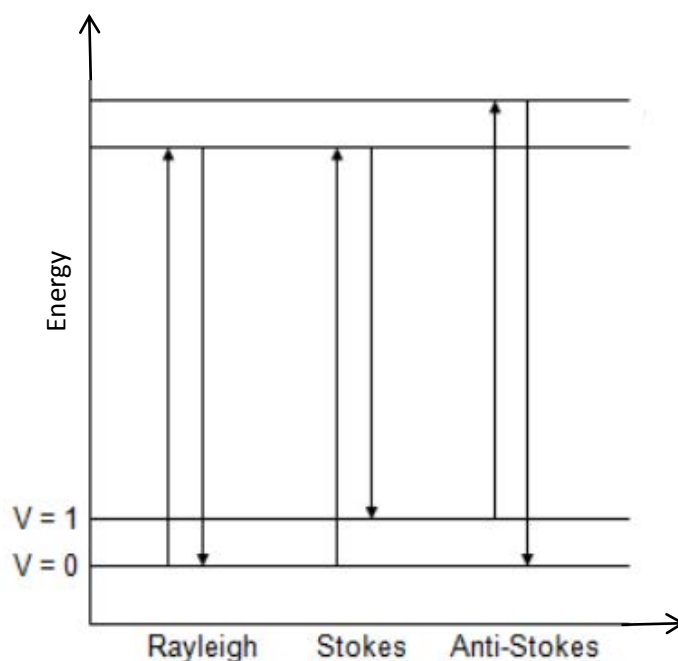


Figure 2-12 Raman spectroscopy energy transitions with Rayleigh and Stokes and Anti-Stokes lines.

This excited state is the distortion of the electron cloud of a covalent bond, and is highly unstable and short lived. It will emit radiation of another wavelength to compensate. The

difference in energy from the ground vibrational state of the molecule to the excited state and the resultant emitted radiation (photon) is what is of interest (Figure 2-12).

In Rayleigh scattering or elastic scattering the energy of the incident radiation to promote the molecule to the excited state will equal the emitted radiation back down to the ground state, and no change in the molecules vibrational energy level is observed. Since the initial radiation has only interacted with the electron cloud, and due to the low mass of electrons, this results in very little scattering and no measurable difference in the energy of the emitted photon.

However, when inelastic or Raman scattering is observed the incident radiation's energy and the emitted energy will differ greatly. The initial radiation will scatter with the electron cloud and a significant transfer of energy may be seen between the radiation and the molecule, which will introduce motion within the molecule in the form of molecular vibrations. The resulting radiation emitted will therefore be different in energy and the molecules will not fall back to the original vibrational energy levels. This can happen in two ways, Stokes or Anti-Stokes. Raman scattering to give Stokes lines are a result of emitted radiation being reduced in energy by the transfer of energy to the molecule. In Anti-Stokes lines the molecule is in the excited vibration state and so increases the energy to the emitted radiation.

The intensities of the Stokes and Anti-Stokes lines are relative to the occupancy of the ground vibrational states. An increase in temperature will increase the intensity of anti-stoke lines, as there are more molecules in the $V=1$ ground vibrational state.

Raman spectroscopy can provide both quantitative and qualitative data. The intensity of the peaks are proportional to the amount of Raman active components in the molecule, and the bands seen in the Raman spectra can characterise different groups in a material.

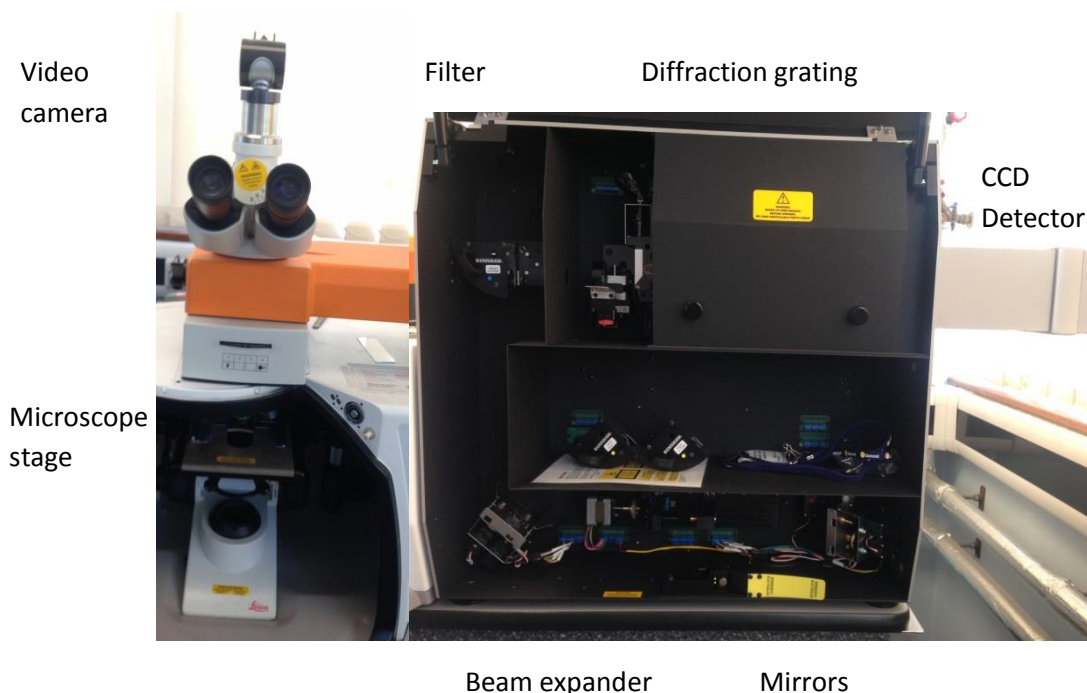


Figure 2-13 Raman microscope Renishaw 532nm optics and web camera active

In this work a 532nm wavelength ion laser was used to irradiate the powder samples, being collected on a Renishaw InVia Raman microscope (Figure 2-13).¹²² This instrumentation works via a monochromatic beam of light being produced from the laser which is focused via mirror optics and directed on to the sample. The beam can be focused on a specific area of the sample, which can be viewed via a video camera.

To stop the high proportion of Rayleigh scattering photons overwhelming the detector they are removed by a holographic notch filter, which leaves the weaker Raman scattering lines. The Raman lines are sorted and detected by a diffraction grating and a charge-coupled detector (CCD) to give the Raman spectra displayed.

2.4 Thermal analysis

Thermal analysis techniques allow the investigation of chemical and physical changes of a material over a set temperature range. The techniques used can be quantitative and/or qualitative. Table 2-4 shows a list of the thermal analysis techniques used in this work.

Table 2-4 Thermal analysis techniques

Thermal techniques	Key result
Thermogravimetry Analysis (TGA)	Mass change
Differential Thermal Analysis (DTA)	Detection of relative endothermic or exothermic reaction.
Gas analysis (GA-MS)	Gas evolved from a sample coupled with mass spectrometry for detection.
Dilatometry	The thermal expansion or contraction.

2.4.1 TGA coupled with DTA and GA-MS

The technique of thermogravimetric analysis (TGA) is used to heat a known mass of a sample using a specific heating rate for a specific time, and measures the mass gained or lost.¹²³ The sample is placed inside a platinum or alumina crucible with an associated lid added. This is positioned on a precision thermobalance to record the mass changes next to a reference crucible. The pre-set temperature programme allows a specified temperature ramp rate, a holding time at the end temperature, and a desired cooling rate. A correction file is used for which an empty crucible has undergone the same heating conditions as the sample, so that any fluctuation in the crucible mass (due to e.g. buoyancy effects) over the temperature programme can be subtracted from the sample data.¹²³

Furthermore, the TGA data can be collected in a range of atmospheres, in this work a N₂ protective gas for the machine is always used. Additional testing gases such as H₂, N₂, O₂ and CO₂, depending on the experiment, were used; e.g. N₂ was used to give an inert atmosphere, in order to prevent oxidation of the sample.

The TGA instrument is incorporated with a differential thermal analyser (DTA) and coupled to a gas analyser mass spectrometer (TGA-MS). The DTA uses the reference crucible and sample crucible which are undergoing the same temperature programme to determine phase transitions. The temperature of each crucible is recorded and the difference between the sample and reference allows an exothermic (sample crucible higher temperature) or endothermic (sample crucible lower temperature) reaction to be evaluated. The TGA instrument is coupled to a gas analyser mass spectrometer (GA-MS) which measures the mass to charge ratio of the gases given off during the measurement, this allowing the gases of decomposition or desorption of the sample to be measured.

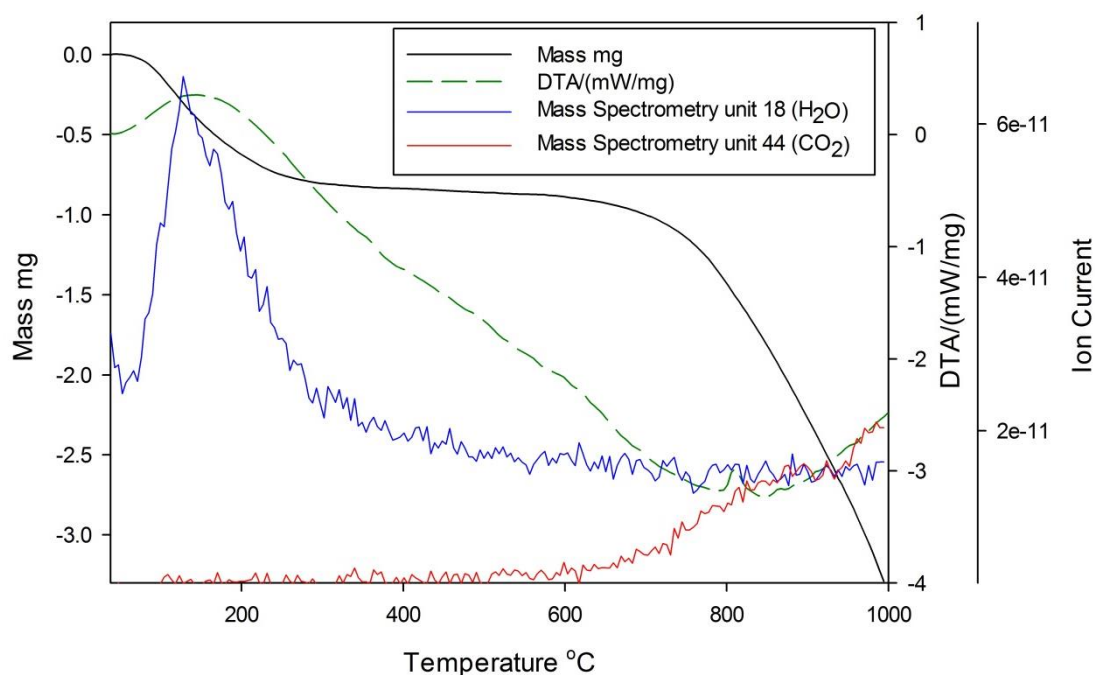


Figure 2-14 Example TGA – Mass (black line), DTA (green line), m/z 18 H₂O (blue) and m/z 44 (CO₂)

In this project the Netzsch STA 449 F1 Jupiter thermal analyser coupled to a Netzsch MS 403C Aeolos mass spectrometer was used to study the water content and CO₂ stability for both the electrolyte and electrode materials studied. Sample data collected are shown in Figure 2-14 (temperature programme of 10°C a minute to 1000°C, in N₂ atmosphere). There is a significant mass loss between 100-300°C, which corresponds to the water loss and the mass spectrometer peak for 18 m/z clearly confirms this.

2.4.2 Dilatometry

Dilatometry was used to measure the expansion or contraction of a material as temperature is increased or decreased. Measurable properties include the thermal expansion coefficient (TEC), the sintering temperature and phase transitions.¹²⁴

The programmable system allows the use of a specific heating and cooling rate, in addition to the use of a range of atmospheres e.g. H₂ and O₂. The technique can be performed on ceramic materials or metals or polymers, and in most cases as a material is heated it expands.¹²⁴

In SOFCs it is the TEC of an individual material that is measured and compared to the adjacent components. In an ideal fuel cell, the TEC of each material (the electrolyte, the electrodes and the interconnectors) would be the same over the temperature range RT-800°C. A difference in the TEC values of each component may initially cause sealing issues, thermal cracking and delamination affecting the efficiency of the fuel cell. Overall major differences would cause the complete failure of the cell and the hazardous mixing of fuel and oxidant gases.

The thermal expansion is a change in volume of a material as the temperature increases and is caused due to an increase in the atoms average bond lengths. The bond lengths

effect on the expansion will depend upon the components, the structure, and their relative angles within the crystal lattice i.e. a cubic perovskite has length and angles all equal so there is uniform expansion as temperature increases. See equation 2-10 for the calculation of linear thermal expansion coefficient (L_i = initial length, L_f = final length, T_i = initial room temperature and T_f = final temperature).¹²⁴

$$TEC = \frac{L_f \cdot L_i}{L_i(T_f - T_i)} \text{ Equation 2-10}$$

In this work a Netzsch 409C dilatometer was used; it is a pushrod encased within a furnace running on a temperature programme from 25°C to 800°C at 10°C min⁻¹. Samples were prepared by pressing 10mm diameter and 10 mm in length bar pellets, which were sintered at their corresponding temperatures before being polished and the initial length accurately measured.

2.5 DC Conductivity

The conductivities of SOFC materials have been measured in this project in two ways depending on the type of material. For electrolyte materials which ideally will have negligible electronic conductivity and will be ionic conductors only, AC impedance measurements are used (conductivity of magnitudes between 10⁻² and 10⁻⁵ S cm⁻¹ (see section 2.6)). However, for electrode materials which have higher conductivity via electronic conduction pathway, magnitudes of 10⁻¹ and 10³ S cm⁻¹ are seen, and so alternative dc conductivity techniques are required. There are two DC conductivity techniques that are possible, a Van de Pauw technique and a standard 4 probe DC technique.

2.5.1 Van de Pauw technique

This technique requires four Pt wires or contact points to be attached to the pellet at 90° angles, Figure 2-15 shows how the resistance is measured using Ohm's law, between the two points for R_1 and R_2 .¹²⁵ The reversing of the voltage and current contacts is possible, and this would provide us with R_3 and R_4 but this would be equivalent to R_1 and R_2 due to the symmetry of the pellet and contact points. The resistance is determined through equation 2-11.

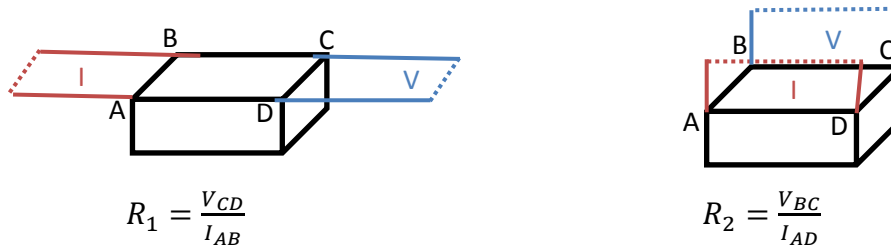


Figure 2-15 Van de Pauw method two measurement for 4 probe.

$$R_{total} = \frac{\pi l}{\ln(2)} \frac{R_1 + R_2}{2} f(r) \quad \text{Equation 2-11}$$

[l = thickness, $f(r)$ ratio of $r = R_1/R_2$]

2.5.2 Standard 4 probe DC technique

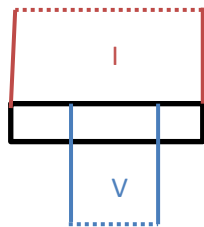


Figure 2-16 Schematic of 4 probe DC conductivity technique

Similar to the other method four platinum wires or contact points are attached to act as electrical contact points for the conductivity measurements. However, the configuration of the 4 wires is different, with two placed slightly apart on the top of the pellet (inner wires) and two on either side (outer wires). The voltage is measured across the two inner electrodes and the current is applied to the outer electrodes (Figure 2-16).

The resistance is calculated by equation 2-12 taking into account the dimension of the pellet (diameter, depth and distance between the inner electrodes). The inverse of resistivity providing the conductivity.

$$R = \frac{V}{I} \quad \sigma = \frac{1}{R} \times \frac{\text{Distance between inner electrodes}}{\text{Diameter} \times \text{Depth}} \quad \text{Equation 2-12}$$

The unattached ends of the contact points were attached to the measurement rig and placed in to a vertical furnace allowing the conductivity to be measured at different temperatures. The standard four probe DC method was used in this work; as it was simpler to set up, easier to test, and previous results within the group on similar series' have shown that each of the techniques provided similar results.¹¹³

2.6 AC Impedance conductivity measurements

Alternating current (AC) impedance also known as electrochemical impedance or impedance spectroscopy is an electrochemical analysis technique first used in the 1960's by Sluyter.¹²⁶ Since then it has become a widely used technique to characterise the electrochemical behaviour of a system.^{127, 128} Both the intrinsic and interface properties (Table 2-5) of a system can be measured, with these results being used to determine the materials mass transport rates, reaction rates and conductivities.¹²⁹

Table 2-5 Properties that are possible to be calculated by AC impedance.

Intrinsic	Interface
Conductivity	Capacitance at interface region
Dielectric constants	Adsorption reaction rate constant
Charge carriers	
Equilibrium constant of charged species	

2.6.1 Electrical impedance theory

The impedance set up in this work consists of sintered pellets coated in platinum paste on both sides with platinum foil electrodes attached. The data collected allowed conductivities of electrolytes and the activation energies for conduction to be determined. In addition, the method was used to determine the area specific resistance of cathodes deposited on fuel cell electrolytes.

Impedance in our case is defined as the combined effect of resistance and capacitive reactance.^{130, 131}

Resistance (R) – measures the difficulty to push an electric current through a circuit.

Capacitance (C) – is the amount of energy a capacitor can store (this depends upon its area, thickness, type of material and temperature).

AC impedance measurements take place over a range of frequencies, in our case 1Hz-13MHz. A voltage of 0.1mV was applied across the sample and a current response is measured at each frequency. The voltage was applied sinusoidally and can be expressed as

$$v_o = E_v \sin \omega t \quad \text{Equation 2-13}$$

[v_o = observed voltage at time (t) E_v = Amplitude, $\omega=2\pi f$ (f = frequency in Hz)]

The observed voltage can be seen in Figure 2-17 as a rotating vector at the point shown.^{130,}

131

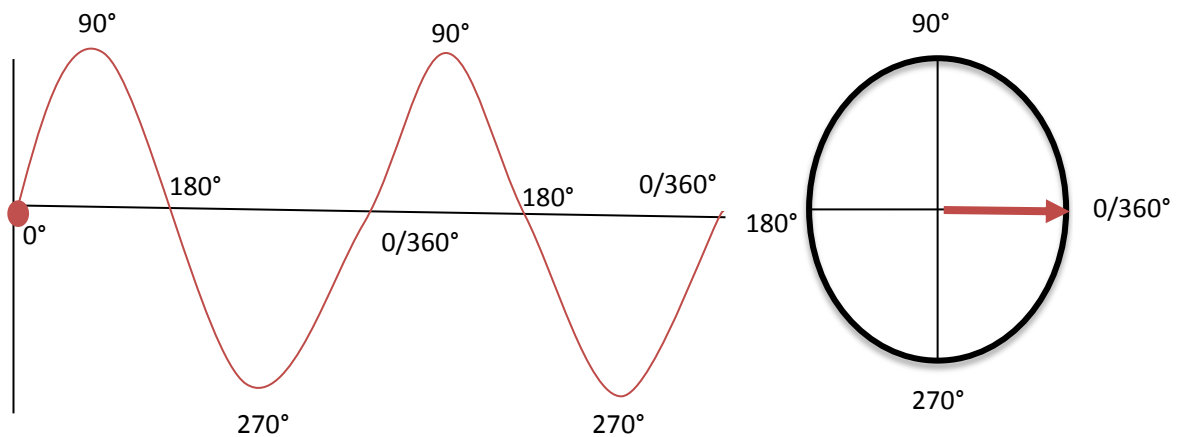


Figure 2-17 Waveform and Phasor diagram for sinusoidal voltage.

The resulting current response will be sinusoidal if the voltage is. However, whether they are in phase or out of phase with one another will depend on the material.

$$I_o = E_i \sin \omega t + \phi \quad \text{Equation 2-14}$$

[I_o = observed current at time (t) ϕ phase angle]

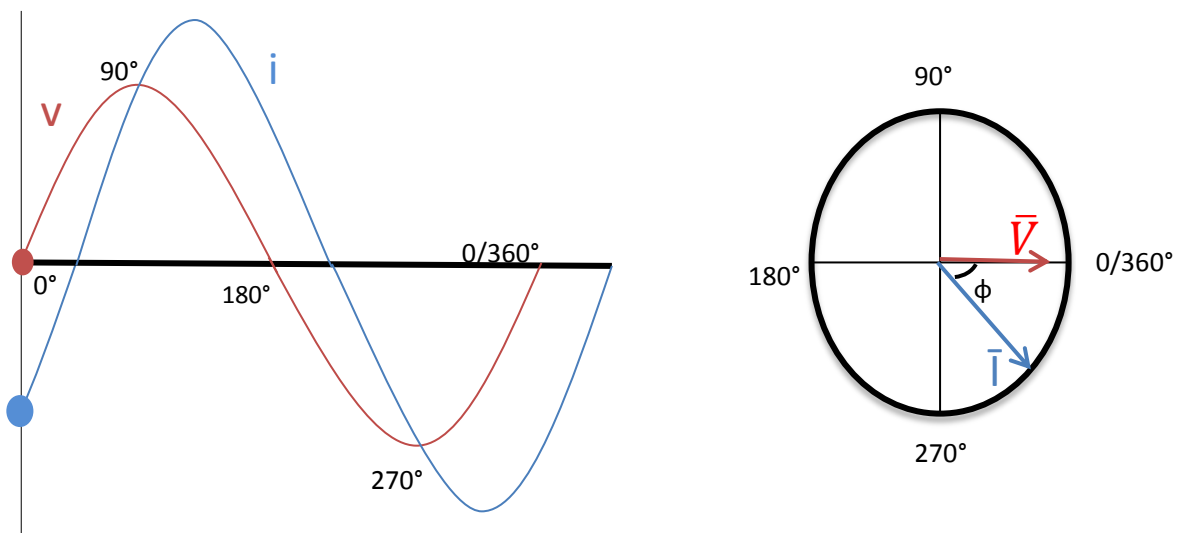


Figure 2-18 Waveform and phasor diagram showing the shift between the voltage and the current at a known frequency ω

A phase angle for the voltage and current can be measured to give a defined value, but it is the phase angle (ϕ) between them that is important and this remains essentially constant throughout a wave. The phase angle is usually measured from the voltage vector as the reference, with a + or – sign denoting whether the current is ahead or lagging the voltage. This allows for the phase angles to be plotted as vectors as shown in Figure 2-18.^{130, 131}

If a sinusoidal voltage is applied to a pure resistor circuit the current can be expressed as equation 2-15 (when Ohm's law is obeyed equation 2-16), and this will result in Figure 2-19. The voltage and current waveforms are in phase with each other ($\phi=0$), both passing through zero and peaking at the same angles. The resistor is frequency independent and therefore the magnitude does not decrease.

$$i = \frac{V}{R} \sin(\omega t + 0) \text{ Equation 2-15}$$

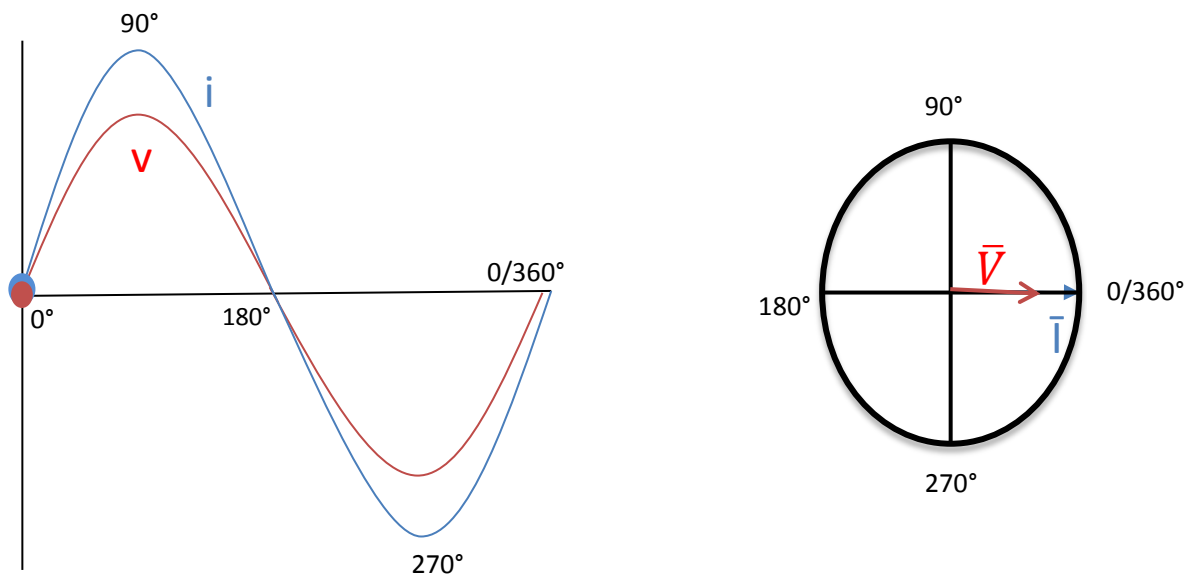


Figure 2-19 Waveform and phasor diagram showing the voltage and current in phase for a pure resistor.

$$V=IR \text{ Equation 2-16}$$

[I=current, V = voltage, R = resistance]

However, if instead of a pure resistor circuit, we replace this with a pure capacitor circuit, and apply the same sigmoidal voltage, then the current can be expressed as equation 2-17, with a pure capacitor relationship being given by equation 2-18. ^{130, 131}

$$i = \frac{V}{X_c} \sin(\omega t + \frac{\pi}{2}) \quad \text{Equation 2-17}$$

$$i = C \left(\frac{dV}{dt} \right) \quad \text{Equation 2-18}$$

[Capacitive reactance = $X_c = \frac{1}{\omega C}$, C = capacitance]

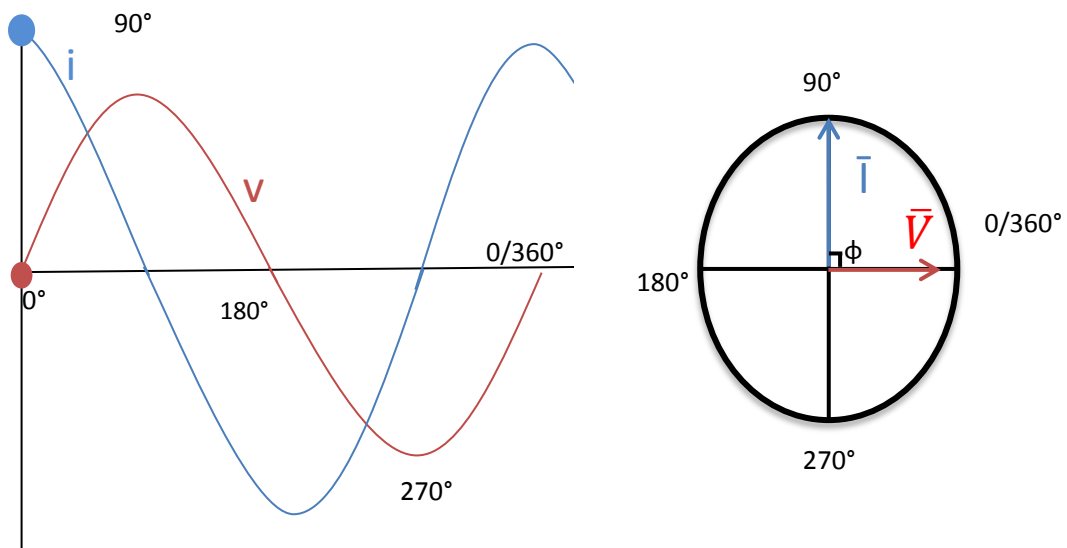


Figure 2-20 Waveform and phasor diagram showing the voltage and current out of phase for a pure capacitor.

In a pure capacitor the voltage and the current are out of phase by $\phi = +90^\circ$. The current is leading the voltage with the \bar{I} vector being perpendicular to \bar{V} (Figure 2-20). The capacitor is frequency dependent and therefore the magnitude decreases as frequency increases. The data are expressed in such a way that allows the notation of the voltage to be equation 2-19 (Ohm's law must be obeyed). Therefore as $V=IR$ the capacitance reactance must also have a resistive component explaining the fall in magnitude ($-jX_c = R$).

$$\bar{V} = -jX_c \bar{I} \quad (j = \sqrt{-1}) \quad \text{Equation 2-19}$$

While these are ideal scenarios of a pure resistor and capacitor, systems that are not purely either will contain both components. Consequently, when they are in series as a resistance capacitor (RC) circuit, and a voltage is applied across, it must be equal to the sum of the individual voltages (Equation 2-20/21).

$$\bar{V} = \bar{V}_{Resistance} + \bar{V}_{capacitance} \quad \text{Equation 2-20}$$

$$[\bar{V}_{Resistance} = \bar{I}R, \quad \bar{V}_{capacitance} = -jX_c\bar{I}]$$

$$\bar{V} = \bar{I}(R - jX_c) \quad \text{Equation 2-21}$$

This provides what is known as the impedance vector \bar{Z} (equal to $R - jX_c$) for each frequency in the range. It can sometimes be referred to as a generalised form of resistance, (equation 2-22).

$$\bar{V} = \bar{I}\bar{Z} \quad \text{Equation 2-22}$$

$$[\bar{Z} = R - jX_c]$$

The impedance vector for the RC circuit consists of a magnitude and a phase angle for each frequency, same as for the pure resistor and capacitor. In an RC circuit the impedance changes with frequency when the voltage is applied and therefore so must the magnitude and the phase angle. In all cases, the data would be plotted on a complex Nyquist plot and presented as real Z_{re} vs imaginary Z_{im} component, or more commonly known as Z' and Z'' . Consequently the impedance vector \bar{Z} contains both the real part and imaginary part at each frequency (Equation 2-23)

$$\bar{Z}(\omega) = \bar{Z}_{Real} - j\bar{Z}_{imaginary} \quad \text{Equation 2-23}$$

$$[\bar{Z}_{Real} = R, \bar{Z}_{imaginary} = X_c]$$

The magnitude of the vector is calculated through Pythagoras relationship see equation 2-24/25

$$\bar{V}^2 = \bar{V}_R^2 + \bar{V}_C^2 \text{ Equation 2-24}$$

$$[(IZ)^2 = (IR)^2 + (IX_C)^2 \quad (Z)^2 = (R)^2 + (X_C)^2]$$

$$\text{Magnitude} = \sqrt{R^2 + X_C^2} = \sqrt{\bar{Z}_{Real}^2 + \bar{Z}_{imaginary}^2} \text{ Equation 2-25}$$

The phase angle is given by trigonometry.

$$\phi = \tan^{-1}\left(\frac{X_C}{R}\right) = \tan^{-1}\left(\frac{Z_{im}}{Z_{re}}\right) \text{ Equation 2-26}$$

An annotated sketched Nyquist plot for an imaginary RC circuit is shown in Figure 2-21, whilst figure 2-22 shows a pure resistor and pure capacitor of actual Nyquist plots.^{127, 130,}

131

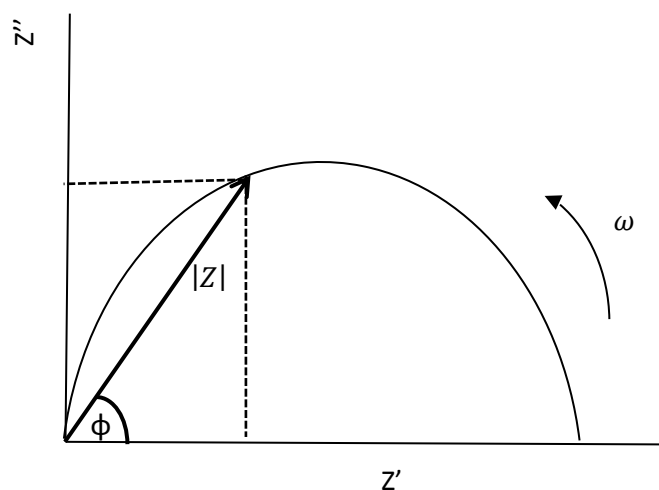


Figure 2-21 Sketched Nyquist plot for an imaginary RC circuit showing the components involved in a complex impedance plane plot

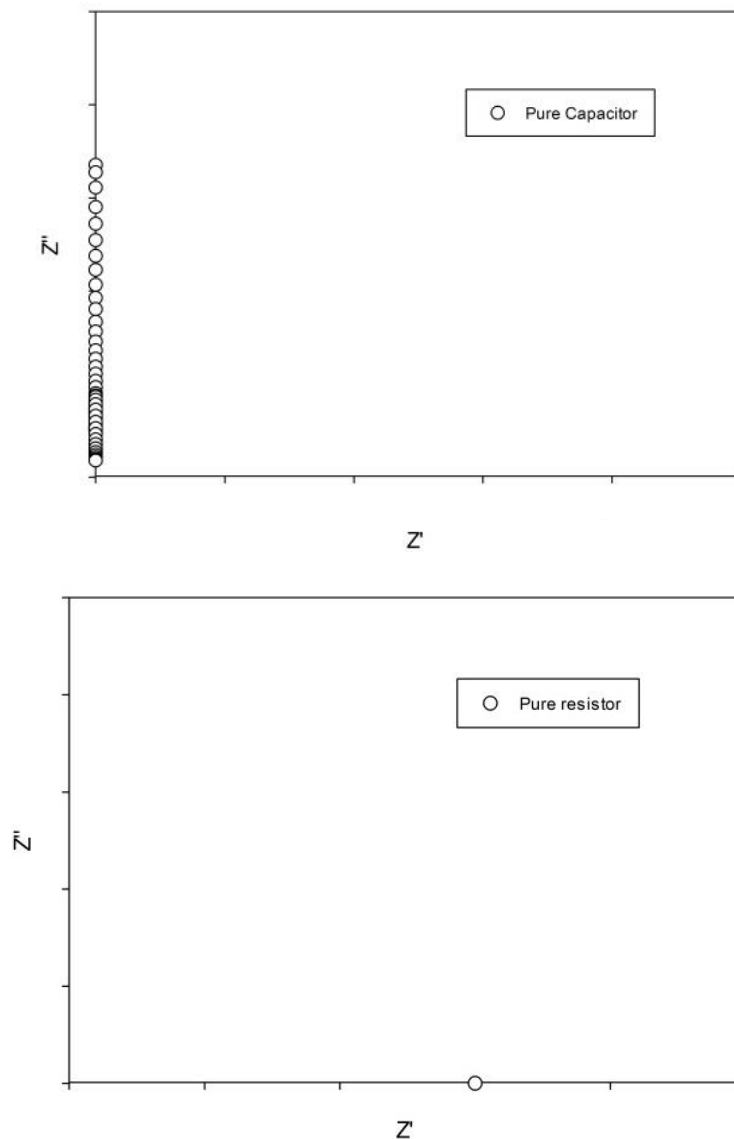


Figure 2-22 Nyquist plot of pure resistor and pure capacitor

2.6.2 Analysis of impedance data

2.6.2.1 Equivalent circuit elements

In order to fully understand and analyse the processes involved in an electrical system, a single model for the system cannot be used as it would be far too complicated. Consequently, a simplified fitting model must be constructed, which is a mathematical model based upon the researchers understanding and knowledge of their material.

The electrochemical behaviour of an ionic conductor in a fuel cell has a similar set up to a resistor and a capacitor circuit applied in parallel for each response component. The characteristic relaxation time, which is a product of the resistance and capacitance, can be defined as the time it takes for the capacitor component to be charged through the resistor equation 2-27.^{127, 129}

$$\tau = RC = \frac{1}{\omega_{max}} \text{ Equation 2-27}$$

From a complex impedance plot both R and C can be calculated for each component of a conductor through a fitting model. R values can be obtained from the fitting of the semi-circle giving the intercept of x axis, but assigning this to the relevant component regions of the ionic conductor depends upon the capacitance.¹²⁷

Table 2-6 Typical capacitance values from a corresponding response on a 1 cm³ material

Capacitance (F)	Response component
10 ⁻¹²	Bulk
10 ⁻¹¹ -10 ⁻⁸	Grain Boundary
10 ⁻¹⁰ -10 ⁻⁹	Bulk Ferroelectric
10 ⁻⁹ -10 ⁻⁷	Surface layer
10 ⁻⁷ -10 ⁻⁵	Sample-electrode interface
10 ⁻⁴	Electrochemical reactions

Typically capacitance magnitudes for ionic conductors component regions are as displayed in Table 2-6.¹²⁷ A fitting programme (in our case, the programme Z-view was used) is usually used to construct equivalent circuits, that match the properties of your material. The

programme fits a calculated semi-circle to the data's semicircle using the equivalent circuit that has been constructed and produces R and C data values from this.

If the relaxation times (product of resistance and capacitance) are different by several orders of magnitudes for each of the component i.e. bulk and grain, separate semicircles would be observed throughout the frequency range. Each semi-circle corresponding to a different response component in our analysis, in these cases an equivalent circuit model is required to fit the data that contained both RC in parallel and in series, similar to the equivalent circuit shown in Figure 2-23.^{127, 129}

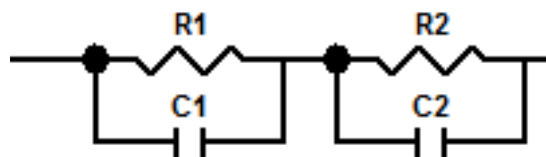


Figure 2-23 equivalent fitting circuit for impedance plots containing separate definable semicircles

If the relevant relaxation time does not differ greatly then the semi-circles will overlap producing distortions or, in non-ideal cases, a single semicircle only. These must also be fitted using this programme, and a relevant equivalent circuit used where possible. If this is not possible then the total conductivity of the material can be simply estimated from the high intercept of the x axis and the samples parameters.

2.6.2.2 Bulk and grain electrolyte analysis and fitting model

The ionic conduction of a sintered material can be explained using a brick layer model. Pictorially this involves cubes as the bulk or grain interior of the material, and a secondary phase between each of them corresponding to the grain boundary phase (Figure 2-24).^{127,}

129

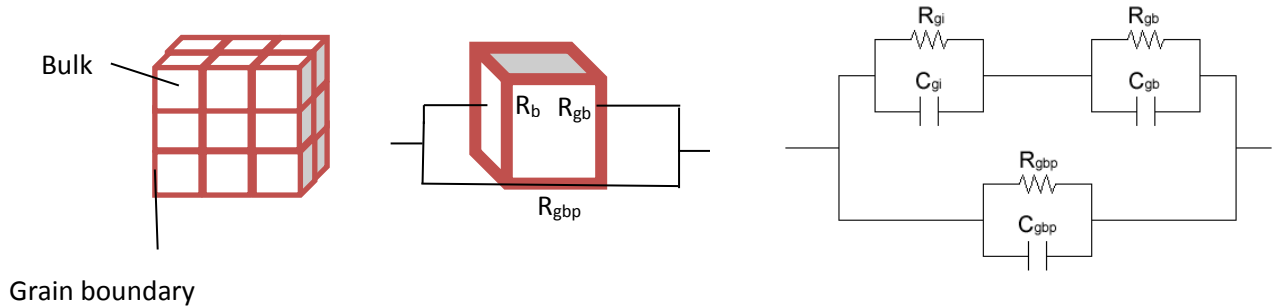


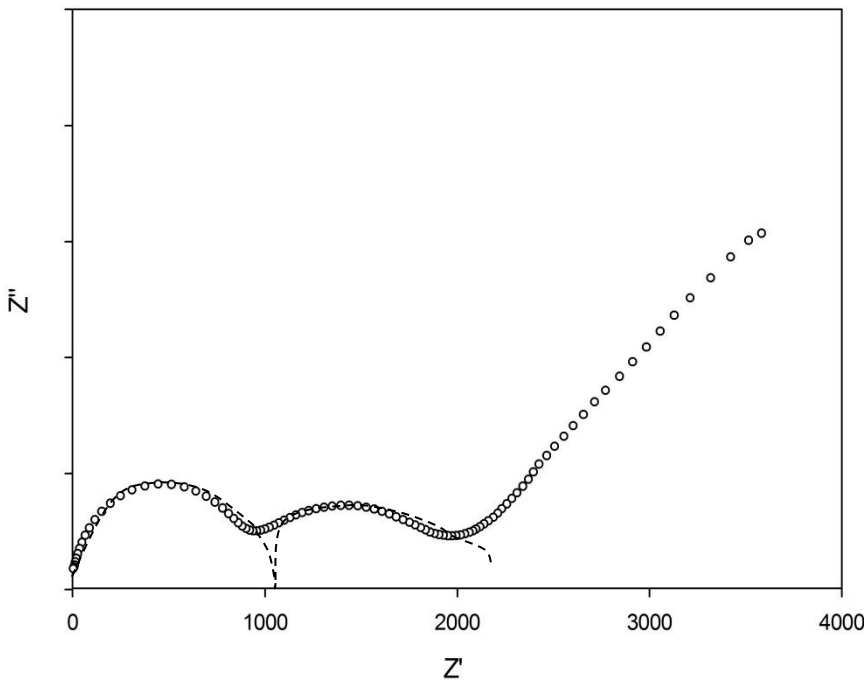
Figure 2-24 Brick layer schematic of conduction for a polycrystalline sample and equivalent circuit.

Conduction can either occur through the bulk and the grain boundary or just the grain boundary. The corresponding equivalent circuits from both are shown in Figure 2-24. The conduction pathway must be understood for the fitting, and the capacitance values would help in the assignment of each component as either bulk or grain. Grain boundary phases can be a result of

- The polycrystalline materials having random orientation of the bulk.
- The occurrence of other phases such as sintering aids or impurities in these regions.
- The density of the pellet – Low density causes small gaps between the bulk grains.

In order to remove grain boundary effects a dense single crystal would be required with growth in a particular direction. However, this is not usually possible and so sintered powders pellets are analysed.^{127, 129}

Ideally the fitting model should have resulted in an equivalent circuit containing both bulk and grain RC circuits to determine separate conductivity contributions.^{127, 129} However, when separation was not possible due to complete overlap of the semicircles, a total conductivity was determined. Figure 2-25 below shows an equivalent fitting of example data of $\text{BaSc}_{0.3}\text{Yb}_{0.35}\text{B}_{0.05}\text{Ti}_{0.3}\text{O}_{3-\delta}$ the bulk component can be assigned to the higher frequency semicircle and the grain boundary component to the lower, with an electrode response line corresponding to the Pt contact.^{127, 129}



Resistance (Ω)	Capacitance (F)
1011.3 (<i>Bulk</i>)	2.22E-10
1399.4 (<i>Grain</i>)	1.20E-08

Figure 2-25 Impedance plot of $\text{BaSc}_{0.3}\text{Yb}_{0.35}\text{B}_{0.05}\text{Ti}_{0.3}\text{O}_{3-\delta}$ in a dry N_2 at 350°C data fitted with a RC circuit equivalent fitting of the bulk and grain boundary responses

2.6.2.3 Area specific resistance (ASR) analysis and fitting model

Area Specific Resistance (ASR) is a resistance measurement between the opposite faces of a material over a known area. It uses the same equipment and analysis software as the AC impedance measurements.^{127, 129} An alternative current is passed across the sample over a range of frequencies and the resistance is measured. The ASR measurements throughout this work were obtained using an electrolyte pellet with a painted layer of cathode ink on each side dried at the required temperatures (with pure cathode materials, and cathode composites made up of both the cathode and the electrolyte, being used). A current collector (platinum contacts) was then placed on each side and heated to 800°C for 1 hr. The ASR of a cathode material is measured, as it is a major contributor to the resistance of the overall cell.^{127, 129} Ideally, the measurement will involve four responses, two from the electrolyte, bulk (1) and the grain boundary (2) semicircles and two from the cathode. For the cathode, one semicircle is associated with the microstructure of the composite cathode (electrode-electrolyte interface) and is independent of the partial pressure of oxygen (3). The other semicircle at lower frequency is associated with the adsorption of O₂ at the TPB surface, which is dependent on the partial pressure of oxygen (4).¹²⁹

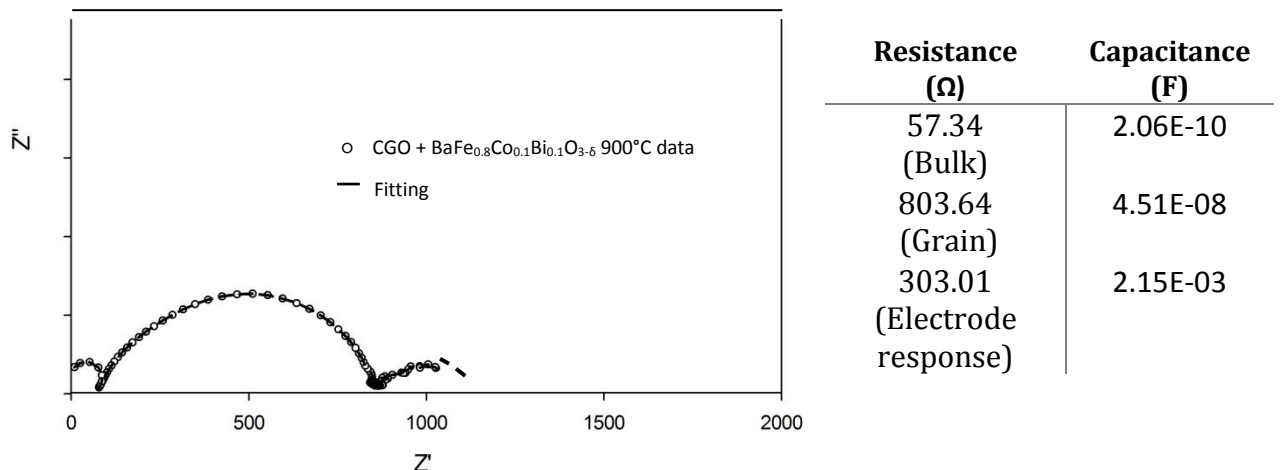


Figure 2-26 Impedance plot of CGO + BaFe_{0.8}Co_{0.1}Bi_{0.1}O_{3-δ} electrode on a CGO pellet at 900°C fitted with an equivalent circuit fitting of the bulk grain boundary responses and electrode response.

However, these response semicircles can be distorted and overlapping. Therefore, a total of two to three elements were constructed in an equivalent circuit-fitting model. The three fitting model is displayed above in Figure 2-26.

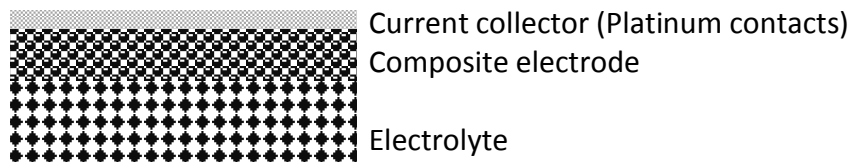


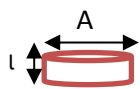
Figure 2-27 Physical representation of an ASR measurement

For the ASR data analysis, the electrode response is only measured and therefore the resistance of the Nyquist plot does not start at zero. It is usually measured from the electrode semi-circle high and low intercepts on the x-axis (equation 2-28 I_h = high intercept, I_L = low intercept, 2 = number of sides to pellet, A = Area of the pellet).

$$ASR = \frac{I_h - I_L}{2} \times A \quad \text{Equation 2-28}$$

2.6.2.4 Reporting of conductivity

In the analysis of impedance spectroscopy, it is the resistance (R) that was obtained, however it is the convention for the conductivity to be presented. The conductivity of the sample was acquired through the inverse of the resistance multiplied by the geometric factor of the pellet (equation 2-29).



$$Gf = \frac{\text{Area } (A)}{\text{Thickness } (l)} \quad \sigma = \frac{1}{R} \times Gf \quad \text{Equation 2-29}$$

The impedance data was collected over a series of temperatures usually 350°C-800°C. The activation energy is calculated from equation 2-30; this is an Arrhenius style function and the activation energy is calculated from the gradient of a plot of $\log_{10}(\sigma T)$ vs $1000/T$.

$$\sigma T = A \frac{-Ea}{RT} \text{ Equation 2-30}$$

[R = gas constant, Ea = activation energy, A constant]

2.6.3 Instrumentation

The conductivity instrumentation consisted of a vertical tube furnace, a removable rig port and an impedance analyser combination. The pellet was attached to the rig by the Pt foil electrodes, which are wrapped around the Pt wire on the rig to act as a contact points. The rig was then lowered into the furnace, and connected to either a PSM 148 analyser or a Hewlett Packard 4182A analyser by plug connector points with shielded wires to remove background noise on the analyser. In addition if controlled atmospheres were needed i.e. N₂ to remove any contribution of p-type conduction, then the gas needed was bubbled through concentrated sulphuric acid or water for dry and wet environments respectively.

2.7 Fuel Cell Test

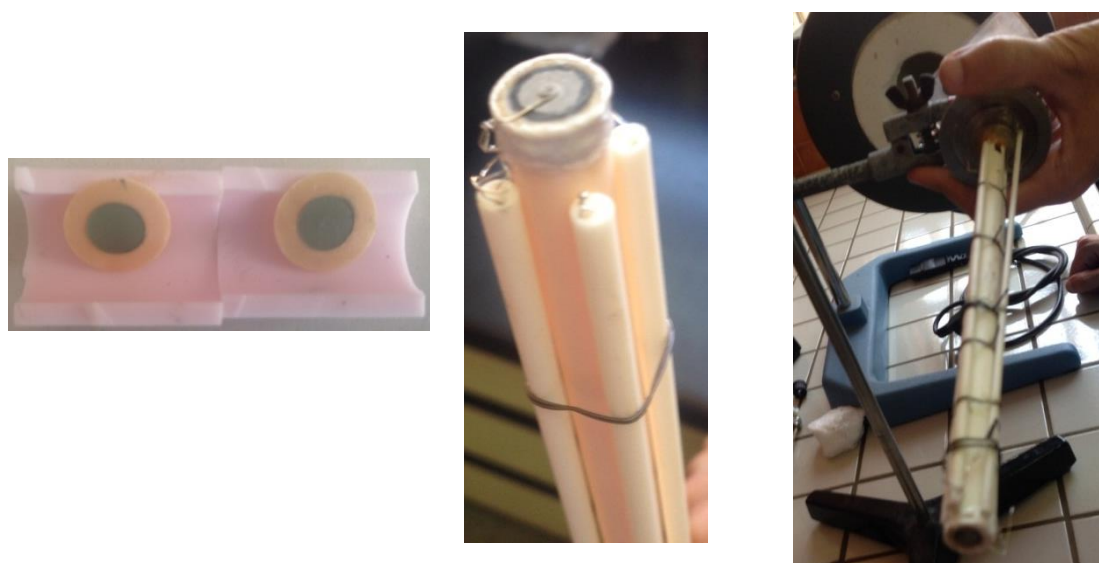


Figure 2-28 fuel cell setup a) individual pellets top layer Pt current collector, b) pellet bonded to rig with cermet, c) full rig setup.

Fuel cell tests were carried out during a 1-month placement at the School of Science at the University of Malaga. Simple button cells were constructed consisting of an electrolyte supported pellet which were sintered at 1500°C for 12hrs at a heating and cooling rate of 5°C a minute. A NiO-CGO composite anode was painted on one side and the specific research cathode composite material on to the other. These pellets were first fired at 1200°C for 1hr for the anode and then at 900°C for 1hr for the cathode materials. The cells were then coated with Pt paste over the surface of the electrodes and fired at 800°C for 30 minutes, (Figure 2-28a) and then a short length of Pt wire was attached to either side. Cell construction was duplicated for concordant results and the electrode surface area was 0.25cm². The pellet in Figure 2-28b was cemented to the custom built test rig using cermabond 668 (Aremco) and cermabond thinner, and fired at 500°C overnight, with the NiO-CGO layer facing down the tube. Once set up, the custom-built rig allows H₂ gas to be flowed on the inner tube to supply to the anode. The cathode/current collector is exposed to the air, and the rig is inserted in to a vertical tube furnace with the temperature varied up to 700°C (a schematic of the rig is shown in Figure 2-29).

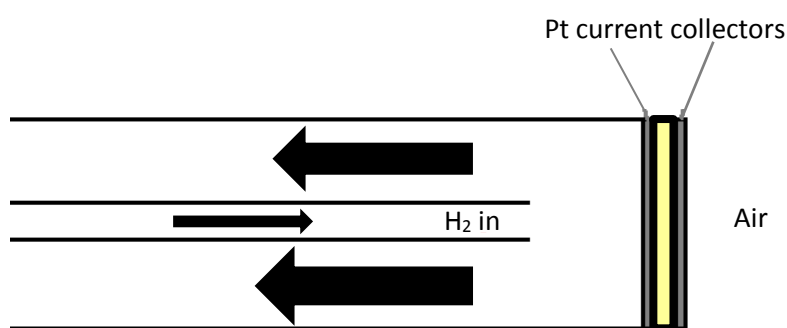


Figure 2-29 Schematic diagram of custom rig fuel cell set up

The initial reduction of the anode material (to reduce NiO to Ni metal) took place for 1 h in hydrogen at 500°C. The open circuit voltage (OCV) was then measured, with ≈1V predicted by the Nernst equation, if lower values are seen this indicates that there may be either

broken seals on the cell and a mixing of oxidant and fuel, or electronic conduction through the electrolyte. This is partially expected with CGO for temperatures $>600^{\circ}\text{C}$ as it is known to display electronic conduction. Maximum power densities can be calculated and compared with the commercial target value above 500 mWcm^{-2} in mind.¹³² The instrumentation recorded the power curves for a temperature range of $500\text{--}700^{\circ}\text{C}$ in 50°C steps with a waiting time of 30 min between each measurement. The tests were carried out with humidified hydrogen as the fuel, and air as the oxidant. Fuel gases were passed through a bubbler of water at a temperature of 20°C to ensure a constant water content of about 3%. The power curves were collected by a VSP-biologic cyclic-voltammeter at a scan rate of 5 mVs^{-1} .¹³²

2.8 Scanning electron microscope

Scanning electron microscopes (SEM) was used to provide much higher resolution images than would be possible by optical microscopes, on a scale of $100\mu\text{m} - 1\text{ nm}$. SEMs are used to study the samples surface, providing information on the particles composition, morphology and topography.¹³³

It works through focusing an electron beam on to the surface of the sample, which excites atoms at or near the surface. They release electrons which are measured and used to produce an image created from their position from the detector. These are known as the secondary electrons and it is these electrons that are most commonly used in SEM.¹³³ There are also back scattered electrons which are electrons from the beam which have reflected off the samples surface. In addition to the characteristic X-ray ejected from elements in the sample when electrons are bombarding the surface. Back scattered electrons and ejected

X-rays can be used to provide elemental composition of the sample, which is used in a technique known as energy dispersive X-ray spectroscopy (EDAX).

In this research the SEM was used to study the surface and cross sectional morphologies of sintered pellets and constructed SOFCs. The samples were spluttered in gold before measurement to reduce the electrostatic charge build up at the surface and were attached to conducting pads. The SEM measurements were carried out using a JEOL SM-6490LV operating under high vacuum and fitted with an INCA energy EDAX system at the University of Malaga (Figure 2-30).



Figure 2-30 Scanning electron microscopy used for the measurements - JEOL SM-6490LV.

Chapter 3

3 Evaluation of $\text{Sr}_{0.8}\text{Ca}_{0.2}\text{Mn}_{0.9}\text{Si}_{0.1}\text{O}_{3-\delta}$ composite cathode material with apatite and fluorite electrolytes

3.1 Introduction

Early SOFC electrolyte research has primarily focused on fluorite and perovskite based structures, which conduct via an oxygen vacancy mechanism. However at the end of the last century apatite silicates were proposed as alternative electrolyte systems, involving a interstitial oxide ion conduction mechanism.¹³⁴ Studies involving the development of silicate apatite electrolytes for SOFC applications increased at the turn of the century. Research included the lowering of the synthesis and sintering temperatures to reduce production costs, as well as thin film fabrication to reduce ohmic losses incurred.^{53,135} There is a need however, to identify the more pressing issue of the electrolyte-cathode interfaces. Prior studies have examined cathode materials consisting of a transition metal containing perovskite materials, for example doped LaMnO_3 and LaCoO_3 . Doping these materials with strontium increases the p-type electronic conductivity, due to the introduction of mixed valency; e.g. $\text{La}_{1-x}\text{Sr}_x\text{MnO}_3$ (LSM) has high electronic conductivity and high catalytic activity for ORR but low ionic conductivity, so a balanced trade-off for all the features must be examined.¹³⁶⁻¹³⁸

Previous work in the group has shown that doping materials such as SrMnO_3 with silicon leads to an increase in electronic conductivity. This is due to a change from a hexagonal

(containing face sharing of octahedra) to a cubic (corner linked octahedral) perovskite structure. However, for $\text{SrMnO}_{3-\delta}$, high levels (15%) of silicon were required to stabilise the cubic perovskite, and while the Si doping is beneficial in this respect, it might also be expected to show some detrimental effects in terms of partially disrupting the electronic conducting pathways.^{139, 140}

Using this as a starting point, and building on previous work within our group, has allowed the development of a $\text{Sr}_y\text{Ca}_{1-y}\text{MnO}_{3-\delta}$ cathode material with a view to lowering the amount of silicon doping required.^{139, 140} The end member SrMnO_3 ($y=1$) has a hexagonal cell, while CaMnO_3 ($y=0$) is orthorhombic. Work performed within our group showed that the $\text{Sr}_y\text{Ca}_{1-y}\text{MnO}_{3-\delta}$ samples were either hexagonal perovskites at high strontium levels, $y = 0.8$, or a mixture of hexagonal and cubic perovskites for $y = 0.7$, and a mixture of tetragonal and orthorhombic for $y = 0.5/0.6$.

In this work $\text{Sr}_{0.8}\text{Ca}_{0.2}\text{Mn}_{1-x}\text{Si}_x\text{O}_{3-\delta}$ ($x = 0, 0.05, 0.075, 0.1, 0.125$) would be investigated in an effort to reduce the amount of silicon required to lead to a symmetry phase change from hexagonal to cubic. The most conductive material would undergo compatibility testing with $\text{La}_9\text{SrSi}_6\text{O}_{26.5}$ (LSSO) and $\text{La}_{10}\text{GaSi}_5\text{O}_{26.5}$ (LGSO) electrolytes, which have been reported to show high oxide ion conductivity.^{107, 141, 142} The use of strontium and silicon in both the electrolytes and the cathode in theory reduces the cross component reactions at the interface. CGO electrolyte would also be examined for a commercial equivalent. Area specific resistance (ASR) measurements would then be recorded to measure the resistance of the cathode/electrolyte, and if possible will be initially analysed through the construction of an equivalent circuit-fitting model. This involves three resistors in series and capacitors for each in parallel. In theory, the individual bulk and grain boundaries from the electrolyte

are fitted to the first two resistors and capacitors, and the capacitance values would correspond to 10^{-11} F cm⁻¹ and 10^{-8} F cm⁻¹ respectively. The third would be fit to the electrode response with a capacitance of 10^{-4} F cm⁻¹ expected; each response component has a different capacitance magnitude due to the difference in the relaxation times. The electrode response components capacitance and resistance values would correspond to the ASR value.

3.2 Experimental

Sr_{0.8}Ca_{0.2}Mn_{1-x}Si_xO_{3-δ} (x=0, 0.05, 0.075, 0.1, 0.125) electrode material were prepared from stoichiometric amounts of CaCO₃ (99.9%), SrCO₃ (99.9%), MnO₂ (99%), and SiO₂ (99.9%) (a pre-drying step was included if required). The powders were intimately ground together and heated to between 1200-1300°C for 12 hours. They were then ball-milled (350 rpm for 1 hour, Fritsch Pulverisette 7 Planetary Mill) and subjected to a second heat treatment of between 1200-1300°C for a further 12 hours (higher silicon content usually required the slightly higher temperature). Powder X-ray diffraction at room temperature was used to confirm the phase purity of the samples as well as for cell parameter determination using GSAS (Bruker D8 diffractometer with Cu Kα₁ radiation = 1.5406 Å).

To gain further information into the silicon environment, ²⁹Si Solid state MAS NMR spectroscopic studies were collected, with samples prepared in the same way but using ²⁹Si-enriched SiO₂ (Cortecnet, 97.1%). These measurements were collected and analysed in the solid state NMR department at the University of Warwick. The samples were acquired through a single pulse experiment and a MAS frequency of ν_r = 15 kHz.

Conductivity measurement were performed using 4 probe dc measurements, on the samples which were pressed pellets at a pressure of 5000 kg cm⁻² in a 1.3 cm die set and

sintered for 12hrs at 1350°C. The four Pt electrodes were attached with Pt paste and the pellet fired at 800°C for 1 hour to produce contact points.

The apatite electrolytes $\text{La}_9\text{SrSi}_6\text{O}_{26.5}$ and $\text{La}_{10}\text{GaSi}_5\text{O}_{26.5}$, were prepared with the required amounts of La_2O_3 (99.9%), Ga_2O_3 (99.9%), SrCO_3 (99.9%) and SiO_2 (99.9%) (a pre-drying step was included if required) which were ground together and then heat treated at a temperature of 1200°C for 12 hours. The sample was then reground, ball milled (350rpm for 1 hour, Fritsh Pulverisette 7 Planetary Mill) and reheated for 12 hours at 1400°C. For a commercial comparison the fluorite electrolyte $\text{Ce}_{0.9}\text{Gd}_{0.1}\text{O}_{1.95}$ (CGO) was also examined, which was obtained from Sigma-Aldrich. Powder X-ray diffraction at room temperature was used to confirm the phase purity of the samples as well as for cell parameter determination using GSAS refinement software (Bruker D8 diffractometer with $\text{Cu K}\alpha_1$ radiation = 1.5406Å).

The chemical compatibility studies of the electrodes with the electrolytes were performed on a 1:1 wt% mixture, ground together and fired separately at 800°C, 900°C and 1000°C for 24hr with the phase purity and cell parameters determined.

For the area specific resistance (ASR) measurements, the most promising material $\text{Sr}_{0.8}\text{Ca}_{0.2}\text{Mn}_{0.9}\text{Si}_{0.1}\text{O}_{3-\delta}$ was mixed with each of the electrolytes $\text{La}_9\text{SrSi}_6\text{O}_{26.5}$ and CGO separately along with the binder decoflux (WB41, Zschimmer and Schwarz) using a ball mill (350rpm for 1 hour, Fritsh Pulverisette 7 Planetary Mill) . The resulting electrode inks were painted on to $\text{La}_9\text{SrSi}_6\text{O}_{26.5}$ and CGO electrolyte pellets on both sides and dried at 70°C; this was repeated a further 2 times to guarantee full covering of the pellets surfaces. The symmetric pellets were then heat treated for 1 hr at the required electrolyte temperatures (900°C and 1000°C). The pellets were then coated with Pt paste, with Pt foil attached to act

as a current collector layer before heating to 800°C for 45 minutes, to bind the paste and foil to the pellet. The ASR values were determined in air and recorded between 500°C-800°C in 50°C steps, using AC impedance measurements in a frequency range of 5Hz-13MHz (Hewlett Packard 4182A impedance analyser). The ASR data were investigated using the Z-view software programme, an equivalent circuit fitting model was produced however, it was not always possible to accurately extract individual contributions across the entire range.¹⁴³ Therefore, this ideal equivalent circuit fitting model could not be undertaken as even though at lower temperatures, there was partial separation of the individual response components (bulk, grain, electrode), overlapping was still witnessed. Furthermore at the required intermediate fuel cell temperatures (>500°C), a broad semicircle was observed, this corresponded to the electrode resistance only which was calculated from the low and high intercept values and had capacitance values ranging from $10^{-3} \text{ F cm}^{-1}$ to $10^{-5} \text{ F cm}^{-1}$.

Single fuel cells were prepared using 500 µm thick electrolytes with a 50:50wt% composite cathode and a 60:40wt% composite anode. A composite anode was heated at 1200°C for 1 hr on one side of the electrolyte pellet and then the composite cathode was heated at 900°C for 1 hr on the other. For a current collector of Pt paste and a Pt coil wire were attached on both sides and then heated to 800°C for 1 hr. The electrode surface area each side was 0.25 cm². The cell was sealed to the electrochemical setup using a ceramic-based material (Ceramabond 668/668A, Aremco). Fuel cell tests were carried out at the University of Malaga with Jose M Porras-Vazquez during my month long placement. Using a VSP – biologic Pro-s machine, with humidified pure hydrogen as the fuel and atmospheric air as the oxidant, operating between temperatures of 500-700°C. Fuel gases were humidified

using a bubbler of water at 20°C to ensure constant water content of 3%. Current-voltage (I-V) curves were obtained by cyclic-voltammetry at a scan rate of 5mVs⁻¹. The electrochemical tests were performed after reducing the anode material for 1 hr at 500°C.

3.3 Structural studies - $\text{Sr}_{0.8}\text{Ca}_{0.2}\text{Mn}_{1-x}\text{Si}_x\text{O}_{3-\delta}$

The undoped $\text{Sr}_{0.8}\text{Ca}_{0.2}\text{MnO}_{3-\delta}$ perovskite has a hexagonal unit cell. Doping of 7.5% silicon on to the manganese site resulted in a mixture of cubic and hexagonal phases at room temperature. In order to completely stabilise the cubic perovskite structure at room temperature 10% Si doping was required (Figure 3-1). The difference in the structures between undoped and silicon doped samples can be related to the tolerance factor, which ideally should be 1.0 for a cubic perovskite.¹⁴⁴

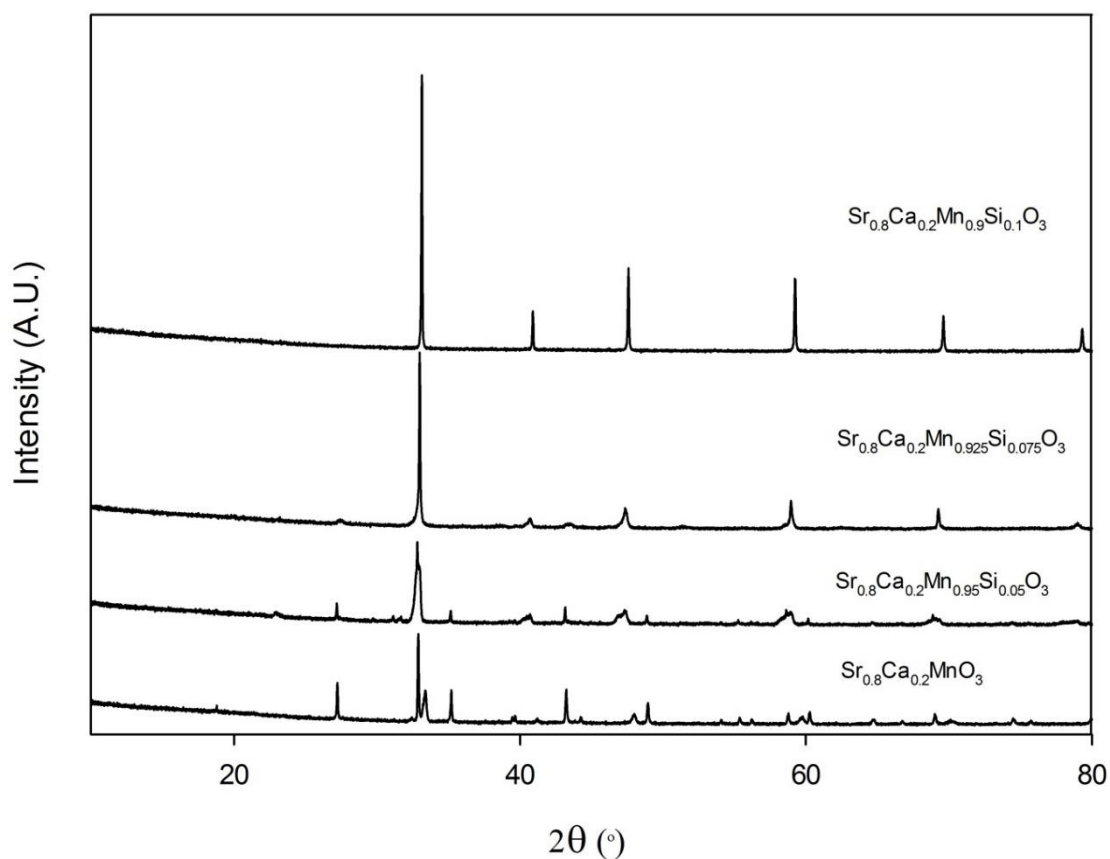


Figure 3-1 XRD patterns for $\text{Sr}_{0.8}\text{Ca}_{0.2}\text{Mn}_{1-x}\text{Si}_x\text{O}_{3-\delta}$ $x = 0, 0.05, 0.075$ and 0.1

The undoped $\text{Sr}_{0.8}\text{Ca}_{0.2}\text{MnO}_{3-\delta}$ system has a tolerance factor >1 and so adopts a hexagonal perovskite structure. The addition of Si^{4+} should at first glance cause a decrease in the average r_B cation size and we might therefore have expected an increase in the tolerance factor, further favouring the formation of the hexagonal perovskite. However, this is not the case, and can be related to the fact that the above argument does not consider the resulting oxide ion vacancies introduced. In particular the silicon is incorporated as SiO_4^{4-} replacing the octahedrally co-ordinated Mn^{4+} , thus leading to the production of oxide ion vacancies. This loss of oxygen, in turn causes the partial reduction of Mn^{4+} (0.53 Å) to Mn^{3+} (0.60 Å) increasing the average r_B , and decreasing the tolerance factor in favour of the cubic phase.^{140, 145} This is shown by the defect equation below (Equation 3-1).



Furthermore equation 3-1 also accounts for the increase in the cell volume on Si doping, with the reduction on the Mn^{4+} to form the larger Mn^{3+} out weighing the effect of the smaller sized Si^{4+} , and so an increase in the cell parameter is observed (Table 3-1)

Table 3-1 $\text{Sr}_{0.8}\text{Ca}_{0.2}\text{Mn}_{1-x}\text{Si}_x\text{O}_3$ cubic cell parameter and cell volumes

Compositions	a parameter Å	Cell Volume Å ³
$\text{Sr}_{0.8}\text{Ca}_{0.2}\text{Mn}_{0.9}\text{Si}_{0.1}\text{O}_{3-\delta}$	3.8127(2)	55.42(1)
$\text{Sr}_{0.8}\text{Ca}_{0.2}\text{Mn}_{0.875}\text{Si}_{0.125}\text{O}_{3-\delta}$	3.8157(1)	55.55(1)

In order to provide evidence that the silicon was incorporated into the structure, and to rule out that the silicon was simply collecting at the grain boundaries, ^{29}Si MAS NMR was performed and analysed by the University of Warwick solid state NMR department. The NMR data were collected on both a physical mixture of ^{29}Si enriched SiO_2 with the undoped

$\text{Sr}_{0.8}\text{Ca}_{0.2}\text{MnO}_{3-\delta}$ and our heat treated $\text{Sr}_{0.8}\text{Ca}_{0.2}\text{Mn}_{0.9}\text{Si}_{0.1}\text{O}_{3-\delta}$ sample (Figure 3-2). The physical mixture results in a single ^{29}Si resonance peak only, seen at δ -133 ppm (Figure 3-2 a). The $\text{Sr}_{0.8}\text{Ca}_{0.2}\text{Mn}_{0.9}\text{Si}_{0.1}\text{O}_{3-\delta}$ sample produces two peaks, a sharp narrow peak of low intensity at δ -70 ppm and a very broad resonance peak with a large downfield shift centred around 3000-3500 ppm (Figure 3.3 b and c). The physical mixture peak at -113 ppm is characteristic of $^{29}\text{SiO}_2$ only whilst the weak -70 ppm peak with narrow line width and long T_1 (>180 s) represents a small diamagnetic impurity phase formed under Si integration, and from the chemical shift obtained it is probably a strontium/calcium silicate impurity i.e. $(\text{Sr}/\text{Ca})_2\text{SiO}_4$ phase. The main broad peak centred around 3000-3500 ppm can be attributed as a Si environment that has a large shift and broad line width (over 4000 ppm) due to interaction with paramagnetic centres, i.e. the Mn^{3+} in the $\text{Sr}_{0.8}\text{Ca}_{0.2}\text{Mn}_{0.9}\text{Si}_{0.1}\text{O}_{3-\delta}$ structure. The paramagnetic influence of the Mn centres provides clear evidence of silicon incorporation into the perovskite structure, not just gathering at grain boundaries, as in the physical mixture.

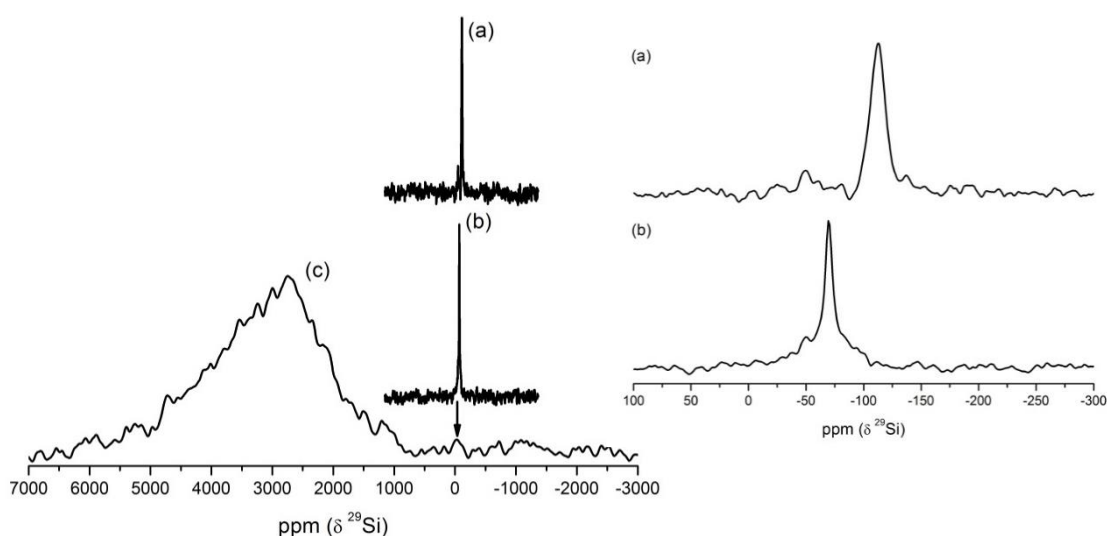


Figure 3-2 Solid state NMR data for (a) Physical mixtures of $^{29}\text{SiO}_2$ and $\text{Sr}_{0.8}\text{Ca}_{0.2}\text{MnO}_{3-\delta}$ -113 ppm and (b and c) the ^{29}Si doped $\text{Sr}_{0.8}\text{Ca}_{0.2}\text{Mn}_{0.9}\text{Si}_{0.1}\text{O}_{3-\delta}$

3.4 Conductivity measurements

The conductivity of the undoped hexagonal $\text{Sr}_{0.8}\text{Ca}_{0.2}\text{MnO}_3$ phase, as well as the Si doped cubic phases were examined. The conductivity measurements showed an improvement (Figure 3-3) on initial Si doping. Further doping to produce the pure cubic structure ($x=0.1$) produced the highest electronic conductivity ($\approx 26 \text{ S cm}^{-1}$ at 800°C).

Addition of silicon above this level to $x = 0.125$, where the pure cubic phase is still formed, resulted in a decrease in the conductivity. The increase in conductivity can be related to two factors, namely the change from face sharing of octahedra to corner sharing leading to increased orbital overlap allowing easier electron movement, along with the presence of mixed valency $\text{Mn}^{3+/4+}$. The decrease observed on increasing Si content above 10% is most likely a result of silicon in the structure starting to block the electronic conductivity pathways.

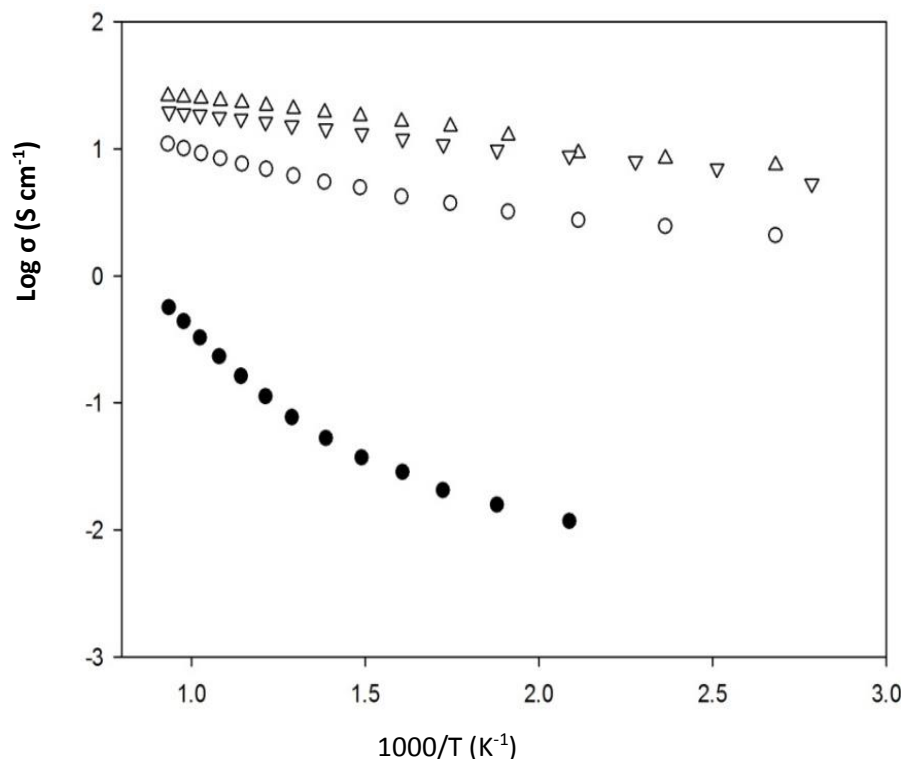


Figure 3-3 Conductivity data for $\text{Sr}_{0.8}\text{Ca}_{0.2}\text{Mn}_{1-x}\text{Si}_x\text{O}_{3-\delta}$ $x = 0$ (black circle), 0.075 (white circle), 0.1 (white triangle) and 0.125 (white inverse triangle)

Table 3-2 Conductivity values for $\text{Sr}_{0.8}\text{Ca}_{0.2}\text{Mn}_{1-x}\text{Si}_x\text{O}_{3-\delta}$ ($x=0, 0.075, 0.1$ and 0.125) at 800°C

Composition	$\sigma \text{ S cm}^{-1} (800^\circ\text{C})$
$\text{Sr}_{0.8}\text{Ca}_{0.2}\text{MnO}_{3-\delta}$	0.6
$\text{Sr}_{0.8}\text{Ca}_{0.2}\text{Mn}_{0.925}\text{Si}_{0.075}\text{O}_{3-\delta}$	10.34
$\text{Sr}_{0.8}\text{Ca}_{0.2}\text{Mn}_{0.9}\text{Si}_{0.1}\text{O}_{3-\delta}$	26.08
$\text{Sr}_{0.8}\text{Ca}_{0.2}\text{Mn}_{0.875}\text{Si}_{0.125}\text{O}_{3-\delta}$	19.53

3.5 Chemical compatibility results

Chemical compatibility tests were performed to simulate the effects of temperature on the electrolyte-cathode interfaces. Commercially used electrodes, for example LSM, have been found to form with some electrolytes at elevated temperatures non-conducting layers between electrode and electrolyte composites. The $\text{Sr}_{0.8}\text{Ca}_{0.2}\text{Mn}_{0.9}\text{Si}_{0.1}\text{O}_3$ (SCMS) cathode material was tested against two alternative apatite electrolytes of $\text{La}_9\text{SrSi}_6\text{O}_{26.5}$ (LSSO), $\text{La}_{10}\text{GaSi}_5\text{O}_{26.5}$ (LGSO), in a 50:50 weight percent mixture. These were fired at 1000°C for 24hrs, and showed limited reactivity between the SCMS and LSSO, with the observation of an impurity peak corresponding to the formation of an additional strontium/lanthanum manganite phase perovskite (Figure 3-4).

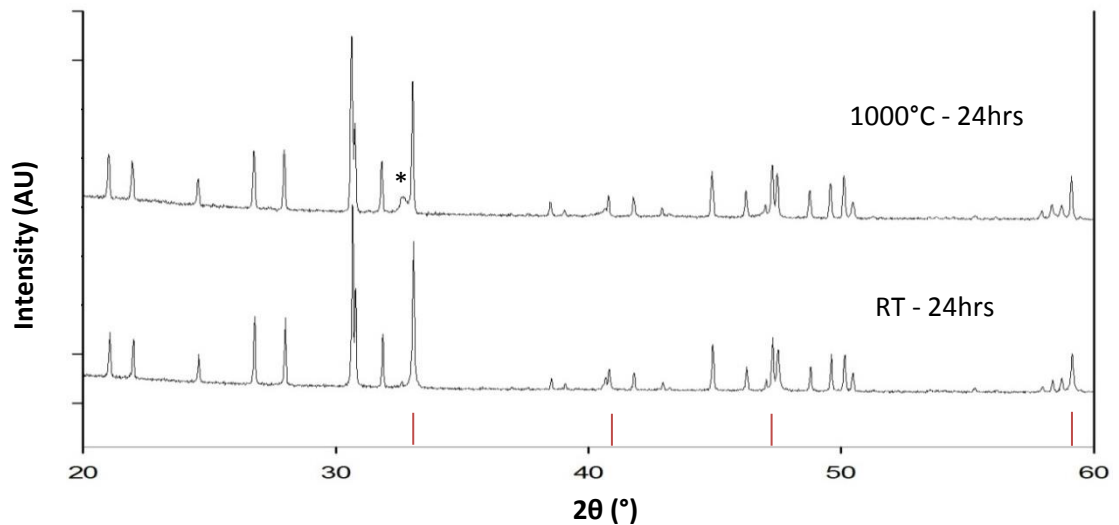


Figure 3-4 X-ray diffraction patterns for composite electrode, LSSO-SCMS at room temperature and fired at 1000°C for 24hrs (impurity highlighted *, red lines SCMS peak positions)

Further chemical compatibility tests at lower temperatures were therefore performed, and at 900°C for 24hrs there was no emergence of the additional perovskite impurity in the X-ray diffraction pattern (Figure 3-5).

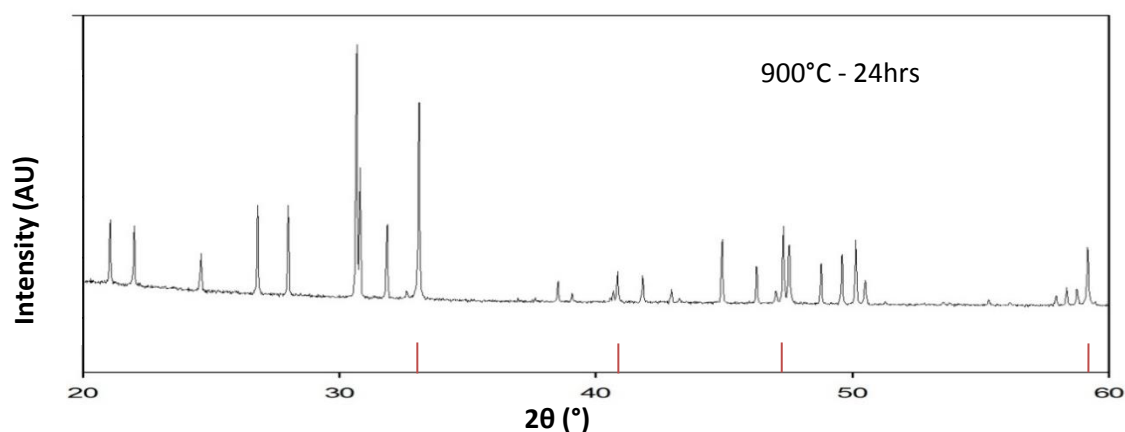


Figure 3-5 X-ray diffraction patterns for composite electrode, LSSO-SCMS fired at 900°C for 24hrs (red lines SCMS peak positions)

Further chemical compatibility tests involving the LGSO electrolyte and the same SCMS electrode were performed under the same conditions; fired at 900°C and 1000°C for 24hr, to compare the electrolytes and their cross reactions (Figure 3-6). The emergence of impurities at 900°C and at a 1000°C provides compelling evidence that the LGSO and SCMS undergo a more extensive chemical reaction. The reaction produces an additional strontium/lanthanum manganite perovskite impurity phase even at 900°C. However, it should be noted that, while the 900°C data suggested negligible reaction between LSSO and SCMS, it is possible that while no impurities were observed there may have been some intersubstitution between the two phases.

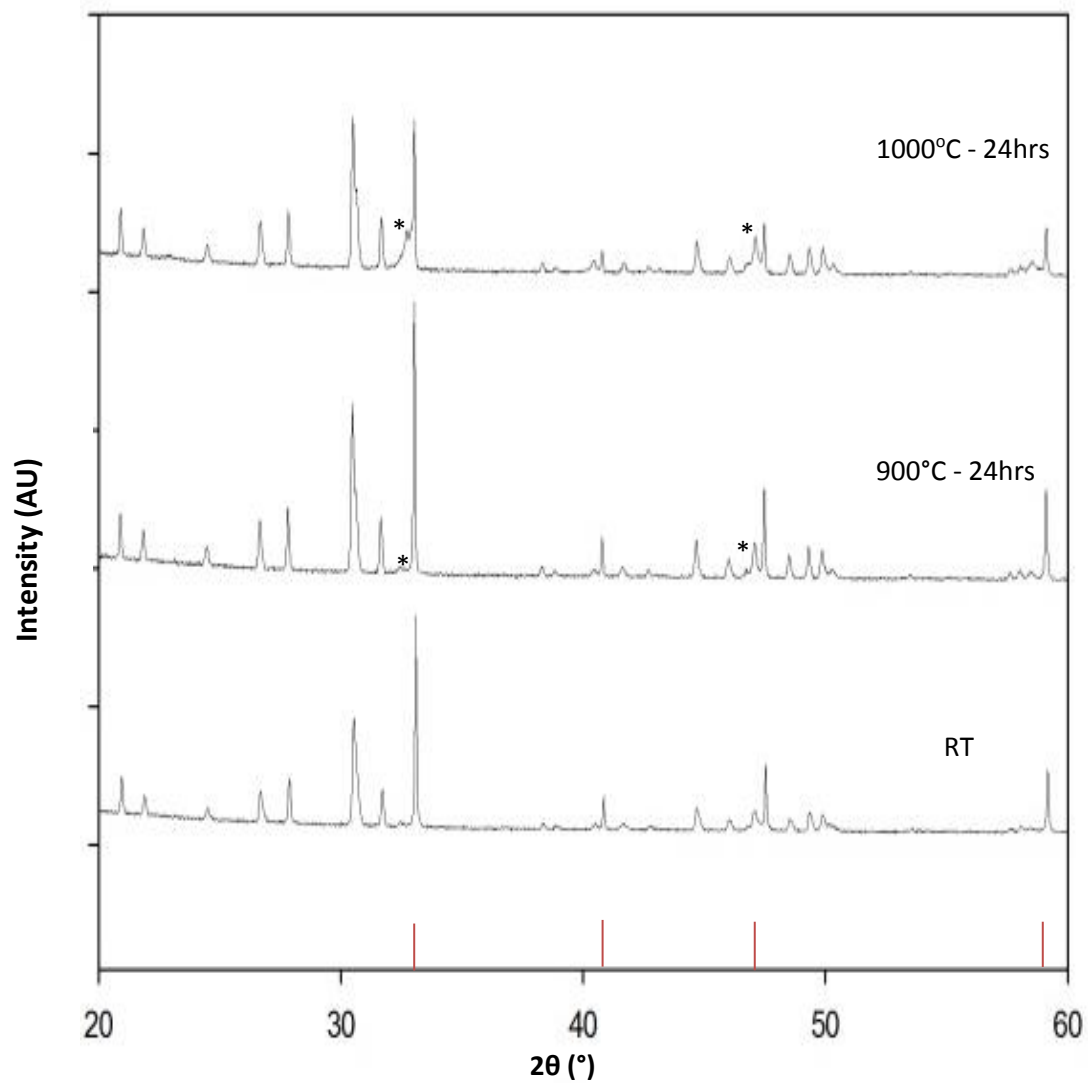


Figure 3-6 X-ray Diffraction patterns for composite electrode, LGSO–SCMS at room temperature and fired at RT, 900°C and 1000°C for 24hrs (impurities highlighted *, red lines SCMS peak positions)

Therefore, all of the XRD data were further analysed through the GSAS suite of programs for cell parameter determination. This analysis showed small cell parameter and volume changes for all the heat treated composites. Small cell parameter changes were even recorded for the SCMS:LSSO heated at 900°C suggesting that even though there were no apparent impurities seen in the diffraction pattern (Table 3-3 and Table 3-4), there was some reaction leading to cation intermixing.

Table 3-3 Cell parameters for composite electrode LSSO and SCMS 50:50 mix

	Composite	Unit Cell parameters (Å)			Unit Cell volume (Å ³)
	constituents	(a)	(b)	(c)	
RT	SCMS	3.81857(6)	-	-	55.687(3)
	LSSO	9.6997(1)	-	7.2168(1)	588.02(2)
900°C 24hrs	SCMS	3.81873(5)	-	-	55.681(3)
	LSSO	9.7024(1)	-	7.2109(1)	587.87(2)
1000°C 24hrs	SCMS	3.81800(9)	-	-	55.656(4)
	LSSO	9.6999(2)	-	7.2115(2)	587.62(3)

Similar effects were also seen in previous apatite chemical compatibility research with conventional La based electrode materials.⁵³ This suggests that there is some cation migration between the electrolyte and the electrode in these systems (depending on reaction conditions).

Table 3-4 Cell parameters for composite electrode LSGO and SCMS 50:50 mix.

	Composite	Unit Cell parameters (Å)			Unit Cell volume (Å ³)
	constituents	(a)	(b)	(c)	
RT	SCMS	3.8185(1)	-	-	55.679
	LSGO	9.7502(3)	-	7.2458(3)	596.55(5)
900°C 24hrs	SCMS	3.8206(1)	-	-	55.770(5)
	LSGO	9.7489(2)	-	7.2366(3)	595.63(4)
1000°C 24hrs	SCMS	3.82.02(2)	-	-	55.75(1)
	LSGO	9.7447(7)	-	7.2311(7)	594.6(1)

Following these chemical compatibility tests with apatite electrolytes, further experiments were performed between SCMS and a commercial electrolyte, gadolinium doped ceria ($\text{Ce}_{0.9}\text{Gd}_{0.1}\text{O}_{1.95}/\text{CGO}$). In prior work it has also been used as a buffer material with apatite electrolytes to reduce the interaction between the apatite electrolyte and the electrode.^{53,}
¹⁴⁶ Chemical compatibility tests were therefore also performed between LSSO and CGO electrolytes. As the LSSO showed less apparent reactivity with the electrode, only this electrolyte was studied further. A SCMS and CGO 50:50 wt% composite cathode was prepared for use with this LSSO electrolyte pellet. The XRD data for the 50:50 wt% composites of CGO-LSSO and CGO-SCMS are shown in Figure 3-7 and Figure 3-8 respectively.

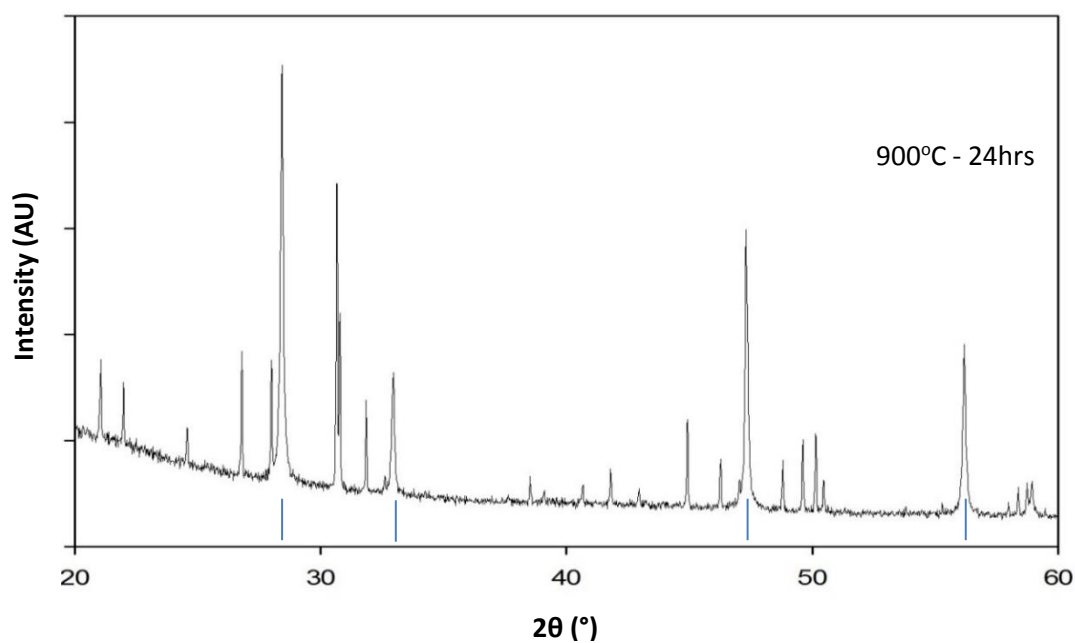


Figure 3-7 X-ray diffraction patterns for 50:50 wt% electrolyte mixture, CGO-LSSO fired at 900°C (blue lines CGO peak positions)

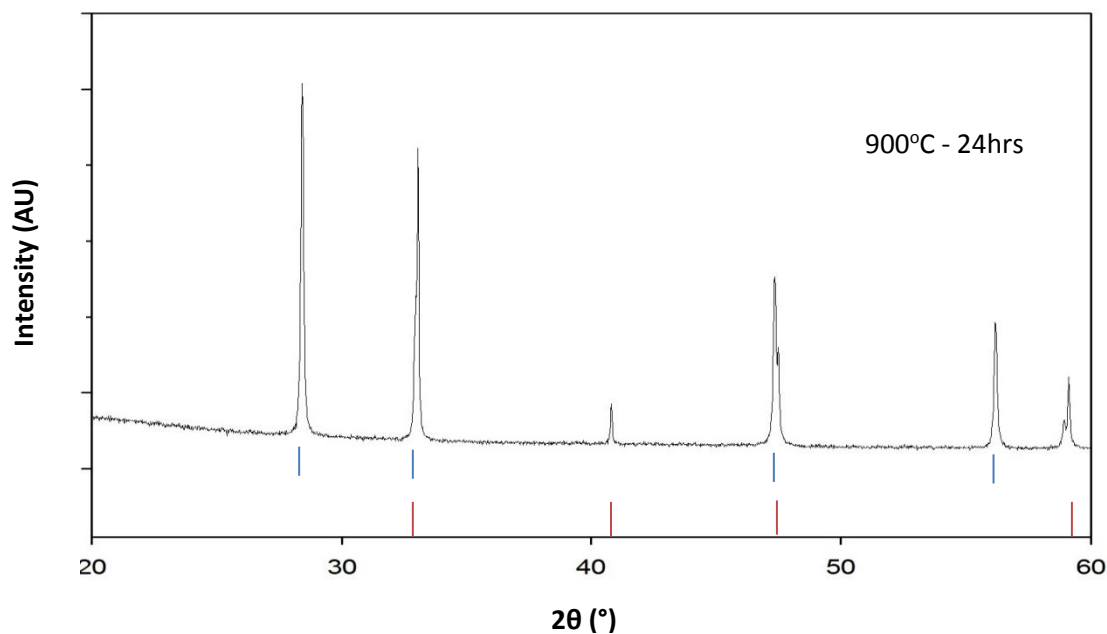


Figure 3-8 X-ray diffraction for 50:50wt% composite electrode, CGO-SCMS fired at 900°C, (red lines SCMS peak positions and blue lines CGO peak positions)

For LSSO and CGO there are no extra peaks visible but the cell parameters/volume (Table 3-5) show a small reduction for LSSO and an increase for the CGO. For the SCMS:CGO composite there is a no evidence of additional peaks due to impurities and there is limited expansion in the unit cells up to 900°C. However, above 900°C minor additional peaks were observed which were due to a $\text{Sr}_3\text{Mn}_2\text{O}_7$ impurity.

Table 3-5 Cell parameters for composite electrode CGO and SCMS 50:50 mix.

Conditions	Composite constituents	Unit Cell parameters (Å)			Unit Cell volume (Å ³)
		(a)	(b)	(c)	
RT	CGO	5.4181(1)	-	-	159.0(1)
	SCMS	3.81855(4)	-	-	55.680(1)
900°C 24hrs	CGO	5.4178(1)	-	-	159.10(6)
	SCMS	3.8200(1)	-	-	55.747(6)
RT	CGO	5.4179(1)	-	-	159.04(1)
	LSSO	9.7098(2)	-	7.2165(1)	589.23(3)
900°C 24hrs	CGO	5.4195(1)	-	-	159.18(1)
	LSSO	9.7038(2)	-	7.2196(1)	588.74(3)

These results are concordant with previous composite experiments, which suggest cation migration between two phases of the composite is occurring. While such interdiffusion is worrying it may not necessarily have a negative effect on the electrode performance, providing the resultant phases are not insulators.

3.6 Area specific resistance results

Following on from the chemical compatibility studies, area specific resistance (ASR) tests were performed. The ASR experiments involved separately a 100% SCMS cathode and a 50:50 wt% SCMS and LSSO composite painted on to LSSO pellets at a binding temperature of 900°C. However it was found that the cathode didn't attach and so ASR measurement were unable to be completed. So the previous limiting temperature of 900°C for 1hr suggested by the chemical compatibility results was removed, and the binding temperature was increased to 1000°C for 1hr. This higher temperature was in theory to allow better binding of the composites to the LSSO pellets, and even though weak impurities were previously seen through the XRD patterns at this temperature, these may not necessarily be detrimental to the conductivity or even present due to the shorter reaction time (1hr comparison to 24hr). This increased temperature still proved ineffective at binding the cathode to the pellets with ASR measurements still impossible.

Drawing on previous ASR research a CGO composite electrode on an apatite electrolyte was attempted.^{53, 138} A mixed composite layer involving CGO:SCMS of 50:50 wt% and 75:25 wt% with LSSO pellets were produced and fired at 900°C for 1 hr. The composite ratio were selected due to previous theoretical and experimental results suggesting that only a low amount of cathode material was required in the composite to provide the resulting high electronic conductivity.¹⁴⁷ The composite successfully attached and impedance

measurements were performed using this data. An equivalent circuit fitting programme was attempted to separate each circuit's contributing resistance (see experimental section 2.6.2). However this was unsuccessful due to the severity of the overlapping semicircles in nyquist plot, so each circuit could not be resolved and total electrode-electrolyte resistance was reported from the low and high intercepts.

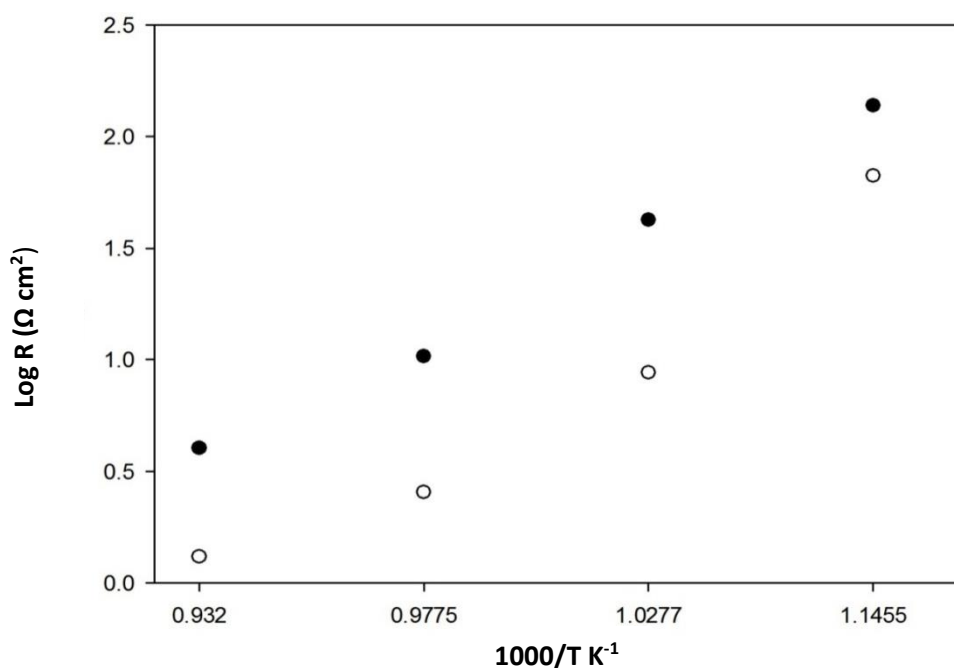


Figure 3-9 ASR data plotted logR (ASR) vs 1000/T in air for composite electrodes SCMS-CGO mixed in 50:50 ● and 25:75 ○ on a LSSO electrolyte.

Table 3-6 Area specific resistance values for composite electrodes deposited on a $\text{La}_9\text{SrSi}_6\text{O}_{26.5}$ electrolyte pellet at 900°C 1hr.

<u>Composition (ratio)</u>	<u>ASR ($\Omega \text{ cm}^2$) at 800°C</u>	<u>ASR ($\Omega \text{ cm}^2$) at 700°C</u>
CGO-SCMS (50:50) ●	4.02	42.31
CGO-SCMS (75:25) ○	1.31	8.75

Figure 3-9 and Table 3-6 show the ASR data for SCMS-CGO (50:50wt%) and SCMS-CGO (25:75wt%) composite cathodes on LSSO electrolyte. Overall the resistance is too high in these composites for applications suggesting problems with using these composites with apatite electrolytes.

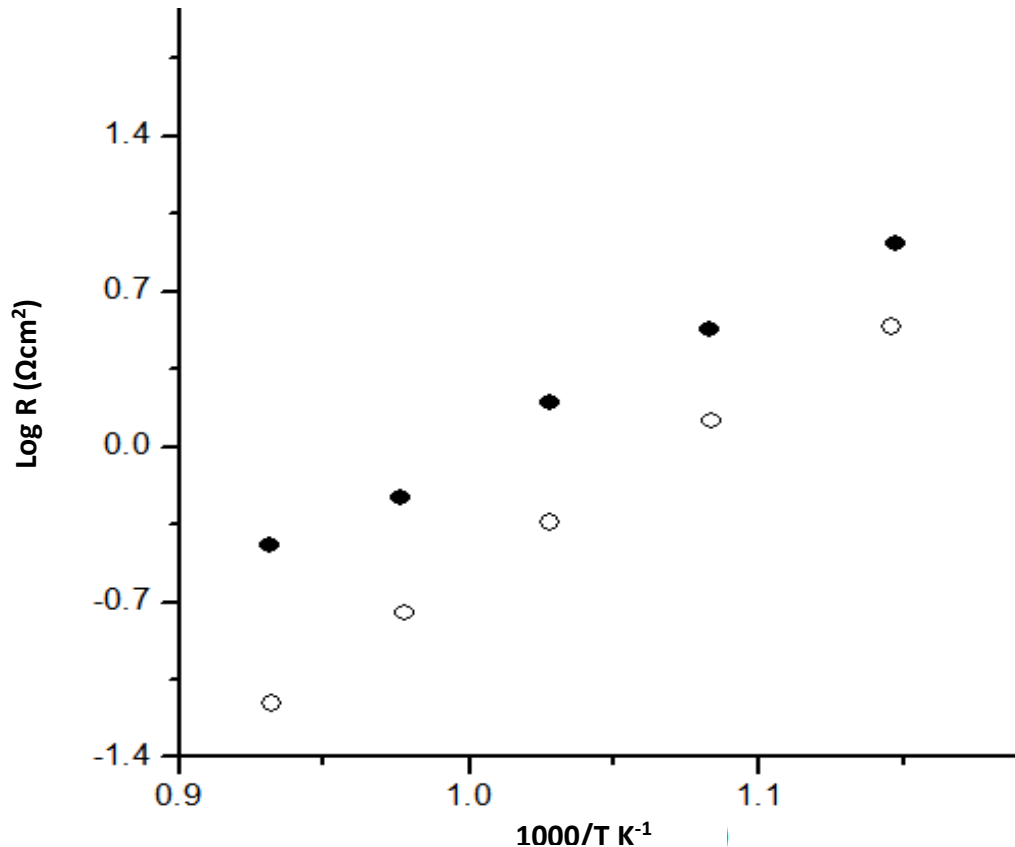


Figure 3-10 ASR data plotted logR (ASR) vs 1000/T in air for composite electrodes SCM-CGO (50:50wt%) ● and SCMS-CGO (50:50wt%) ○ on a CGO electrolyte pellet.

Therefore, further ASR measurements were performed and instead of using CGO as simply part of the electrode composite, a CGO electrolyte pellet was used instead of the apatite electrolyte. A SCMS-CGO (50:50wt%) composite cathode as well as composite parent cathode (undoped $\text{Sr}_{0.8}\text{Ca}_{0.2}\text{MnO}_{3-6}$ CGO(50:50wt%) were prepared and analysed. These tests were performed by Dr Jose M. Porras-Vazquez. The resulting ASR dependency with temperature is shown in Figure 3-10 with ASR values at 700°C and 800°C given in Table 3-7.

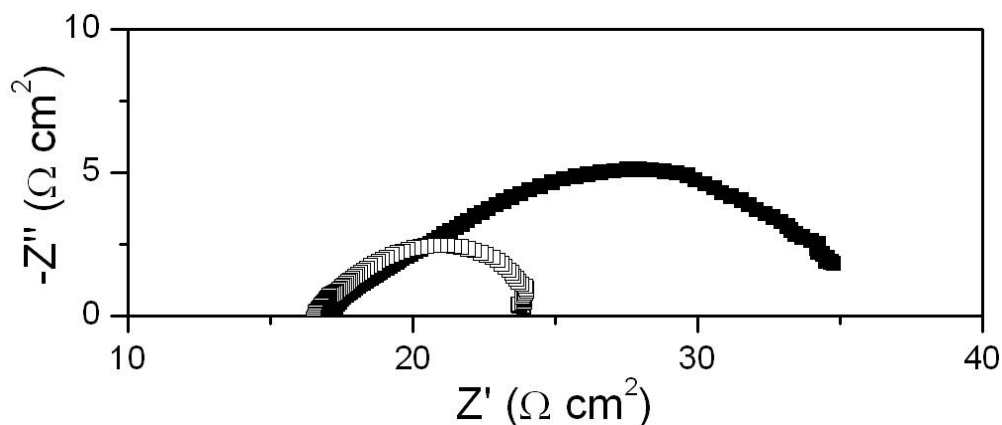


Figure 3-11 Impedance spectra of the symmetrical cells for $\text{Sr}_{0.8}\text{Ca}_{0.2}\text{MnO}_3$ (■) and $\text{Sr}_{0.8}\text{Ca}_{0.2}\text{Mn}_{0.9}\text{Si}_{0.1}\text{O}_{3-\delta}$ (□)/CGO10 composites at 700 °C. The serial resistance was subtracted for better comparison of the spectra.

Table 3-7 Area specific resistance values for composite electrodes deposited on a CGO electrolyte pellet at 900°C 1hr.

<u>Composition (ratio)</u>	<u>ASR ($\Omega \text{ cm}^2$) at 800°C</u>	<u>ASR ($\Omega \text{ cm}^2$) at 700°C</u>
CGO-SCM (50:50) ●	0.36	1.60
CGO-SCMS (50:50) ○	0.07	0.49

Furthermore, the Nyquist plot at 700°C from the impedance measurements are shown in Figure 3–11. The ASR data showed an improvement, when comparisons are made between the Si doped cathode and undoped cathode on a CGO pellet. The CGO/SCMS composite possesses significantly lower ASR values on a CGO pellet than the CGO/SCM composite. In addition the CGO/SCM and CGO/SCMS composites have better ASR results than any of the composites on a LSSO apatite pellet. This suggests that the previously mentioned cation intermixing of the perovskite and the apatite electrolyte is severely hindering the cathodes performance. This may be due to the lowering of the interstitial oxide ion content of the apatite phase at the interface; through for example Sr incorporation in to the apatite in place of La which would lower the interstitial oxide content, and hence reduce its

performance. Therefore, further fuel cell work will concentrate on the CGO pellet and composite.

3.7 Fuel cell test

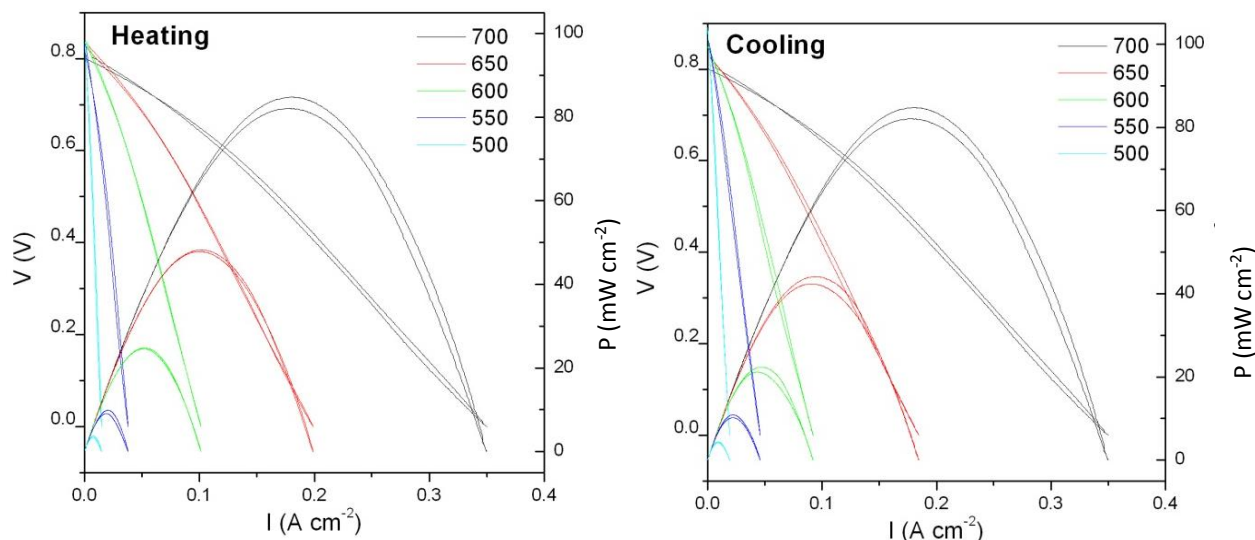


Figure 3-12 Power density and cell voltage as a function of current density between 500-700°C using air and H₂.

Building on all of this work a full SOFC was assembled with a CGO/SCMS cathode which had showed the lowest ASR values in the symmetrical cells. For this SOFC, a CGO electrolyte (500 μ m thick), a CGO/SCMS 50:50 composite cathode and commercial NiO-CGO composite anode were used. Power density curves and current-voltage data for SCMS-CGO/CGO/NiO-CGO at a temperature range of 500°C - 700°C, using air as oxidant and H₂ as fuel, are shown in Figure 3-12. The open circuit voltage (OCV) obtained at 500°C = 0.892 V which is lower than would be expected and predicted by the Nernst equation of 1 V. This suggests a poor seal of the cell. The OCV drops further as temperature increases, due to the fact that the CGO electrolytes electronic conduction is no longer negligible, with the Ce⁴⁺ being reduced to Ce³⁺. This is as expected with CGO being known to electronically conduct at temperatures above 600°C. The OCV voltage drops to 0.850 V at 600°C and 0.832 V at

700°C. Maximum power densities of 84 and 27 mW cm⁻² were obtained at 700 and 600°C respectively. These are extremely low values of power density which are not-commercially viable. This can be attributed to both the poor cell sealing and the large electrolyte response seen in the AC-impedance plot, which was above what would be expected for the CGO fuel cell electrolyte and requires further analysis. Further studies are therefore planned to perform replicate tests to optimise the production of the cells and consequently their performance.

3.8 Conclusion

Sr_{0.8}Ca_{0.2}Mn_{1-x}Si_xO_{3-δ} cathode materials x= 0, 0.005, 0.075, 0.1 and 0.125 were prepared by solid state synthesis. X-ray diffraction analysis confirms the change from a hexagonal to cubic perovskite on silicon doping. Clear evidence of silicon incorporation into the structure is shown through ²⁹Si NMR results. On silicon doping there is a noticeable increase in conductivity which is attributed to the tetrahedral silicon replacing the octahedral Mn⁴⁺. This results in oxide ion vacancies and partial reduction of Mn leading to mixed valence. Chemical compatibility tests involving the highest conducting cathode (Sr_{0.8}Ca_{0.2}Mn_{0.9}Si_{0.1}O_{3-δ}) and apatite electrolytes La₉SrSi₆O_{26.5} and La₁₀GaSi₅O_{26.5}, along with fluorite electrolyte Ce_{0.9}Gd_{0.1}O_{1.95} were examined. Limited reactivity at 900°C was observed during the compatibility tests for La₉SrSi₆O_{26.5} and CGO, and so area specific resistance (ASR) tests were undertaken. Issues were however, identified with the poor bonding of the electrode to the apatite electrolyte. So a composite electrodes of Sr_{0.8}Ca_{0.2}Mn_{0.9}Si_{0.1}O_{3-δ} and CGO were examined, and successfully deposited onto La₉SrSi₆O_{26.5} pellet. The ASR values were however very high and it is suggested that cation intermixing of the perovskite and the apatite is affecting the cathodes performance. Further ASR tests for the composites

were conducted on CGO electrolyte pellets and gave improved ASR values for the silicon doped cathode when compared to both the apatite tests and the undoped cathode ($\text{Sr}_{0.8}\text{Ca}_{0.2}\text{MnO}_{3-\delta}$). Fuel cell tests were performed for a SCMS-CGO/CGO/NiO-CGO cell and achieved maximum power densities of 84 mW cm^{-2} at 700°C respectively. This is a low value although the power density could be substantially improved if the cell sealing and hence the OCV could be improved.

Chapter 4

4 Evaluation of $\text{Ba}(\text{Co}/\text{Fe})_{0.9}\text{Bi}_{0.1}\text{O}_{3-\delta}$ perovskite as a fuel cell cathode

4.1 Introduction

The success of SOFCs is dependant on the performance and the properties of the individual components, as well as the interfaces between them. Previous studies have shown that there are key performance problems with the cathode in both proton and oxide conducting fuel cell systems, with the former having major limitations.³⁵ In this area, research has been dominated by either cobalt or manganese containing perovskites due to the high electronic conductivity that they possess.^{95, 148} However, Mn based perovskites are limited by poor ionic conductivity, while Co based systems suffer from large thermal expansion coefficients and poor chemical stability with commercial electrolytes.¹⁴⁹

The work in this chapter has involved doping iron and bismuth, on to the cobalt cation site of a BaCoO_3 perovskite material. The introduction of other transition metal dopants into these materials has previously produced promising cathode candidates, which have shown mixed ionic-electronic conduction ($\text{La}_{0.6}\text{Sr}_{0.4}\text{Co}_{0.2}\text{Fe}_{0.8}\text{O}_{3-\delta}$)^{149, 150, 151, 152} Iron has been used as one of the most successful dopants in mixed ionic-electronic conductors (MIECs), due to its similar radius size to cobalt, its variable oxidation state and its lower cost.¹⁵³⁻¹⁵⁶ In addition iron containing perovskite compounds have a lower thermal expansion co-efficient than Co based systems (e.g. LaFeO_3 has a similar co-efficient to conventional electrolytes)^{157, 158}. In this respect, Table 4-1 shows thermal expansion co-efficients for a range of conventional electrolytes and perovskite cathodes.

Table 4-1 Thermal expansion co-efficient RT-800°C for a range of electrolytes and cathodes^{36, 95, 157, 159,158, 160}

Conventional Electrolytes	Thermal expansion co-efficient ($\times 10^{-6} \text{ K}^{-1}$) RT-800°C
YSZ (10%)	10.8
CGO (10%)	13.5
LSGM	11.1
Electrodes	Thermal expansion co-efficient ($\times 10^{-6} \text{ K}^{-1}$) RT-800°C
$\text{LaCoO}_{3-\delta}$	28.1
$\text{LaFeO}_{3-\delta}$	11.6
La_2NiO_4	13.0
$\text{La}_{1-x}\text{Sr}_x\text{Co}_y\text{Fe}_{1-y}\text{O}_{3-\delta}$	17.1

The main problem of iron based materials is that they have a much lower electronic conductivity than ideal for SOFCs. Therefore mixed cobalt/iron on the B site allows for a balance between high conductivity and added stability.^{23, 161-163} The involvement of bismuth in this MIEC is due to previous work which showed that bismuth doping in $\text{BaCoO}_{3-\delta}$ led to a material with a good reactivity for the ORR at intermediate temperatures.^{151, 164} The higher (0.1-0.3) the bismuth content the higher the reactivity.^{165, 166} However Shao et al. suggested that a lower amount of bismuth was more favourable for fuel cells applications due to high Bi contents leading to increased TEC values, caused by a valence change that can occur on heating Bi^{5+} to Bi^{3+} .¹⁶⁴ The targeting of a barium based perovskite rather than strontium or calcium is due to favourable chemical compatibility with barium containing proton conducting electrolytes. In theory this should reduce cross component reactions at the cathode and electrolyte interfaces. In this work barium cobalt bismuth ferrites are synthesized and investigated with respects to their composition, conductivity, compatibility with conventional electrolytes and their electrode performance.

4.2 Experimental

BaCO₃ (99.9%), Co₃O₄ (99%), Fe₂O₃, (99.9%) and Bi₂O₃ (99.9%) were used to prepare a range of BaCo_{0.9-x}Fe_xBi_{0.1}O_{3-δ} samples (x ranging from 0.0-0.8). These starting materials were intimately ground together in stoichiometric amounts and heated at 1000°C for 12 hours (a pre-drying step was included if required). They were then ball-milled (350 rpm for 1 hour, Fritsch Pulverisette 7 Planetary Mill) and reheated to 1000°C for a further 12 hours. The pure phases were pressed as pellets at a pressure of 5000 kg cm⁻² in a 1.3 cm die set and sintered at 1100°C for 12hrs. For the electrode testing, both the performance on oxide ion conducting electrolyte and a proton conducting electrolyte were examined. The proton conducting electrolyte Ba₂In_{1.6}Zr_{0.2}Si_{0.2}O_{5.2} was chosen. This was synthesised from stoichiometric amounts of BaCO₃ (+3 wt% excess due to high temperature evaporation (99.9%)), In₂O₃ (99.9%), ZrO₂ (99.9%) and SiO₂ (99.9%) which were ground together and then heat treated at a temperature of 1000°C for 12 hours. The sample was then reground, ball milled (350 rpm for 1 hour, Fritsh Pulverisette 7 Planetary Mill) and reheated for 50 hours at 1000°C. The resulting powder was pressed as pellets at a pressure of 2500 kg cm⁻² in a 1.0 cm die set and sintered at 1400°C for 8hrs. For a comparison against this proton conducting electrolyte, oxide ion conducting electrolyte Ce_{0.9}Gd_{0.1}O_{1.95} (CGO Sigma Aldrich), was pressed as pellets at a pressure of 2500 kg cm⁻² in a 1.0 cm die set and sintered at 1500°C for 12hrs.

Powder X-ray diffraction at room temperature was used to confirm the phase purity of the samples and characterise the cell parameters using a Bruker D8 diffractometer with Cu Kα₁ radiation (1.5406Å) over a 2θ range of 20-80° and a step size of 0.02°. Variable temperature XRD data were collected by Dr Oliver Clemens at the University of Darmstadt on a Bruker

D8 diffractometer with an Anton Paar HTK 1200N heating stage. The sample was heated from RT to 1000°C at 10°C a minute with XRD measurements taken every 50°C, multiphase refinements were performed to give cell parameters and weight percent fractions of each phase within the sample.

Oxygen contents were determined using thermogravimetric analysis, (Netzsch STA 449 F1 Jupiter Thermal Analyser) samples were heated to 1000 °C at 10 °C min⁻¹ under N₂ atmosphere. The nitrogen's atmosphere will reduce the iron and manganese to an oxidation states of 3+ and allow the original oxygen content to be calculated from the oxygen mass loss.

Dilatometry measurements were performed using a Netzsch 409C dilatometer. Samples were prepared by ball milling the cathode powders in a Fritsch Pulverisette 7 Planetary Mill at 350 rpm for 1 hour. The samples were pressed into rods of 10mm in diameter and 10mm in length and sintered at 1100°C for 12hrs at a heating rate of 5°C min. Samples were then placed in the push rod case of the dilatometer and heated in air from 35°C to 1000°C at 10°C min⁻¹ to measure the thermal expansion.

The water contents of hydrated perovskite samples were determined using thermogravimetric analysis (Netzsch STA 449 F1 Jupiter Thermal Analyser). The measurements were carried out by heating the samples to 800°C at 10°C minute, water contents were determined from the observed mass loss, with mass spectrometry confirming that the weight loss was due to water.

The CO₂ stability was also studied using TGA; the samples were heated at 10°C min⁻¹ to 800°C in a CO₂ atmosphere, with any mass gains used to determine the temperature at which CO₂ is picked up and hence the maximum thermal stability. Furthermore XRD

analysis was used to show the phase purity comparison before and after heating the samples to 800°C in CO₂.

The conductivities of the pellets were measured on cooling from 800°C to 500°C in air at 50°C intervals, following the four probe dc method. Four Pt electrodes were attached with Pt paste, and then the sample was fired to 800°C in air for 30 minutes to ensure bonding to the sample.

The chemical compatibility between the perovskite cathodes and electrolyte materials were also studied. The materials were mixed in a 1:1 wt% ratio, then ground and fired at 800°C and 900°C for 24hr, with X-ray diffraction being used to examine whether any reactions had occurred. For the electrode area specific resistance (ASR) measurements, the cathodes of 100%, and 50:50 by wt% ratio of cathode and electrolyte were prepared using the ball mill (350rpm for 1 hr, Fritsh Pulverisette 7 Planetary Mill), with added decoflux as the binder (WB41, Zschimmer and Schwarz). The resulting solutions were painted on to the corresponding electrolyte pellets on both sides and dried at 70°C for 10 minutes. Repeated painting was conducted a further 2 times to guarantee full covering of the pellets surfaces. The pellets were then heated for 1 hr at the required temperature, then Pt foil electrodes were attached and heated to 800°C for 1 hr. The ASR was determined using AC impedance measurements in a frequency range of 0.005-13000 kHz (Hewlett Packard 4182A impedance analyser) with the data analysed in Z-view.¹⁴³

The impedance spectra were recorded between 500°C-800°C; ideally three responses were expected, the two separate semi circles that corresponded to the bulk and grain of the electrolyte, and thirdly the electrode response. It was not possible to accurately extract individual contributions across the entire range, at lower temperatures there was partial

separation of the individual components, with capacitance and resistance values determined through an extended equivalent circuit fitting model. However at higher temperatures there was more distortion on the individual components and broad electrolyte semicircles were observed. The ASR data analysis though only requires the electrode response measurement data from the entire range, which has a capacitance value of 10^{-5} to 10^{-3} F cm⁻¹. Therefore the resistance of the Nyquist plot does not start at zero and was calculated through the single semi-circle fitting programme within Z-view.¹⁴³

Single fuel cells were prepared using approximately 500 µm thick electrolytes, with a 60:40wt% composite anode and a 50:50wt% composite cathode. Initially the composite anode was painted on one side of the electrolyte pellet, and heated to 1200°C for 1 hr, then the composite cathode was painted on to the other side and heated at 900°C for a further hr. At this point, Pt paste and coiled Pt wire were used as current collectors, being attached on both sides and heated to 800°C for 1 hr. The electrode surface area each side was 0.25 cm². The cell was sealed to the electrochemical setup using a ceramic-based material (Ceramabond 668/668A, Aremco). Fuel cell tests were carried out at the University of Malaga by Dr Jose M Porras-Vazquez and analysed using a VSP–biologic Pro-s machine. They were carried out between 500-700°C in pure humidified hydrogen (bubbled through water at 20°C) and atmospheric air. Current-voltage (I-V) curves were obtained by cyclic-voltammetry at a scan rate of 5 mVs⁻¹. The sealed anode material side was reduced at 500°C for 1hr before electrochemical tests were performed. The morphology of the electrodes and the electrode/electrolyte interfaces were studied using SEM images collected at the University of Malaga by Dr Jose M Porras-Vazquez on a JEOL SM-6490LV (20Kv). The samples were gold coated to avoid charge build up on the surface.

4.3 Synthesis and X-ray Diffraction analysis of $\text{BaCo}_{0.9-x}\text{Fe}_x\text{Bi}_{0.1}\text{O}_{3-\delta}$

The cathode series $\text{BaCo}_{0.9-x}\text{Fe}_x\text{Bi}_{0.1}\text{O}_{3-\delta}$ ($x = 0.0-0.8$), was successfully prepared with varying Fe contents. XRD showed the introduction of Fe caused a conversion from the hexagonal perovskite to cubic perovskite to be observed. An Fe content equal to $x = 0.6$ was required in order to fully stabilise the pure cubic perovskite. It was noticed however that mixed hexagonal and cubic phases were formed for $0.4 \leq x < 0.6$, (as seen in Figure 4-1 a,b).

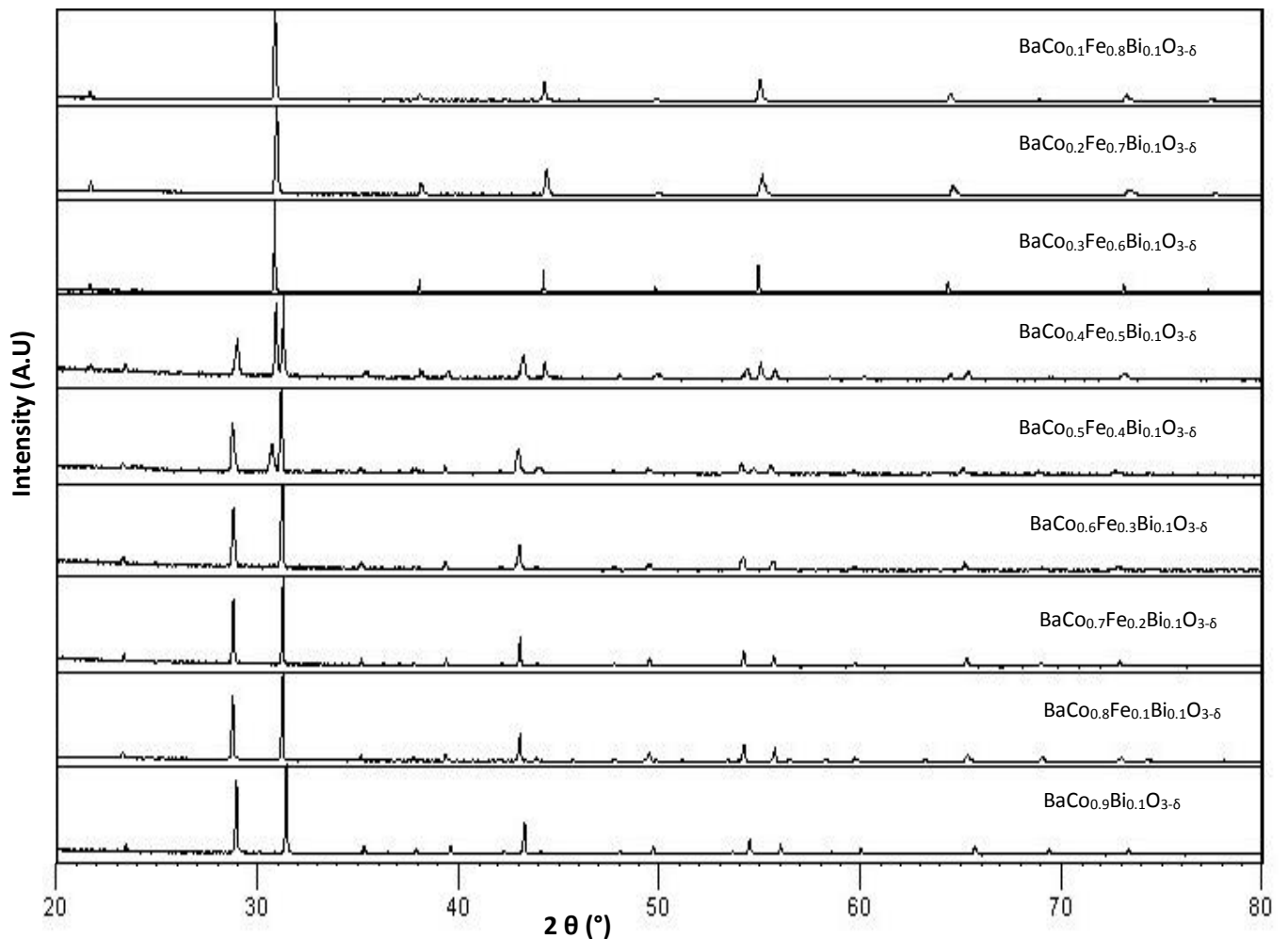


Figure 4-1a XRD patterns for $\text{BaCo}_{0.9-x}\text{Fe}_x\text{Bi}_{0.1}\text{O}_{3-\delta}$ $x = 0.0-0.8$, showing a hexagonal perovskite for $0 \leq x < 0.4$, a mixture of hexagonal and cubic perovskite for $0.4 \leq x < 0.6$, and a cubic perovskite for $x \geq 0.6$

The hexagonal cubic conversion can be related to changes in the tolerance factor on Fe doping. Co is smaller than Fe and so for high Co contents the perovskites tolerance factor is > 1 . Which favours a hexagonal perovskite structure at room temperature. The doping of larger cations i.e. iron and bismuth, on to the B site affects the R_b component, pushing the tolerance factor towards 1 and so for higher Fe contents a cubic perovskite is observed. In terms of applications, cubic systems are preferable as these consists of corner shared octahedra. Which increases the orbital overlap allowing easier electron movement, resulting in increased conductivity. In addition all sites are equivalent and therefore less likely to trap oxide ion vacancy defects and hence may help to optimise the ionic conductivity. Figure 1b shows an expanded region of the main perovskite peaks in each phase. The $\text{BaCo}_{0.5}\text{Fe}_{0.4}\text{Bi}_{0.1}\text{O}_{3-\delta}$ and $\text{BaCo}_{0.4}\text{Fe}_{0.5}\text{Bi}_{0.1}\text{O}_{3-\delta}$ samples show the crossover of the structure from hexagonal to cubic.

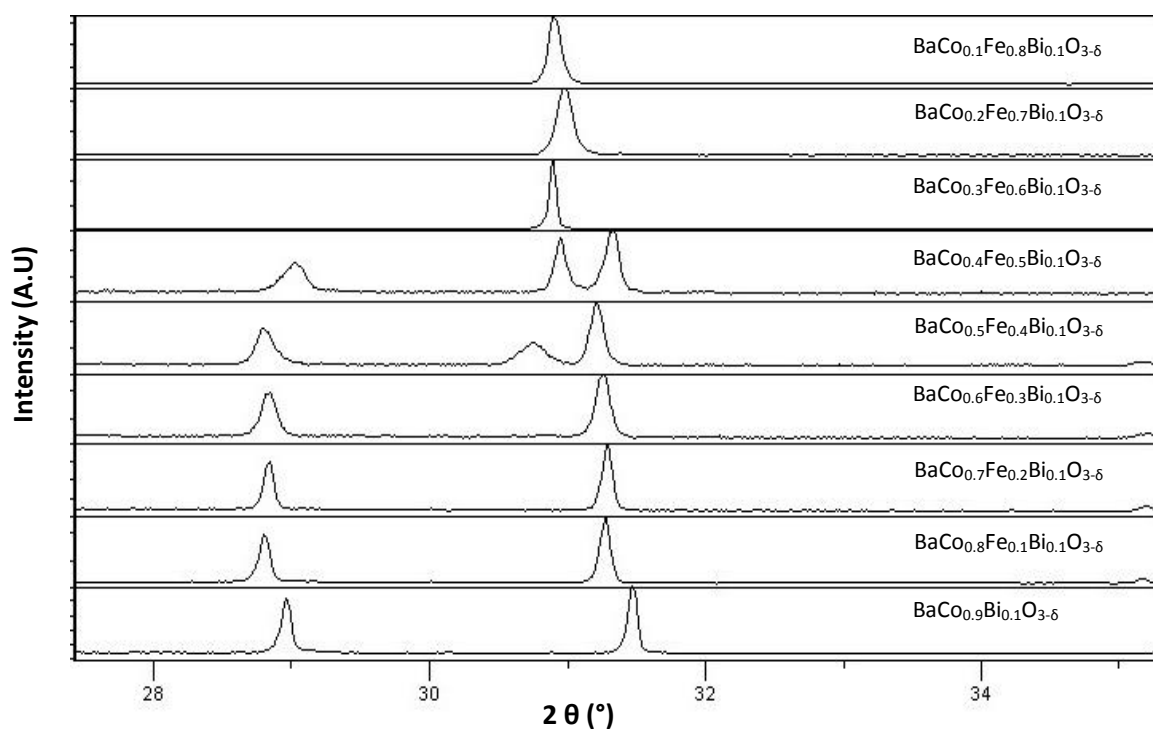


Figure 4-1b Expanded XRD patterns for $\text{BaCo}_{0.9-x}\text{Fe}_x\text{Bi}_{0.1}\text{O}_{3-\delta}$ ($x = 0.0-0.8$) in the region between $27.5-35.5^\circ$

Table 4-2 Cell parameters for BaCo_{0.9-x}Fe_xBi_{0.1}O_{3-δ} (x=0-0.8)

Sample Composition	Unit cell parameter (Å)			Unit cell volume (Å ³)
	a	b	c	
BaCo _{0.9} Bi _{0.1} O _{3-δ}	5.6731(4)	-	11.8378(8)	329.95(4)
BaCo _{0.8} Fe _{0.1} Bi _{0.1} O _{3-δ}	5.6966(3)	-	11.8696(7)	333.58(5)
BaCo _{0.7} Fe _{0.2} Bi _{0.1} O _{3-δ}	5.7053(3)	-	11.8719(7)	334.66(5)
BaCo _{0.6} Fe _{0.3} Bi _{0.1} O _{3-δ}	5.7161(4)	-	11.8797(8)	336.16(6)
BaCo _{0.3} Fe _{0.6} Bi _{0.1} O _{3-δ}	4.07190(8)	-	-	67.514(4)
BaCo _{0.2} Fe _{0.7} Bi _{0.1} O _{3-δ}	4.06949(5)	-	-	67.394(3)
BaCo _{0.1} Fe _{0.8} Bi _{0.1} O _{3-δ}	4.0605(1)	-	-	66.952(8)

The refined unit cell parameters and volumes of the BaCo_{0.9-x}Fe_xBi_{0.1}O_{3-δ} series are listed in table 4-2. These data show an expansion of the unit cell on Fe doping for the hexagonal samples, as expected due to the larger size of Fe (0.585 Å) compared with Co (0.53 Å). At the cross over region from hexagonal to cubic (x = 0.4, 0.5), two phase refinements were performed allowing the individual weight percent fraction (WPF) of each phase to be determined. On increasing iron doping the hexagonal phase fraction decreases as the cubic phase increases. The WPF of each phases was calculated and is shown in table 4-3, along with the unit cell parameters and volumes for each phase.

Table 4-3 Refined cell parameters, volumes and weight percent fractions of BaCo_{0.5}Fe_{0.4}Bi_{0.1}O_{3-δ} and BaCo_{0.4}Fe_{0.5}Bi_{0.1}O_{3-δ}

Sample Composition	Unit cell parameter (Å)			Unit cell volume (Å ³)	WPF %
	a	b	c		
Hexagonal BaCo _{0.5} Fe _{0.4} Bi _{0.1} O _{3-δ}	5.7169(2)	-	11.8653(5)	335.85(3)	74.7
Cubic BaCo _{0.5} Fe _{0.4} Bi _{0.1} O _{3-δ}	4.0794(1)	-	-	67.890(8)	25.3
Hexagonal BaCo _{0.4} Fe _{0.5} Bi _{0.1} O _{3-δ}	5.7107(6)	-	11.777(8)	332.64(8)	72.7
Cubic BaCo _{0.4} Fe _{0.5} Bi _{0.1} O _{3-δ}	4.0816(3)	-	-	67.999(2)	27.3

After the formation of the pure cubic perovskite, unexpectedly the unit cell parameters decrease with further additions of Fe. An early suggestion for this decrease was a change in the oxygen content over the series, therefore oxygen contents were estimated from TGA measurements (mass loss) assuming that the iron and manganese would be reduced in N₂ to 3+. The oxygen contents however showed a rise on increasing iron, so could not account for the decrease in unit cell volumes (Table 4-4). Another possible origin of this decrease could be that for the cubic system there is a change in the spin state (high to low) in one or both of the transition metals; however further analysis (e.g. magnetic measurements) is required.¹⁶⁰ Figure 4-2 shows a comparison of the normalised unit cell volumes of the pure hexagonal and cubic systems with the largest volume seen for cubic BaCo_{0.3}Fe_{0.6}Bi_{0.1}O_{3-δ}.

Table 4-4 Oxygen content for the cubic perovskites BaCo_{0.9-x}Fe_xBi_{0.1}O_{3-δ} (x=0.6-0.8)

Sample Composition	Estimated oxygen content (3-δ)	% Mass Change
BaCo _{0.3} Fe _{0.6} Bi _{0.1} O _{3-δ}	2.841	1.54
BaCo _{0.2} Fe _{0.7} Bi _{0.1} O _{3-δ}	2.843	1.55
BaCo _{0.1} Fe _{0.8} Bi _{0.1} O _{3-δ}	2.850	1.6

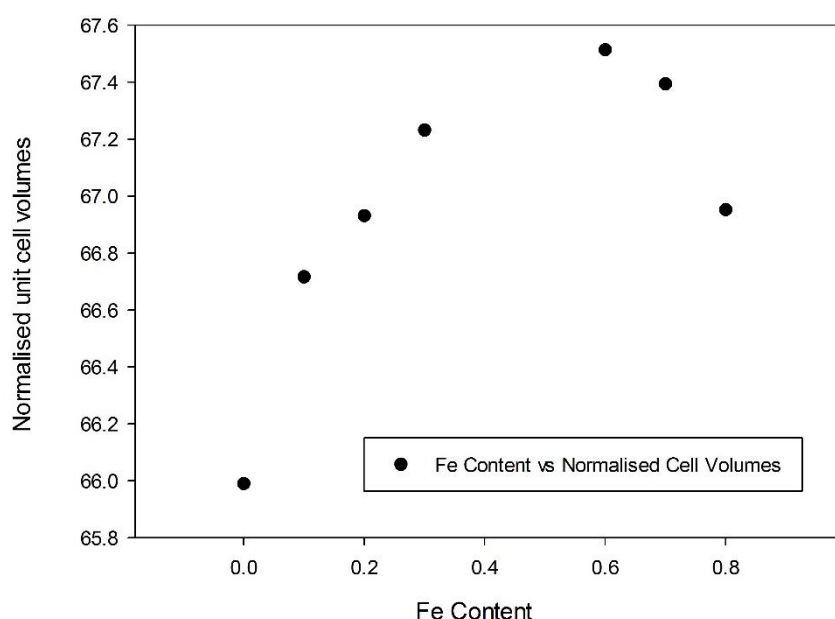


Figure 4-2 Normalised (one formula unit) unit cell volume of BaCo_{0.9-x}Fe_xBi_{0.1}O_{3-δ} hexagonal perovskites x=0-0.3 and cubic x= 0.6-0.8.

One of the mixed hexagonal/cubic systems ($x=0.5$) was analysed further by variable temperature X-ray diffraction. This was used to observe the effect of temperature on the phase transition within a mixed perovskite sample. Only $\text{BaCo}_{0.4}\text{Fe}_{0.5}\text{Bi}_{0.1}\text{O}_{3-\delta}$ was studied, as it was the closest to the pure cubic perovskite. Phase transitions in perovskites are well known and increases in properties such as conductivity have been explained due to an observed transition. X-ray diffraction patterns were carried out in 50°C steps from RT- 1000°C , Figure 4-3 shows the XRD patterns of $\text{BaCo}_{0.4}\text{Fe}_{0.5}\text{Bi}_{0.1}\text{O}_{3-\delta}$ at 850 - 1000°C as well as one at RT. Rietveld refinements have shown an increase in cell parameters and cell volumes, as well as a drop in the hexagonal weight percent fraction (WPF) on heating (Table 4-5). The peaks intensity corresponding to the hexagonal perovskite decreases until the structure appears to be pure cubic at 950°C .

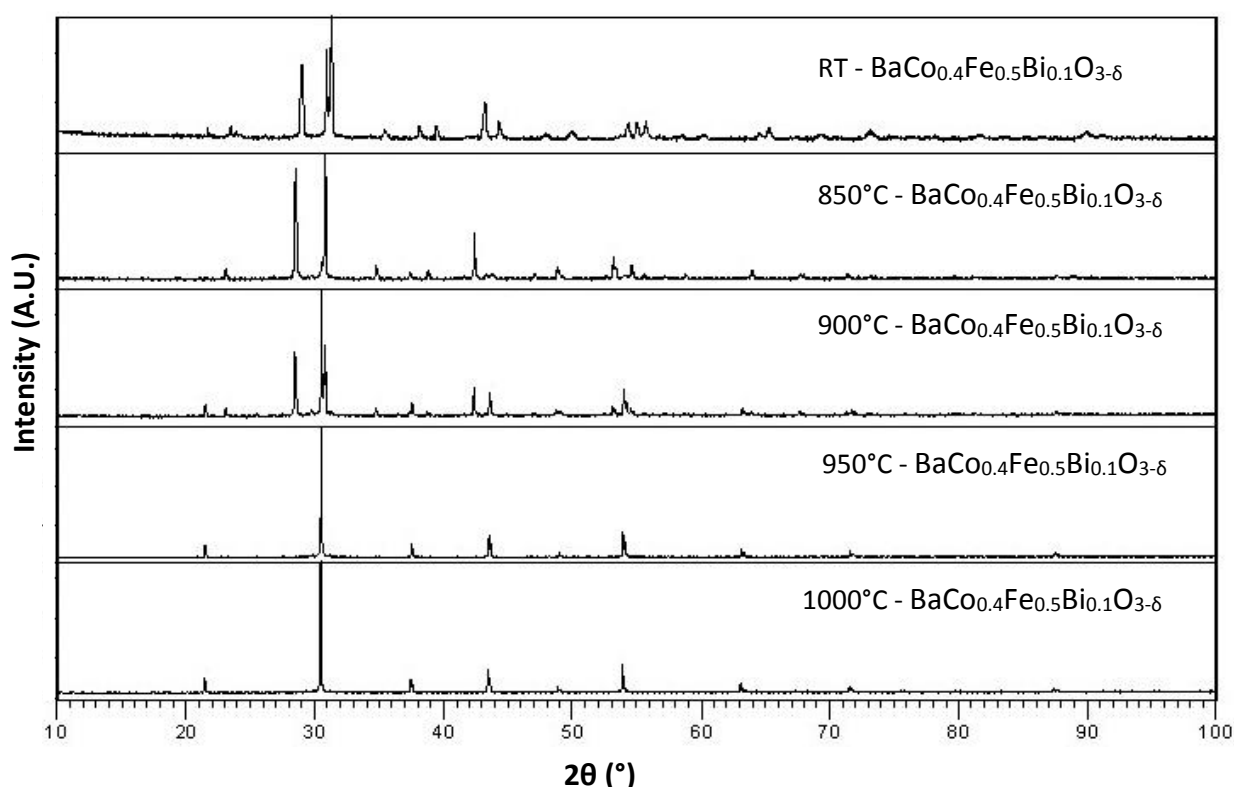


Figure 4-3 High Temperature X-ray Diffraction of $\text{BaCo}_{0.4}\text{Fe}_{0.5}\text{Bi}_{0.1}\text{O}_{3-\delta}$ shown at RT and between 850 - 1000°C .

Table 4-5 BaCo_{0.4}Fe_{0.5}Bi_{0.1}O_{3-δ} cell parameters, volumes and weight percent fraction at RT and between 850-1000°C.

Sample Composition BaCo _{0.4} Fe _{0.5} Bi _{0.1} O _{3-δ}	Unit cell parameter (Å)			Unit cell volume (Å ³)	WPF %
	a	b	c		
Hexagonal RT	5.7107(6)	-	11.777(8)	332.64(8)	72.7
Cubic RT	4.0816(3)	-	-	67.999(2)	27.3
Hexagonal 850°C	5.8330(3)	-	12.073(6)	355.82(6)	87.0
Cubic 850°C	4.1608(2)	-	-	72.033(4)	13.0
Hexagonal 900°C	5.8416(6)	-	12.0929(7)	357.37(6)	50.3
Cubic 900°C	4.1665(4)	-	-	72.329(3)	49.7
Cubic 950°C	4.1725(5)	-	-	72.645(7)	100
Cubic 1000°C	4.1786(8)	-	-	72.961(3)	100

The high temperature causes the combination of the hexagonal and cubic phases into a single cubic phase, which can be collated to the oxygen loss on heating. This leads to partial reduction of the B site cations, which therefore leads to an increase in the average B cation site size. As a result, the tolerance factor decreases towards 1.0 leading to the observed change to a single phase cubic perovskite. On cooling, phase separation occurs due to oxygen pick up, which destabilises the cubic phase as the tolerance factor changes are reversed.

4.4 Thermal analysis

4.4.1 Dilatometry

Preliminary dilatometry studies were performed on $\text{BaCo}_{0.9-x}\text{Fe}_x\text{Bi}_{0.1}\text{O}_{3-\delta}$, with x ranging from 0.0-0.3 (hexagonal) and 0.6-0.8 (cubic). The thermal expansion is measured from RT to 800°C, this range is being used as it's the maximum ideal fuel cell operating temperature. Generally the thermal expansion co-efficient (TEC) is affected by the components of the structures and their positions and bond angles in relation to each other. The dilatometry data for $\text{BaCo}_{0.9-x}\text{Fe}_x\text{Bi}_{0.1}\text{O}_{3-\delta}$ (x = 0-0.3, 0.6-0.8) is shown below in Figure 4-4 with the TEC and temperature profile.

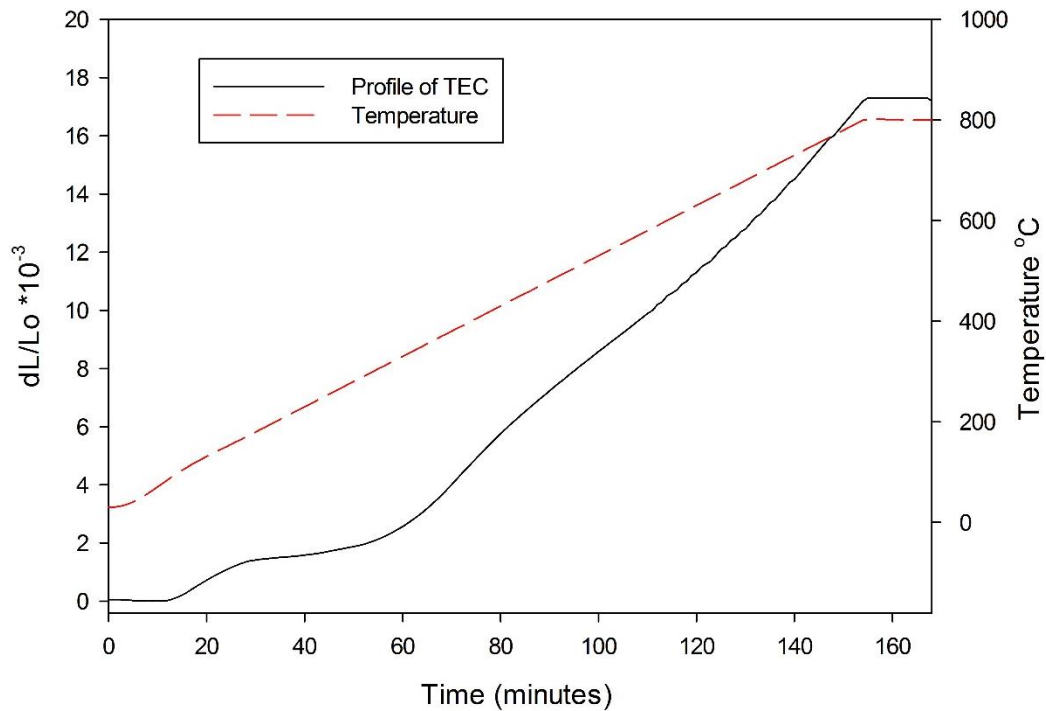


Figure 4-4 Dilatometry data for $\text{BaCo}_{0.3}\text{Fe}_{0.6}\text{Bi}_{0.1}\text{O}_{3-\delta}$ from 35°C-800°C at 10°C min⁻¹ in air (dashed red line – temperature profile, Solid black line is TEC profile)

As expected the materials expand on heating. Figure 4-4 and Table 4-6 show the TEC as the doping of iron increases. The TEC have been calculated at RT-800°C, RT-400°C and 400-800°C. The overall RT-800°C TEC values are higher than the electrolytes TEC, but a decrease

is observed in comparison to other high cobalt containing barium cathodes for example;

$\text{BaBi}_{0.05}\text{Co}_{0.9}\text{Nb}_{0.1}\text{O}_{3-3}$ $22.0 \times 10^{-6} \text{ K}^{-1}$.¹⁵¹

Table 4-6 Thermal Expansion co-efficient at RT-800°C, RT-400°C and 400-800°C for $\text{BaCo}_{0.9-x}\text{Fe}_x\text{Bi}_{0.1}\text{O}_{3-6}$ ($x=0-0.3, 0.6-0.8$).

Sample Composition	Thermal expansion co-efficient ($\times 10^{-6} \text{ K}^{-1}$)		
	RT-800	RT-400	400-800
$\text{BaCo}_{0.9}\text{Bi}_{0.1}\text{O}_{3-6}$	19.8	15.7	38.0
$\text{BaCo}_{0.8}\text{Fe}_{0.1}\text{Bi}_{0.1}\text{O}_{3-6}$	19.8	14.5	38.3
$\text{BaCo}_{0.7}\text{Fe}_{0.2}\text{Bi}_{0.1}\text{O}_{3-6}$	19.2	14.0	37.3
$\text{BaCo}_{0.6}\text{Fe}_{0.3}\text{Bi}_{0.1}\text{O}_{3-6}$	19.0	13.0	36.9
$\text{BaCo}_{0.3}\text{Fe}_{0.6}\text{Bi}_{0.1}\text{O}_{3-6}$	19.9	10.0	41.8
$\text{BaCo}_{0.2}\text{Fe}_{0.7}\text{Bi}_{0.1}\text{O}_{3-6}$	19.7	7.4	38.2
$\text{BaCo}_{0.1}\text{Fe}_{0.8}\text{Bi}_{0.1}\text{O}_{3-6}$	21.8	5.5	42.3

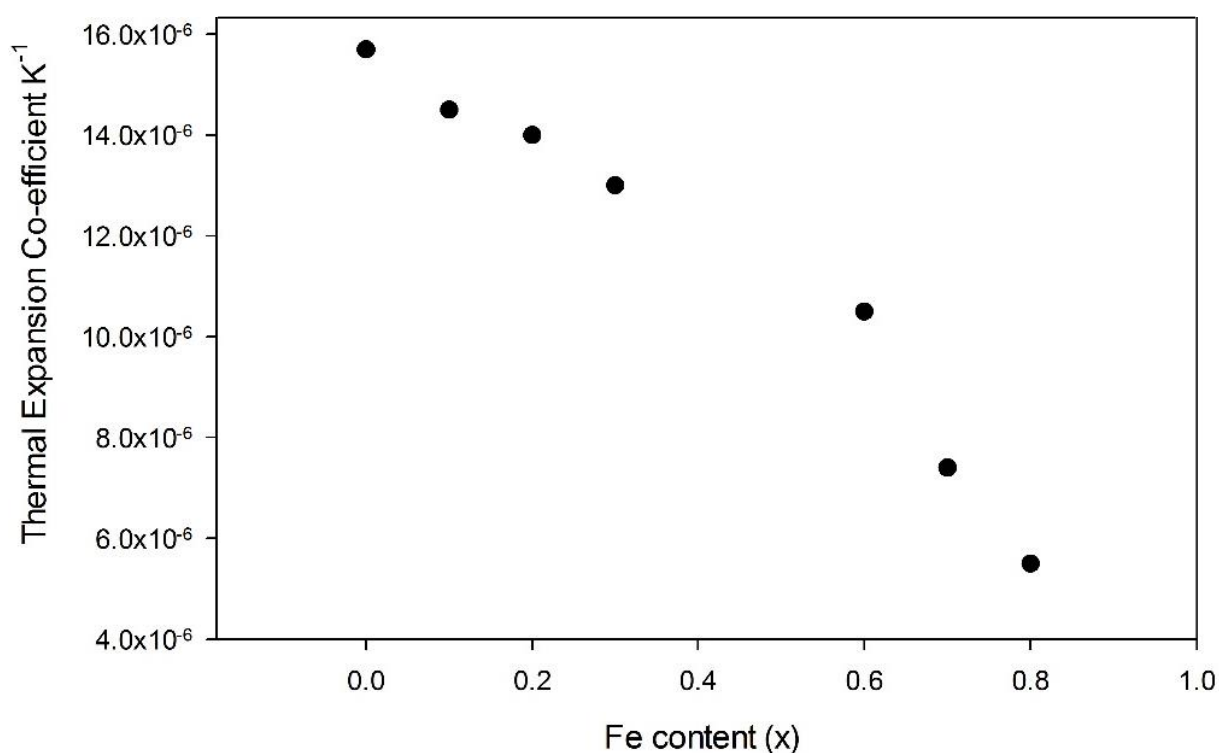


Figure 4-5 Thermal expansion co-efficient for $\text{BaCo}_{0.9-x}\text{Fe}_x\text{Bi}_{0.1}\text{O}_{3-6}$ hexagonal perovskites $x=0-0.3$ and cubic $0.6-0.8$ between RT-400°C in air.

The dilatometry data is analysed and split before and after 400°C. Figure 4-5 shows the reduction in the RT-400°C TEC on increasing iron content, with a steeper decrease around $x=0.6$ due to the resulting structure change from hexagonal to cubic. Above 400°C the TEC increases due to the loss of oxygen, which can cause the reduction of $\text{Co}^{4+}/\text{Fe}^{4+}$ to the $\text{Co}^{3+}/\text{Fe}^{3+}$ increasing the TEC. A preliminary TGA was performed which showed the expected oxygen mass loss at around 375-400°C depending on the sample (Figure 4-6). The earlier mass loss in the samples ($\approx 100^\circ\text{C}$) is due to the surface water.

To explain the larger TEC of each sample between 400-800°C further work is required, including slower heating rates, the exact temperature and region corresponding to the oxygen loss (400-800°C) and the rate of loss. This loss will vary from sample to sample, and have a profound effect on the B site metal oxidation states and therefore their ionic radii.

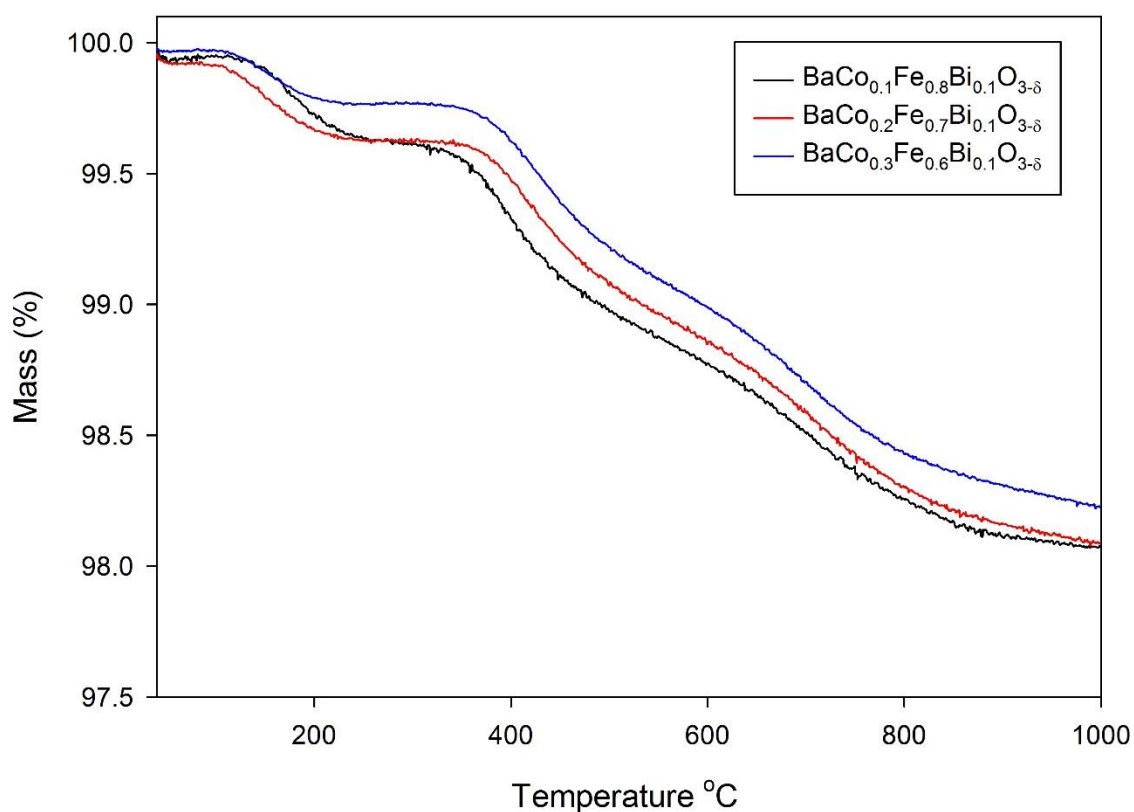


Figure 4-6 TG profiles ($10^\circ\text{C min}^{-1}$ to 1000°C in N_2 protection gas) for $\text{BaCo}_{0.1}\text{Fe}_{0.8}\text{Bi}_{0.1}\text{O}_{3-\delta}$, $\text{BaCo}_{0.2}\text{Fe}_{0.7}\text{Bi}_{0.1}\text{O}_{3-\delta}$ and $\text{BaCo}_{0.3}\text{Fe}_{0.6}\text{Bi}_{0.1}\text{O}_{3-\delta}$.

4.4.2 Water contents

The cubic ($x = 0.6-0.8$) and hexagonal ($x = 0.0-0.3$) powders of $\text{BaCo}_{0.9-x}\text{Fe}_x\text{Bi}_{0.1}\text{O}_{3-\delta}$ were heated (under wet N_2) up to 800°C , and then slowly cooled down to room temperature at the rate of $0.4^\circ\text{C min}^{-1}$. XRD patterns of the cubic phases showed that on hydration the cubic cell remains, but there is a peak shift to lower angles, suggesting that H_2O is incorporated giving rise to a larger cell; the data for $\text{BaCo}_{0.3}\text{Fe}_{0.6}\text{Bi}_{0.1}\text{O}_{3-\delta}$ are shown below in Figure 4-7. For the hexagonal systems, additional changes were observed, in these cases, although the main phase remains small unknown impurities are present Figure 4-8.

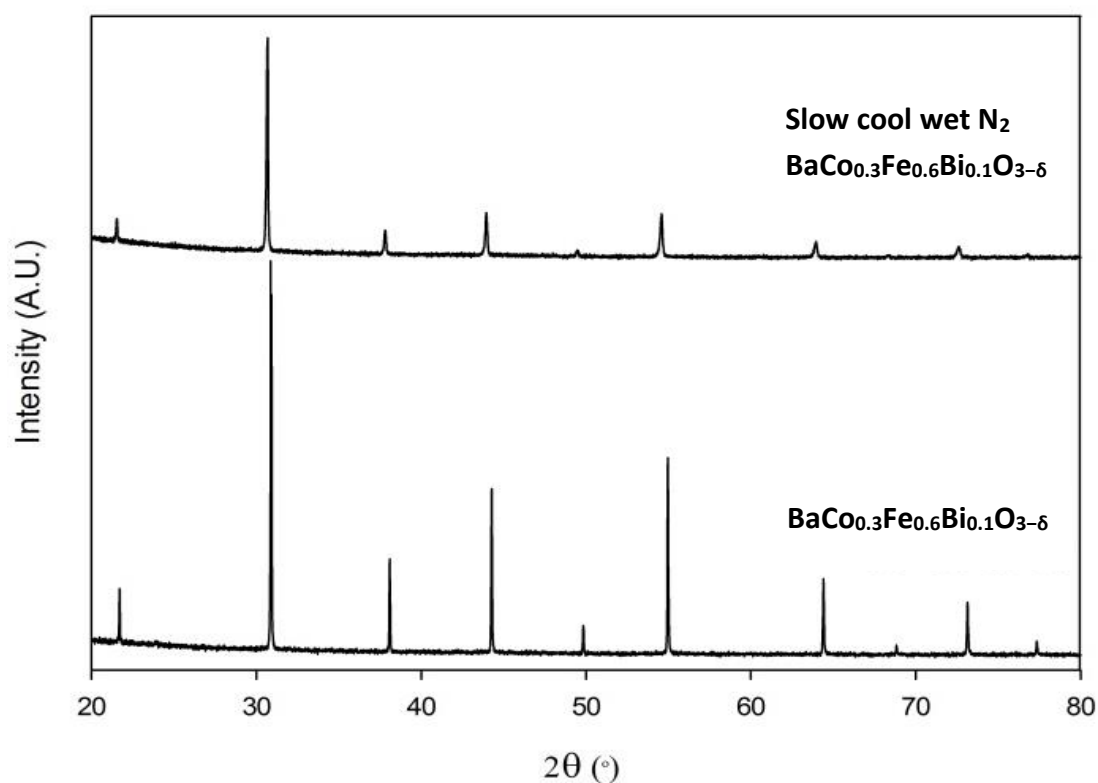


Figure 4-7 XRD pattern for $\text{BaCo}_{0.3}\text{Fe}_{0.6}\text{Bi}_{0.1}\text{O}_{3-\delta}$ before and after hydration.

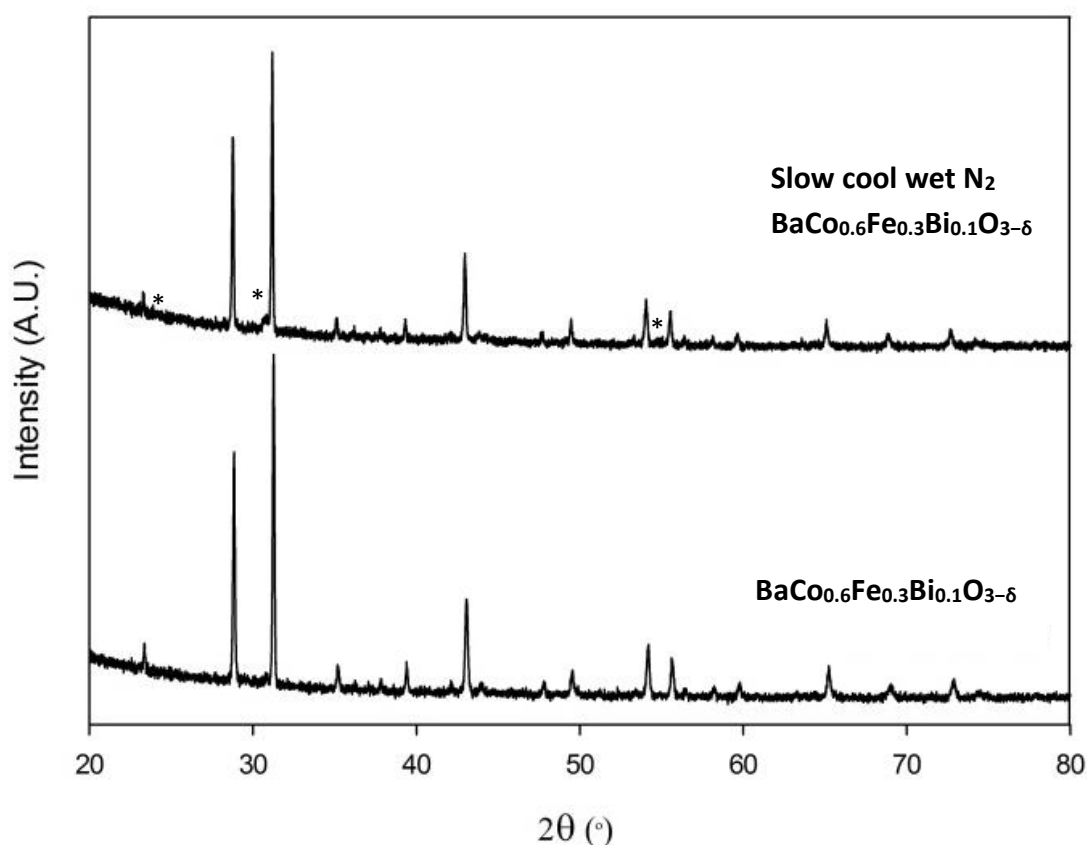


Figure 4-8 XRD pattern for BaCo_{0.6}Fe_{0.3}Bi_{0.1}O_{3-δ} before and after hydration. (* denotes the impurities)

The resulting water contents of the cubic samples were determined by TGA measurement.

Figure 4-9 shows the mass loss and differential thermal analysis trace for BaCo_{0.1}Fe_{0.8}Bi_{0.1}O_{3-δ}, with the corresponding mass spectrometry spectra for m/z 18 (H₂O). The water contents are all shown in Table 4-7, and range between 0.1 and 0.4 molecules per formula unit, with BaCo_{0.3}Fe_{0.6}Bi_{0.1}O_{3-δ} showing the most significant water incorporation. This phase corresponds to the lowest Fe content required to give a pure cubic perovskite phase, and the higher water content may in some way be related to this closeness to the hexagonal-cubic phase boundary. In this respect further studies of other compositions close to this boundary are warranted.

Table 4-7 Water contents for hydrated $\text{BaCo}_{0.9-x}\text{Fe}_x\text{Bi}_{0.1}\text{O}_{3-\delta}$ ($x = 0.6-0.8$).

Composition	Moles of water per formula unit
$\text{BaCo}_{0.1}\text{Fe}_{0.8}\text{Bi}_{0.1}\text{O}_{3-\delta}$	0.105
$\text{BaCo}_{0.2}\text{Fe}_{0.7}\text{Bi}_{0.1}\text{O}_{3-\delta}$	0.145
$\text{BaCo}_{0.3}\text{Fe}_{0.6}\text{Bi}_{0.1}\text{O}_{3-\delta}$	0.398

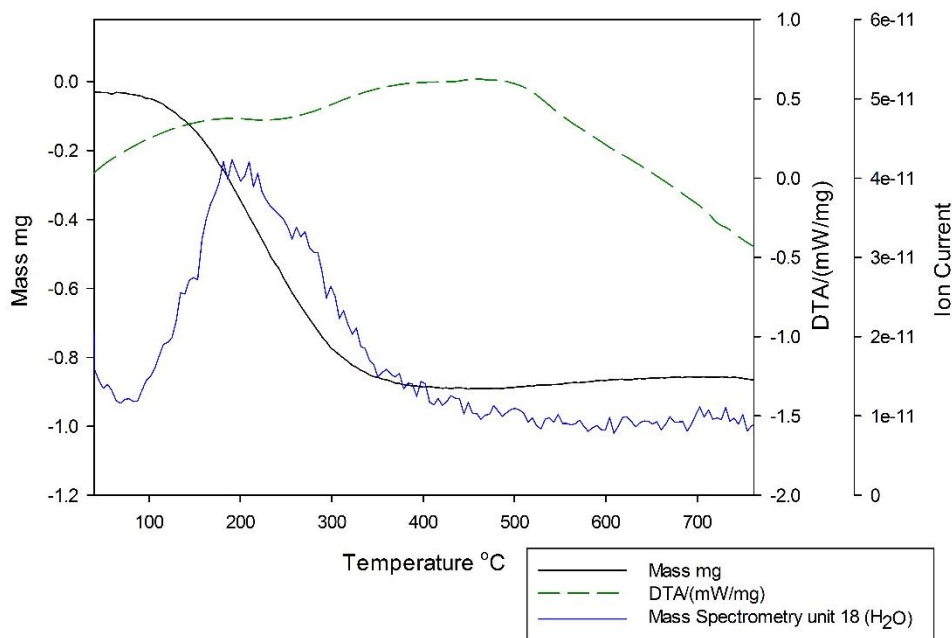


Figure 4-9 TGA-MS plot of $\text{BaCo}_{0.1}\text{Fe}_{0.8}\text{Bi}_{0.1}\text{O}_{3-\delta}$ (m/z 18 water)

4.4.3 CO_2 Stability results

As previous studies have shown that, barium containing perovskites can have poor stability on heating in CO_2 (e.g. BaCeO_3), the stabilities of $\text{BaCo}_{0.9-x}\text{Fe}_x\text{Bi}_{0.1}\text{O}_{3-\delta}$ ($x=0-0.3, 0.6-0.8$) in a CO_2 environment were examined. X-ray diffraction data are shown in Figure 4-10 for $x = 0.3$ and 0.6 samples (heated to 800°C in 100% dry CO_2). These conditions are extreme but are used to show how the perovskite phase could degrade overtime within the presence of CO_2 . The data showed that the cathodes partially decomposed, with small BaCO_3 impurities produced. The decomposition of the cathode occurred in varying amounts, with the high cobalt containing samples seemingly more unstable. However for all systems the decomposition level was much lower than seen for many other Ba containing perovskites under similar condition e.g. BaCeO_3 .

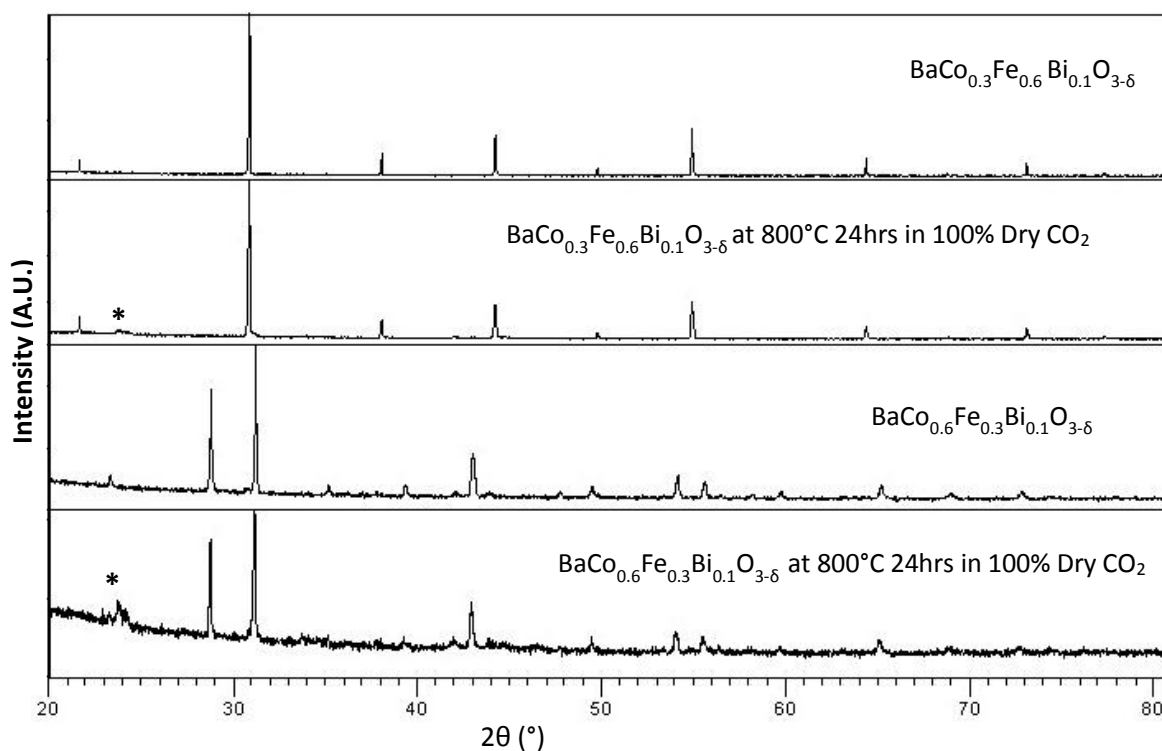


Figure 4-10 X-ray diffraction data for $\text{BaCo}_{0.6}\text{Fe}_{0.3}\text{Bi}_{0.1}\text{O}_{3-\delta}$ and $\text{BaCo}_{0.3}\text{Fe}_{0.6}\text{Bi}_{0.1}\text{O}_{3-\delta}$ before and after a heat treatment at 800°C in 100% dry CO_2 for 24hrs. (*highlights main BaCO_3 peak impurity)

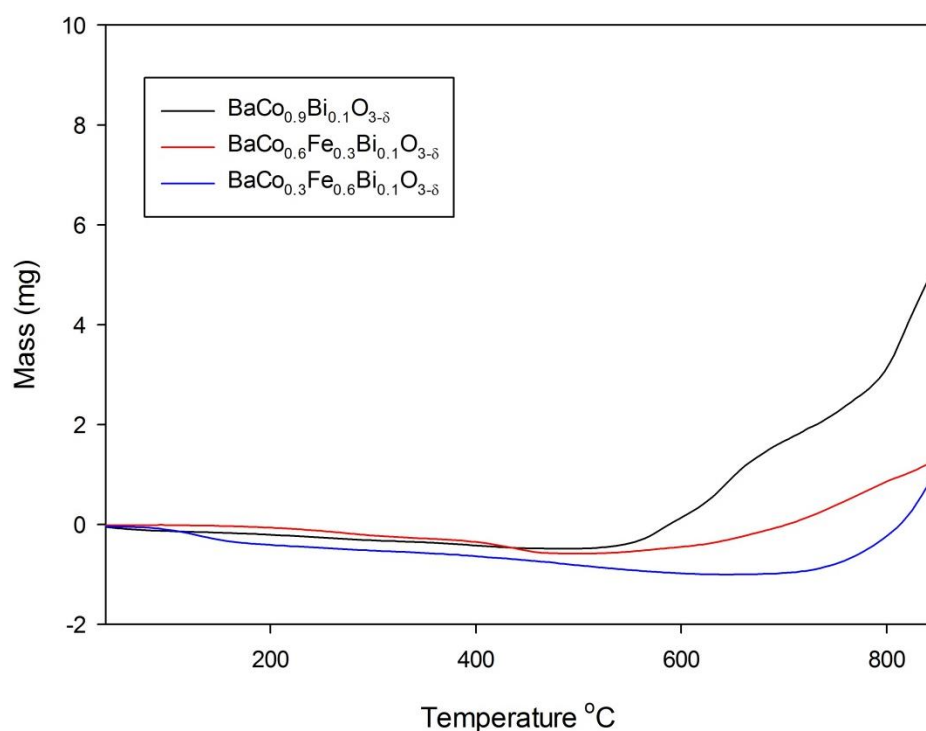


Figure 4-11 TG profiles ($10^\circ\text{C min}^{-1}$ to 1000°C in 1:1 CO_2 and N_2 mixture) for $\text{BaCo}_{0.9}\text{Bi}_{0.1}\text{O}_{3-\delta}$, $\text{BaCo}_{0.6}\text{Fe}_{0.3}\text{Bi}_{0.1}\text{O}_{3-\delta}$ and $\text{BaCo}_{0.3}\text{Fe}_{0.6}\text{Bi}_{0.1}\text{O}_{3-\delta}$

Additional TGA work was performed on the $x = 0.0, 0.3$ and 0.6 samples to identify the temperature at which CO_2 pick up begins. The TGA profiles on heating from RT-850°C in CO_2 environment are shown in Figure 4-11. The $\text{BaCo}_{0.9}\text{Bi}_{0.1}\text{O}_{3-\delta}$ sample shows a clear mass increase at around 550°C. On introducing iron doping this mass increase is shifted to slightly higher temperatures with $\text{BaFe}_{0.6}\text{Co}_{0.3}\text{Bi}_{0.1}\text{O}_{3-\delta}$ increasing the onset temperature to around 730°C. Thus these results indicate that the iron doping enhances the stability towards CO_2 although some instability is still seen at the higher temperatures.

4.5 Conductivity

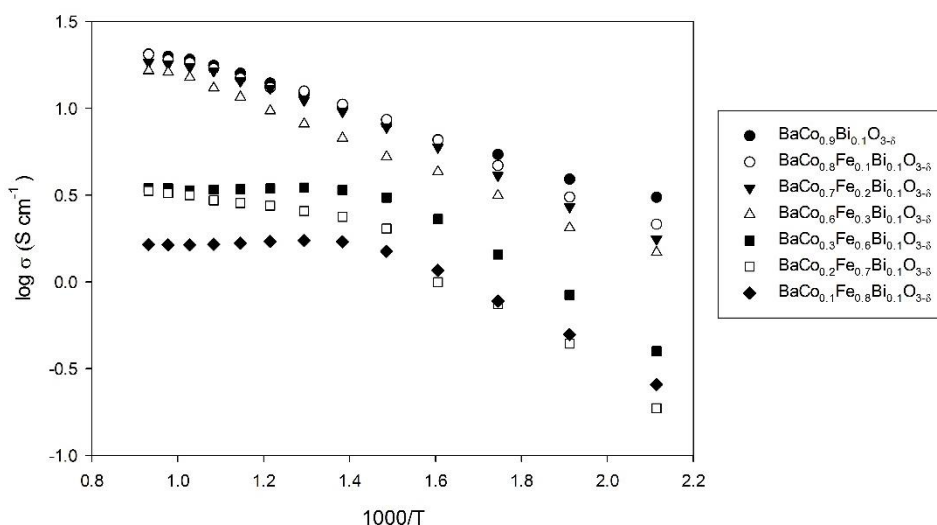


Figure 4-12 Conductivity data for $\text{BaCo}_{0.9-x}\text{Fe}_x\text{Bi}_{0.1}\text{O}_{3-\delta}$ $x = 0.0-0.8$

Conductivities of both the pure hexagonal and cubic samples were also analysed. These measurements showed a reduction in conductivity on iron doping (Figure 4-12). The non-linearity of the conductivity at higher temperatures is due to the loss of oxygen, which reduces the oxidation state of iron and cobalt and hence alters the charge carrier concentration. Even though higher conductivities were expected for the cubic perovskites, this was found not to be the case, with the results indicating that the Co content was the most crucial aspect for high electronic conductivity.

4.6 Chemical Compatibility

In order to determine the potential of these materials as PC-SOFC or SOFC cathode, chemical compatibility tests were performed against known electrolytes. In an effort to simulate the effects of temperature on the electrolyte-cathode interfaces, the cathode materials were tested against two different types of electrolytes. A proton conducting electrolyte synthesized within our group $\text{Ba}_2\text{In}_{1.6}\text{Zr}_{0.2}\text{Si}_{0.2}\text{O}_{5.2}$ (BIZS), and commercially available oxide ion conducting electrolyte $\text{Ce}_{0.9}\text{Gd}_{0.1}\text{O}_{1.95}$ (CGO).

4.6.1 $\text{Ba}_2\text{In}_{1.6}\text{Zr}_{0.2}\text{Si}_{0.2}\text{O}_{5.2}$ + $\text{BaCo}_{0.9-x}\text{Fe}_x\text{Bi}_{0.1}\text{O}_{3-\delta}$

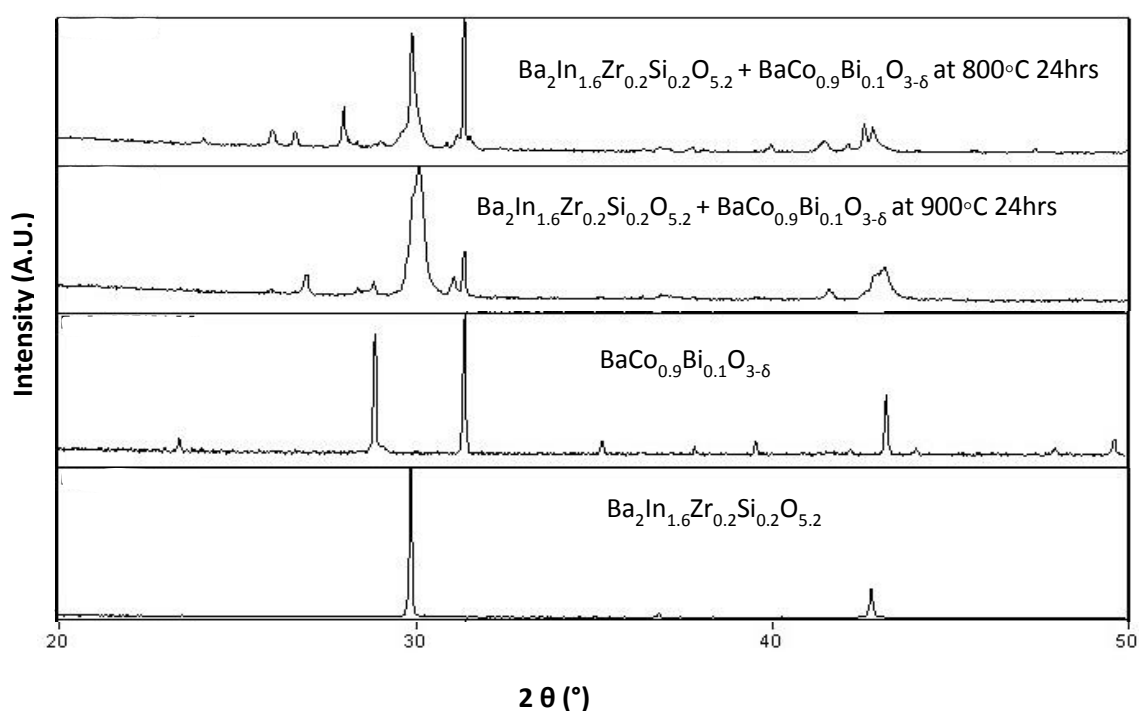


Figure 4-13 X-ray Diffraction patterns for composite electrode, BIZS– $\text{BaCo}_{0.9}\text{Bi}_{0.1}\text{O}_{3-\delta}$ 50:50 wt% each at room temperature and then ground/fired at 800°C and 900°C for 24hrs

Chemical compatibility tests involving the BIZS electrolyte and the iron undoped $\text{BaCo}_{0.9}\text{Bi}_{0.1}\text{O}_{3-\delta}$ cathode were performed, with the composites being fired at 800°C, 900°C and 1000°C for 24hr, to compare the cross reactions. These tests were not promising with the emergence of impurities at 800°C/900°C (Figure 4-13) and further reactions at a 1000°C indicating its low chemical compatibility with BIZS. The reaction broadens and shifts the main BIZS perovskite peaks indicating the formation of a cobalt doped BIZS derivative and further additional impurities. The iron doped hexagonal systems also reacted forming shoulders peaks and additional impurity peaks, Figure 4-14 shows $\text{BaCo}_{0.6}\text{Fe}_{0.3}\text{Bi}_{0.1}\text{O}_{3-\delta}$ at 800°C and 900°C after 24hrs. This provides further evidence towards the instability of high cobalt containing cathodes in line with other research.^{151, 155}

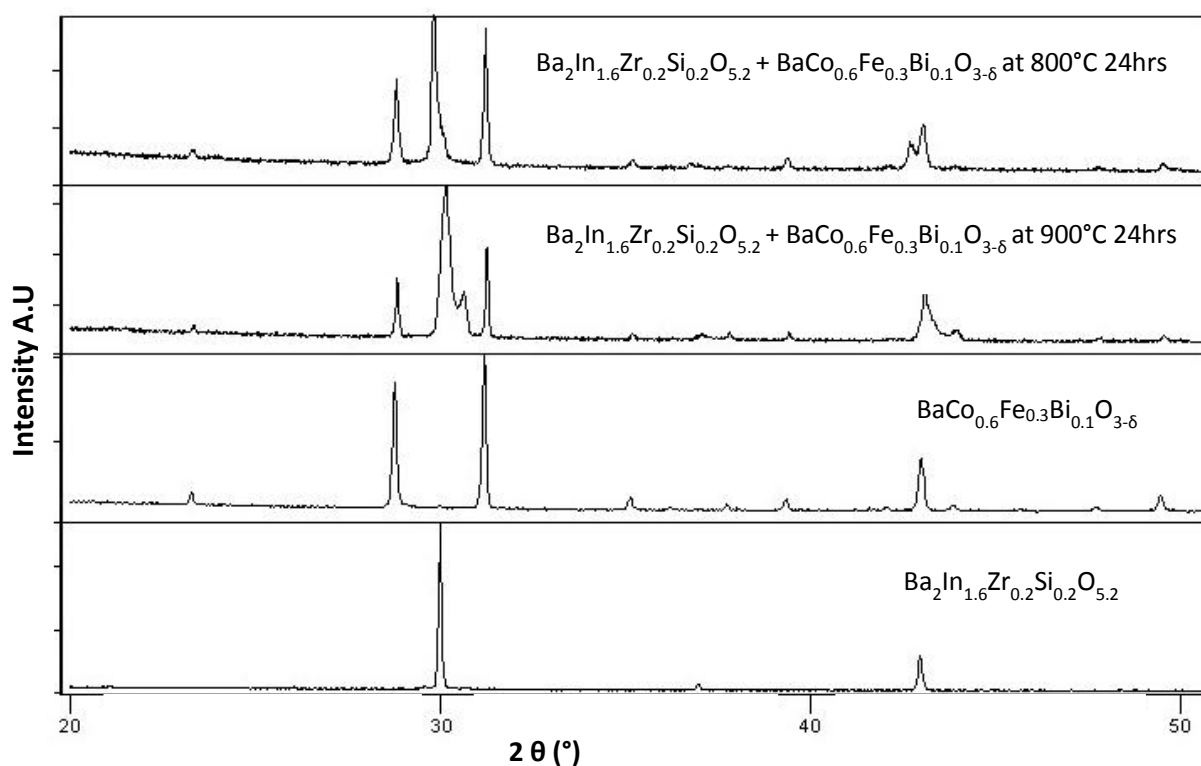


Figure 4-14 X-ray Diffraction patterns for composite electrode, BIZS– $\text{BaCo}_{0.6}\text{Fe}_{0.3}\text{Bi}_{0.1}\text{O}_{3-\delta}$ 50:50 wt% each at room temperature and then ground/fired at 800°C and 900°C for 24hrs

The BIZS compatibility with the cubic systems were more promising, with $\text{BaFe}_{0.6}\text{Co}_{0.3}\text{Bi}_{0.1}\text{O}_{3-\delta}$ showing visible stability up to 900°C (Figure 4-15). However the XRD data did show small changes to the unit cell parameter and volumes when heated. These small cell parameter changes suggest that, even though there were no apparent impurities seen in the diffraction patterns, there were still some reactions occurring through cation interdiffusion. This interdiffusion is occurring on a small scale and it may not have a negative effect on any of the cathodes performances, providing the resultant phases are not insulators. Indeed it may lead to the effective formation of a compositional gradient interface, which may be beneficial to performance.

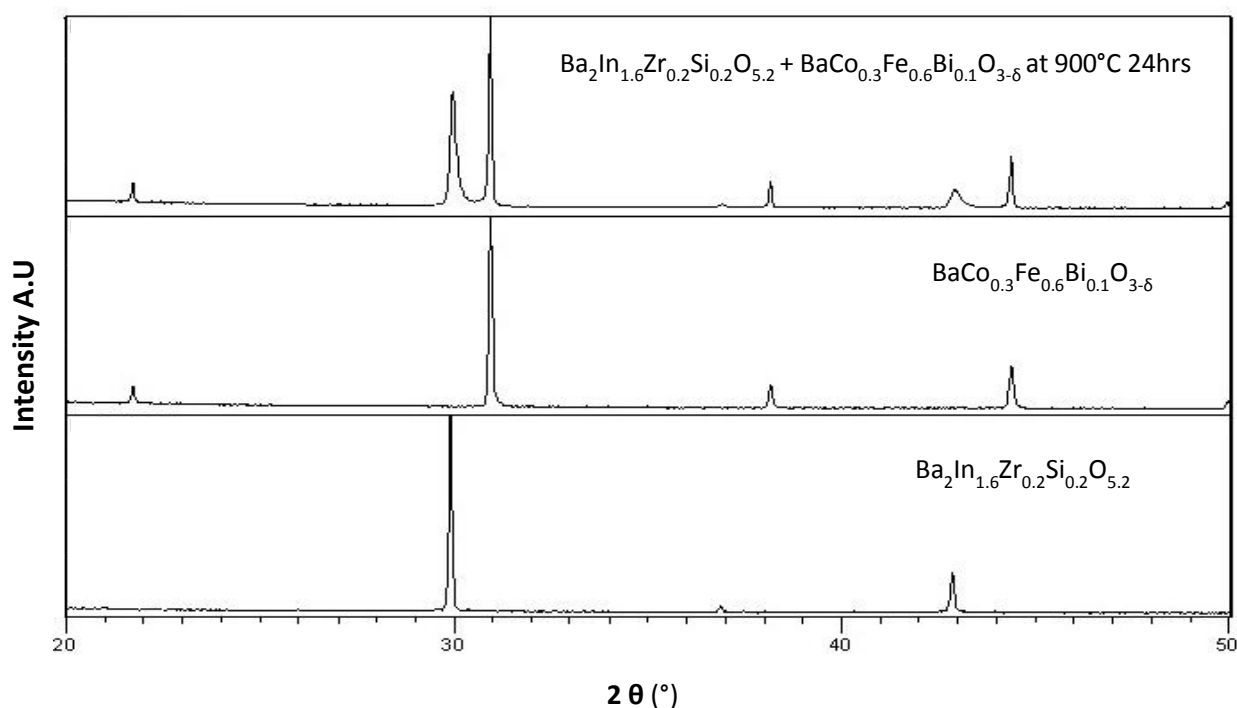


Figure 4-15 X-ray Diffraction patterns for composite electrode, BIZS– $\text{BaCo}_{0.3}\text{Fe}_{0.6}\text{Bi}_{0.1}\text{O}_{3-\delta}$ 50:50 wt% each at room temperature and then ground/fired at 900°C for 24hrs

4.6.2 Chemical Compatibility CGO + $\text{BaCo}_{0.9-x}\text{Fe}_x\text{Bi}_{0.1}\text{O}_{3-\delta}$

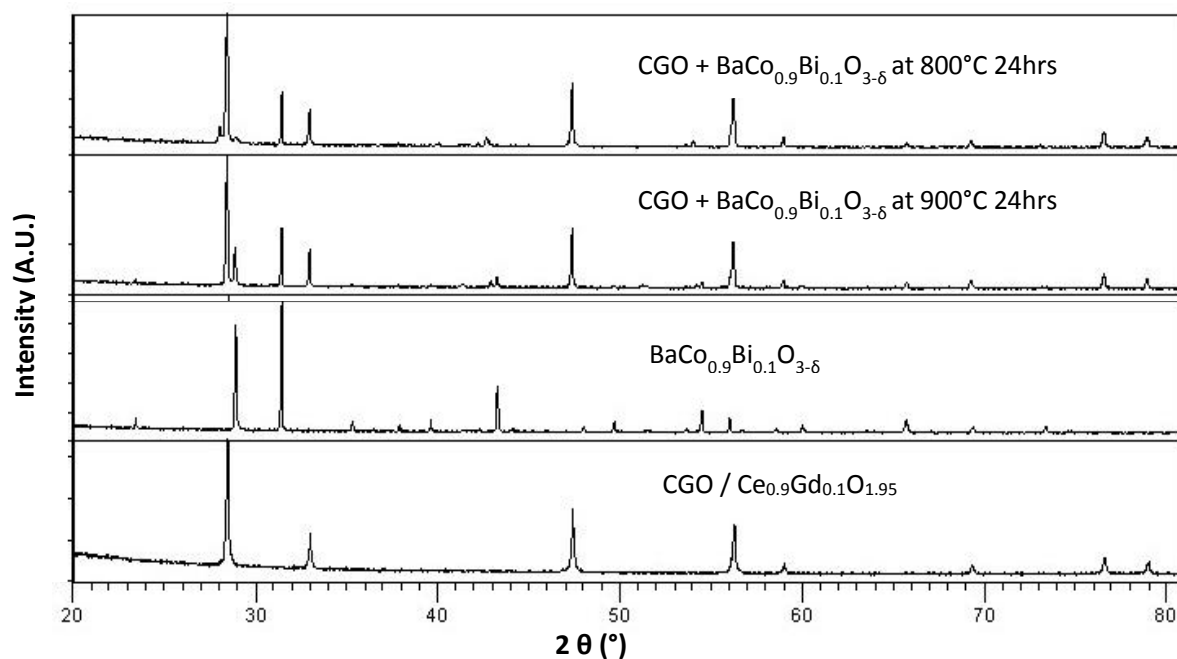


Figure 4-16 X-ray Diffraction patterns for composite electrode, CGO– $\text{BaCo}_{0.9}\text{Bi}_{0.1}\text{O}_{3-\delta}$ 50:50 wt% each at room temperature and then ground/fired at 800°C and 900°C for

Following these chemical compatibility tests with the proton conducting electrolyte $\text{Ba}_2\text{In}_{1.6}\text{Zr}_{0.2}\text{Si}_{0.2}\text{O}_{5.2}$, further experiments were performed on a commercial electrolyte, gadolinium doped ceria ($\text{Ce}_{0.9}\text{Gd}_{0.1}\text{O}_{1.95}$ /CGO). In Figure 4-16, Figure 4-17 and Figure 4-18 the XRD data illustrating the reactivity of the CGO and respective cathode compositions at 800°C and 900°C are shown.

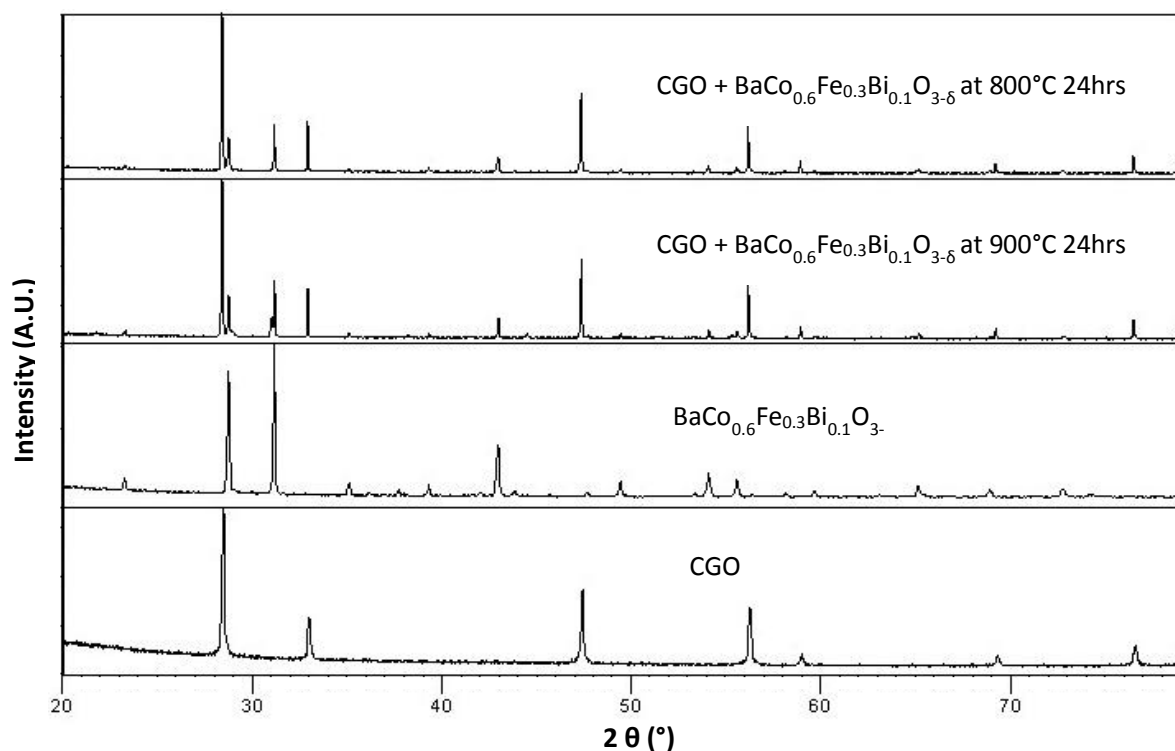


Figure 4-17 X-ray Diffraction patterns for composite electrode, CGO–BaCo_{0.6}Fe_{0.3}Bi_{0.1}O_{3-δ} 50:50 wt% each at room temperature and then ground/fired at 800°C and 900°C for 24hr

These results were not encouraging as the entire series reacted with CGO to form impurities, although as before the cubic phases reacted the least. The cross reactivity therefore seems to correlate with the amount of cobalt present in the sample. Area specific resistance (ASR) work is required to investigate whether these minor impurities will affect the cathodes performance in SOFC systems, or whether the conductivity of both the electrolyte and cathode material is maintained.

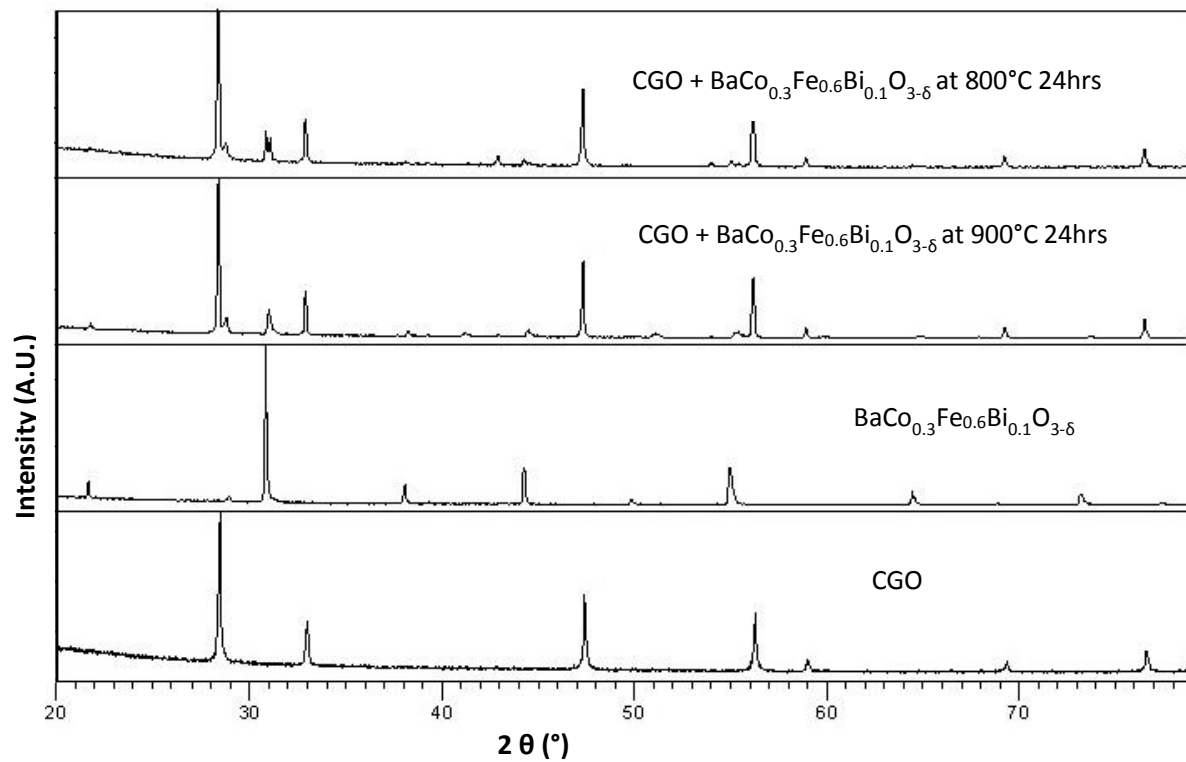


Figure 4-18 X-ray Diffraction patterns for composite electrode, CGO–BaCo_{0.3}Fe_{0.6}Bi_{0.1}O_{3-δ} 50:50 wt% each at room temperature and then ground/fired at 800°C and 900°C for

4.7 Area specific resistance on $\text{Ba}_2\text{In}_{1.6}\text{Zr}_{0.2}\text{Si}_{0.2}\text{O}$ and $\text{Ce}_{0.9}\text{Gd}_{0.1}\text{O}_{1.95}$ pellet in wet N_2 and O_2 .

Following on from the chemical compatibility studies symmetrical electrode tests were performed on both electrolytes BIZS and CGO in order to determine electrode area specific resistance (ASR). The electrolyte were pressed in to 10mm pellets and sintered at their respective temperatures to ensure a high density >90% theoretical. They were then painted on each of the surfaces with the respective cathodes, fired to a binding temperature ranging between 800°C and 1000°C for 1hr.

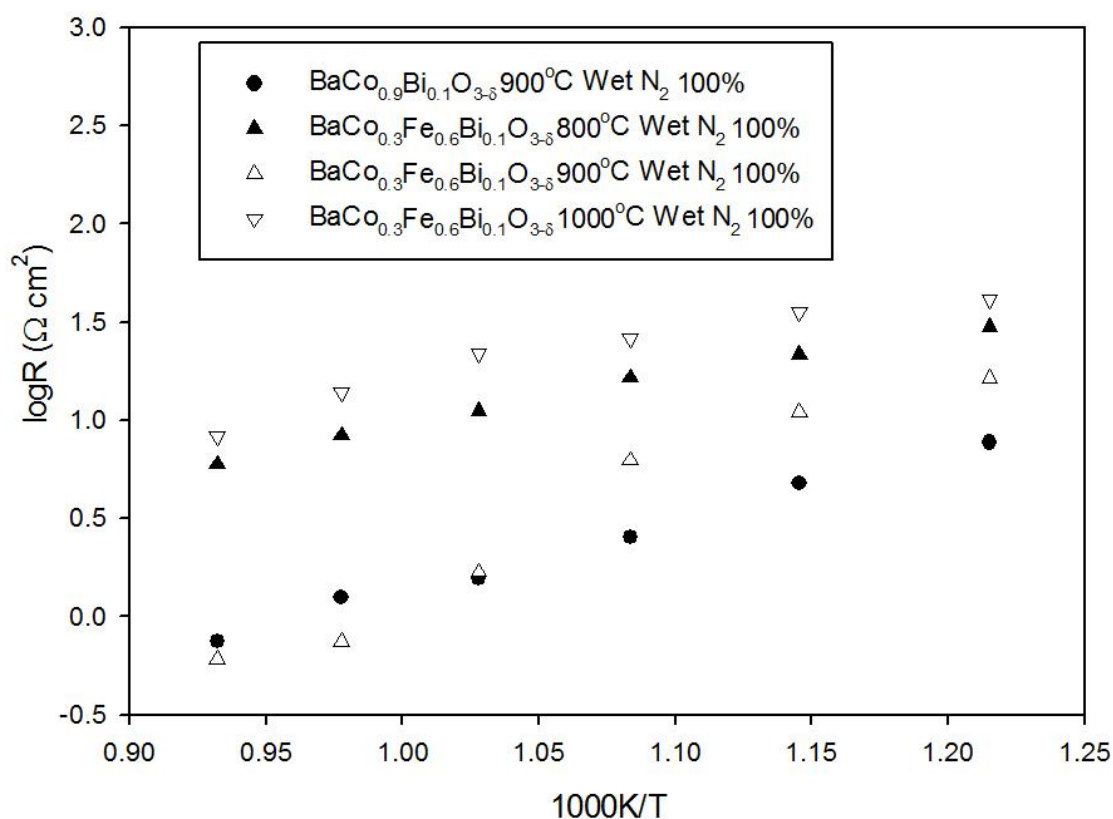


Figure 4-19 ASR data plotted $\log R$ (ASR) vs $1000/T$ in wet N_2 for electrodes $\text{BaFe}_{0.6}\text{Co}_{0.3}\text{Bi}_{0.1}\text{O}_{3-\delta}$ (100%) and $\text{BaCo}_{0.9}\text{Bi}_{0.1}\text{O}_{3-\delta}$ (100%) on a BIZS electrolyte pellet at binding temperature range of 800-1000°C.

The ASR was investigated in both wet nitrogen and wet oxygen atmospheres to gather information on the range of $p(O_2)$'s that a cathode may experience i.e. at the electrode surface a high $p(O_2)$ would be expected, whereas at the interface region the $p(O_2)$ is likely to be significantly lower. Iron doped $BaFe_{0.6}Co_{0.3}Bi_{0.1}O_{3-\delta}$ is displayed in detail due to it having the first stabilised cubic structure of the series, an inherent chemical stability with BIZS and an increased CO_2 stability temperature compared to other compositions. In addition $BaCo_{0.9}Bi_{0.1}O_{3-\delta}$ with a binding temperature of $900^\circ C$ is also shown as this sample was the highest conducting via 4 probe method. The ASR data is shown for a 100% cathode in Figure 4-19 and Figure 4-20 in both wet N_2 and O_2 for $BaFe_{0.6}Co_{0.3}Bi_{0.1}O_{3-\delta}$ ($800-1000^\circ C$).

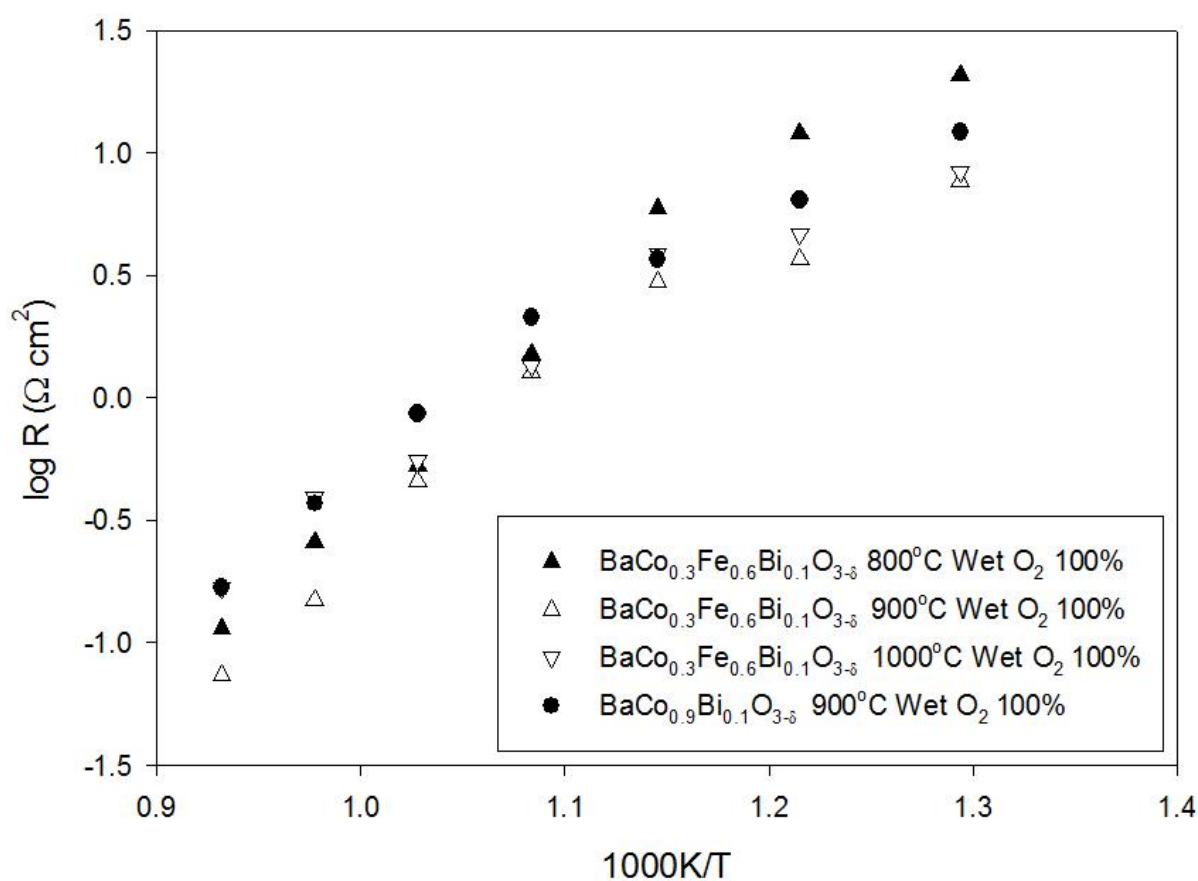


Figure 4-20 ASR data plotted $\log R$ (ASR) vs $1000/T$ in wet O_2 for electrodes $BaFe_{0.6}Co_{0.3}Bi_{0.1}O_{3-\delta}$ (100%) and $BaCo_{0.9}Bi_{0.1}O_{3-\delta}$ (100%) on a BIZS electrolyte pellet at binding temperature range of $800-1000^\circ C$

The binding temperature of 900°C appeared to be optimum in both atmospheres, giving successful binding to the BIZS surface and the lowest ASR result. The lower temperature results in poor binding and the higher temperature causes chemical compatibility issues with weak impurities forming that must be detrimental to the conductivity. In the wet N₂ atmosphere with the binding temperature at 900°C both the BaCo_{0.3}Fe_{0.6}Bi_{0.1}O_{3-δ} and BaCo_{0.9}Bi_{0.1}O_{3-δ} showed comparable results at higher temperatures (700-800°C), although the BaCo_{0.9}Bi_{0.1}O_{3-δ} sample was better at lower temperatures (<700°C). In the wet O₂ atmosphere the ASR were significantly lower than in the wet N₂ for all temperatures. Furthermore the ASR of BaCo_{0.3}Fe_{0.6}Bi_{0.1}O_{3-δ} cathode was lower than BaCo_{0.9}Bi_{0.1}O_{3-δ} was at 900°C. Table 4-8 shows the ASR resistivity results at 500°C and 800°C for the respective cathode composition and binding temperature.

The changes in the ASR in the different atmospheres is most likely due to the partial reduction of Co⁴⁺/Fe⁴⁺ to Co³⁺/Fe³⁺ in wet N₂, which significantly reduces the electronic conductivity. As noted earlier it is only at the electrode-electrolyte interfaces that such low P (O₂)'s may be observed. All further ASR tests with BIZS were performed with a cathode binding temperature of 900°C and in an O₂ atmosphere.

Table 4-8 BaCo_{0.3}Fe_{0.6}Bi_{0.1}O_{3-δ} and BaCo_{0.9}Bi_{0.1}O_{3-δ} cathodes (100%) in wet N₂/O₂ on a Ba₂In_{1.6}Zr_{0.2}Si_{0.2}O₅ pellet at binding temperature range of 800-1000°C.

<u>Composition (100)</u>	<u>ASR (Ω cm²) at 800 C</u>	<u>ASR (Ω cm²) at 500°C</u>
BaCo _{0.9} Bi _{0.1} O _{3-δ} 900°C Wet N ₂	0.75	14.71
BaCo _{0.3} Fe _{0.6} Bi _{0.1} O _{3-δ} 800°C Wet N ₂	5.9	34.38
BaCo _{0.3} Fe _{0.6} Bi _{0.1} O _{3-δ} 900°C Wet N ₂	0.61	24.48
BaCo _{0.3} Fe _{0.6} Bi _{0.1} O _{3-δ} 1000°C Wet N ₂	8.33	50.16
BaCo _{0.9} Bi _{0.1} O _{3-δ} 900°C Wet O ₂	0.17	12.15
BaCo _{0.3} Fe _{0.6} Bi _{0.1} O _{3-δ} 800°C Wet O ₂	0.11	20.61
BaCo _{0.3} Fe _{0.6} Bi _{0.1} O _{3-δ} 900°C Wet O ₂	0.073	7.69
BaCo _{0.3} Fe _{0.6} Bi _{0.1} O _{3-δ} 1000°C Wet O ₂	0.17	8.32

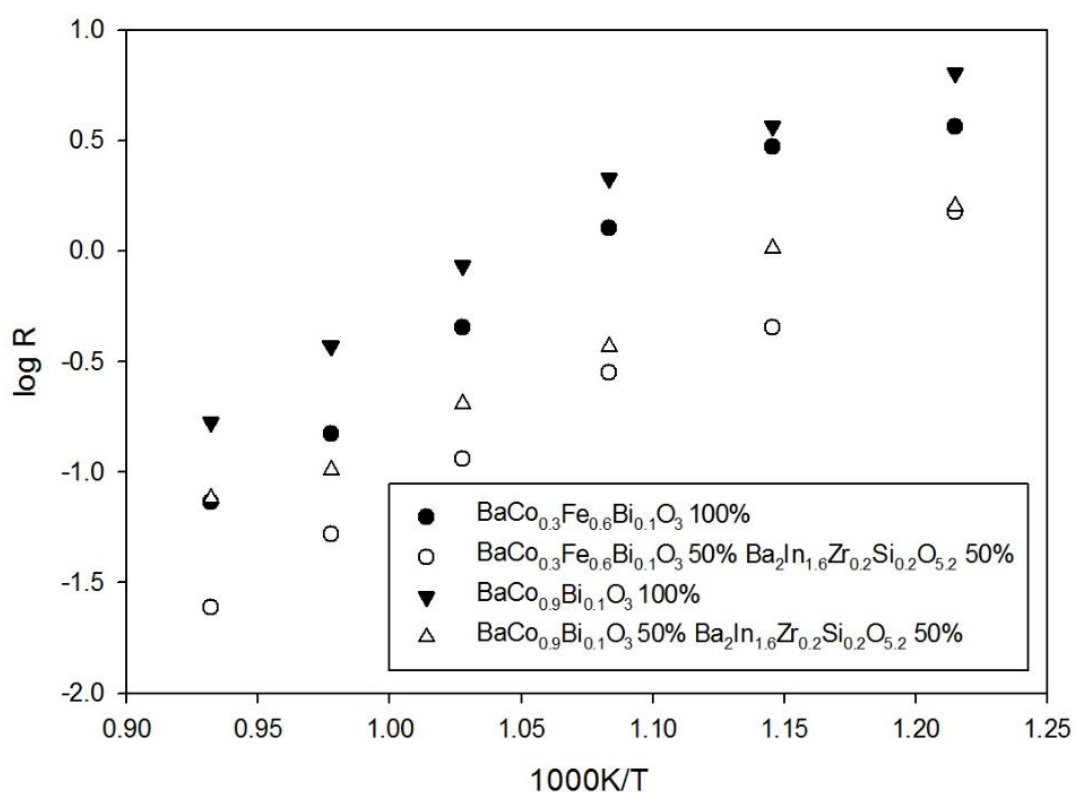


Figure 4-21 ASR data plotted $\log R$ (ASR) vs $1000/T$ in wet O_2 for composite BIZS electrodes $BaFe_{0.6}Co_{0.3}Bi_{0.1}O_{3-\delta}$ (100%/50:50wt%) and $BaCo_{0.9}Bi_{0.1}O_{3-\delta}$ (100%/50:50wt%) on a BIZS electrolyte pellet.

As previously shown the ASR can be improved by using a composite cathode in a 50:50 wt% ratio with the BIZS electrolyte. This ratio is in line with previous electrode research and the chemical compatibility tests performed. The composite cathode increases the amount of TPB present and therefore the number of active sites for the ORR, whilst keeping the required high electronic conductivity. The resulting ASR data for the composite electrodes are presented in Figure 4-21. The data shows an improvement in the values, especially at lower temperatures when comparing the 50:50wt% composite cathodes and 100% cathode on a BIZS pellet for both $BaCo_{0.3}Fe_{0.6}Bi_{0.1}O_{3-\delta}$ and $BaCo_{0.9}Bi_{0.1}O_{3-\delta}$.

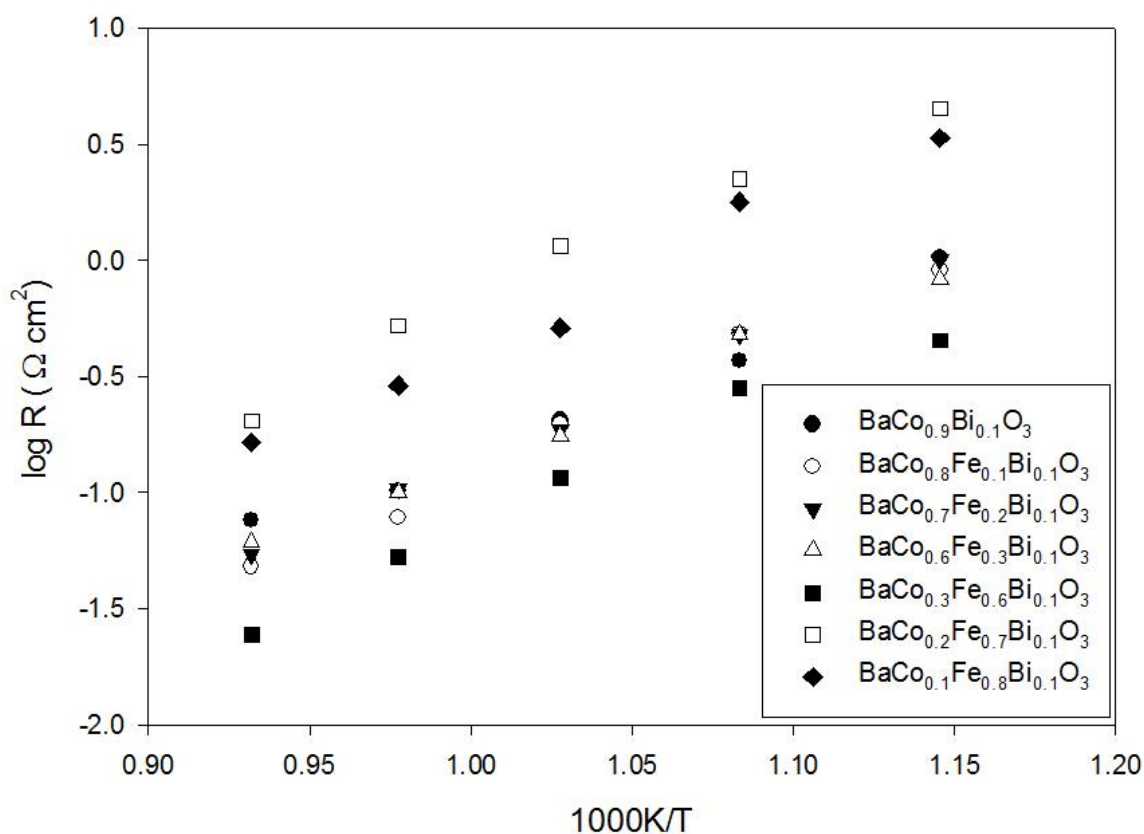


Figure 4-22 ASR data plotted logR (ASR) vs 1000/T in O₂ for composite electrodes BIZS/BaCo_{0.9-x}Fe_xBi_{0.1}O_{3-δ} x=0-0.3 0.6-0.8 (50:50wt%) on a BIZS electrolyte pellet.

Following these successful results, the electrode performance of other compositions were studied. Figure 4-22 and Table 4-9 show the ASR data for these BIZS/BaCo_{0.9-x}Fe_xBi_{0.1}O_{3-δ} (x=0-0.3 and 0.6-0.8) (50:50wt%) electrodes between 800-500°C on a BIZS electrolyte pellet. The ASR data showed an improvement when doping with iron, producing significant values comparable with industry and academic fuel cell standards.^{167, 168} Increasing the iron concentration to form the pure cubic structure (x=0.6) resulted in the lowest ASR value as predicted. However further increases in Fe content to x=0.7 and 0.8 somewhat surprisingly caused a significant rise in the ASR values. For these samples the ASR values are too high suggesting problems with using such high iron doped composites, this could be related to the observed reduction in electronic conductivity on Fe doping.

Table 4-9 ASR values at 800°C and 500°C for BIZS/BaCo_{0.9-x}Fe_xBi_{0.1}O_{3-δ} x=0-0.3 and 0.6-0.8 (50:50wt%) on a BIZS electrolyte pellet in wet O₂.

Composition 900°C Wet O ₂ 50% 50% BIZS	ASR (Ω cm ²) at 800°C	ASR (Ω cm ²) at 500°C
BaCo _{0.9} Bi _{0.1} O _{3-δ}	0.076	3.35
BaCo _{0.8} Fe _{0.1} Bi _{0.1} O _{3-δ}	0.048	3.82
BaCo _{0.7} Fe _{0.2} Bi _{0.1} O _{3-δ}	0.054	4.21
BaCo _{0.6} Fe _{0.3} Bi _{0.1} O _{3-δ}	0.061	5.91
BaCo _{0.3} Fe _{0.6} Bi _{0.1} O _{3-δ}	0.025	3.84
BaCo _{0.2} Fe _{0.7} Bi _{0.1} O _{3-δ}	0.21	11.2
BaCo _{0.1} Fe _{0.8} Bi _{0.1} O _{3-δ}	0.17	12.1

Following on from the Ba₂In_{1.6}Zr_{0.2}Si_{0.2}O_{5.2} electrolyte work, further ASR measurements were performed using an oxide ion conductor CGO. Composite electrodes of the perovskite and CGO were deposited on a CGO electrolyte pellet. The composite used was a 50:50wt% CGO and respective BaCo_{0.9-x}Fe_xBi_{0.1}O_{3-δ} (x=0-0.3 0.6-0.8) cathode material. The binding temperature was 900°C for 1hr even though reactions were seen at this temperature in the chemical compatibility tests. This was so a direct comparison could be made against the BIZS ASR data. Figure 4-23 and Table 4-10 show the ASR data obtained.

Table 4-10 Resistivity at 800°C and 500°C for CGO/BaCo_{0.9-x}Fe_xBi_{0.1}O_{3-δ} x=0-0.3 and 0.6-0.8 (50:50wt%) on a CGO electrolyte pellet

Composition 900°C Wet O ₂ 50% 50% CGO	ASR (Ω cm ²) at 800°C	ASR (Ω cm ²) at 500°C
BaCo _{0.9} Bi _{0.1} O _{3-δ}	0.0997	6.79
BaCo _{0.8} Fe _{0.1} Bi _{0.1} O _{3-δ}	0.033	18.78
BaCo _{0.7} Fe _{0.2} Bi _{0.1} O _{3-δ}	0.048	30.48
BaCo _{0.6} Fe _{0.3} Bi _{0.1} O _{3-δ}	0.11	42.91
BaCo _{0.3} Fe _{0.6} Bi _{0.1} O _{3-δ}	0.056	21.78
BaCo _{0.2} Fe _{0.7} Bi _{0.1} O _{3-δ}	0.044	25.72
BaCo _{0.1} Fe _{0.8} Bi _{0.1} O _{3-δ}	0.12	29.14

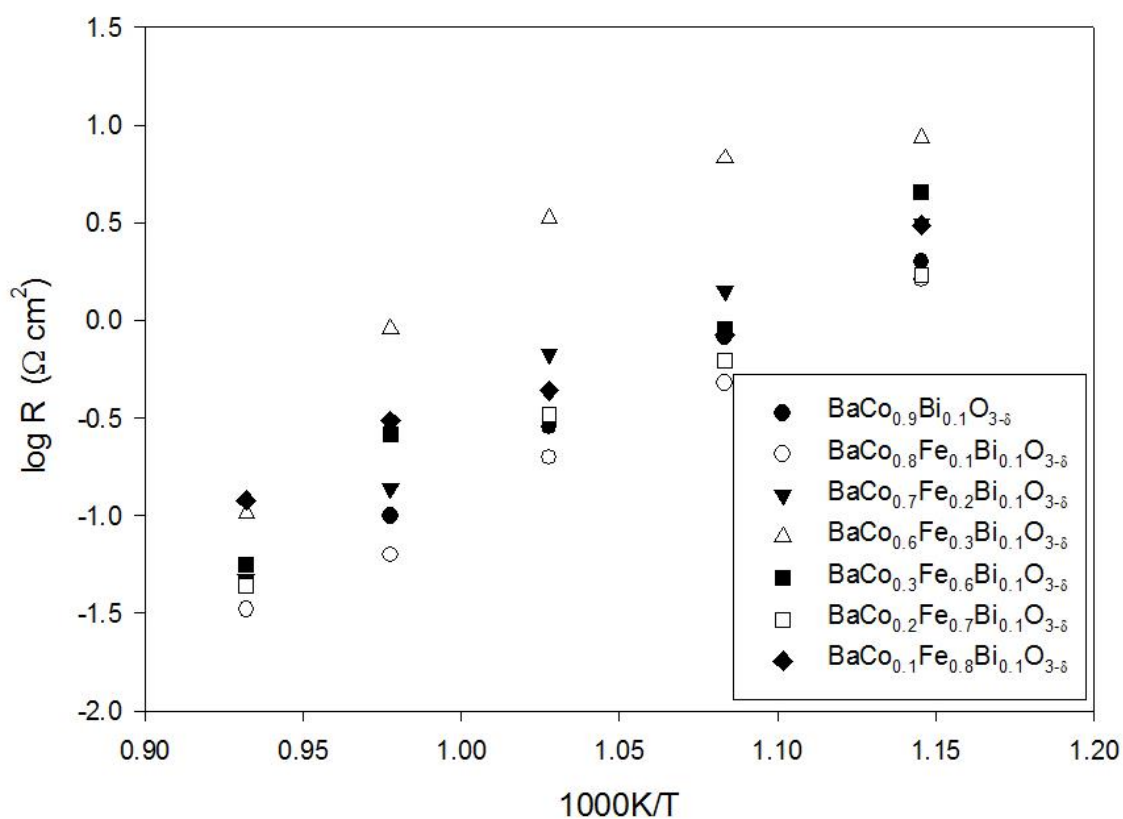


Figure 4-23 ASR data plotted $\log R$ (ASR) vs $1000/T$ in O_2 for composite electrodes CGO/BaCo_{0.9-x}Fe_xBi_{0.1}O_{3-δ} $x=0-0.8$ (50:50wt%) on a CGO electrolyte pellet

The ASR values for the CGO/BaCo_{0.9-x}Fe_xBi_{0.1}O_{3-δ} ($x=0-0.3$ and $0.6-0.8$) composites on CGO show higher values at lower temperatures than those on the BIZS pellets. However at higher temperatures the ASR values become similar. Overall the ASR at high temperatures are adequate for fuel cell tests but at low temperatures the ASR may be cause for concern.

4.8 Fuel Cell Test

Two fuel tests were assembled at the University of Malaga with a NiO-BIZS/BIZS/BIZS-BaFe_{0.6}Co_{0.3}Bi_{0.1}O_{3-δ} cell for a PC-SOFC and a NiO-CGO/CGO/CGO-BaFe_{0.6}Co_{0.3}Bi_{0.1}O_{3-δ} cell for a SOFC. The BaFe_{0.6}Co_{0.3}Bi_{0.1}O₃ cathode material was used as it showed low ASR values and higher stability than other cathode materials. The BIZS electrolyte fuel cell test was unsuccessful, as the pellets density was insufficient ($\approx 90\%$ theoretical). This density was

acceptable for conductivity and ASR measurements but too porous when used in the fuel cell test. For the SOFC test, a sufficiently dense CGO pellet ($\approx 500\mu\text{m}$ thick, 98% theoretical) was used, along with the $\text{CGO}/\text{BaFe}_{0.6}\text{Co}_{0.3}\text{Bi}_{0.1}\text{O}_{3-\delta}$ 50wt%:50wt% composite cathode and a NiO-CGO 50wt%:50wt% composite anode. Power density curves and current-voltage data for $\text{CGO}/\text{BaFe}_{0.6}\text{Co}_{0.3}\text{Bi}_{0.1}\text{O}_{3-\delta}$ / $\text{CGO}/\text{NiO-CGO}$ in the temperature range of 500°C - 700°C , using air as oxidant and H_2 as fuel, are shown in Figure 4-24.

The open circuit voltage (OCV) fluctuated between 0.892 and 0.832 V over the temperature range of 500°C - 700°C which is lower than would be expected and predicted by the Nernst equation (1), and so suggests that the cell wasn't fully sealed. The OCV drops further as temperature increases, due to the electronic conductivity in CGO at high temperatures. As a result of incomplete sealing a maximum power density of only 50 mW cm^{-2} at 700°C was obtained which is low. Further fuel cell tests are planned once the pellet density of the BIZS has been increased, via either the addition of sintering aids or plasm sintering.

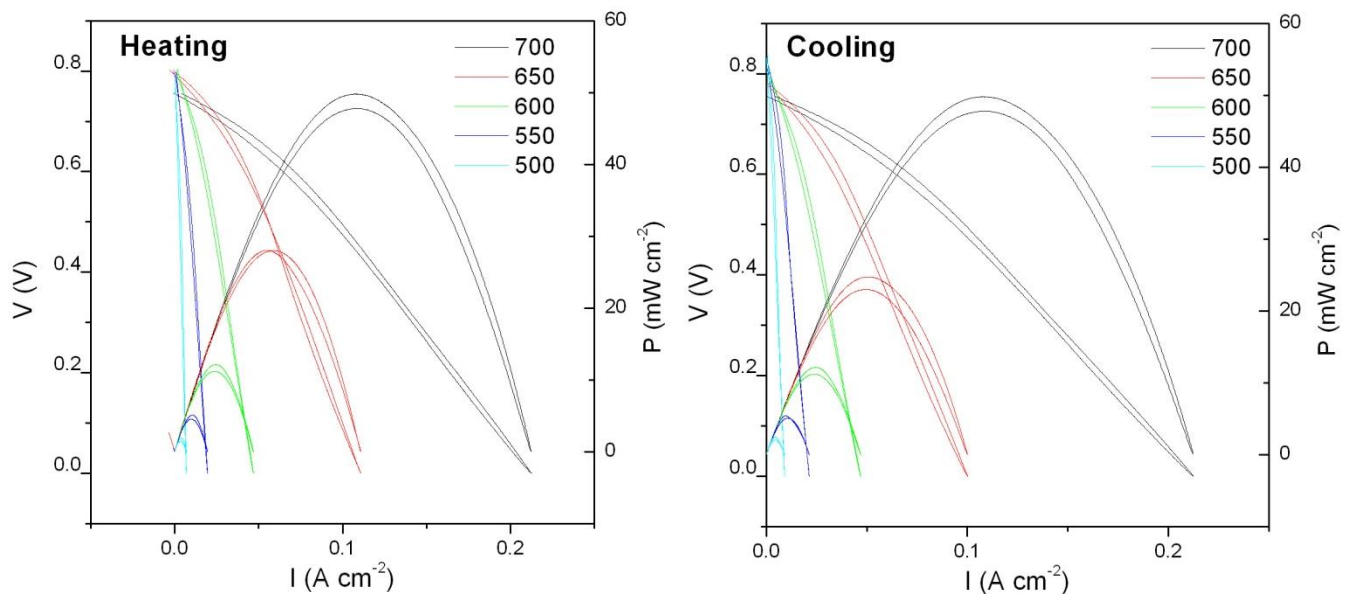


Figure 4-24 Cell voltage and power density as a function of current density between $700\text{--}500^\circ\text{C}$ using air as the oxidant and H_2 as the fuel.

4.9 Cross sectional structure of the fuel cell

The fuel cell interfaces were analysed by scanning electron microscopy (SEM) at the University of Malaga by Dr Jose M. Porras-Vazquez, to gain insight into the electrode/electrolyte interfaces. The anode/electrolyte interfaces have been widely studied, with a NiO anode being used commercially. It has been shown to adhere to the sintered electrolyte pellets without excessive reactivity. The CGO pellet with NiO is shown below in Figure 4-25 after a 1hr attachment heat treatment at 1200°C. There were two very distinct layers seen and neither showed any significant inter-diffusion between them, this is concurrent with other research.^{169, 170} This boundary is ideal for a fuel cell with the porous anode, no visible cross sectional reactions and an extremely dense electrolyte. The electrolyte/cathode interface needs to have similar characteristics to this boundary layer.

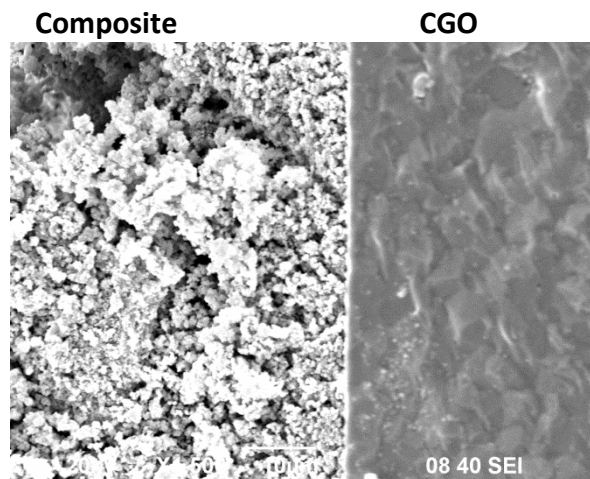


Figure 4-25 NiO-CGO 5050 composite / CGO pellet

The perovskite cathode $\text{BaFe}_{0.6}\text{Co}_{0.3}\text{Bi}_{0.1}\text{O}_{3-\delta}$ was used with both the BIZS and CGO electrolyte, and successful attachment to each pellet occurred by heating at 900°C for 1hr. Even though the chemical compatibility tests did predict some minor reactions, this was the lowest temperature possible that resulted in adequate adherence to the pellet.

At the electrolyte/cathode interface of BIZS/ $\text{BaFe}_{0.6}\text{Co}_{0.3}\text{Bi}_{0.1}\text{O}_{3-\delta}$ shown in Figure 4-26a the reactivity and inter-diffusion between the two layers was not significant, agreeing with the chemical compatibility results. However the lower than ideal density of BIZS electrolyte seen in the fuel cell test ($\approx 90\%$) is shown to be a limiting factor of this electrolyte. The SEM image shows a high electrolyte porosity, with some pores measuring $20\mu\text{m}$ in length. This would easily allow hydrogen gas to pass through electrolyte removing the seal of the cell and therefore no power output would be produced.

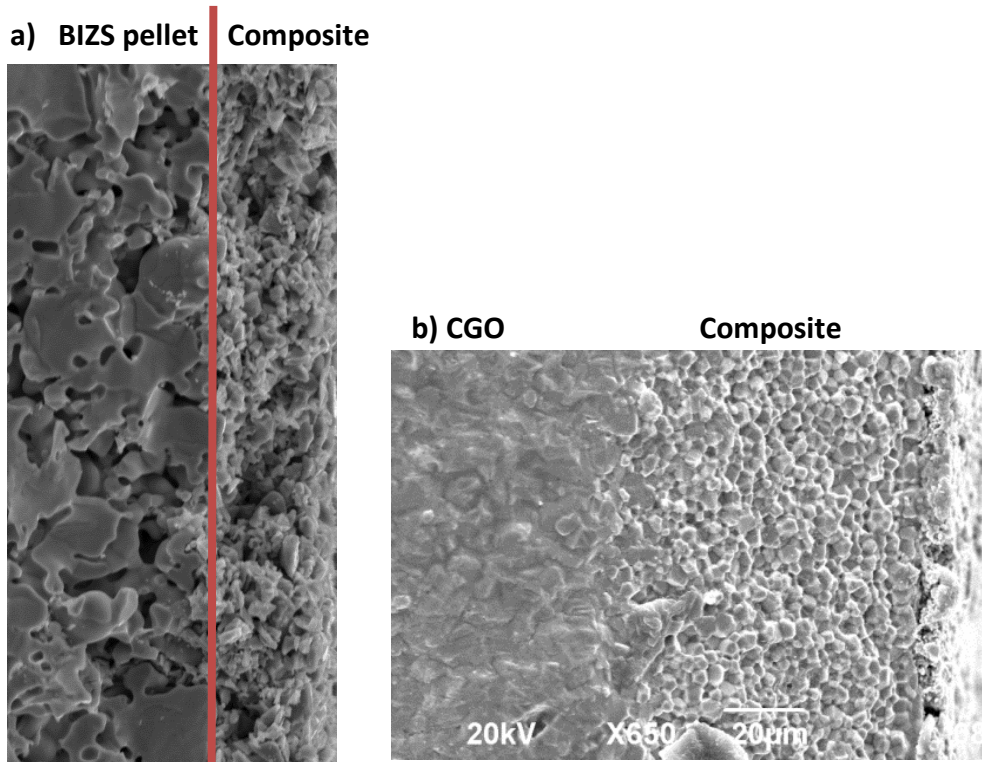


Figure 4-26 a)BIZS- $\text{BaCo}_{0.3}\text{Fe}_{0.6}\text{Bi}_{0.1}\text{O}_{3-\delta}$ 50:50wt% composite/ BIZS pellet
b)CGO pellet/CGO- $\text{BaCo}_{0.3}\text{Fe}_{0.6}\text{Bi}_{0.1}\text{O}_{3-\delta}$ 50:50wt% composite

The cathode composite of CGO- $\text{BaFe}_{0.6}\text{Co}_{0.3}\text{Bi}_{0.1}\text{O}_{3-\delta}$ on a CGO pellet is shown in Figure 4-26b. There is no definite boundary between the electrode and electrolyte as in the anode case. As previously commented the CGO electrolyte pellet density is more than adequate

and the SEM portrays this. Also some reactions can be seen between the CGO and the composite cathode as expected from their chemical compatibility reaction. In addition to the cell sealing issues, minor phases may have caused the negative effects on the fuel cells performance.

4.10 Conclusion

Perovskite type $\text{BaCo}_{0.9-x}\text{Fe}_x\text{Bi}_{0.1}\text{O}_{3-\delta}$ phases, with x ranging from 0.0-0.8 were prepared via a solid state route. X-ray diffraction confirmed that on Fe doping there is a change from a hexagonal to a cubic perovskite. High temperature X-ray diffraction of $\text{BaCo}_{0.4}\text{Fe}_{0.5}\text{Bi}_{0.1}\text{O}_{3-\delta}$ (mixed hexagonal cubic structure) showed a phase transition to pure cubic at $\approx 950^\circ\text{C}$. The iron doping into the system also resulted in a lower thermal expansion co-efficient than $\text{BaCo}_{0.9}\text{Bi}_{0.1}\text{O}_{3-\delta}$, at lower temperatures (RT- 400°C), although over the higher temperature range (RT- 800°C) the TEC values were comparable. A noticeable result was the observation of increased stability in both steam and CO_2 rich atmospheres for heavily iron doped systems. However the conductivity values are less than ideal with increased iron doping decreasing the conductivity. The chemical compatibility data was performed between the cathodes and a proton conducting SOFC electrolyte $\text{Ba}_2\text{In}_{1.6}\text{Zr}_{0.2}\text{Si}_{0.2}\text{O}_{5.2}$ (BIZS) and an oxide ion conductor $\text{Ce}_{0.9}\text{Gd}_{0.1}\text{O}_{1.95}$ (CGO). They revealed that with BIZS the increasing iron doping reduced the cross reactions, with no visible reactions seen for $x \geq 0.6$ at either 800°C or 900°C . For the electrolyte CGO all cathodes showed reactivity at 800°C and 900°C with the high cobalt containing compounds reacting the most.

ASR tests were performed on both BIZS and CGO electrolytes using 50:50 wt% cathode composite materials $\text{BaCo}_{0.9-x}\text{Fe}_x\text{Bi}_{0.1}\text{O}_{3-\delta}$ ($x = 0.0-0.3$ and $0.6-0.8$). The lowest ASR $0.025 \Omega \text{ cm}^2$ was observed at 800°C for a $\text{BaCo}_{0.3}\text{Fe}_{0.6}\text{Bi}_{0.1}\text{O}_{3-\delta}$ /BIZS composite on a BIZS pellet, which

is comparable with the reported literature systems. However for the CGO pellet of the same composite, the ASR was higher ($0.11 \Omega \text{ cm}^2$) which may be related to the minor impurity phases seen in the chemical compatibility tests.

Fuel cell tests were attempted for both electrolytes (BIZS and CGO) using the $\text{BaFe}_{0.6}\text{Co}_{0.3}\text{Bi}_{0.1}\text{O}_{3-\delta}$ cathode in 50:50wt% composites. The $\text{BaFe}_{0.6}\text{Co}_{0.3}\text{Bi}_{0.1}\text{O}_{3-\delta}$ -BIZS/BIZS/NiOBIZS cell was unsuccessful due to the poor density of the electrolyte pellet. For the $\text{BaFe}_{0.6}\text{Co}_{0.3}\text{Bi}_{0.1}\text{O}_{3-\delta}$ -CGO/CGO/NiO-CGO cell a test was successfully performed. However a maximum power density of only 50 mW cm^{-2} at 700°C was achieved. This low value, was most likely related mainly to poor cell sealing as evidenced by the low open circuit voltage.

Chapter 5

5 Doping in Ba₂Sc₂O₅ to reduce costs and increase stability

5.1 Introduction

Materials with the perovskite structure have attracted significant interest in the fuel cell area for application as both electrolyte and electrode materials. For electrolyte materials, a range of perovskite systems have been investigated displaying high oxide ion conductivity and/or proton conductivity.^{38, 73, 171} In terms of proton conducting perovskites, systems with a large A site cation (Ba/Sr) which has low electronegativity and a tetravalent B site cation (Zr⁴⁺/Ce⁴⁺) have attracted the most interest.^{172, 173} Such systems allow the introduction of acceptor dopants, in the most successful systems to date a small amount (10% or 20%) of trivalent rare earths (Y³⁺ Yb³⁺) have been doped into BaZrO₃ and BaCeO₃.¹⁷⁴⁻¹⁷⁶ These have been shown to display high protonic conductivities in humid atmospheres, by the incorporation of water into oxide ion vacancies created as a result of the doping.^{177, 178}

The cerate and the zirconate systems have been the most researched in the perovskite proton conducting area.¹⁷⁹ Less work has focused on examining systems with inherent high oxide ion vacancy contents such as Ba₂In₂O₅ and Ba₂Sc₂O₅.¹⁸⁰ Indeed, the lack of research on the latter is highlighted by the fact that it has only recently been shown that Ba₂Sc₂O₅ actually is an oxide carbonate Ba₂Sc_{2-x}C_xO_{5+x/2+}, which accounts for its thermally instability above 1000°C.^{181, 182} Though suitable oxoanion (phosphate, sulphate) or high valent cation doping (Ti⁴⁺) by Shin et al. and Knee et al. show that it can be stabilised.^{181, 183} The doping

of barium scandate with titanium results in an oxygen deficient perovskite system $\text{BaTi}_{1-x}\text{Sc}_x\text{O}_{3-\delta}$ (0.1-0.8) that shows a much higher proton conduction than the undoped analogue. The author's work on this system has shown that varying the Ti dopant level results in differences in the perovskite cell symmetry; 0.1-0.2 hexagonal, 0.3-0.4 two phase mixture, 0.5-0.7 cubic and ≥ 0.8 impure/unidentifiable perovskites.¹⁸⁴ The highest proton conductivity was observed for $\text{BaSc}_{0.7}\text{Ti}_{0.3}\text{O}_{3-\delta}$ ($\sigma_{600} = 0.0025 \text{ S cm}^{-1}$) which is comparable to yttrium doped BaZrO_3 or BaCeO_{3-y} .¹⁸⁴ However, very high sintering temperatures (1550°C, 48 hrs) were required, which still did not lead to fully dense membranes (the resulting density was below 90% and contained grain of 1-5 μm on average size, limiting its uses as a fuel cell electrolyte). Furthermore, such high temperature sintering results in barium evaporation and secondary phase formations are possible which reduces conductivity.^{183,185} In addition to this, the most successful systems contain high amounts of scandium which limits its commercial applications due to scandium's high cost (starting material is $\text{Sc}_2\text{O}_3 = \text{£}52.50$ per gram). (Sigma Aldrich 30/05/2016)

Consequently in this chapter work has involved doping $\text{BaTi}_{0.3}\text{Sc}_{0.7}\text{O}_{3-\delta}$ with other rare earths in order to examine the effects on the conductivity and in order to reduce or completely remove the high cost scandium with other elements. The doping strategy has been two fold; firstly, it has involved doping ytterbium on to scandium with the same charge and similar size. Secondly a small amount of boron as a dopant and sintering aid has been added in an effort to lower the melting point and promote grain growth, therefore enhancing the sinterability ($\text{BaYb}_{0.7-x-y}\text{Sc}_x\text{B}_y\text{Ti}_{0.3}\text{O}_{3-\delta}$) and thus allowing the sintering temperature to be lowered. The initial work showed that some Sc was still required to form the perovskite phase. However, following on from this initial work, the complete

replacement of scandium has also been attempted in such systems, by adding low levels of iron to form $\text{BaYb}_{0.65-z}\text{Fe}_z\text{B}_{0.05}\text{Ti}_{0.3}\text{O}_{3-\delta}$ phases.

5.2 Experimental

High purity BaCO_3 , Sc_2O_3 , Yb_2O_3 , H_3BO_3 , Fe_2O_3 and TiO_2 were used to prepare a range of $\text{BaYb}_{0.7-x-y}\text{Sc}_x\text{B}_y\text{Ti}_{0.3}\text{O}_{3-\delta}$ ($x = 0, 0.05, 0.1, 0.15, 0.2, 0.25, 0.3, 0.35$ and $y = 0, 0.05$) and $\text{BaYb}_{0.65-z}\text{Fe}_z\text{B}_{0.05}\text{Ti}_{0.3}\text{O}_{3-\delta}$ ($z = 0.05, 0.1, 0.2$) electrolyte samples. A small (5%) excess of BaCO_3 was employed, in order to overcome barium loss at elevated temperatures and so eliminate barium deficient impurity phases as shown to be successful in previous studies of related systems.^{186, 187} In each case, the powders were ground and heated initially to 1000°C for 12 hours (a pre-drying step was included if required). They were then reheated to 1100°C for 12 hours with an intermediate regrind. The resulting powders were then reground again, pressed as pellets (1.3 cm diameter) and sintered between 1350°C and 1400°C for 6 hours. The pellets were covered in sacrificial sample powder and the crucible was covered with a lid in an effort to limit the amount of barium loss during the synthesis/sintering process. Powder X-ray diffraction data were collected over a $20-80^\circ 2\theta$ range with a step size of 0.02° (Bruker D8 diffractometer with $\text{Cu K}\alpha_1$ radiation). In order to demonstrate phase purity, as well as for cell parameter determination. The latter utilised the GSAS suite of programmes.¹¹⁸

The respective powder samples were heated under wet N_2 to 800°C and held for 2 hours, before slowly cooling them down to room temperature at $0.4^\circ\text{C min}^{-1}$ to hydrate the phases. The water contents of hydrated samples were determined from thermogravimetric analysis (Netzsch STA 449 F1 Jupiter Thermal Analyser). Samples were heated at $10^\circ\text{C min}^{-1}$

to 800°C in N₂, and the water contents were determined from the observed mass loss, with a mass spectrometer attachment confirming that the mass loss was due to water. The stability of the hydrated systems after hydration were confirmed through X-ray diffraction analysis. The CO₂ stabilities of the samples were determined using X-ray diffraction and thermogravimetric analysis as well. The X-ray diffraction data were used to elucidate any differences before and after heating the samples to 800°C in dry CO₂, and so allow the identification of any decomposition. In the TGA experiments, samples were heated at 10°C min⁻¹ to 800°C in CO₂ to determine if CO₂ would be picked up and at what temperature this occurred.

Scanning electron microscopy images were collected on a JEOL SM-6490LV electron microscope, to study the effect of the addition of the sintering aid boron on the samples microstructure and porosity. The samples were gold coated to avoid charge build up on the surface.

Conductivity measurements were performed on BaYb_{0.7-x}Sc_xB_{0.05}Ti_{0.3}O_{2.65} (x= 0.05, 0.1, 0.2, 0.3) and BaYb_{0.65-z}Fe_zB_{0.05}Ti_{0.3}O_{3-δ} (z= 0.05, 0.1, 0.2) electrolyte samples. The sintered pellets ranged in densities between 76%-99%; each pellet was coated with Pt paste and Pt electrodes were attached and heated to 800°C in air for 1 hour to ensure bonding to the pellets surface. Conductivities were then measured by AC impedance measurements (PSM 1735 N4L interface impedance analyser) in the frequency range of 1Hz to 13 MHz. Conductivity measurements were performed in dry N₂ and wet N₂ (in which the gas was bubbled at room temperature through concentrated sulphuric acid and water respectively) to identify any protonic contribution to the conductivity. The impedance spectra were recorded between 350°C-800°C; it was not possible to accurately extract individual bulk

and grain boundary contributions across the entire range. Therefore the resistance was calculated from the high intercept of the semicircle based on the Z-view fitting programme and corresponds to the total (bulk + grain boundary) resistance.¹⁴³

5.3 Synthesis results

The initial X-ray powder diffraction data of undoped barium scandate correlates with previous work on this material. These data showed that it is unstable above 1000°C forming $\text{Ba}_3\text{Sc}_4\text{O}_9$, leaving it unable to be sintered for fuel cell applications. Below 1000°C a perovskite related structure was observed, and previous work within the group has indicated that this structure was not actually “ $\text{Ba}_2\text{Sc}_2\text{O}_5$ ” but rather a carbonate doped barium scandate $\text{Ba}_2\text{Sc}_{2-x}\text{C}_x\text{O}_{5+x/2}$. The presence of carbonate stabilises the high number of oxide ion vacancies, but is lost above 1000°C, hence the thermal instability (Figure 5-1).^{180,}

181

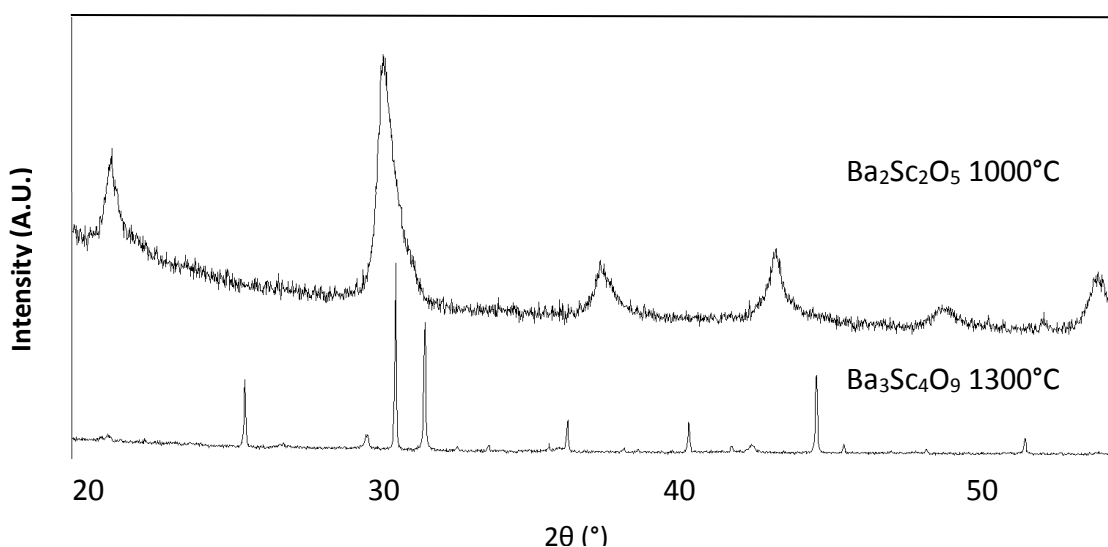


Figure 5-1 X-ray diffraction of $\text{Ba}_2\text{Sc}_2\text{O}_5$ at temperatures of 1000°C and 1300°C (the later showing the formation of $\text{Ba}_3\text{Sc}_4\text{O}_9$)

In order to stabilise the perovskite structure to higher temperatures and reduce the scandium content, the dopants ytterbium (Yb^{3+}) titanium (Ti^{4+}) and boron (B^{3+}) were used.

X-ray diffraction patterns of the highly doped samples showed the emergence of perovskite peaks at synthesis temperatures above 1300°C. A constant titanium and boron content of 0.3 and 0.05 respectively was employed, and the scandium, ytterbium content was then varied.

Compositions of $\text{BaYb}_{0.65-x}\text{Sc}_x\text{B}_{0.05}\text{Ti}_{0.3}\text{O}_{2.65}$ were prepared, with the focus on the lower Sc ($x = 0.05, 0.1, 0.2$ and 0.3) levels because of its higher cost. All compositions in this range were successfully prepared, with cell parameters shown in Table 5-1 and X-ray diffraction patterns in Figure 5-2. The data show a gradual decrease in the cell parameters on increasing scandium contents, due to the smaller size of Sc^{3+} (0.745 Å) to Yb^{3+} (0.868 Å).

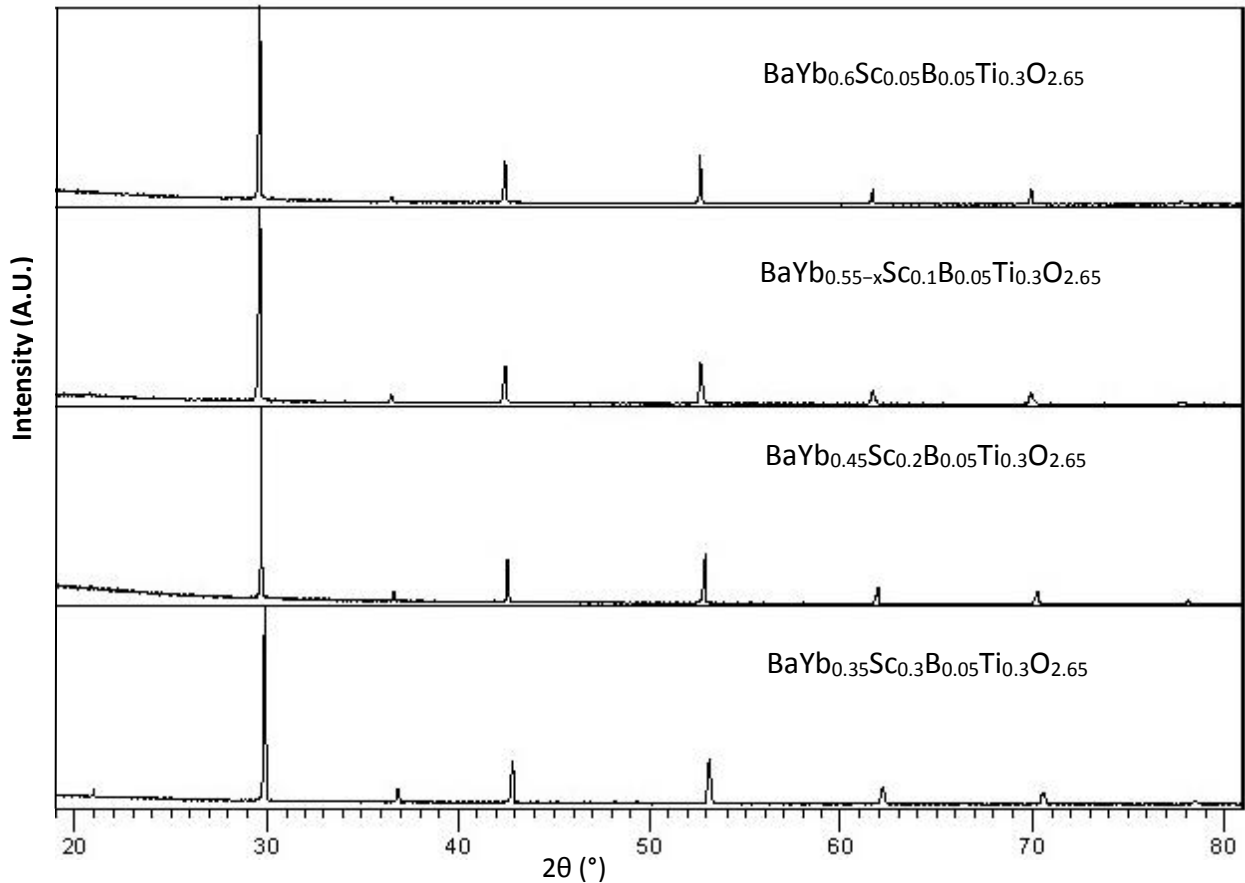


Figure 5-2 X-ray diffraction pattern for $\text{BaYb}_{0.65-x}\text{Sc}_x\text{B}_{0.05}\text{Ti}_{0.3}\text{O}_{2.65}$ ($x = 0.05, 0.1, 0.2, 0.3$)

Table 5-1 Cell parameter data for $\text{BaYb}_{0.7-x}\text{Sc}_x\text{B}_{0.05}\text{Ti}_{0.3}\text{O}_{3-\delta}$ ($x = 0.05, 0.1, 0.2, 0.3$)

Sample composition	Unit cell parameter a (Å)	Unit cell volume (Å ³)
$\text{BaYb}_{0.6}\text{Sc}_{0.05}\text{B}_{0.05}\text{Ti}_{0.3}\text{O}_{2.65}$	4.24336(5)	76.406(3)
$\text{BaYb}_{0.55}\text{Sc}_{0.1}\text{B}_{0.05}\text{Ti}_{0.3}\text{O}_{2.65}$	4.24106(7)	76.283(4)
$\text{BaYb}_{0.45}\text{Sc}_{0.2}\text{B}_{0.05}\text{Ti}_{0.3}\text{O}_{2.65}$	4.22780(2)	75.56(1)
$\text{BaYb}_{0.35}\text{Sc}_{0.3}\text{B}_{0.05}\text{Ti}_{0.3}\text{O}_{2.65}$	4.21475(6)	74.872(3)

The complete removal of scandium was also attempted, and whilst a perovskite phase formed, the resultant sample did include significant impurity phases (in particular $\text{Ba}_3\text{Yb}_4\text{O}_9$) (Figure 5-3), suggesting enhanced problems with Ba loss without some Sc being present. In addition corresponding samples without boron were also examined $\text{BaYb}_{0.55}\text{Sc}_{0.15}\text{Ti}_{0.3}\text{O}_{2.65}$, $\text{BaYb}_{0.45}\text{Sc}_{0.25}\text{Ti}_{0.3}\text{O}_{2.65}$ and $\text{BaYb}_{0.35}\text{Sc}_{0.35}\text{Ti}_{0.3}\text{O}_{2.65}$. These phases, however, showed the presence of impurities which indicates that the successful replacement of the scandium with a larger ytterbium dopant requires boron to be present to achieve pure samples. All samples showed the presence of impurities until the $\text{BaYb}_{0.35}\text{Sc}_{0.35}\text{Ti}_{0.3}\text{O}_{2.65}$ sample, which appeared to be a mixture of a cubic and tetragonal perovskite.

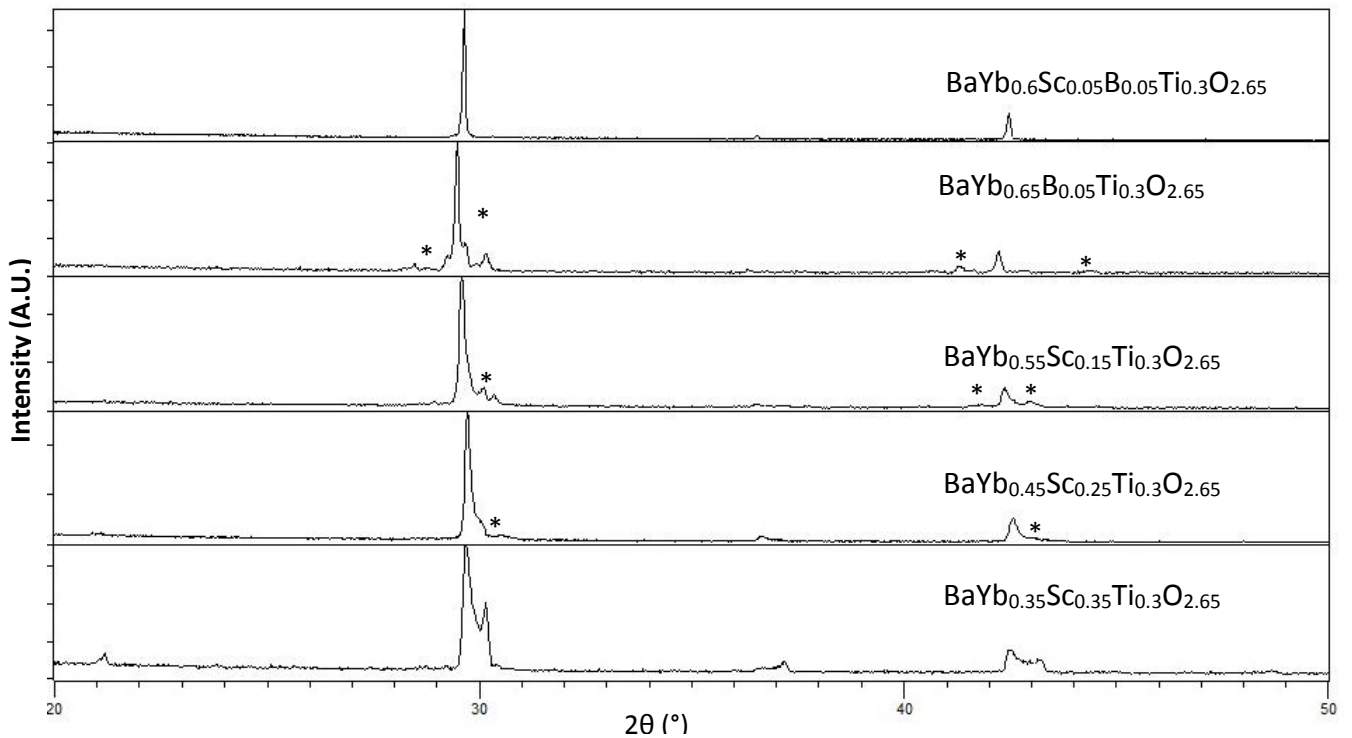


Figure 5-3 XRD patterns for $\text{BaYb}_{0.6}\text{Sc}_{0.05}\text{B}_{0.05}\text{Ti}_{0.3}\text{O}_3$, $\text{BaYb}_{0.65}\text{B}_{0.05}\text{Ti}_{0.3}\text{O}_3$, $\text{BaYb}_{0.55}\text{Sc}_{0.15}\text{Ti}_{0.3}\text{O}_{3-\delta}$, $\text{BaYb}_{0.45}\text{Sc}_{0.25}\text{Ti}_{0.3}\text{O}_{3-\delta}$ and $\text{BaYb}_{0.35}\text{Sc}_{0.35}\text{Ti}_{0.3}\text{O}_{3-\delta}$ in a zoomed region of 20-50° with * denoting the impurities.

5.4 Scanning electron microscopy studies

Scanning electron microscopy was used to investigate whether the pellets of $\text{BaYb}_{0.65-x}\text{Sc}_x\text{B}_{0.05}\text{Ti}_{0.3}\text{O}_{2.65}$ ($x = 0.05, 0.1, 0.2, 0.3$) had sintered successfully, and if the sintering aid (boron) was having an effect on the grain growth. These SEM tests were performed at the University of Malaga by Dr Jose M. Porras-Vazquez.

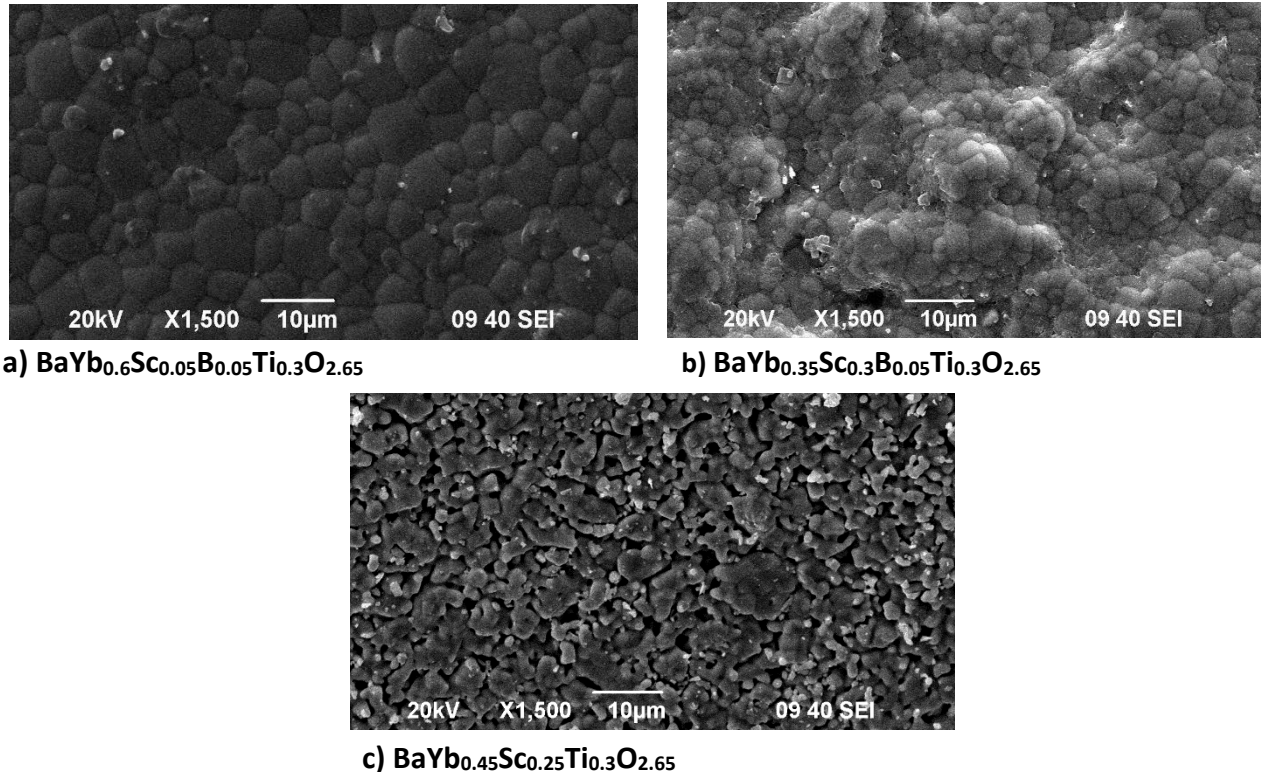


Figure 5-4 Scanning electron microscopy images of a) $\text{BaYb}_{0.6}\text{Sc}_{0.05}\text{B}_{0.05}\text{Ti}_{0.3}\text{O}_{2.65}$ b) $\text{BaYb}_{0.35}\text{Sc}_{0.3}\text{B}_{0.05}\text{Ti}_{0.3}\text{O}_{2.65}$ and c) $\text{BaYb}_{0.45}\text{Sc}_{0.25}\text{Ti}_{0.3}\text{O}_{2.65}$

Table 5-2 % theoretical density of $\text{BaYb}_{0.65-x}\text{Sc}_x\text{B}_{0.05}\text{Ti}_{0.3}\text{O}_{2.65}$ ($x = 0.05, 0.1, 0.2, 0.3$) and $\text{BaYb}_{0.45}\text{Sc}_{0.25}\text{Ti}_{0.3}\text{O}_{2.65}$ samples (*denotes impure)

Composition	Density %
$\text{BaYb}_{0.6}\text{Sc}_{0.05}\text{B}_{0.05}\text{Ti}_{0.3}\text{O}_{2.65}$	87
$\text{BaYb}_{0.6}\text{Sc}_{0.1}\text{B}_{0.05}\text{Ti}_{0.3}\text{O}_{2.65}$	94
$\text{BaYb}_{0.6}\text{Sc}_{0.2}\text{B}_{0.05}\text{Ti}_{0.3}\text{O}_{2.65}$	99
$\text{BaYb}_{0.6}\text{Sc}_{0.3}\text{B}_{0.05}\text{Ti}_{0.3}\text{O}_{2.65}$	95
$\text{BaYb}_{0.6}\text{Sc}_{0.25}\text{Ti}_{0.3}\text{O}_{2.65}$ *	74

Figure 5-4 shows the SEM images of $\text{BaYb}_{0.6}\text{Sc}_{0.05}\text{B}_{0.05}\text{Ti}_{0.3}\text{O}_{2.65}$, $\text{BaYb}_{0.35}\text{Sc}_{0.3}\text{B}_{0.05}\text{Ti}_{0.3}\text{O}_{2.65}$ and the impure $\text{BaYb}_{0.45}\text{Sc}_{0.25}\text{Ti}_{0.3}\text{O}_{2.65}$. The B doped samples $\text{BaYb}_{0.6}\text{Sc}_{0.05}\text{B}_{0.05}\text{Ti}_{0.3}\text{O}_{2.65}$ and $\text{BaYb}_{0.35}\text{Sc}_{0.3}\text{B}_{0.05}\text{Ti}_{0.3}\text{O}_{2.65}$ show similar results illustrating a dense material and continuously defined grain boundaries. In contrast the sample without B, $\text{BaYb}_{0.45}\text{Sc}_{0.25}\text{Ti}_{0.3}\text{O}_{2.65}$ shows less distinct features, and it contains a much more porous structure with varying grain sizes. Table 5-2 lists the densities of the pellets, with the boron doped samples showing high densities, with values ranging from 87-99 % theoretical, whilst the non-boron doped system $\text{BaYb}_{0.45}\text{Sc}_{0.25}\text{Ti}_{0.3}\text{O}_{2.65}$ had a much lower density of 74%. Thus, the presence of boron appears to be having the desired effect of increasing the densification, whilst also producing a pure phase most likely as a result of enhancing reaction through lowering the overall sample melting point. Furthermore, due to the small impurities, and the lower than ideal density of the $\text{BaYb}_{0.7-\gamma}\text{Sc}_{\gamma}\text{Ti}_{0.3}\text{O}_{2.65}$ electrolytes ($\gamma = 0.15, 0.25$ and 0.35), they are unusable in a fuel cell and therefore further measurements were performed only on the B doped samples $\text{BaYb}_{0.65-x}\text{Sc}_x\text{B}_{0.05}\text{Ti}_{0.3}\text{O}_{2.65}$ ($x = 0.05, 0.1, 0.2, 0.3$).

5.5 Thermogravimetric analysis (TGA)

5.5.1 Hydration

In order to hydrate the samples, powders of $\text{BaYb}_{0.65-x}\text{Sc}_x\text{B}_{0.05}\text{Ti}_{0.3}\text{O}_{2.65}$ ($x = 0.05, 0.1, 0.2, 0.3$) were heated under wet N_2 to 800°C , before slowly cooling them down to room temperature ($0.4^\circ\text{C min}^{-1}$). X-ray diffraction was carried out after the heat treatment in order to confirm that there was no decomposition on hydration (Figure 5-5).

Table 5-3 Water contents for hydrated $\text{BaYb}_{0.65-x}\text{Sc}_x\text{B}_{0.05}\text{Ti}_{0.3}\text{O}_{2.65}$ ($x = 0.05, 0.1, 0.2, 0.3$) from TGA studies.

Sample composition	Water content (per formula unit)
$\text{BaYb}_{0.6}\text{Sc}_{0.05}\text{B}_{0.05}\text{Ti}_{0.3}\text{O}_{2.65}$	0.186(4)
$\text{BaYb}_{0.55}\text{Sc}_{0.1}\text{B}_{0.05}\text{Ti}_{0.3}\text{O}_{2.65}$	0.133(4)
$\text{BaYb}_{0.45}\text{Sc}_{0.2}\text{B}_{0.05}\text{Ti}_{0.3}\text{O}_{2.65}$	0.108(2)
$\text{BaYb}_{0.35}\text{Sc}_{0.3}\text{B}_{0.05}\text{Ti}_{0.3}\text{O}_{2.65}$	0.076(9)

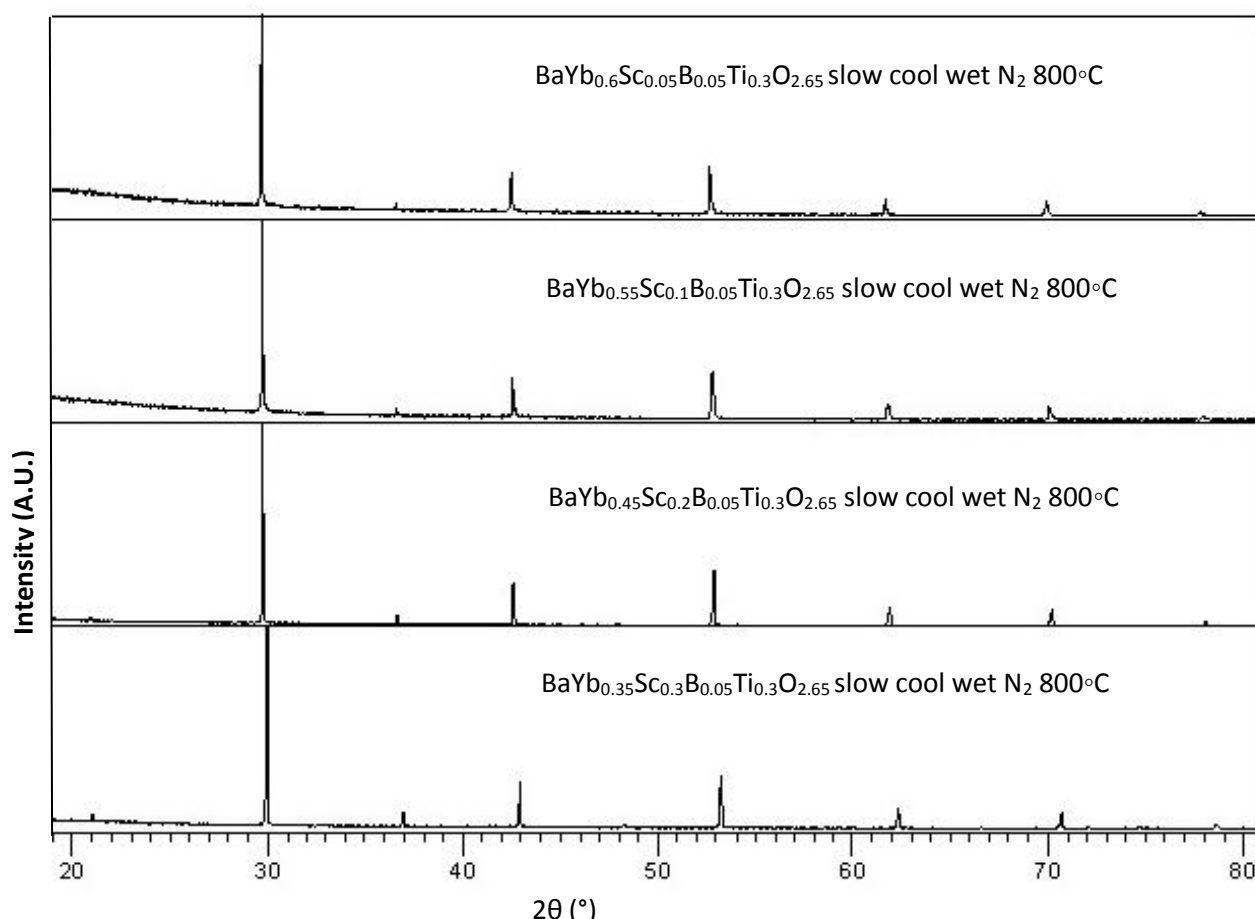


Figure 5-5 XRD patterns for hydrated $\text{BaYb}_{0.65-x}\text{Sc}_x\text{B}_{0.05}\text{Ti}_{0.3}\text{O}_{2.65}$ ($x = 0.05, 0.1, 0.2, 0.3$)

The water contents were determined through TGA measurement in a dry nitrogen atmosphere, heating the hydrated samples at $10^\circ\text{C min}^{-1}$ to 800°C . The calculated water contents ranged from 0.08-0.19 H_2O per formula unit (table 6-3), with the water content decreasing with increasing Sc content. The origin of this decrease requires further study but may indicate changes in oxide ion vacancy defect trapping, such that hydration becomes less favourable. Overall, however the data indicates incomplete filling of the oxide ion vacancies by H_2O for all samples.

5.5.2 CO₂ stability

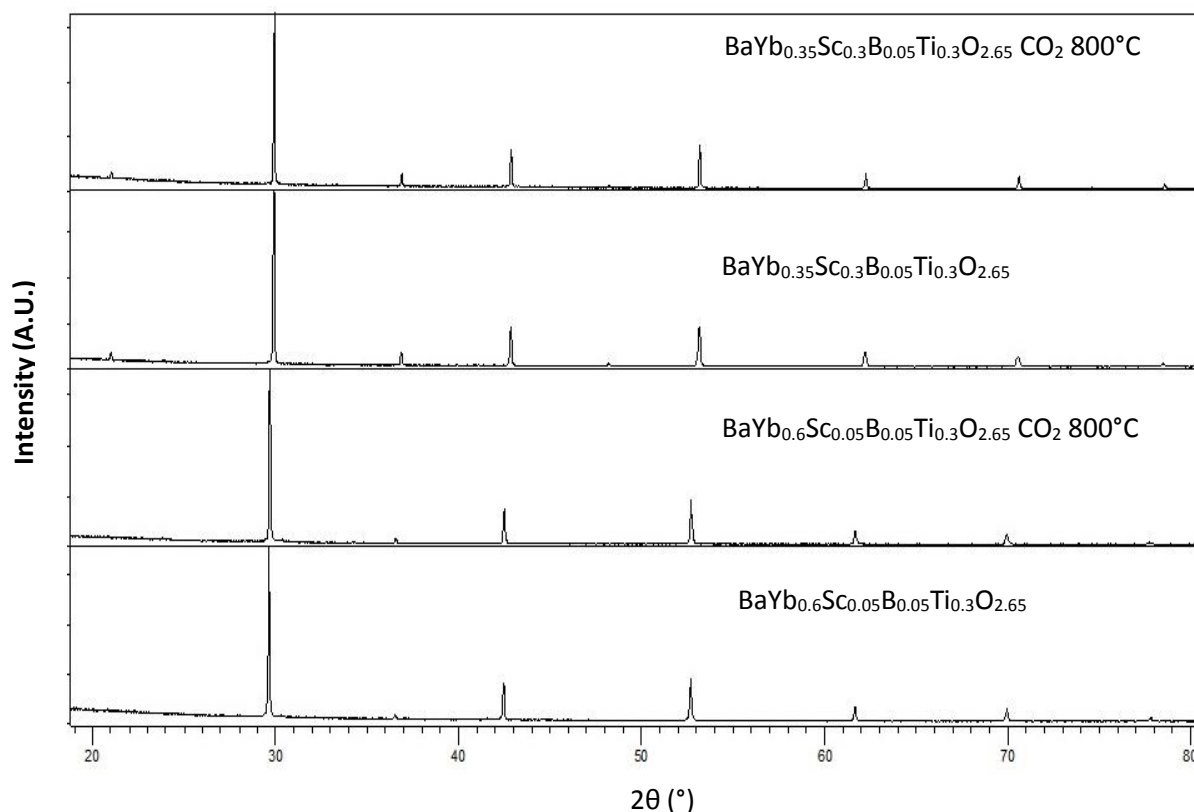


Figure 5-6 X-ray diffraction data for $\text{BaYb}_{0.35}\text{Sc}_{0.3}\text{B}_{0.05}\text{Ti}_{0.3}\text{O}_{2.65}$ and $\text{BaYb}_{0.6}\text{Sc}_{0.05}\text{B}_{0.05}\text{Ti}_{0.3}\text{O}_{2.65}$ before and after a heat treatment to 800°C in 100% dry CO_2 for 24hrs.

The CO_2 stability of the $\text{BaYb}_{0.7-x}\text{Sc}_x\text{B}_{0.05}\text{Ti}_{0.3}\text{O}_{2.65}$ ($x = 0.05, 0.1, 0.2, 0.3$) samples has also been investigated, as many proton conductors, such as BaCeO_3 , undergo significant decomposition reactions when heating in a CO_2 containing atmosphere (forming barium carbonate).¹⁸⁸ Figure 5-6 shows the X-ray diffraction patterns of $\text{BaYb}_{0.35}\text{Sc}_{0.3}\text{B}_{0.05}\text{Ti}_{0.3}\text{O}_{2.65}$ and $\text{BaYb}_{0.55}\text{Sc}_{0.05}\text{B}_{0.05}\text{Ti}_{0.3}\text{O}_{2.65}$ before and after heating to 800°C in dry CO_2 for 24 hrs. The conditions used are extreme conditions for a fuel cell electrolyte, but despite these extreme conditions the data shows that this perovskite is stable in such CO_2 environments up to 800°C .

TGA measurements were also performed on these perovskites, as well as undoped “ $\text{Ba}_2\text{Sc}_2\text{O}_5$ ” and $\text{BaCe}_{0.9}\text{Y}_{0.1}\text{O}_{3-\delta}$ for comparison. The TGA profiles in Figure 5-7 are from

heating in a CO₂ atmosphere up to 800°C at 10°C min⁻¹; the data show that “Ba₂Sc₂O₅” and BaCe_{0.9}Y_{0.1}O_{3-δ} are susceptible to partial decomposition in a CO₂ atmosphere as expected, gaining significant mass at temperatures above 475°C and 550°C respectively. However, the data for BaYb_{0.65}Sc_{0.05}B_{0.05}Ti_{0.3}O_{2.65} and BaYb_{0.35}Sc_{0.3}B_{0.05}Ti_{0.3}O_{2.65} showed no mass increases up to 800°C, indicating that these perovskite phases are very stable in a high CO₂ atmosphere.

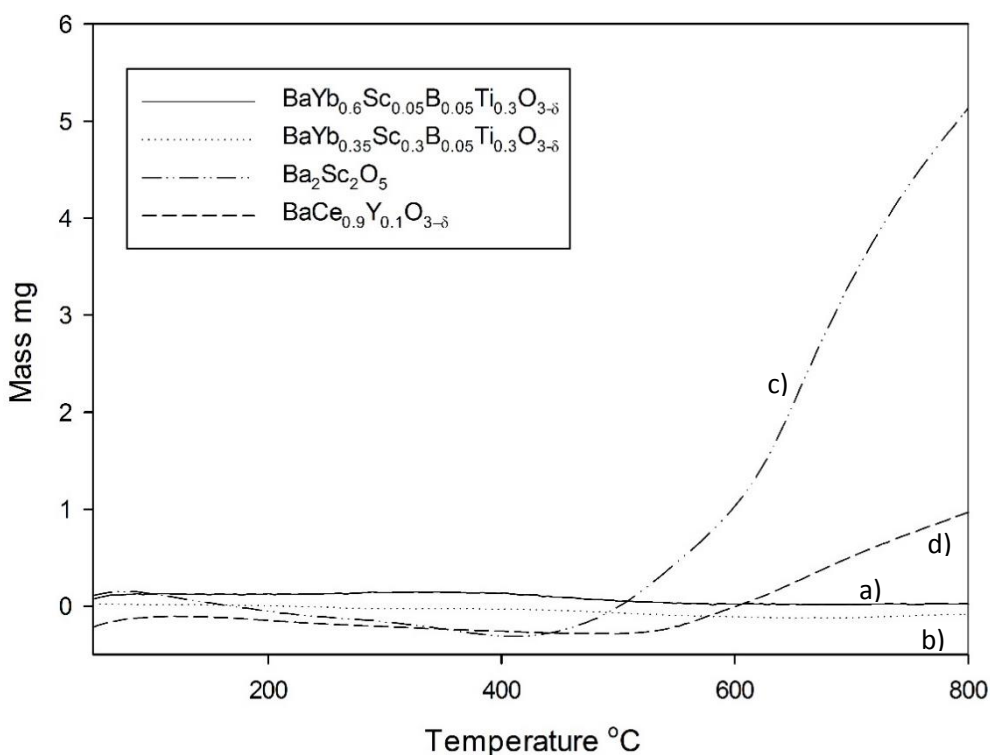


Figure 5-7 TG profiles (10°C min⁻¹ to 800°C in CO₂) for a) BaYb_{0.65}Sc_{0.05}B_{0.05}Ti_{0.3}O_{3-δ}, b) BaYb_{0.35}Sc_{0.3}B_{0.05}Ti_{0.3}O_{3-δ}, c) Ba₂Sc₂O₅ and d) BaCe_{0.9}Y_{0.1}O_{3-δ}

5.6 Conductivity measurements

The conductivities of BaYb_{0.7-x}Sc_xB_{0.05}Ti_{0.3}O_{2.65} (x = 0.05, 0.1, 0.2, 0.3) pellets were investigated in both dry and wet N₂ atmospheres, in order to determine if proton conductivity was observed over the 350-800°C range. As noted earlier, all sample pellets showed high theoretical densities (values given in Table 5-4).

Table 5-4 % Theoretical Densities of $\text{BaYb}_{0.7-x}\text{Sc}_x\text{B}_{0.05}\text{Ti}_{0.3}\text{O}_{2.65}$ ($x = 0.05, 0.1, 0.2, 0.3$)

Sample composition	% Theoretical Density
$\text{BaYb}_{0.6}\text{Sc}_{0.05}\text{B}_{0.05}\text{Ti}_{0.3}\text{O}_{2.65}$	87
$\text{BaYb}_{0.55}\text{Sc}_{0.1}\text{B}_{0.05}\text{Ti}_{0.3}\text{O}_{2.65}$	94
$\text{BaYb}_{0.45}\text{Sc}_{0.2}\text{B}_{0.05}\text{Ti}_{0.3}\text{O}_{2.65}$	99
$\text{BaYb}_{0.35}\text{Sc}_{0.3}\text{B}_{0.05}\text{Ti}_{0.3}\text{O}_{2.65}$	95

The impedance data revealed a partial separation of the individual boundary components at low temperatures (350-450°C), with a separate grain boundary contribution being observed, which became less significant at higher temperature. Figure 5-8 shows the impedance and fitting data for $\text{BaYb}_{0.6}\text{Sc}_{0.05}\text{B}_{0.05}\text{Ti}_{0.3}\text{O}_{2.65}$ at 350°C, 450°C and 550°C in a dry N_2 atmosphere.

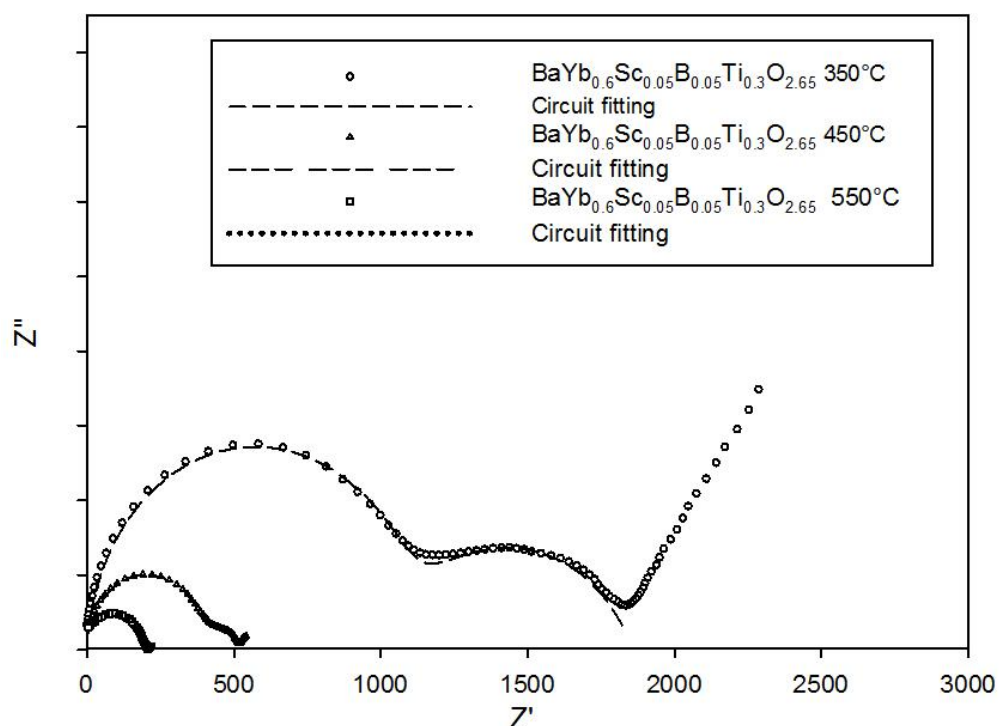


Figure 5-8 Impedance and fitting data for $\text{BaYb}_{0.6}\text{Sc}_{0.05}\text{B}_{0.05}\text{Ti}_{0.3}\text{O}_{2.65}$ at 350°C, 450°C and 550°C in a dry N_2 atmosphere, showing the reduction and splitting components in the resistance over temperature.

The semicircles at high frequencies relate to the bulk conductivities and have corresponding capacitance values equal to $10^{-11} \text{ F cm}^{-1}$. The second semicircles at lower frequencies are consistent with grain boundary conductivities having a calculated

capacitance of $10^{-8} \text{ F cm}^{-1}$ (equivalent circuit fitting model). The low temperature data showed a significant grain boundary contribution, which disappeared at higher temperatures. However at the required intermediate fuel cell temperatures $>500^\circ\text{C}$, a single broad semicircle was observed for the total conductivity. These single semicircles essentially appeared to mainly correspond to the bulk conductivity (capacitance = $10^{-11} \text{ F cm}^{-1}$) with the resolved grain boundary being no longer observed.

Table 5-5 Fitted bulk (B) and grain boundary (GB) conductivities and capacitances for $\text{BaYb}_{0.6}\text{Sc}_{0.05}\text{B}_{0.05}\text{Ti}_{0.3}\text{O}_{2.65}$ at 350°C , 450°C and 550°C .

Composition $\text{BaYb}_{0.6}\text{Sc}_{0.05}\text{B}_{0.05}\text{Ti}_{0.3}\text{O}_{2.65}$	Conductivity (S cm^{-1})	Capacitance (F cm^{-1})
at 350°C	$B = 1.32 \times 10^{-4}$	6.81×10^{-11}
	$GB = 1.86 \times 10^{-3}$	7.30×10^{-8}
at 450°C	$B = 3.68 \times 10^{-4}$	4.81×10^{-11}
	$GB = 1.01 \times 10^{-3}$	4.80×10^{-8}
at 550°C	$B = 7.00 \times 10^{-4}$	3.15×10^{-11}

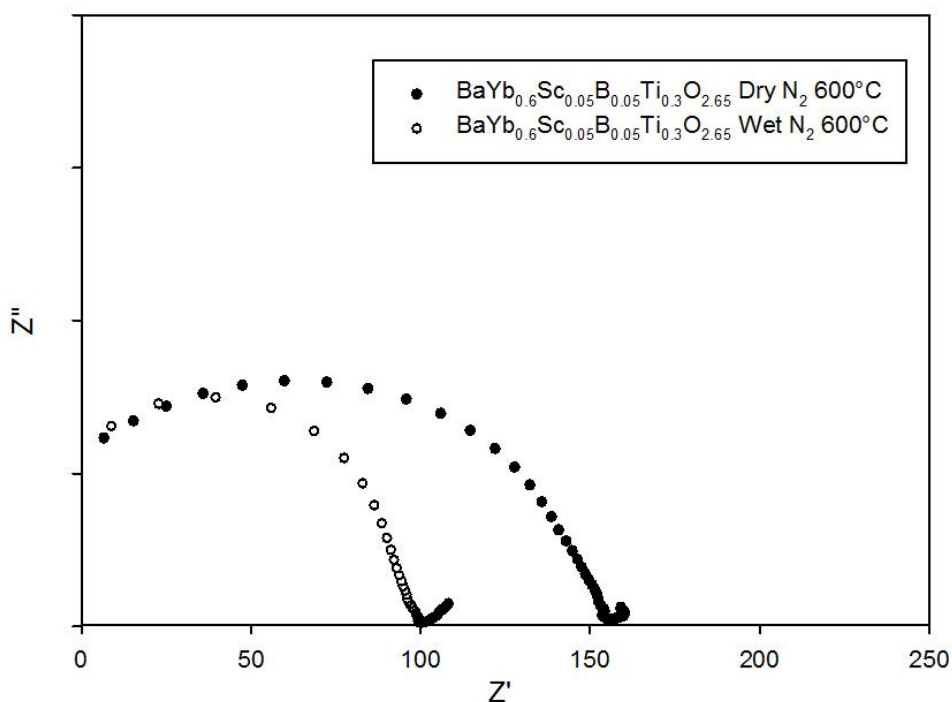


Figure 5-9 Impedance data for $\text{BaYb}_{0.6}\text{Sc}_{0.05}\text{B}_{0.05}\text{Ti}_{0.3}\text{O}_{2.65}$ at 600°C in dry and wet N_2 atmosphere, showing the reduction in the resistance for the latter, indicative of a protonic contribution to the conductivity

As an example, Figure 5-9 shows the impedance data for $\text{BaYb}_{0.6}\text{Sc}_{0.05}\text{B}_{0.05}\text{Ti}_{0.3}\text{O}_{2.65}$ in both dry and wet N_2 600°C illustrating a reduction in the total resistance for the latter, which is indicative of a protonic contribution to the conductivity.

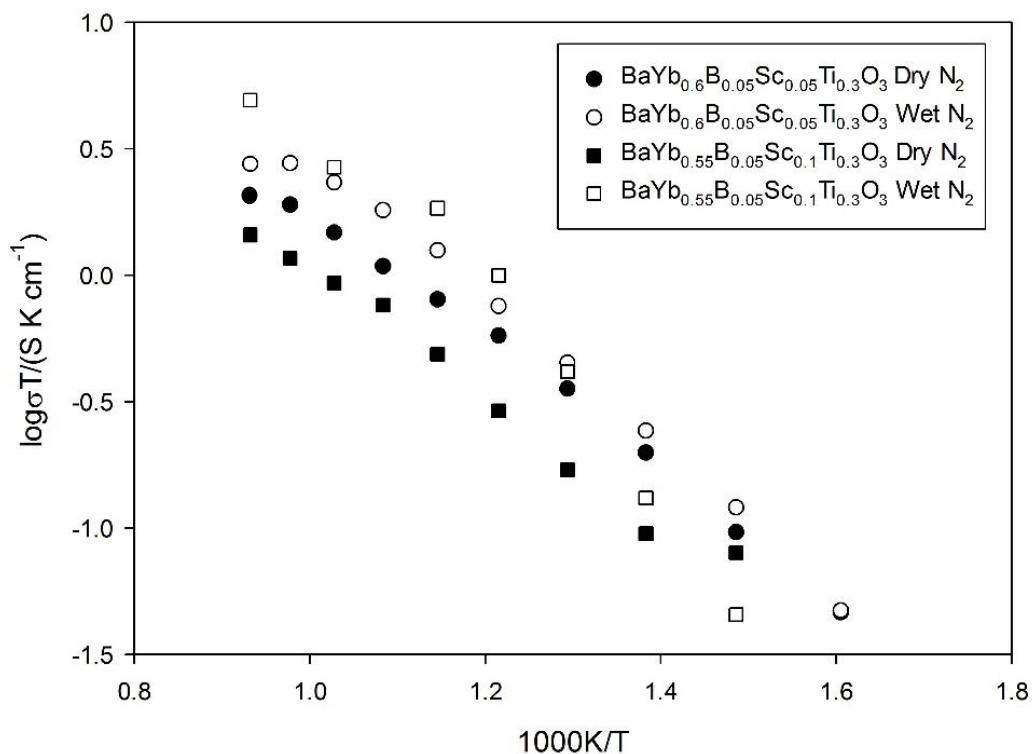


Figure 5-10 Conductivity data for $\text{BaYb}_{0.6}\text{Sc}_{0.05}\text{B}_{0.05}\text{Ti}_{0.3}\text{O}_{3-\delta}$ in dry N_2 (black Circle), wet N_2 (white circle), and $\text{BaYb}_{0.55}\text{Sc}_{0.1}\text{B}_{0.05}\text{Ti}_{0.3}\text{O}_{3-\delta}$ dry N_2 (black square) and wet N_2 (white square).

Figure 5-10 show the total conductivity data versus $1000\text{K}/T$ for $\text{BaYb}_{0.6}\text{Sc}_{0.05}\text{B}_{0.05}\text{Ti}_{0.3}\text{O}_{2.65}$ and $\text{BaYb}_{0.55}\text{Sc}_{0.1}\text{B}_{0.05}\text{Ti}_{0.3}\text{O}_{2.65}$ in dry and wet N_2 , with Figure 5-11 showing the same conductivity data for $\text{BaYb}_{0.45}\text{Sc}_{0.2}\text{B}_{0.05}\text{Ti}_{0.3}\text{O}_{2.65}$ and $\text{BaYb}_{0.35}\text{Sc}_{0.3}\text{B}_{0.05}\text{Ti}_{0.3}\text{O}_{2.65}$. Both figures show that there is an improvement in the conductivity in wet N_2 for the samples containing lower amounts of scandium across the range. This shows that there is a significant protonic contribution to the conductivity for these samples, consistent with the higher water incorporations. However for the highest scandium content sample $\text{BaYb}_{0.35}\text{Sc}_{0.3}\text{B}_{0.05}\text{Ti}_{0.3}\text{O}_{2.65}$ similar conductivities were observed in both dry and wet N_2

atmospheres, suggesting a reduction in the relative contribution of the proton conductivity on increasing Sc content.

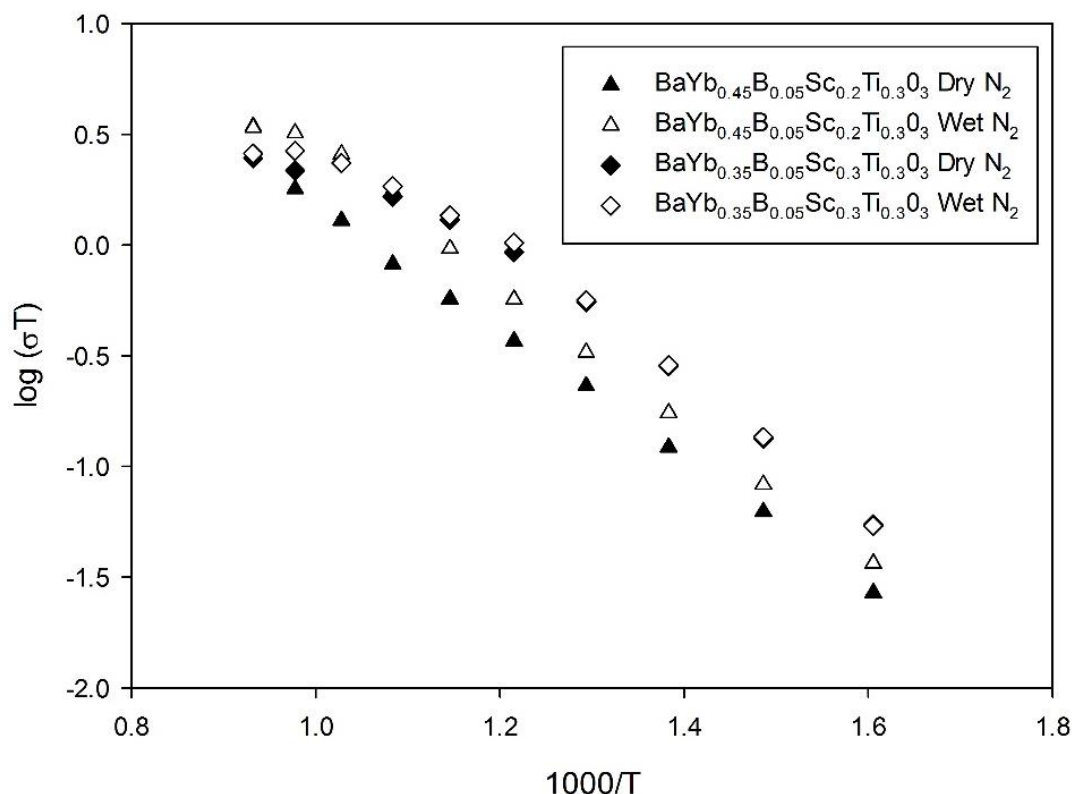


Figure 5-11 Conductivity data for BaYb_{0.45}Sc_{0.2}B_{0.05}Ti_{0.3}O_{3-δ} in dry N₂ (black triangle), wet N₂ (white triangle), and BaYb_{0.35}Sc_{0.3}B_{0.05}Ti_{0.3}O_{3-δ} dry N₂ (black diamond) and wet N₂ (white diamond).

For each sample, the total conductivities at 500°C and 800°C are given below in Table 5-6.

The conductivity values in a dry atmosphere are similar to the values reported for other doped Ba₂Sc₂O₅ perovskites. However, they are close to an order of magnitude lower than these literature systems in wet atmosphere i.e. BaSc_{0.8}P_{0.2}O_{2.7} ($\sigma_{500^\circ\text{C}} = 2.3 \times 10^{-3} \text{ S cm}^{-1}$) and BaSc_{0.7}Ti_{0.3}O_{2.7} ($\sigma_{600^\circ\text{C}} = 2.5 \times 10^{-3} \text{ S cm}^{-1}$).^{181,184}. This may be due to an increased level of proton trapping in BaYb_{0.7-x}Sc_xB_{0.05}Ti_{0.3}O_{2.65} ($x = 0.05, 0.1, 0.2, 0.3$). In this respect preliminary studies within the group on B doping in BaSc_{1-x}P_xO_{2.5+x} samples have also shown a reduction in the total conductivities, which coupled with the results here, may indicate

that defect trapping around the borate group is an issue, but this needs further investigation.¹⁸⁹

Table 5-6 Total conductivity data for $\text{BaYb}_{0.7-x}\text{Sc}_x\text{B}_{0.05}\text{Ti}_{0.3}\text{O}_{3-\delta}$ ($x = 0.05, 0.1, 0.2, 0.3$) in dry and wet N_2 atmospheres at 500°C and 800°C

Sample (nominal composition)	Conductivity (S cm^{-1})			
	500 °C		800 °C	
	Dry N_2	Wet N_2	Dry N_2	Wet N_2
$\text{BaYb}_{0.6}\text{Sc}_{0.05}\text{B}_{0.05}\text{Ti}_{0.3}\text{O}_{3-\delta}$	4.61×10^{-4}	5.85×10^{-4}	1.93×10^{-3}	2.57×10^{-3}
$\text{BaYb}_{0.55}\text{Sc}_{0.1}\text{B}_{0.05}\text{Ti}_{0.3}\text{O}_{3-\delta}$	2.20×10^{-4}	5.37×10^{-4}	1.35×10^{-3}	4.59×10^{-3}
$\text{BaYb}_{0.45}\text{Sc}_{0.2}\text{B}_{0.05}\text{Ti}_{0.3}\text{O}_{3-\delta}$	2.99×10^{-4}	4.24×10^{-4}	3.20×10^{-3}	3.16×10^{-3}
$\text{BaYb}_{0.35}\text{Sc}_{0.3}\text{B}_{0.05}\text{Ti}_{0.3}\text{O}_{3-\delta}$	7.16×10^{-4}	7.30×10^{-4}	2.30×10^{-3}	2.41×10^{-3}

Thus these samples show promising results in terms of CO_2 stability, although the total conductivities were lower than ideal, although it should be noted that they are comparable to a number of other highly researched CO_2 stable proton conductors such as $\text{Sr}^{2+}/\text{Ca}^{2+}$ doped lanthanum niobates.^{69, 81, 190}

5.7 Synthesis and characterisation of $\text{BaYb}_{0.6-z}\text{Fe}_z\text{B}_{0.05}\text{Ti}_{0.3}\text{O}_{3-\delta}$ ($z = 0.05, 0.1, 0.2$)

The above results show that it was possible to replace most of the scandium with ytterbium, boron and titanium, however small amounts of scandium (0.05) were still required to produce the pure cubic perovskite phase. Moreover while these phases showed enhanced CO_2 stability and good densification on sintering, the conductivity values were lower than ideal for electrolyte applications. Consequently an attempt was made to replace the scandium with iron.

5.7.1 XRD analysis of $\text{BaYb}_{0.6-z}\text{Fe}_z\text{B}_{0.05}\text{Ti}_{0.3}\text{O}_{3-\delta}$ ($z = 0.05, 0.1, 0.2$)

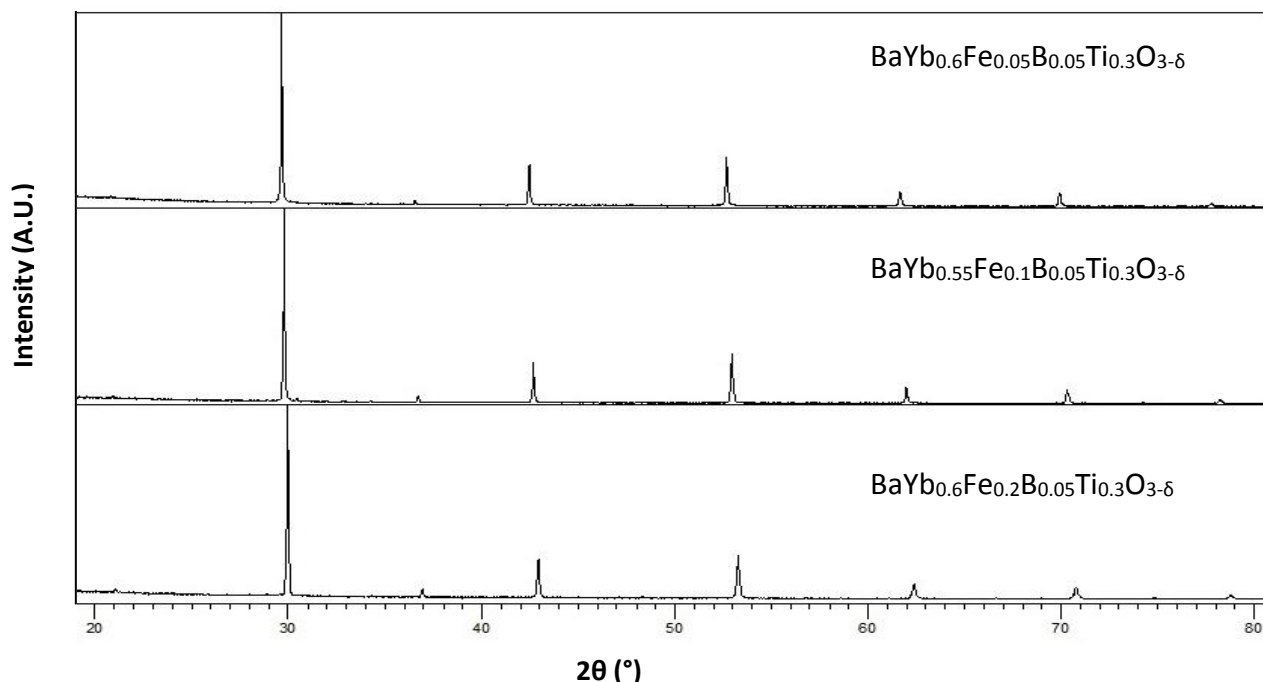


Figure 5-12 XRD patterns for $\text{BaYb}_{0.6}\text{Fe}_{0.05}\text{B}_{0.05}\text{Ti}_{0.3}\text{O}_{3-\delta}$, $\text{BaYb}_{0.55}\text{Fe}_{0.1}\text{B}_{0.05}\text{Ti}_{0.3}\text{O}_{3-\delta}$ and $\text{BaYb}_{0.6}\text{Fe}_{0.2}\text{B}_{0.05}\text{Ti}_{0.3}\text{O}_{3-\delta}$

Table 5-7 Cell parameter data for $\text{BaYb}_{0.6-z}\text{Fe}_z\text{B}_{0.05}\text{Ti}_{0.3}\text{O}_{3-\delta}$ ($z = 0.05, 0.1, 0.2$)

Sample composition	Unit cell parameter a (Å)	Unit cell volume (Å ³)
$\text{BaYb}_{0.6}\text{Fe}_{0.05}\text{B}_{0.05}\text{Ti}_{0.3}\text{O}_{3-\delta}$	4.24819(5)	76.668 (3)
$\text{BaYb}_{0.55}\text{Fe}_{0.1}\text{B}_{0.05}\text{Ti}_{0.3}\text{O}_{3-\delta}$	4.22526(5)	75.43(3)
$\text{BaYb}_{0.45}\text{Fe}_{0.2}\text{B}_{0.05}\text{Ti}_{0.3}\text{O}_{3-\delta}$	4.20127(6)	74.155(3)

The use of small levels of Fe to replace Sc was investigated due to its previous successful use in other ionic conducting electrolytes, as both a dopant and a sintering aid to encourage grain growth. A lower sintering temperature (1350°C) was required in these systems and a pure cubic perovskite was observed up to 20% ($z = 0.2$) iron doping; for Fe contents >0.2 barium ferrite impurities resulted. Figure 5-12 and Table 5-7 shows the X-ray diffraction patterns and cell parameters for these $\text{BaYb}_{0.6-z}\text{Fe}_z\text{B}_{0.05}\text{Ti}_{0.3}\text{O}_{3-\delta}$ ($z = 0.05, 0.1$, and 0.2) samples. The data show a decrease in cell parameters on increasing iron content consistent with the smaller size of $\text{Fe}^{3+/4+}$ (0.645/ 0.585 Å) versus Yb^{3+} (0.868 Å).

5.7.2 Conductivity measurements

The sintered pellets of $\text{BaYb}_{0.6}\text{Fe}_{0.05}\text{B}_{0.05}\text{Ti}_{0.3}\text{O}_{3-\delta}$ and $\text{BaYb}_{0.55}\text{Fe}_{0.1}\text{B}_{0.05}\text{Ti}_{0.3}\text{O}_{3-\delta}$ were analysed using SEM before the conductivity measurements were made. The SEM data were recorded at the University of Malaga by Dr Jose M. Porras-Vazquez. The results (Table 5-8 and Figure 5-13) showed that the effect of Fe doping on the density is complex; in particular, the lowest Fe content sample $\text{BaYb}_{0.6}\text{Fe}_{0.05}\text{B}_{0.05}\text{Ti}_{0.3}\text{O}_{3-\delta}$ shows a very dense pellet with the density decreasing for the higher Fe contents. The origin of this requires further study but overall it appears as if the lowest Fe content sample is the most promising.

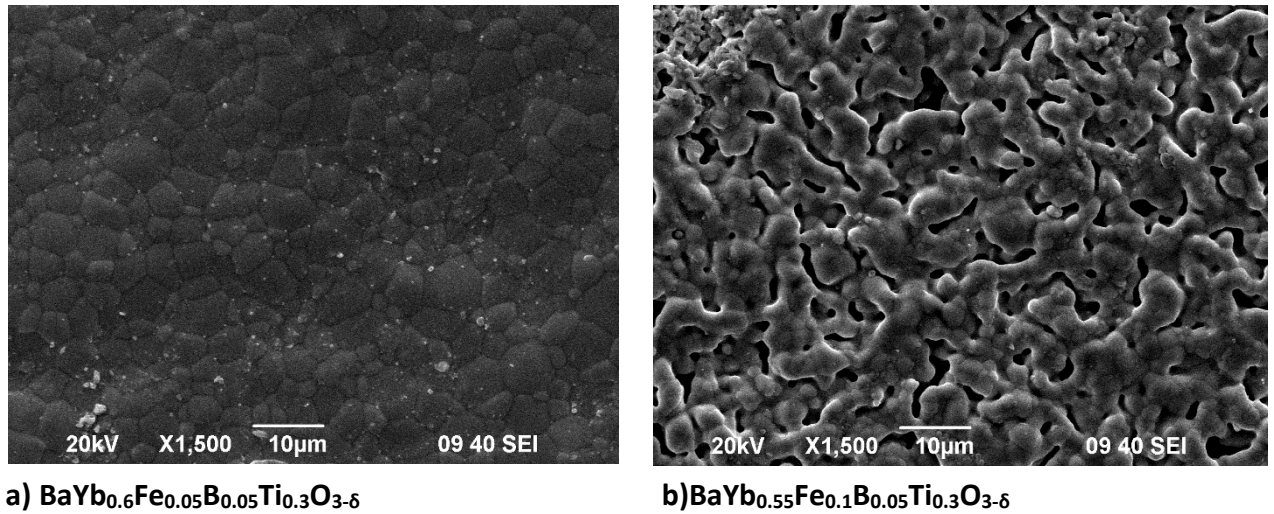


Figure 5-13 Scanning electron microscopy images of a) $\text{BaYb}_{0.6}\text{Fe}_{0.05}\text{B}_{0.05}\text{Ti}_{0.3}\text{O}_{3-\delta}$ and b) $\text{BaYb}_{0.55}\text{Fe}_{0.1}\text{B}_{0.05}\text{Ti}_{0.3}\text{O}_{3-\delta}$

Table 5-8 % Theoretical density of $\text{BaYb}_{0.6-z}\text{Fe}_z\text{B}_{0.05}\text{Ti}_{0.3}\text{O}_{3-\delta}$ $z = 0.05, 0.1$, and 0.2 pellets.

Sample composition	% Theoretical density
$\text{BaYb}_{0.6}\text{Fe}_{0.05}\text{B}_{0.05}\text{Ti}_{0.3}\text{O}_{3-\delta}$	97
$\text{BaYb}_{0.55}\text{Fe}_{0.1}\text{B}_{0.05}\text{Ti}_{0.3}\text{O}_{3-\delta}$	76
$\text{BaYb}_{0.45}\text{Fe}_{0.2}\text{B}_{0.05}\text{Ti}_{0.3}\text{O}_{3-\delta}$	85

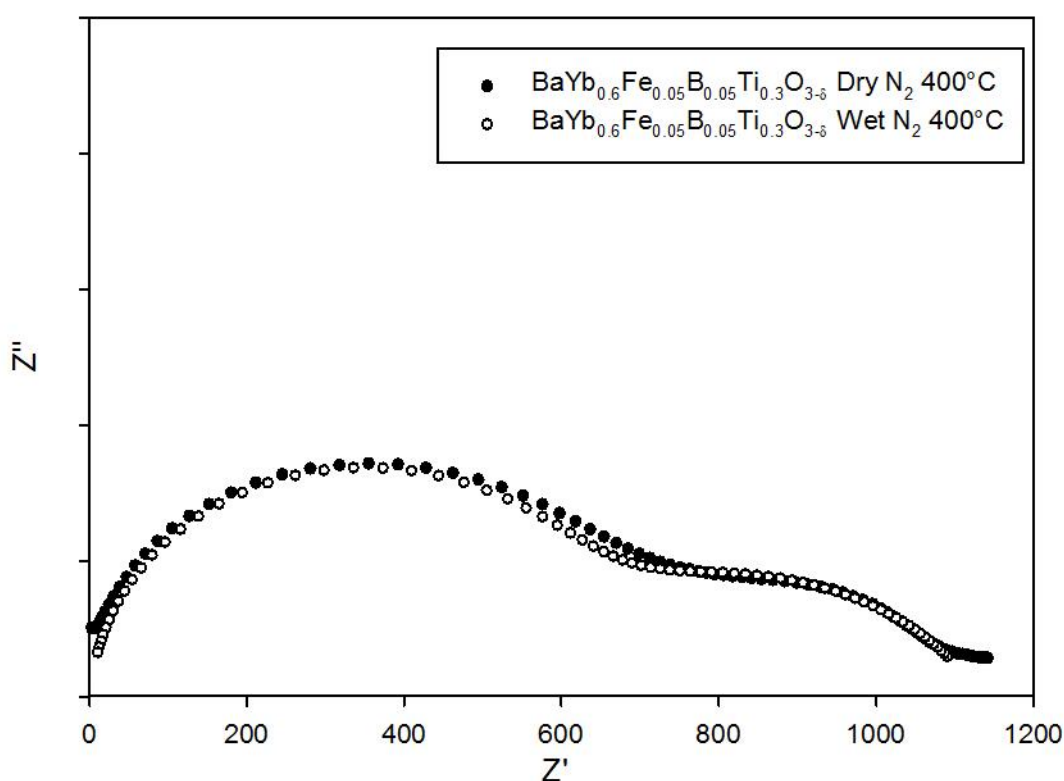


Figure 5-14 Impedance data for $\text{BaYb}_{0.6}\text{Fe}_{0.05}\text{B}_{0.05}\text{Ti}_{0.3}\text{O}_{2.65}$ at 400°C in dry and wet N_2 atmosphere, showing similar resistance for both bulk and grain components.

Figure 5-14 shows a Nyquist plot of $\text{BaYb}_{0.6}\text{Fe}_{0.05}\text{B}_{0.05}\text{Ti}_{0.3}\text{O}_{3-\delta}$ in dry and wet conditions at 400°C; similar conductivities were observed in both atmospheres suggesting that the protonic contribution did not exceed other contributions to the conductivity. The conductivity reduces further on increasing iron content, in both the dry and wet conditions, (shown in Table 5-9) and this may be related to the drop in density and the increase in porosity observed.

The complete conductivity measurements are shown in Figure 5-15 for $\text{BaYb}_{0.6-z}\text{Fe}_z\text{B}_{0.05}\text{Ti}_{0.3}\text{O}_{3-\delta}$ ($z = 0.05, 0.1, 0.2$), in both dry and wet N_2 atmospheres, and the conductivities are of similar magnitudes to $\text{BaYb}_{0.7-x}\text{Sc}_x\text{B}_{0.05}\text{Ti}_{0.3}\text{O}_{3-\delta}$ ($x = 0.05, 0.1, 0.2, 0.3$) under the same conditions. An interesting observation is that, especially for the higher Fe content samples, there is a decrease in conductivity in wet N_2 compared to dry N_2 . This is

indicative of the presence of a significant p- type contribution to the conductivity. This is consistent with water incorporating partially full vacant site and thus suppressing the oxygen incorporation reaction (equation 5-1) and hence the hole concentration.

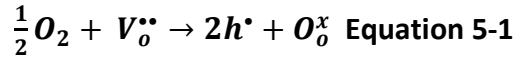


Table 5-9 Total conductivity data for BaYb_{0.6-z}Fe_zB_{0.05}Ti_{0.3}O_{3-δ} (z= 0.05, 0.1, 0.2) in dry and wet N₂ atmospheres at 500°C and 800°C

Sample (nominal composition)	Conductivity (S cm ⁻¹)			
	500 °C		800 °C	
	Dry N ₂	Wet N ₂	Dry N ₂	Wet N ₂
BaYb _{0.6} Fe _{0.05} B _{0.05} Ti _{0.3} O _{3-δ}	4.21x10 ⁻⁴	4.68x10 ⁻⁴	1.90x10 ⁻³	1.61x10 ⁻³
BaYb _{0.55} Fe _{0.1} B _{0.05} Ti _{0.3} O _{3-δ}	4.73x10 ⁻⁴	4.61x10 ⁻⁴	1.49x10 ⁻³	9.93x10 ⁻⁴
BaYb _{0.45} Fe _{0.2} B _{0.05} Ti _{0.3} O _{3-δ}	2.67x10 ⁻⁴	2.42x10 ⁻⁴	2.68x10 ⁻³	1.53x10 ⁻³

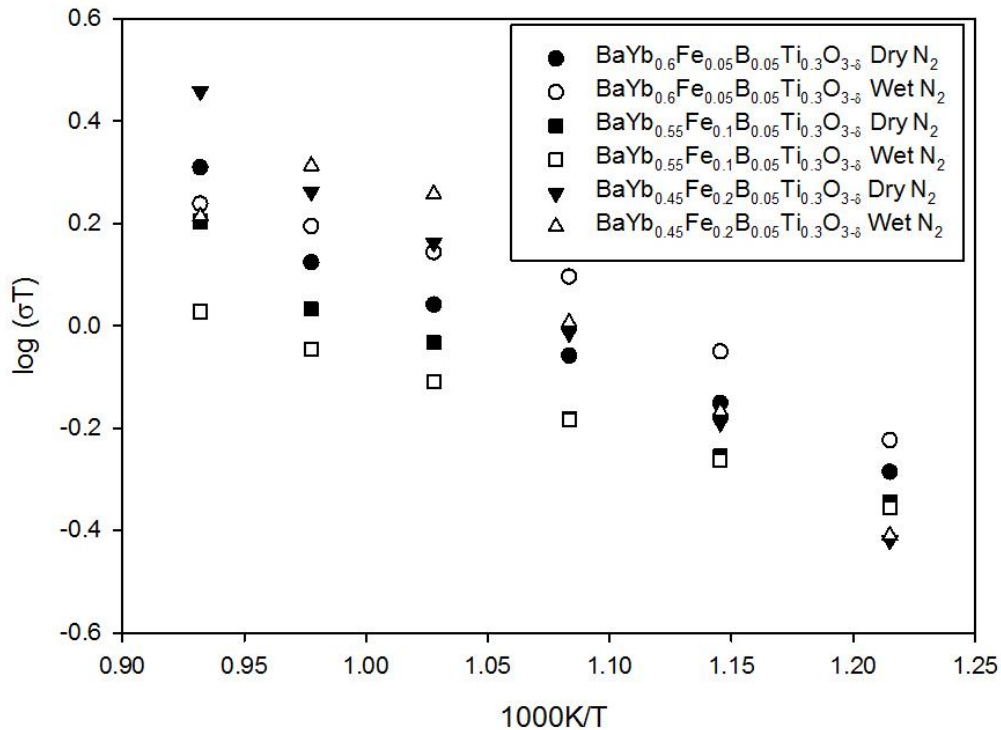


Figure 5-15 Conductivity data for BaYb_{0.6}Fe_{0.05}B_{0.05}Ti_{0.3}O_{3-δ} in dry N₂ (black circle), wet N₂ (white circle), BaYb_{0.55}Fe_{0.1}B_{0.05}Ti_{0.3}O_{3-δ} dry N₂ (black square) and wet N₂ (white square) and BaYb_{0.45}Fe_{0.2}B_{0.05}Ti_{0.3}O_{3-δ} dry N₂ (black triangle) and wet N₂ (white triangle).

5.8 Conclusion

While prior studies have examined Ti doped $\text{Ba}_2\text{Sc}_2\text{O}_5$, the results here shows that it is possible to replace most of the scandium with ytterbium whilst co-doping with boron.^{183,184}

The boron is required to prepare pure samples of these heavily ytterbium doped phases, and leads to improved sintering. These $\text{BaYb}_{0.7-x}\text{Sc}_x\text{B}_{0.05}\text{Ti}_{0.3}\text{O}_{2.65}$ ($x = 0.05, 0.1, 0.2, 0.3$) samples show good thermal stability above 1000°C and stability in CO_2 atmospheres.

However the conductivities are significantly lower when compared to other scandium based perovskites, e.g. $\text{BaSc}_{0.8}\text{P}_{0.2}\text{O}_{2.7}$ $\sigma_{500} = 5.9 \times 10^{-3} \text{ S cm}^{-1}$ and $\text{BaSc}_{0.7}\text{Ti}_{0.3}\text{O}_{2.7}$ $\sigma_{600^\circ\text{C}} = 2.5 \times 10^{-3} \text{ S cm}^{-1}$ in wet N_2 atmospheres.^{183, 184} This may be due to partial defect trapping, perhaps related to the borate group. The conductivity is however better than many other proposed CO_2 stable proton conductors such as Ca^{2+} doped LaNbO_4 (0.001 S cm^{-1} at 800°C)^{81, 82} or Sr^{2+} doped LaPO_4 ($3 \times 10^{-4} \text{ S cm}^{-1}$ at 900°C) in a wet atmosphere.^{77, 191}

Furthermore, the complete replacement of scandium was also possible through further doping with iron. Phase pure $\text{BaYb}_{0.6-z}\text{Fe}_z\text{B}_{0.05}\text{Ti}_{0.3}\text{O}_{3-\delta}$ samples were prepared for $z = 0.05, 0.1, 0.2$. While the lowest iron content sample ($z = 0.05$) showed excellent sinterability, increasing the iron content further appeared to have a detrimental effect on the sintering, although the origin of this is at present unclear.

Overall, the data shows that by the introduction of suitable dopants the replacement of scandium in “ Ba_2ScO_5 ” can be achieved to form cubic perovskites, improving the sintering and stability. However, with respect to the conductivity for fuel cell applications the lower total conductivities observed suggest that further work is needed to optimise them and understand the origin of the observed conductivity decrease relative to high scandium content systems.

Chapter 6

6 Synthesis and characterization of phosphate doped Ba(Y/Yb/Tm)_yO_{3-δ}

6.1 Introduction

In the previous chapter, the effect of doping with the boron and other lower cost metals ytterbium and titanium was shown to stabilise the cubic phase of the scandium system Ba₂Sc₂O₅. The phase had increased densification, stability in CO₂ and was stable above a 1000°C allowing it to be sintered for fuel cell electrolyte applications. However, unsatisfactory conductivity was observed and the pure cubic structure was still only stable if some scandium was present.

Previous doping within the group of oxyanions (MO₄ⁿ⁻; M = Si, P, S,) has been shown to enhance the oxide ion conductivity in perovskite systems containing high levels of oxide ion vacancies, i.e. Ba₂(In/Sc)₂O₅ (Si, P S of the MO₄ⁿ⁻ group resides on the B cation site in the perovskite). The surrounding oxide ions would fill only 4 of the available 6 oxide ion positions around the B site (displaced so as to achieve tetrahedral co-ordination). In addition to this, oxyanion doping has been shown to enhance the CO₂ stability of the doped Ba₂(In/Sc)₂O₅ systems, which is attributed to the introduction of these acidic dopants reducing the basicity of the system.^{186,187,192,193} These oxyanion dopants have also been shown to be able to be accommodated into a range of other perovskites, both electrolyte and electrode systems, showing that the perovskite structure is amenable to their incorporation.^{140,194-197}

Another perovskite system that has attracted considerable interest from the research community is rare earth doped BaPrO₃.^{198,199,200,201} This material was initially proposed as a proton conducting electrolyte by Fukui et al.²⁰² Subsequent work, however, indicated that the conductivity in this system was p-type rather than proton conductivity.¹⁹⁸ Furthermore, issues have been raised regarding the instability of BaPrO₃ in CO₂ containing environments.^{203,204} A range of further studies have been performed on this system, examining the effect of different rare earth dopants on the conductivity and cell symmetry. However prior studies have focused on low levels of rare earth (Ln) dopants, i.e. BaPr_{1-x}Ln_xO_{3-y} (x≤0.2).

In this chapter, these two areas have been combined, while previous studies within our group focused on doping with oxyanion on to the scandates and the indates (Felix et al.).^{192,195} This work removes the scandium and the indium all together, instead focusing on praseodymium. The aim was to investigate the BaPrO₃ system, with a view to co-dope with phosphate and different rare earths (Y³⁺, Yb³⁺, Tm³⁺), so as to allow us to reduce the praseodymium content and therefore reduce the high electronic conductivity. In addition this strategy was expected to improve the CO₂ stability and so reintroduce the possibility of using this system as a proton conducting electrolyte. Later this work was extended to include the complete replacement of praseodymium with the phosphate and the rare earths i.e. yttrium, ytterbium and thulium.

6.2 Experimental

High purity BaCO₃, Pr₆O₁₁, Y₂O₃, Yb₂O₃, Tm₂O₃ and NH₄H₂PO₄ were used to prepare the praseodymium containing samples BaPr_{0.25}(Y/Yb/Tm)_{0.5}P_{0.25}O_{3-y} and BaPr_{0.75}P_{0.25}O_{3-y} as well as the non-containing samples Ba(Y/Yb/Tm)_{0.75}P_{0.25}O_{3-y}. A small (5%) excess of BaCO₃ was

employed to produce the $\text{BaPr}_{0.25}(\text{Y/Yb/Tm})_{0.5}\text{P}_{0.25}\text{O}_{3-y}$ samples, this was done so as to try to counteract barium loss at elevated temperatures, and so eliminate barium deficient impurity phases such as $\text{Ba}_3(\text{Y/Yb/Tm})_4\text{O}_9$. Which have been seen in other studies synthesising similar barium containing phases.^{186,187} For the samples without praseodymium ($\text{Ba}(\text{Y/Yb/Tm})_{0.75}\text{P}_{0.25}\text{O}_{3-y}$), and without additional rare earths ($\text{BaPr}_{0.75}\text{P}_{0.25}\text{O}_{3-y}$); higher BaCO_3 excess (10%) was required to overcome Ba loss and hence limit the formation of Ba deficient impurities. In these particular cases, even with this higher level of Ba excess, such impurities could not be completely eliminated. In each case, a pre-drying stage was performed on the starting materials if required, and the powders were intimately ground and heated initially to 1000°C for 12 hours. They were then ball-milled (350 rpm for 1 hour, Fritsch Pulverisette 7 Planetary Mill) and reheated to 1300°C-1400°C for 12-24 hours (with intermediate regrind). The resulting powders were then ball-milled (350 rpm for 1 hour, Fritsch Pulverisette 7 Planetary Mill) a second time and pressed as pellets (1.3 cm diameter) and sintered at 1500°C for 4 hours. The pellets were covered in sample powder and the crucible was covered with a lid to limit the amount of Ba loss during the synthesis/sintering processes. The $\text{Ba}(\text{Y/Yb/Tm})_{0.75}\text{P}_{0.25}\text{O}_{3-y}$ densities ranged from 77%/78%/81% respectively.

Powder X-ray diffraction (Bruker D8 diffractometer with $\text{Cu K}\alpha_1$ radiation) was used to demonstrate phase purity as well as for cell parameter determination performed through GSAS.¹¹⁸

Raman spectroscopy measurements were made in order to provide evidence for the successful incorporation of phosphate. These measurements utilised a Renishaw in Via Raman microscope with excitation using a Cobolt Samba CW 532 nm DPSS Laser.

Conductivity measurements were performed on the $\text{BaPr}_{0.25}(\text{Y/Yb/Tm})_{0.5}\text{P}_{0.25}\text{O}_{3-y}$ samples and $\text{Ba}(\text{Yb/Tm})_{0.75}\text{P}_{0.25}\text{O}_{2.75}$ samples. The sintered pellets (77-81% density) were coated on each side with Pt paste, and Pt electrodes were attached, and then heated to 800°C in air for 1 hour to ensure bonding to the pellet. Conductivities were then determined by AC impedance measurements (PSM 1735 N4L interface impedance analyser) over the frequency range of 1Hz to 13 MHz. Measurements, when possible, were performed in dry N_2/O_2 and wet N_2/O_2 (in which the gas was bubbled at room temperature through water) to identify any protonic contribution to the conductivity, and to determine if there was a p-type electronic contribution to the conductivity. The impedance spectra typically showed a single broad semicircle, corresponding to overlapping of bulk and grain boundary components, and so it was not possible to accurately extract individual bulk and grain boundary contributions. The total resistance was determined by the high intercept of this semicircle based on the nonlinear least square fitting software Z-view.¹⁴³

The water contents of hydrated samples were determined from thermogravimetric analysis (Netzsch STA 449 F1 Jupiter Thermal Analyser). Samples were heated at 10°C min⁻¹ to 1000°C in N_2 , and the water content was determined from the observed mass loss. The CO_2 stability of samples was determined using thermogravimetric analysis (Netzsch STA 449 F1 Jupiter Thermal Analyser). Samples were heated at 10°C min⁻¹ to 1000°C in CO_2 to determine at what temperature CO_2 pick up occurred and decomposition.

6.3 Structural studies

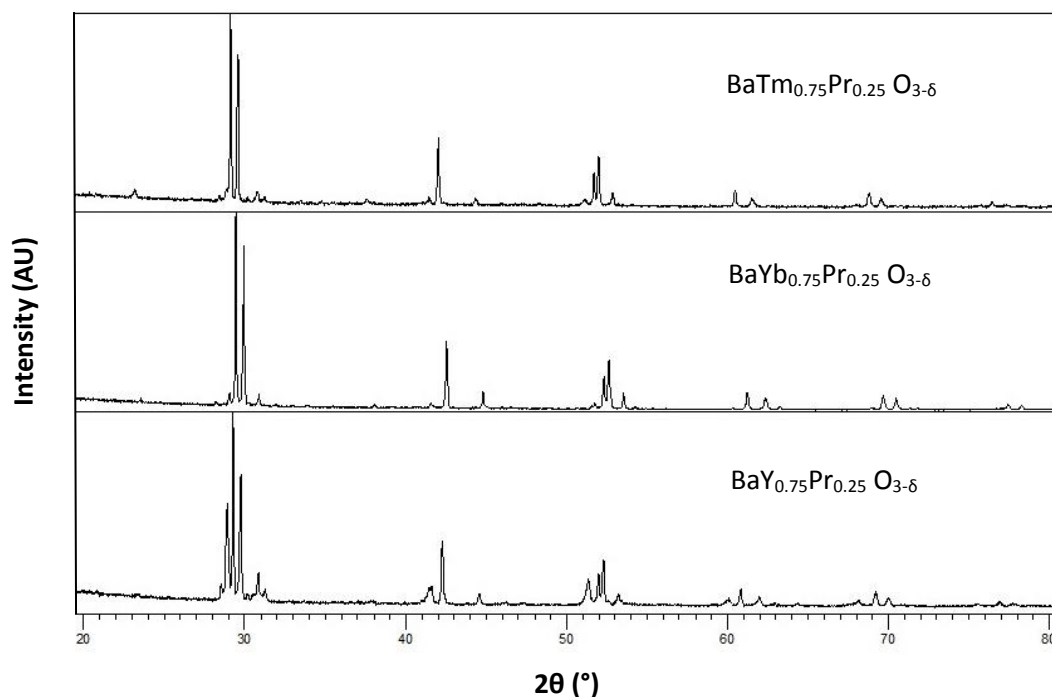


Figure 6-1 XRD patterns for $\text{BaPr}_{0.25}\text{Y}_{0.75}\text{O}_{3-\delta}$, $\text{BaPr}_{0.25}\text{Yb}_{0.75}\text{O}_{3-\delta}$ and $\text{BaPr}_{0.25}\text{Tm}_{0.75}\text{O}_{3-\delta}$

It was not possible to synthesise pure $\text{BaPr}_{1-x}(\text{Y}/\text{Yb}/\text{Tm})_x\text{O}_{3-y}$ samples with the high levels ($\geq 50\%$) of Y/Yb/Tm dopants, and co-doping with phosphate (25%) was required. Without such phosphate co-doping, large levels of impurities were seen for example $\text{Ba}_3(\text{Y}/\text{Yb}/\text{Tm})_4\text{O}_9$, this showing the importance of phosphate doping in stabilising the high Y/Yb/Tm levels (Figure 6-1). Using the phosphate co-doping it was possible to successfully synthesise single phase samples of $\text{BaPr}_{0.25}\text{Y}_{0.5}\text{P}_{0.25}\text{O}_{3-y}$, $\text{BaPr}_{0.25}\text{Yb}_{0.5}\text{P}_{0.25}\text{O}_{3-y}$ and $\text{BaPr}_{0.25}\text{Tm}_{0.5}\text{P}_{0.25}\text{O}_{3-y}$ (Figure 6-2).

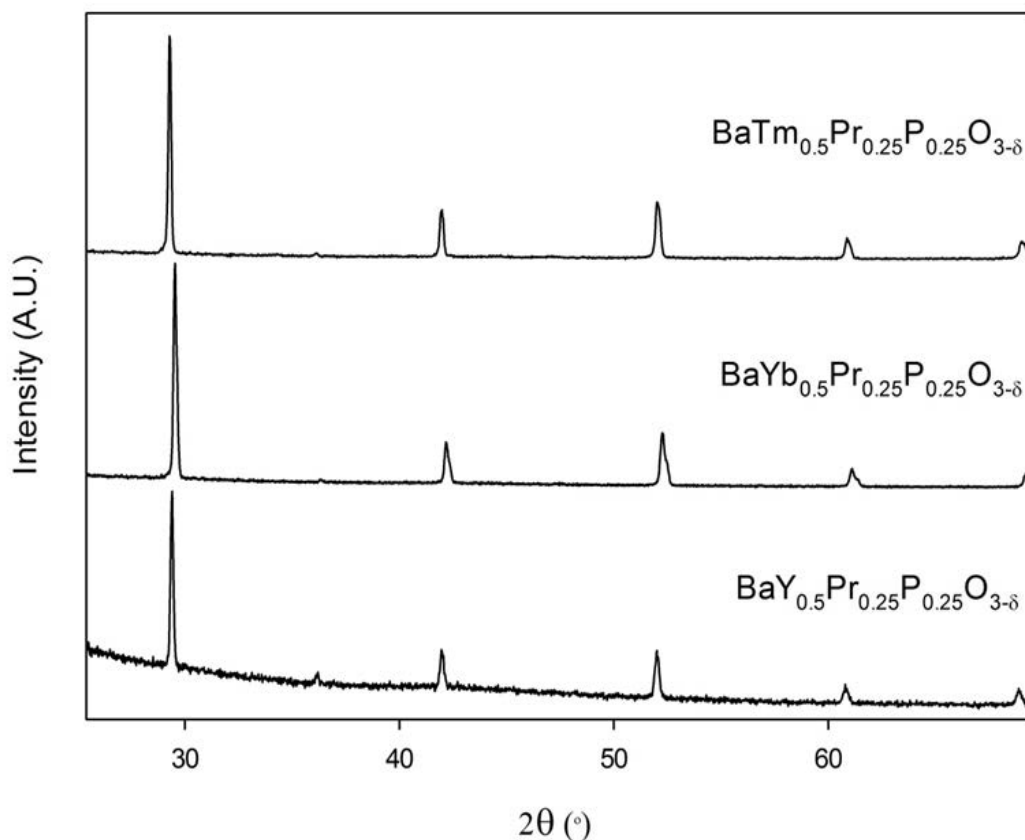


Figure 6-2 XRD patterns for $\text{BaPr}_{0.25}\text{Y}_{0.5}\text{P}_{0.25}\text{O}_{3-\delta}$, $\text{BaPr}_{0.25}\text{Yb}_{0.5}\text{P}_{0.25}\text{O}_{3-\delta}$ and $\text{BaPr}_{0.25}\text{Tm}_{0.5}\text{P}_{0.25}\text{O}_{3-\delta}$

Table 6-1 Cell parameter data for $\text{BaPr}_{0.25}(\text{Y}/\text{Yb}/\text{Tm})_{0.5}\text{P}_{0.25}\text{O}_{3-\delta}$ (cubic cell)

Sample (nominal composition)	Parameter	Unit cell
	a_0 (Å)	volume (Å ³)
$\text{BaPr}_{0.25}\text{Y}_{0.5}\text{P}_{0.25}\text{O}_{3-\delta}$	4.307(1)	79.89(5)
$\text{BaPr}_{0.25}\text{Yb}_{0.5}\text{P}_{0.25}\text{O}_{3-\delta}$	4.283(1)	78.61(4)
$\text{BaPr}_{0.25}\text{Tm}_{0.5}\text{P}_{0.25}\text{O}_{3-\delta}$	4.2891(3)	78.90(1)

Once these phases were pure an attempt to prepare phases with the total replacement of Pr was tried i.e. $\text{Ba}(\text{Y}/\text{Yb}/\text{Tm})_{0.75}\text{P}_{0.25}\text{O}_{2.75}$. While the formation of a perovskite phase was observed, it has so far not been possible to prepare these particular samples without the

presence of small impurities (Figure 6-3). Whilst the addition of further excess barium reduced the minor impurity levels, it was not possible to completely eliminate them, even by increasing the initial phosphate content.

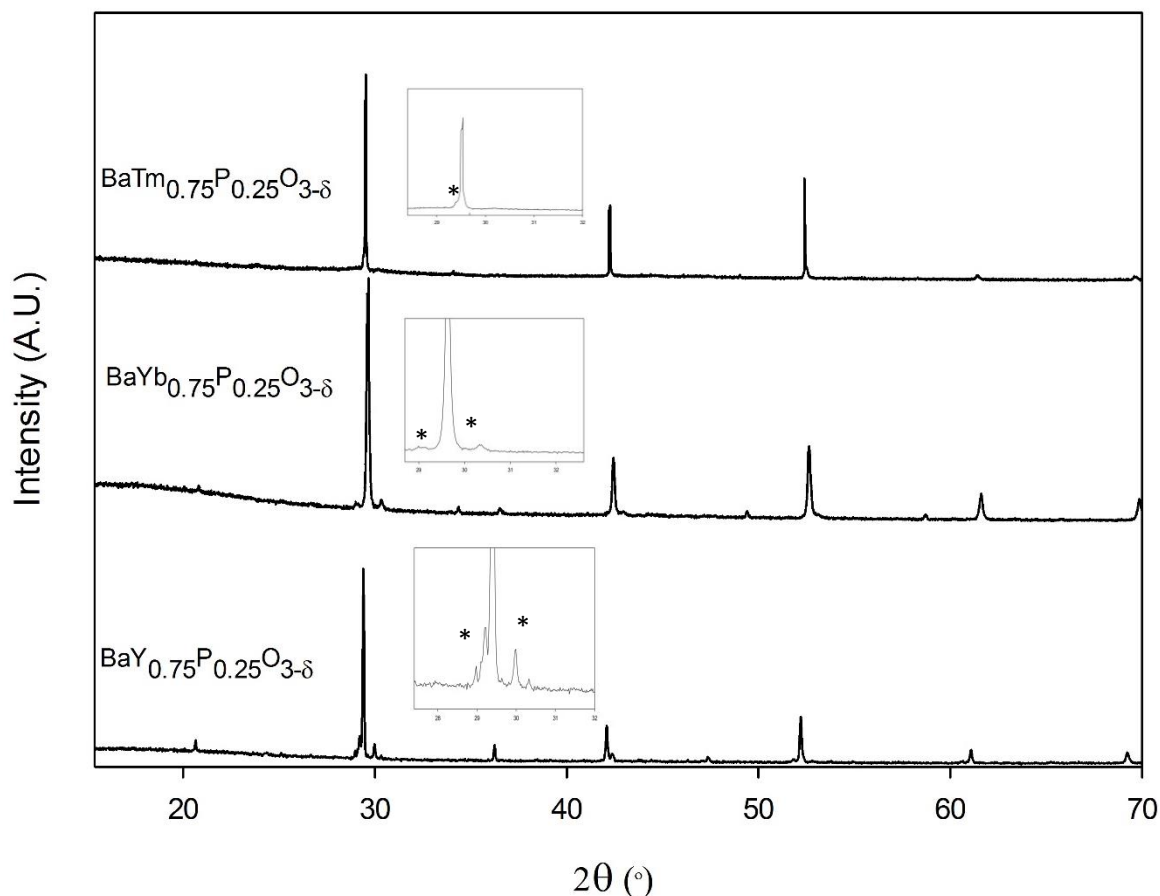


Figure 6-3 XRD patterns for $\text{BaY}_{0.75}\text{P}_{0.25}\text{O}_{2.75}$, $\text{BaYb}_{0.75}\text{P}_{0.25}\text{O}_{2.75}$ and $\text{BaTm}_{0.75}\text{P}_{0.25}\text{O}_{2.75}$

Table 6-2 Cell parameter data for impure $\text{Ba}(\text{Y}/\text{Yb}/\text{Tm})_{0.75}\text{P}_{0.25}\text{O}_{3-\delta}$ (cubic cell)

Sample		
(nominal composition)	Parameter	Unit cell
	a_0 (Å)	volume (Å ³)
BaY _{0.75} P _{0.25} O _{2.75}	4.2819(8)	78.50(4)
BaYb _{0.75} P _{0.25} O _{2.75}	4.2547(7)	77.02(4)
BaTm _{0.75} P _{0.25} O _{2.75}	4.2571(5)	77.15(3)

From the X-ray diffraction data shown in Figure 6-2 and Figure 6-3, the cell parameters for the $\text{BaPr}_{0.25}(\text{Y/Yb/Tm})_{0.5}\text{P}_{0.25}\text{O}_{3-y}$ and $\text{Ba}(\text{Y/Yb/Tm})_{0.75}\text{P}_{0.25}\text{O}_{2.75}$ phases were determined (Table 6-1 and Table 6-2). While the parent BaPrO_3 phase and systems doped with lower levels of rare earths (<20%) have been previously shown to be orthorhombic, the higher dopants level samples reported here appear cubic. The cell parameter data shows a gradual increase in cell volume on changing the dopant from Yb^{3+} (0.868 Å) to Tm^{3+} (0.88 Å) to Y^{3+} (0.9 Å), which can be related to the increase in the ionic radius of the dopant. Somewhat, surprisingly the cell volumes of the $\text{Ba}(\text{Y/Yb/Tm})_{0.75}\text{P}_{0.25}\text{O}_{2.75}$ samples were smaller than the corresponding $\text{BaPr}_{0.25}(\text{Y/Yb/Tm})_{0.5}\text{P}_{0.25}\text{O}_{3-y}$ samples. Knee et al. reported a similar reduction in cell volume on doping 10% Y^{3+} into BaPrO_3 .¹⁹⁸ Such reductions in cell parameters contradicts what might be expected from the complete replacement of Pr^{4+} (0.85 Å) by $\text{Y}^{3+}/\text{Yb}^{3+}/\text{Yb}^{3+}$. This therefore might suggest that either there is a significant proportion of the praseodymium in the Pr^{3+} (0.99 Å) rather than Pr^{4+} oxidation state, or that there is a degree of substitution of Y/Yb/Tm on the Ba site; the latter might account for some of the difficulties in preparing single phase $\text{Ba}(\text{Y/Yb/Tm})_{0.75}\text{P}_{0.25}\text{O}_{2.75}$ samples. In this respect, further investigations are required to clarify these results.

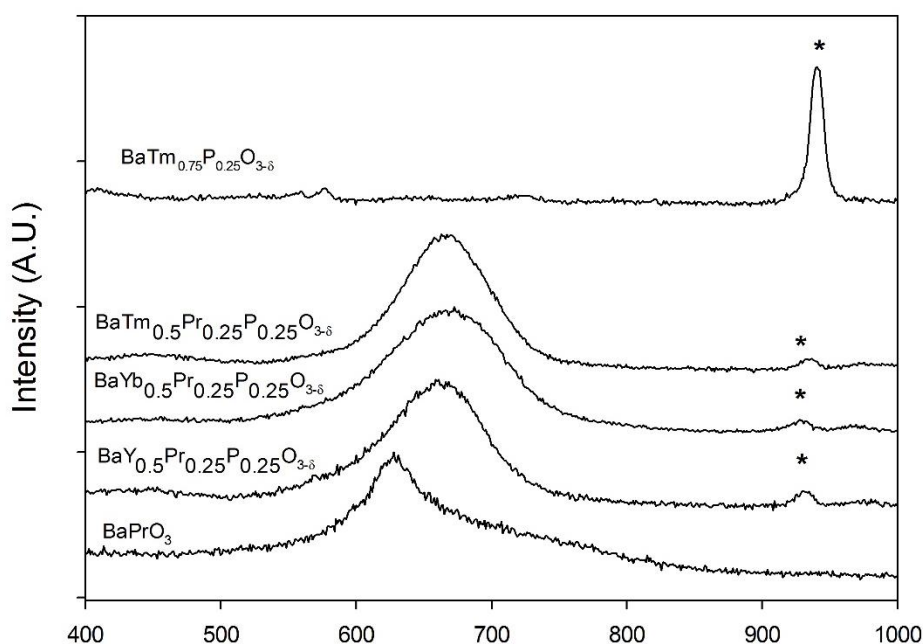


Figure 6-4 Raman spectra of BaPrO_3 , $\text{BaPr}_{0.25}\text{Y}_{0.5}\text{P}_{0.25}\text{O}_{3-\gamma}$, $\text{BaPr}_{0.25}\text{Yb}_{0.5}\text{P}_{0.25}\text{O}_{3-\gamma}$, $\text{BaPr}_{0.25}\text{Tm}_{0.5}\text{P}_{0.25}\text{O}_{3-\gamma}$ and $\text{BaTm}_{0.75}\text{P}_{0.25}\text{O}_{3-\delta}$ with peak showing the presence of phosphate indicated.

Raman data were collected for all the synthesised compositions as well as undoped BaPrO_3 .

For BaPrO_3 and $\text{BaPr}_{0.25}(\text{Y}/\text{Yb}/\text{Tm})_{0.5}\text{P}_{0.25}\text{O}_{3-\gamma}$, bands at ~ 650 and 940 cm^{-1} were observed (Figure 6-4). The broad peak at 650 cm^{-1} can be attributed to the praseodymium oxygen bonds while the peak at 940 cm^{-1} (absent from undoped BaPrO_3) correlates with the phosphate group, confirming the presence of phosphate in the samples. Since, theoretically there should be no Raman active modes for a perfectly cubic perovskite, with the exception of possible second-order effects, the appearance of these bands suggests that although the XRD data indicate that the average structure is cubic for $\text{BaPr}_{0.25}(\text{Y}/\text{Yb}/\text{Tm})_{0.5}\text{P}_{0.25}\text{O}_{3-\delta}$, there must be significant local distortions away from cubic symmetry in the doped systems. For the $\text{Ba}(\text{Y}/\text{Yb}/\text{Tm})_{0.75}\text{P}_{0.25}\text{O}_{2.75}$ samples, the Raman data only showed the presence of the phosphate peak (data for $\text{BaTm}_{0.75}\text{P}_{0.25}\text{O}_{3-\delta}$ are also shown in Figure 6-4).

6.4 Conductivity measurements

The doped systems led to lower than expected densities, considering the sintering temperature of 1500°C for four hours (Table 6-3). The conductivities of the $\text{BaPr}_{0.25}(\text{Y}/\text{Yb}/\text{Tm})_{0.5}\text{P}_{0.25}\text{O}_{3-\delta}$ samples were then investigated under both dry and wet conditions in both nitrogen and oxygen atmospheres. The conductivity data are shown in Figure 6-5, Figure 6-6 and Figure 6-7, comparing dry and wet N_2 conditions, for all of the $\text{BaPr}_{0.25}(\text{Y}/\text{Yb}/\text{Tm})_{0.5}\text{P}_{0.25}\text{O}_{3-\gamma}$ samples.

Table 6-3 Density of individual compositions pellets

Composition	Density %
$\text{BaPr}_{0.25}\text{Y}_{0.5}\text{P}_{0.25}\text{O}_{3-\delta}$	77
$\text{BaPr}_{0.25}\text{Yb}_{0.5}\text{P}_{0.25}\text{O}_{3-\delta}$	78
$\text{BaPr}_{0.25}\text{Tm}_{0.5}\text{P}_{0.25}\text{O}_{3-\delta}$	81

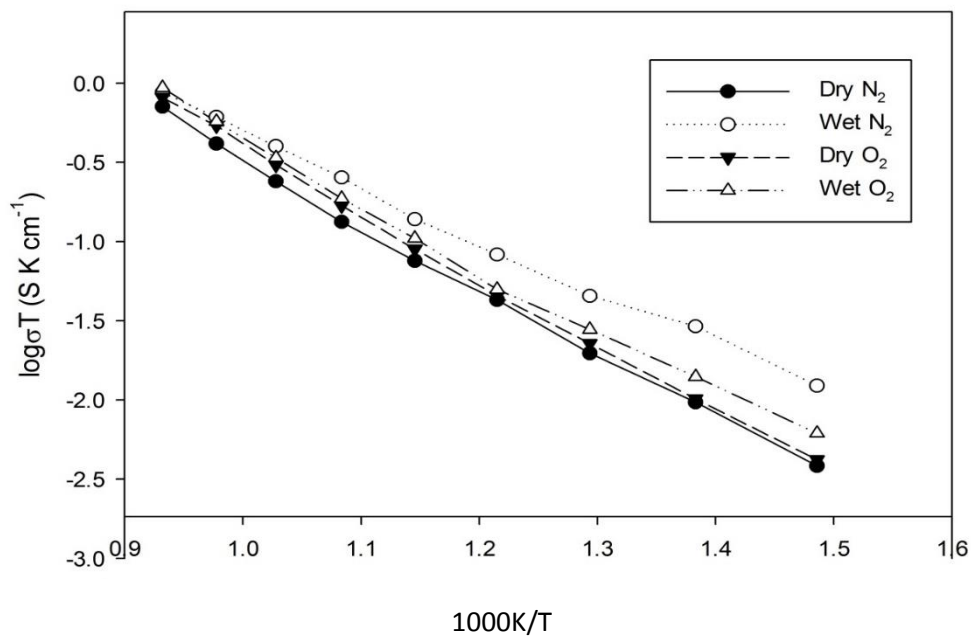


Figure 6-5 Conductivity data for $\text{BaPr}_{0.25}\text{Y}_{0.5}\text{P}_{0.25}\text{O}_{3-\gamma}$ in dry N_2 (black Circle), wet N_2 (white circle), dry O_2 (black triangle) and wet O_2 (white triangle).

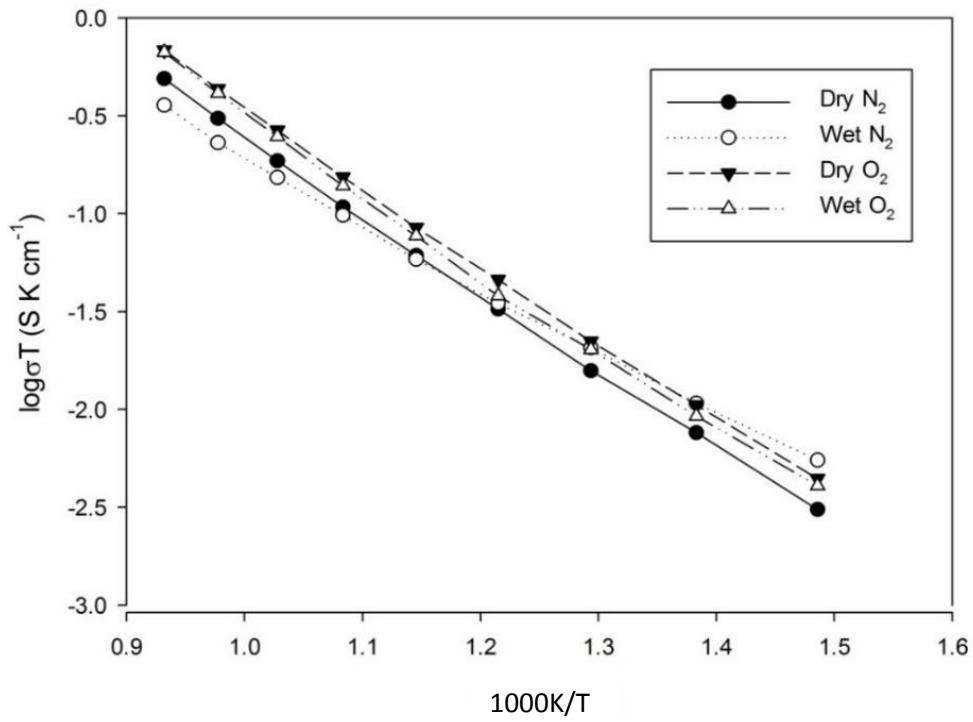


Figure 6-6 Conductivity data for $\text{BaPr}_{0.25}\text{Yb}_{0.5}\text{P}_{0.25}\text{O}_{3-y}$ in dry N_2 (black Circle), wet N_2 (white circle), dry O_2 (black triangle) and wet O_2 (white triangle).

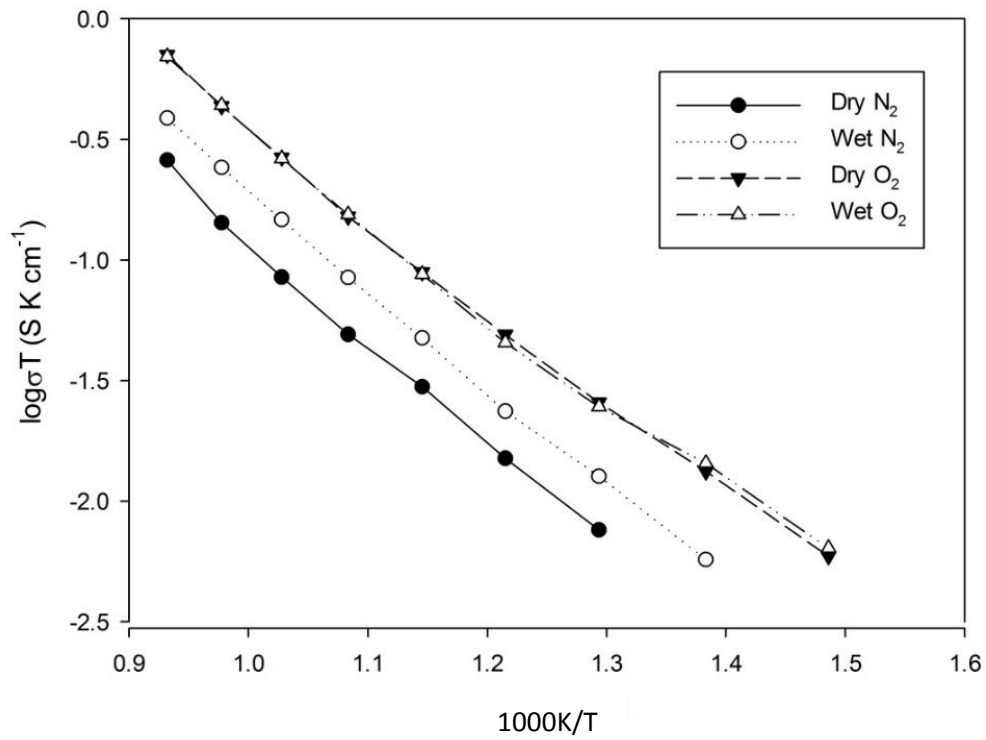


Figure 6-7 Conductivity data for $\text{BaPr}_{0.25}\text{Tm}_{0.5}\text{P}_{0.25}\text{O}_{3-y}$ in dry N_2 (black Circle), wet N_2 (white circle), dry O_2 (black triangle) and wet O_2 (white triangle).

The data shows that there is a small improvement in the conductivity in the wet N₂ atmospheres at lower temperatures, which suggests the presence of a protonic contribution, consistent with the observation of significant water incorporation. Figure 6-8 shows this difference in the dry and wet N₂ data for BaPr_{0.25}Yb_{0.5}P_{0.25}O_{3-y} at 500°C. The total conductivities for BaPr_{0.25}(Y/Yb/Tm)_{0.5}P_{0.25}O_{3-y} are displayed in Table 6-4 for 500°C and 800°C, however, they are substantially lower than reported for undoped BaPrO₃ and 10-20% rare earth doped BaPrO₃.^{198, 200}

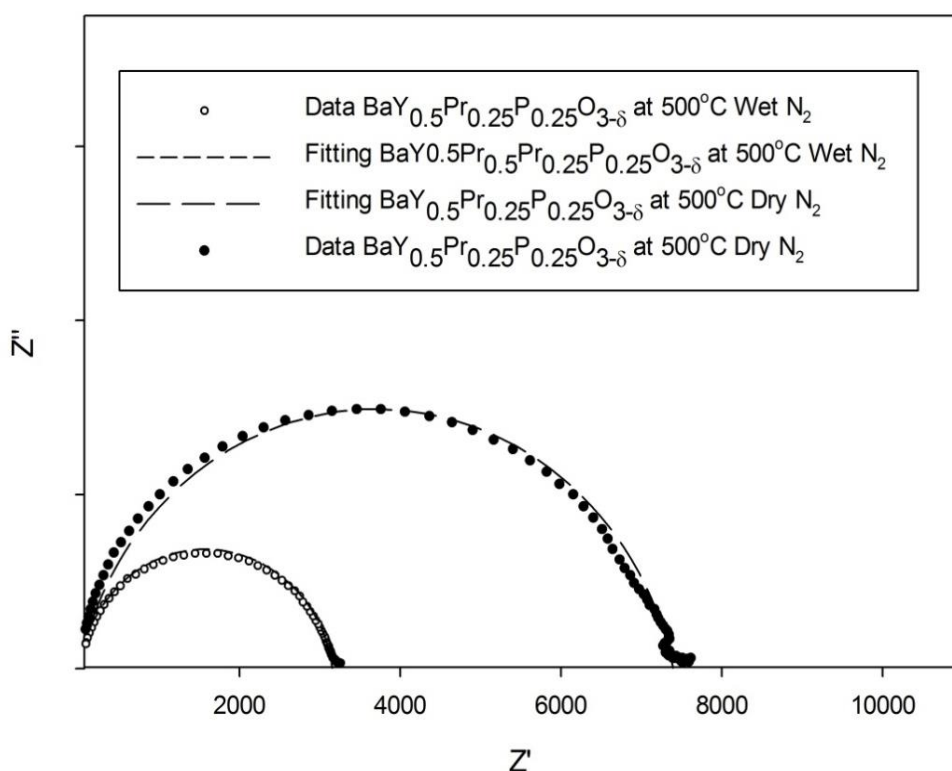


Figure 6-8 Impedance data for BaPr_{0.25}Y_{0.5}P_{0.25}O_{3-y} at 500°C in dry and wet N₂ atmosphere, showing the reduction in the resistance for the latter, indicative of a protonic contribution to the conductivity.

Table 6-4 Total conductivity data for BaPr_{0.25}(Y/Yb/Tm)_{0.5}P_{0.25}O_{3-y} in dry and wet N₂ atmospheres

Sample (nominal composition)	Conductivity (S cm ⁻¹)			
	500 °C		800 °C	
	Dry N ₂	Wet N ₂	Dry N ₂	Wet N ₂
BaPr _{0.25} Y _{0.5} P _{0.25} O _{3-y}	2.5 x 10 ⁻⁵	5.9 x 10 ⁻⁵	6.6 x 10 ⁻⁴	8.1 x 10 ⁻⁴
BaPr _{0.25} Yb _{0.5} P _{0.25} O _{3-y}	2.1 x 10 ⁻⁵	2.7 x 10 ⁻⁵	4.6 x 10 ⁻⁴	3.3. x 10 ⁻⁴
BaPr _{0.25} Tm _{0.5} P _{0.25} O _{3-y}	9.8x 10 ⁻⁶	1.6 x 10 ⁻⁵	3.8 x 10 ⁻⁴	3.6x 10 ⁻⁴

Table 6-5 Total conductivity data for BaPr_{0.25}(Y/Yb/Tm)_{0.5}P_{0.25}O_{3-y} in dry and wet O₂ atmospheres

Sample (nominal composition)	Conductivity (S cm ⁻¹)			
	500 °C		800 °C	
	Dry O ₂	Wet O ₂	Dry O ₂	Wet O ₂
BaPr _{0.25} Y _{0.5} P _{0.25} O _{3-y}	2.9x 10 ⁻⁵	3.6x 10 ⁻⁵	7.6x10 ⁻⁴	8.7x10 ⁻⁴
BaPr _{0.25} Yb _{0.5} P _{0.25} O _{3-y}	2.9 x10 ⁻⁵	2.6x10 ⁻⁵	6.4x10 ⁻⁴	6.2x10 ⁻⁴
BaPr _{0.25} Tm _{0.5} P _{0.25} O _{3-y}	3.3x10 ⁻⁵	3.2x10 ⁻⁵	6.6x10 ⁻⁴	6.5x10 ⁻⁴

In terms of the measurements in O₂, very similar conductivities under dry and wet conditions were observed for BaPr_{0.25}Yb_{0.5}P_{0.25}O_{3-y} and BaPr_{0.25}Tm_{0.5}P_{0.25}O_{3-y}, while BaPr_{0.25}Y_{0.5}P_{0.25}O_{3-y} showed a small increase under wet O₂ conditions, which again may be indicative of a contribution from proton conductivity (Table 6-5). Comparing the conductivities under dry N₂ and dry O₂, the data for BaPr_{0.25}Yb_{0.5}P_{0.25}O_{3-y} and BaPr_{0.25}Tm_{0.5}P_{0.25}O_{3-y}, show a slightly higher conductivity in dry O₂ over the entire temperature range. This is indicative of a p-type electronic contribution to the conductivity also observed for undoped BaPrO₃ and 10-20% rare earth doped BaPrO₃.

Overall the results, indicate that these heavily doped BaPr_{0.25}(Y/Yb/Tm)_{0.5}P_{0.25}O_{3-y} samples show poor conductivities. Thus, while the electronic conductivity appears to have been suppressed compared to prior studies, and there is some evidence in support of a protonic contribution to the conductivity, the values obtained are not sufficiently high for industrial applications. In this respect, the high phosphate levels required to achieve single phase samples may lead to a large degree of vacancy trapping and so be responsible for suppressing the ionic conductivity. Such defect trapping at high oxyanion levels was proposed in prior studies of Ba₂In₂O₅.²⁰⁵ In fact, it is probably this ability of phosphate to accommodate and hence stabilise the oxide ion vacancies around it (due to the preference

for tetrahedral rather than octahedral coordination) that allows for the accommodation of higher levels of acceptor dopants (Y/Yb/Tm) than are achievable normally.

Similar observation were obtained for the $\text{Ba}(\text{Yb/Tm})_{0.75}\text{P}_{0.25}\text{O}_{2.75}$ samples, (the yttrium based sample was not analyzed due to the significant level of impurities); the conductivity data for dry and wet N_2 are shown in Table 6-6 at 500°C and 800°C. These values are similar if not lower than the Pr containing samples and are not suitable for applications.

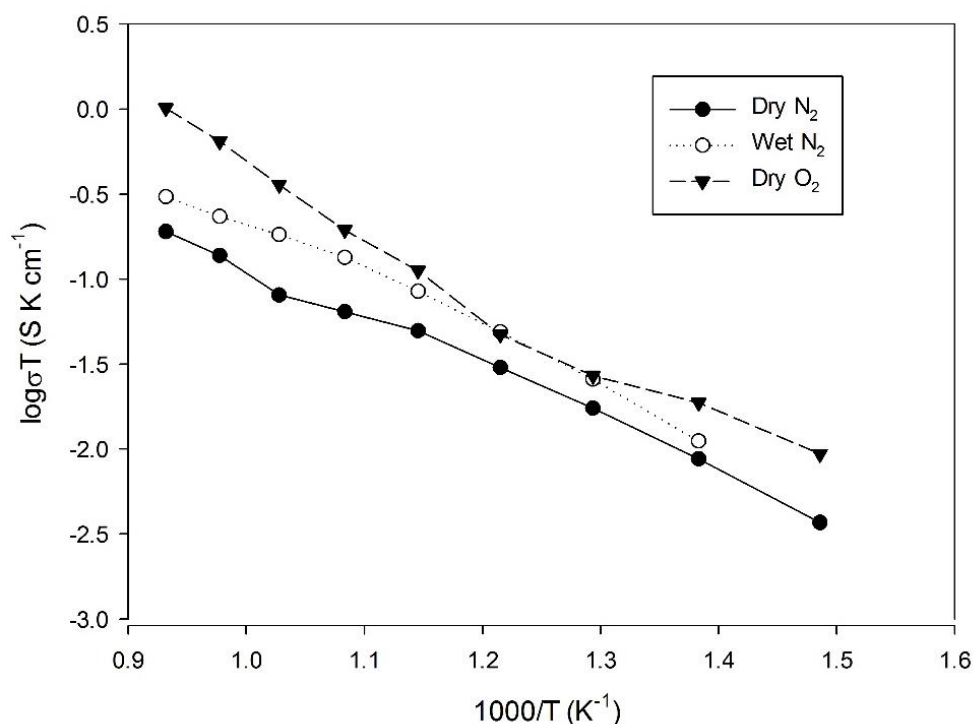


Figure 6-9 Conductivity data for $\text{BaYb}_{0.75}\text{P}_{0.25}\text{O}_{3-y}$ in dry N_2 (black Circle), wet N_2 (white circle) and dry O_2 (black triangle).

Table 6-6 Total conductivity data for $\text{Ba}(\text{Yb/Tm})_{0.5}\text{P}_{0.25}\text{O}_{3-y}$ in dry and wet N_2 atmospheres

Sample (nominal composition)	Conductivity (S cm^{-1})			
	500 °C		800 °C	
	Dry N_2	Wet N_2	Dry N_2	Wet N_2
$\text{BaYb}_{0.75}\text{P}_{0.25}\text{O}_{3-y}$	2.26×10^{-5}	3.3×10^{-5}	1.7×10^{-4}	2.8×10^{-4}
$\text{BaTm}_{0.75}\text{P}_{0.25}\text{O}_{3-y}$	1.21×10^{-5}	1.5×10^{-5}	9.98×10^{-5}	1.6×10^{-4}

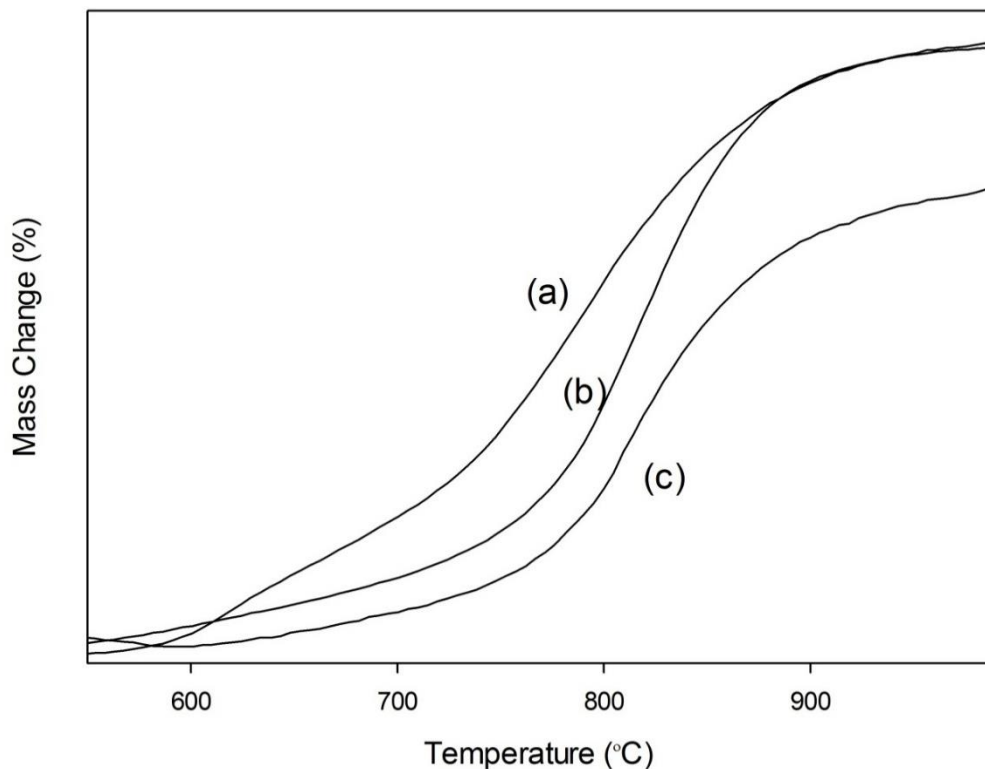
The conductivity in a dry O₂ atmosphere was shown to be better than the N₂ atmosphere as would be expected in line with the other results (Figure 6-9). Wet O₂ measurements were unable to be carried out due to disintegration of the electrode attachment on the pellet, further tests weren't rerun due to the time constraints and the limited conductivity previously observed.

6.5 Thermogravimetric analysis

Hydration and CO₂ stability measurements were restricted to the praseodymium containing single phase BaPr_{0.25}(Y/Yb/Tm)_{0.5}P_{0.25}O_{3-y} samples. While the conductivity data showed a significant reduction on Y/Yb/Tm and phosphate co-doping, the impact on the CO₂ stability and the level of possible water incorporation was also investigated. The respective BaPr_{0.25}(Y/Yb/Tm)_{0.5}P_{0.25}O_{3-y} powder samples were heated under wet N₂ to 800°C, before slow cooling (0.4°C min⁻¹) to room temperature. X-ray diffraction confirmed that there was no decomposition of the samples on hydration under these conditions. The water contents were then determined by a TGA measurement, with the results shown in Table 6-7. Overall water contents between 0.09 and 0.17 moles per formula unit were observed, indicating significant water incorporation. Assuming the oxidation state of praseodymium is Pr³⁺ the maximum theoretical water content is 0.25 per formula unit. The amount of water moles per formula unit are however lower than this, which can be explained by a reluctance of the phosphate group to expand its coordination sphere.

Table 6-7 Water contents for hydrated $\text{BaPr}_{0.25}(\text{Y}/\text{Yb}/\text{Tm})_{0.5}\text{P}_{0.25}\text{O}_{3-y}$

Sample (nominal composition)	Moles of water per formula unit
$\text{BaPr}_{0.25}\text{Y}_{0.5}\text{P}_{0.25}\text{O}_{3-y}$	0.17(1)
$\text{BaPr}_{0.25}\text{Yb}_{0.5}\text{P}_{0.25}\text{O}_{3-y}$	0.09(1)
$\text{BaPr}_{0.25}\text{Tm}_{0.5}\text{P}_{0.25}\text{O}_{3-y}$	0.15(1)

**Figure 6-10 TG profiles ($10^{\circ}\text{C min}^{-1}$ to 1000°C in CO_2) for (a) $\text{BaPr}_{0.25}\text{Y}_{0.5}\text{P}_{0.25}\text{O}_{3-\delta}$ (b) $\text{BaPr}_{0.25}\text{Yb}_{0.5}\text{P}_{0.25}\text{O}_{3-\delta}$ and (c) $\text{BaPr}_{0.25}\text{Tm}_{0.5}\text{P}_{0.25}\text{O}_{3-\delta}$**

The CO_2 stability of perovskite systems has been investigated for a wide range of doped proton conductors such as BaCeO_3 , which has shown poor stability on heating in a CO_2 containing atmosphere. A typical fuel cell operating temperatures of $500 - 700^{\circ}\text{C}$ would result in the observation of significant mass increases, starting at 550°C , due to the formation of BaCO_3 .¹⁸⁸ Therefore the stabilities of $\text{BaPr}_{0.25}(\text{Y}/\text{Yb}/\text{Tm})_{0.5}\text{P}_{0.25}\text{O}_{3-y}$ in a CO_2 environment were examined. The TGA profiles on heating in CO_2 showed that these compositions are also susceptible to partial decomposition in a CO_2 atmosphere. Although

the mass increase was seen at slightly higher temperatures compared to doped BaCeO₃, with a gradual increase at 600°C and a more rapid increase seen around 750°C (Figure 6-10).

6.6 Conclusions

The data shows that it is possible to introduce large levels of Y/Yb/Tm into BaPrO₃ through co-doping with phosphate, forming pure cubic perovskites. It is most likely that this is due to the stabilization of the resulting high levels of oxide ion vacancies by the phosphate group (due to its preference for tetrahedral rather than octahedral coordination). The conductivity measurements showed, however, significantly lower values than for BaPrO₃ or 10-20% rare earth doped BaPrO₃, although in the present systems, there was evidence for a protonic contribution in humid atmospheres. The complete replacement of praseodymium was attempted, however, it was not possible to prepare completely phase pure Ba(Y/Yb/Tm)_{1-x}P_xO_{3-y} samples, most likely due to Ba loss and partial incorporation of Y/Yb/Tm on the Ba site. Overall, the results further highlight the ability of perovskites to accommodate oxyanion groups on the B site, but suggest that in terms of conducting properties, the level of such dopants should be kept low to prevent a high degree of oxygen vacancy trapping.

7 Conclusions

In summary, this research has concentrated on producing new materials for SOFCs focusing on the cathode and electrolyte components. Existing research shows that the perovskite material has a huge potential for SOFCs due to the flexibility of the structure and properties that it can possess. Therefore in this work a variety of perovskites have been successfully prepared via the solid state route and examined using a range of structural, thermal and electrochemical techniques including X-ray diffraction, thermogravimetric analysis and impedance spectroscopy.

7.1 Silicon doped $\text{Sr}_{0.8}\text{Ca}_{0.2}\text{MnO}_{3-\delta}$ perovskite as a fuel cell cathode with apatite and fluorite electrolytes.

The cathode $\text{Sr}_{0.8}\text{Ca}_{0.2}\text{MnO}_{3-\delta}$ was investigated and silicon was shown to be successfully incorporated into the structure. For 10% and above doping the cathode adopted a cubic perovskite structure with enhanced electronic conductivity. $\text{Sr}_{0.8}\text{Ca}_{0.2}\text{Mn}_{0.9}\text{Si}_{0.1}\text{O}_{3-\delta}$ was the most successfully doped perovskite in the series and further work concentrated on this system. Chemical compatibility and area specific resistance (ASR) tests were performed against a range of apatite electrolytes with $\text{Sr}_{0.8}\text{Ca}_{0.2}\text{Mn}_{0.9}\text{Si}_{0.1}\text{O}_{3-\delta}$ composite electrodes. Reactivity between the composites and poor binding to the surface of the pellets was observed and required the addition of CGO. Furthermore, CGO pellets were used with the composites to produce the lowest ASR values. The successes of the CGO/ $\text{Sr}_{0.8}\text{Ca}_{0.2}\text{Mn}_{0.9}\text{Si}_{0.1}\text{O}_{3-\delta}$ composite resulted in a fuel cell test involving a SCMS-CGO/CGO/NiO-CGO cell that achieved a maximum power density of 84 mW cm^{-2} at 700°C . This is lower than expected and the power density could be improved if the cell sealing, and hence, the open circuit voltage (OCV) could be improved.

7.2 Ba(Co/Fe)_{0.9}Bi_{0.1}O_{3-δ} perovskite as a fuel cell cathode for proton and oxide ion conductors.

BaCo_{0.9-x}Fe_xBi_{0.1}O_{3-δ} phases were prepared for x ranging from 0.0-0.8. The iron doping in to the structure resulted in a phase change from a hexagonal to a cubic perovskite. This in turn resulted in a lower thermal expansion co-efficient than the undoped BaCoO_{3-δ} perovskite. Furthermore, the heavily iron doped samples were found to have increased stability in both steam and CO₂ rich atmospheres, however, the conductivity data did decrease. Additionally chemical compatibility, ASR and fuel cell tests were undertaken for both proton and oxide ion conducting electrolytes. It was shown that for the proton conducting electrolyte Ba₂In_{1.6}Zr_{0.2}Si_{0.2}O_{5.2} (BIZS) the cross reactions against the cathodes reduced on increasing the iron content across the series, with no visible reactions seen for x ≥ 0.6. The lowest ASR 0.025 Ω cm² was observed at 800°C for a BaCo_{0.3}Fe_{0.6}Bi_{0.1}O_{3-δ}/BIZS composite on a BIZS pellet. However, fuel cell tests were unsuccessfully performed due to the lower than required density of the BIZS pellet.

The doped cathode series with the oxide ion electrolyte CGO resulted in high chemical reactivity across the entire series, with the high iron doped samples reacting the least. The minor impurity phases formed affected the electrolyte and cathode boundaries, and therefore the ASR tests were magnitudes higher on the oxide ion electrolyte than the proton. The fuel cell test confirmed this further with a maximum power density of only 50mW cm⁻² at 700°C.

7.3 Doping Ba₂Sc₂O₅ to reduce costs and increase stability.

Ba₂Sc₂O₅ has been successfully co-doped with titanium, ytterbium and boron in place of scandium to produce BaYb_{0.7-x}Sc_xB_{0.05}Ti_{0.3}O_{2.65} (x= 0.05, 0.1, 0.2, 0.3) electrolyte samples. Small amounts of scandium were still required to produce pure cubic samples and the

successful doping of the sample caused increased thermal stability above 1000°C, increased chemical stability in CO₂ atmospheres and increased densification. The conductivity showed an improvement when compared to other non-perovskite based CO₂ stable proton conductors such as Ca²⁺ doped LaNbO₄. However, against high scandium containing perovskite systems such as BaSc_{0.7}Ti_{0.3}O_{2.7} it was magnitudes lower.

The doping strategy to the perovskite system was extended and the complete replacement of scandium was achieved through further doping with iron (BaYb_{0.6-z}Fe_zB_{0.05}Ti_{0.3}O_{3-δ} z = 0.05, 0.1, 0.2). However high iron contents were detrimental to the conductivity and densification. Thus the results emphasize the potential doping available to the Ba₂Sc₂O₅ to produce new cubic perovskite phases.

7.4 Synthesis and characterization of phosphate doped

BaPr_{1-y}(Y/Yb/Tm)_yO_{3-δ}.

The doping strategy with rare earths and oxyanions on to the B site of the perovskite structure was extended to the BaPrO₃ perovskite. This involved co-doping with large levels of Y/Yb/Tm and phosphate to form a pure cubic perovskite. Further attempts were made to produce perovskites with high levels of rare earths, without the phosphate dopant, these showed impurities, as did the related praseodymium free samples (Ba(Y/Yb/Tm)_{1-x}P_xO_{3-y}). Therefore, the higher levels of rare earth dopants that are possible depend on the phosphate dopant being present, as it occupies a tetrahedral coordination rather than an octahedral, producing oxygen vacancies. The conductivity measurements for the co-doped BaPr_{0.25}(Y/Yb/Tm)_{0.5}P_{0.25}O_{3-δ} samples showed evidence of proton conduction, however, the measurements were significantly lower than for the BaPrO₃ or 10-20% rare earth doped BaPrO₃. Therefore, the level of rare earth dopants used should be kept at a minimum to avoid any oxygen vacancy trapping and any effect on the conductivity.

8 Further work

The research in this project has indicated that the perovskite structure can exhibit some interesting properties for both the cathode and electrolyte components. The cathode research showed that doping the structure with a range of transition metals or oxyanions can reduce the tolerance factor. This causes a phase change from low to high symmetry and results in a cubic perovskite formation. The change in the tolerance factor is due to the incorporation of oxide ion vacancies on doping, which reduces the oxidation state of the transition metals increasing their size. However, further research could be performed to determine the positions of the oxide ions in the perovskite system via neutron diffraction or ^{17}O NMR experiments to determine if there is any oxygen vacancy ordering effects that might be limiting the conductivity and water contents. Furthermore, the perovskites could undergo Mossbauer experiments to understand the oxidation states of the Mn and Fe. However, this could be problematic for the $\text{BaCo}_{0.9-x}\text{Fe}_x\text{Bi}_{0.1}\text{O}_{3-\delta}$ (0-0.8) series due to the effect of bismuth on gamma rays absorption. In addition, for the $\text{BaCo}_{0.9-x}\text{Fe}_x\text{Bi}_{0.1}\text{O}_{3-\delta}$ series magnetic measurements should be attempted to try to understand the unit cell volume changes over the series and whether any spin states of the Fe or Co are having an effect. Finally, for both cathodes the fuel cell tests should be repeated with fully tight seals and therefore an increased power density should be observed.

For the perovskite electrolyte samples a study on the effect of the boron doping and phosphate doping on the conductivity respectively should be under taken. This in an effort to prove the proton trapping around the boron site and the oxygen vacancy trapping around the phosphate site is lowering the expected ionic conductivity in the electrolyte.

9 Publication list

- 1- **Porras-Vazquez Jose M, Losilla Enrique R, Keenan Philip J, Hancock Cathryn A, Kemp Thomas F, Hanna John V, Slater Peter R, *Investigation into the effect of Si doping on the performance of $Sr_{1-y}Ca_yMnO_{3-\delta}$ SOFC cathode materials*; RSC Dalton transactions Feb 2013**
- 2- **Li Henan, Baikie Tom, Pramana Stevin S, Shin J Felix, Keenan Philip J, Slater Peter R, Brink Frank, Hester James, An Tao, White Tim J, *Hydrothermal synthesis, structure investigation, and oxide ion conductivity of mixed si/ge-based apatite-type phase* ; ASC Inorganic Chemistry May 2014**
- 3- **Anisotropic oxide ion conduction in melilite intermediate temperature electrolytes
Wei Fengxia, Gasparyan Hripsime, Keenan Philip J, Gutmann Matthias, Fang Yanan, Baikie Tom, Claridge John B, Slater Peter R, Kloc Christian L, White, Tim J; *Anisotropic oxide ion conduction in melilite intermediate temperature electrolytes*; J Material Chem A Jan 2015**
- 4- **Baikie Tom, Barrow Nathan. Fang Yanan, Keenan Philip J, Slater Peter R, Piltz Ross, Gutmann Matthias, Mhaisalkar Subodh, White Tim J; *A Combined Single Crystal Neutron/X-ray Diffraction and Solid-State Nuclear Magnetic Resonance Study of the Hybrid Perovskites CH_3NH_3PbX ($X = I, Br$ and Cl)*; Material chemistry A Feb 2015**
- 5- **Hancock Cathryn A, Porras-Vazquez Jose M, Keenan Philip J, Slater Peter R; *Oxyanions in perovskites: from superconductors to solid oxide fuel cells*; RSC Dalton transactions June 2015**
- 6- **Knöchel Patrick, Keenan Philip, Loho Christoph, Reitz Christian, Witte Ralf, Knight Kevin, Wright, Adrian Hahn Horst, Slater Peter, Clemens Oliver, *Synthesis, structural characterisation and proton conduction of two new hydrated phases of barium ferrite $BaFeO_{2.5-x}(OH)_{2x}$* ; Chemistry of Materials Jan 2016**

10 Conference list

MEGs 2012 Christmas conference Poster 2012

Liverpool Energy conference Poster 2013

Solid State Ionics (SSI) 19 Poster 2013

PPCC 2013 Poster 2013

MEGS annual conference Poster 2014

H2FC Supergen Poster 2013

MEGs 2013 Christmas Conference Poster 2013

ISIS Crystallography user meeting Poster 2013

RSC Solid state group Easter conference Poster 2014

University of Birmingham School Symposium Poster 2014

SSPC-17 Oral Presentation 2014

PPCC 2015 Oral Presentation 2015

11 References

1. A. Zuttel, *Die Naturwissenschaften*, 2004, **91**, 157-172.
2. Department of Energy and Climate change, *UK Energy Stat*, 2015, **1** 1-15.
3. D. Cheney, P. O'Neill, G. Norton, A. Veneman, D. Evans, N. Mineta, S. Abraham, S. AllBaugh, *National energy policy*, 2001, **1**, 7-25.
4. E. Kendrick, M. S. Islam and P. R. Slater, *Journal of Materials Chemistry*, 2007, **17**, 3104-3111.
5. A. Onishi, *Journal of Policy Modeling*, 2007, **29**, 797-819.
6. A. Yamasaki, *Journal of Chemical Engineering of Japan*, 2003, **36**, 361-375.
7. K. T. Lee, H. S. Yoon and E. D. Wachsman, *Journal of Materials Research*, 2012, **27**, 2063-2078.
8. M. A. Schilling and M. Esmundo, *Energy Policy*, 2009, **37**, 1767-1781.
9. S. F. Tie and C. W. Tan, *Renewable & Sustainable Energy Reviews*, 2013, **20**, 82-102.
10. S. C. Singhal, *Solid State Ionics*, 2000, **135**, 305-313.
11. L. Leon-Reina, J. M. Porras-Vazquez, E. R. Losilla and M. A. G. Aranda, *Solid State Ionics*, 2006, **177**, 1307-1315.
12. J. Larminie and A. Dicks, *Wiley Fuel Cells Systems Explained*, 2003, **2 ed**, 406.
13. X. W. Zhang, S. H. Chan, G. J. Li, H. K. Ho, J. Li and Z. P. Feng, *Journal of Power Sources*, 2010, **195**, 685-702.
14. E. I. Ortiz-Rivera, A. L. Reyes-Hernandez and R. A. Febo, *IEE conference proceedings*, 2007.
15. A. S. Abdulkareem, A. S. Afolabi, N. Fungura, T. Mokrani and C. Mateescu, *Energy Sources, Part B: Economics, Planning, and Policy*, 2015, **10**, 404-411.
16. Nagamoto, *Encyclopedia of Material Science*, 2001, **1 ed**, 3359-3367.
17. J. M. Andújar and F. Segura, *Renewable and Sustainable Energy Reviews*, 2009, **13**, 2309-2322.
18. C. E. Gibbs and M. C. F. Steel, *Journal of Power Sources*, 1992, **37**, 35-43.
19. P. N. Anunson, G. R. Winlder, J. R. Winkler, B. A. Parkinson and J. D. S. Christus, *Journal of Chemical Education*, 2013, **90**, 1333-1340.
20. A. K. M. Tarigan and S. B. Bayer, *Renewable & Sustainable Energy Reviews*, 2012, **16**, 5535-5544.
21. N. Sammes, *Fuel Cell Technology: Reaching Towards Commercialization*, 2006, **1 ed**, 42.
22. K. Kordesch, G. Simader, *Fuel cells: and their applications*, 2006, **1 ed**, 23--50.
23. Z. P. Shao and S. M. Haile, *Nature*, 2004, **431**, 170-173.
24. J. Carlos Ruiz-Morales, D. Marrero-Lopez, M. Galvez-Sanchez, J. Canales-Vazquez, C. Savaniu and S. N. Savvin, *Journal of Energy & Environmental Science*, 2010, **3**, 1670-1681.
25. L. Malavasi, C. A. J. Fisher and M. S. Islam, *Chemical society reviews*, 2010, **39**, 4370-4387.
26. C. S. Song, *Catalysis Today*, 2002, **77**, 17-49.
27. L. Carrette, K. A. Friedrich and U. Stimming, *Chemphyschem*, 2000, **1**, 162-193.
28. S. Giddey, S. P. S. Badwal, A. Kulkarni and C. Munnings, *Progress in Energy and Combustion Science*, 2012, **38**, 360-399.
29. B. C. H. Steele, I. Kelly, H. Middleton and R. Rudkin, *Solid State Ionics*, 1988, **28**, 1547-1552.
30. B. C. H. Steele and A. Heinzl, *Nature*, 2001, **414**, 345-352.
31. G. F. McLean, T. Niet, S. Prince-Richard and N. Djilali, *International Journal of Hydrogen Energy*, 2002, **27**, 507-526.
32. A. Kulkarni and S. Giddey, *Journal of Solid State Electrochemistry*, 2012, **16**, 3123-3146.
33. S. F. Au, S. J. McPhail, N. Woudstra and K. Hemmes, *Journal of Power Sources*, 2003, **122**, 37-46.

34. S. Authayanun, K. Im-Orb and A. Arpornwichanop, *Chinese Journal of Catalysis*, 2015, **36**, 473-483.
35. D. J. L. Brett, A. Atkinson, N. P. Brandon and S. J. Skinner, *Chemical society reviews*, 2008, **37**, 1568-1578.
36. N. A. Baharuddin, H. Abd Rahman, A. Muchtar, A. Sulong and H. Abdullah, *Journal of Zhejiang University Science A*, 2013, **14**, 11-24.
37. D. Sanchez, R. Chacartegui, A. Munoz and T. Sanchez, *International Journal of Hydrogen Energy*, 2008, **33**, 1834-1844.
38. A. Orera and P. R. Slater, *Chemistry of materials*, 2010, **22**, 675-690.
39. Y. J. Leng, S. H. Chan, K. A. Khor and S. P. Jiang, *International Journal of Hydrogen Energy*, 2004, **29**, 1025-1033.
40. O. A. Marina, N. L. Canfield and J. W. Stevenson, *Solid State Ionics*, 2002, **149**, 21-28.
41. M. J. Escudero, J. T. S. Irvine and L. Daza, *Journal of Power Sources*, 2009, **192**, 43-50.
42. A. Jun, J. Kim, J. Shin and G. Kim, *Chemelectrochem*, 2016, **3**, 511-530.
43. S. Omar, E. D. Wachsman, J. L. Jones and J. C. Nino, *Journal of American Ceramic Society*, 2009, **92**, 2674-2681.
44. E. Kendrick, A. Orera and P. R. Slater, *Journal of Materials Chemistry*, 2009, **19**, 7955-7958.
45. E. Kendrick, J. Kendrick, A. Orera, P. Panchmatia, M. S. Islam and A. R. Slater, *Fuel Cells*, 2011, **11**, 38-43.
46. Singhal, *Encyclopedia of material: science and technology*, 2001, **1 ed**, 9898-9902.
47. H. G. Scott, *Journal of Material Science*, 1975, **10**, 1527-1535.
48. V. V. Kharton, E. N. Naumovich and A. A. Vecher, *Journal of Solid State Electrochemistry*, 1999, **3**, 61-81.
49. E. R. Losilla, M.A.G. Aranda, I. Santacruz, L. Santos-Gomes, J. M. Porras Vazquez, *Ceramics Internationals*, 2012, **38**, 3327-3335.
50. H. L. Tuller and A. S. Nowick, *Journal of Electrochemical Society*, 1975, **122**, 255-259.
51. L. Leon-Reina, J. M. Porras-Vazquez, E. R. Losilla, D. V. Sheptyakov, A. Llobet and M. A. G. Aranda, *RSC Dalton Transactions*, 2007, **20**, 2058-2064.
52. H. Yoshioka and S. Tanase, *Solid State Ionics*, 2005, **176**, 2395-2398.
53. D. Marrero-Lopez, M. C. Martin-Sedeno, J. Pena-Martinez, J. C. Ruiz-Morales, P. Nunez, M. A. G. Aranda and J. R. Ramos-Barrado, *Journal of Power Sources*, 2010, **195**, 2496-2506.
54. H. Gasparyan, S. Neophytides, D. Niakolas, V. Stathopoulos, T. Kharlamova, V. Sadykov, O. Van der Biest, E. Jothinathan, E. Louradour, J. P. Joulin and S. Bebelis, *Solid State Ionics*, 2011, **192**, 158-162.
55. J. R. Tolchard, M. S. Islam and P. R. Slater, *Journal of Materials Chemistry*, 2003, **13**, 1956-1961.
56. P. R. Slater, J. E. H. Sansom and J. R. Tolchard, *The Chemical Record*, 2004, **4**, 373-384.
57. E. Bechade, O. Masson, T. Iwata, I. Julien, K. Fukuda, P. Thomas and E. Champion, *Chemistry of Materials*, 2009, **21**, 2508-2517.
58. A. Jones, P. R. Slater and M. S. Islam, *Chemistry of Materials*, 2008, **20**, 5055-5060.
59. Y. Ma, N. Fenineche, O. Elkedim, M. Moliere, H. Liao and P. Briois, *International Journal of Hydrogen Energy*, 2016, **41**, 9993-10000.
60. S. Nakayama, M. Sakamoto, M. Highchi and K. Kodaira, *Journal of Materials Science*, 2000, **19**, 91-93.
61. H. Yoshioka, Y. Nojiri and S. Tanase, *Solid State Ionics*, 2008, **179**, 2165-2169.
62. J. M. Porras-Vazquez, E. R. Losilla, L. Leon-Reina, D. Marrero-Lopez and M. A. G. Aranda, *Journal of American Ceramic Society*, 2009, **92**, 1062-1068.
63. Y. P. Fu, A. Subardi, M. Y. Hsieh and W. K. Chang, *Journal of the American Ceramic Society*, 2016, **99**, 1345-1352.

64. L. Gan, Q. Zhong, X. L. Zhao, Y. Song and Y. F. Bu, *Journal of Alloys and Compounds*, 2016, **655**, 99-105.
65. Y. H. Ling, X. Y. Lu, J. N. Niu, H. Chen, Y. Z. Ding, X. M. Ou and L. Zhao, *Journal of Alloys and Compounds*, 2016, **666**, 23-29.
66. H. Iwahara, T. Esaka, H. Uchida and N. Maeda, *Solid State Ionics*, 1981, **3-4**, 359-363.
67. K. H. Ryu and S. M. Haile, *Solid State Ionics*, 1999, **125**, 355-367.
68. H. Iwahara, *Solid State Ionics*, 1988, **28**, 573-578.
69. A. Magraso, M. L. Fontaine, Y. Larring, R. Bredesen, G. E. Syvertsen, H. L. Lein, T. Grande, M. Huse, R. Strandbakke, R. Haugsrud and T. Norby, *Fuel Cells*, 2011, **11**, 17-25.
70. H. Iwahara, *Solid State Ionics*, 1996, **86-8**, 9-15.
71. W. Munch, G. Seifert, K. D. Kreuer and J. Maier, *Solid State Ionics*, 1996, **86-8**, 647-652.
72. T. Yajima, H. Suzuki, T. Yogo and H. Iwahara, *Solid State Ionics*, 1992, **51**, 101-107.
73. T. Norby, *Solid State Ionics*, 1999, **125**, 1-11.
74. K. Katahira, Y. Kohchi, T. Shimura and H. Iwahara, *Solid State Ionics*, 2000, **138**, 91-98.
75. H. Iwahara, T. Yajima, T. Hibino, K. Ozaki and H. Suzuki, *Solid State Ionics*, 1993, **61**, 65-69.
76. R. Haugsrud and T. Norby, *Solid State Ionics*, 2006, **177**, 1129-1135.
77. K. Amezawa, Y. Tomii and N. Yamamoto, *Solid State Ionics*, 2005, **176**, 135-141.
78. O. Paschos, J. Kunze, U. Stimming and F. Maglia, *Journal of Physics Condensed Matter*, 2011, **23**, 26.
79. T. Norby and N. Christiansen, *Solid State Ionics*, 1995, **77**, 240-243.
80. K. Amezawa, S. Kjelstrup, T. Norby and Y. Ito, *Journal of The Electrochemical Society*, 1998, **145**, 3313-3319.
81. R. Haugsrud and T. Norby, *Nature Materials*, 2006, **5**, 193-196.
82. Z. Bi, J. Pena-Martinez, J. H. Kim, C. A. Bridges, A. Huq, J. P. Hodges and M. P. Paranthaman, *International Journal of Hydrogen Energy*, 2012, **37**, 12751-12759.
83. S. Li, F. Schonberger and P. Slater, *Chemical Communications.*, 2003, **1**, 2694-2695.
84. E. Kendrick, J. Kendrick, K. S. Knight, M. S. Islam and P. R. Slater, *Nature Materials*, 2007, **6**, 871-875.
85. F. Schonberger, E. Kendrick, M. S. Islam and P. R. Slater, *Solid State Ionics*, 2005, **176**, 2951-2953.
86. T. L. Story, *Mathematical Modeling I: Kinetics, Thermodynamics and Statistical Mechanics*, iUniverse, 2010, **1 ed**, 300.
87. M. Gazda, P. Jasinski, B. Kusz, B. Bochentyn, K. Gdula-Kasica, T. Lendze, W. Lewandowska-Iwaniak, A. Mielewczyk-Gryn and S. Molin, *Environmental Degradation of Engineering & Materials Engineering and Technologies*, 2012, **183**, 65-70.
88. C. de la Calle, A. Aguadero, J. A. Alonso and M. T. Fernandez-Diaz, *Solid State Sciences*, 2008, **10**, 1924-1935.
89. N. Mahato, A. Banerjee, A. Gupta, S. Omar and K. Balani, *Progress in Materials Science*, 2015, **72**, 141-337.
90. A. Mitterdorfer and L. J. Gauckler, *Solid State Ionics*, 1998, **111**, 185-218.
91. S. P. Jiang and X. B. Chen, *International Journal of Hydrogen Energy*, 2014, **39**, 505-531.
92. H. Zhao, Q. Li and L. P. Sun, *Science China Chemistry*, 2011, **54**, 898-910.
93. F. Chauveau, J. Mougin, F. Mauvy, J. M. Bassat and J. C. Grenier, *The Electrochemical Society*, 2009, **25**, 2557-2564.
94. E. Boehm, J. M. Bassat, P. Dordor, F. Mauvy, J. C. Grenier and P. Stevens, *Solid State Ionics*, 2005, **176**, 2717-2725.
95. A. J. Jacobson, *Chemistry of Materials*, 2010, **22**, 660-674.
96. H. Ullmann, N. Trofimenko, F. Tietz, D. Stover and A. Ahmad-Khanlou, *Solid State Ionics*, 2000, **138**, 79-90.

97. V. V. Kharton, A. V. Kovalevsky, M. Avdeev, E. V. Tsipis, M. V. Patrakeev, A. A. Yaremchenko, E. N. Naumovich and J. R. Frade, *Chemistry of Materials*, 2007, **19**, 2027-2033.
98. F. Mauvy, C. Lalanne, J. M. Bassat, J. C. Grenier, H. Zhao, L. H. Huo and P. Stevens, *Journal of The Electrochemical Society*, 2006, **153**, A1547-A1553.
99. A. M. Hernandez, L. Mogni and A. Caneiro, *International Journal of Hydrogen Energy*, 2010, **35**, 6031-6036.
100. M. Mukhopadhyay, J. Mukhopadhyay and R. N. Basu, *Transaction of the Indian Ceramic Society*, 2013, **72**, 145-168.
101. R. Mukundan, E. L. Brosha and F. H. Garzon, *Electrochemical and Solid-State Letters*, 2004, **7**, A5-A7.
102. J. H. Koh, Y. S. Yoo, J. W. Park and H. C. Lim, *Solid State Ionics*, 2002, **149**, 157-166.
103. X. Li, H. Zhao, N. Xu, X. Zhou, C. Zhany and N. Chen, *International Journal of Hydrogen Energy*, 2009, **34**, 6407-6414.
104. M. C. Verbraeken, T. Ramos, K. Agersted, Q. Ma, C. D. Savaniu, B. R. Sudireddy, J. T. S. Irvine, P. Holtappels and F. Tietz, *RSC Advances*, 2015, **5**, 1168-1180.
105. X. W. Zhou, N. Yan, K. T. Chuang and J. L. Luo, *RSC Advances*, 2014, **4**, 118-131.
106. L. Qiu, T. Ichikawa, A. Hirano, N. Imanishi and Y. Takeda, *Solid State Ionics*, 2003, **158**, 55-65.
107. J. E. H. Sansom, J. R. Tolchard, P. R. Slater and M. S. Islam, *Solid State Ionics.*, 2004, **167**, 17-22.
108. 14 Bravais Lattices, Cited 2015, Available from <http://hyperphysics.phy-astr.gsu.edu/hbase/solids/bravais.html>.
109. A. Barron and C. Smith, *Crystal Structure*. Cited 2013; Available from <http://cnx.org/content/m16927>, Last accessed 26/06/2016.
110. K. Pieter, Atomic Form Factor- Cromer Mann Structure Factors, Available from http://commons.wikimedia.org/wiki/File:Cromer-Mann_structure_factors.svg, Last assed 26/06/2016.
111. Chapter 5: X-ray Generation and Powder Diffractions. Cited 2015; Available from: <http://ruby.colorado.edu/smyth/G30105.htm>.
112. S. Billingswe, R.E. Dinnebier, *Powder Diffraction Theory and Practice*, 2008, RSC Publishing, 23-29.
113. C. Hancock and P. Slater, *PhD*, University of Birmingham, 2012.
114. H. M. Rietveld, *Acta Crystallographica Section A*, 1966, **S21**, A228.
115. H. M. Rietveld, *Acta Crystallographica*, 1967, **22**, 151.
116. H. M. Rietveld, *Journal of Applied Crystallography*, 1969, **2**, 65.
117. L. B. McCusker, R. B. Von Dreele, D. E. Cox, D. Louer and P. Scardi, *Journal of Applied Crystallography*, 1999, **32**, 36-50.
118. B. H. Toby, *Journal of Applied Crystallography*, 2001, **34**, 210-213.
119. A. A. Coelho, J. S. O. Evans, I. R. Evans, A. Kern and S. Parsons, *Powder Diffraction*, 2011, **26**, S22-S25.
120. R.A. Young, *The Rietveld Analysis*, Oxford University Press, 2002.
121. M. Pelletier, *Analytical Applications of Raman Spectroscopy*, Wiley-Blackwell Publishing, 1999.
122. Renishaw, *User Guide*, 2006, **1**, 1-7.
123. J. G. Dunn, *Thermogravimetric analysis Characterization of Materials* Wiley, **2 ed**, 2002.
124. P. Zoller, *Dilatometry. Encyclopedia of polymer Science and Technology* Wiley, 2013.
125. G. Rietveld, C. V. Kojmans, L. C. A. Henderson, M. J. Hall, S. Hannon, P. Warnecke and B. Schumacher, *Ieee Transactions on Instrumentation and Measurement*, 2003, **52**, 449-453.
126. J. H. Sluyters, *Recueil Des Travaux Chimiques Des Pays-Bas-Journal of the Royal Netherlands Chemical Society*, 1960, **79**, 1092-1100.

127. J. Irvine and A. West, *Advanced Materials*, 1990, **2**, 132-138.
128. J. R. Macdonald, *Annals of Biomedical Engineering*, 1992, **20**, 289-305.
129. F. Shin and P. Slater, PhD, *University of Birmingham*, 2012.
130. J. Percival and P. Slater, PhD, *University of Surrey*, 2009.
131. R. Macdonald and E. Barsoukov, *Impedance spectroscopy: Theory, Experiment, and Applications*, John Wiley & Sons, 2005, **2 ed**, 616.
132. M. J. Zayas-Rey, L. dos Santos-Gomez, J. M. Porras-Vazquez, E. R. Losilla and D. Marrero-Lopez, *Journal of Power Sources*, 2015, **294**, 483-493.
133. J. Goldstein, D. Newbury, P. Echlin, L. Sawyer and J. Michael. *Scanning Electron Microscopy and X-ray Microanalysis*, Springer US, 2003, **3 ed**, 1-20.
134. S. Nakayama, H. Aono and Y. Sadaoka, *Chemistry Letters*, 1995, **6**, 431-432.
135. H. Yoshioka, T. Mitsui, A. Mineshige and T. Yazawa, *Solid State Ionics*, 2010, **181**, 1707-1712.
136. Q. L. Shi, L. H. Lu, H. J. Jin, H. Zhang and Y. W. Zeng, *Materials Research Bulletin*, 2012, **47**, 719-723.
137. A. A. Yaremchenko, V. V. Kharton, D. O. Bannikov, D. V. Znosak, J. R. Frade and V. A. Cherepanov, *Solid State Ionics*, 2009, **180**, 878-885.
138. J. M. Porras-Vazquez, L. dos Santos-Gomez, I. Santacruz, M. A. G. Aranda, D. Marrero-Lopez and E. R. Losilla, *Ceramics International*, 2012, **38**, 3327-3335.
139. C. A. Hancock and P. R. Slater, *RSC Dalton Transactions*, 2011, **40**, 5599-5603.
140. J. M. Porras-Vazquez, E. R. Losilla, P. J. Keenan, C. A. Hancock, T. F. Kemp, J. V. Hanna and P. R. Slater, *RSC Dalton Transaction*, 2013, **42**, 5421-5429.
141. S. Beaudet-Savignat, A. Vincent, S. Lambert and F. Gervais, *Journal of Materials Chemistry*, 2007, **17**, 2078-2087.
142. Z. X. Huang, B. Y. Li and J. Liu, *High-Performance Ceramics Vi*, 2010, **434-435**, 723-726.
143. D. Johnson, *Z-Plot and Z-view*, Scribner associates Inc, 2007.
144. H. Hayashi, H. Inaba, M. Matsuyama, N. G. Lan, M. Dokiya and H. Tagawa, *Solid State Ionics*, 1999, **122**, 1-15.
145. R.D. Shannon, *Acta Crystallographica Section A*, 1976, **32**, 751-767
146. J. Pena-Martinez, D. Marrero-Lopez, C. Sanchez-Bautista, A. J. Dos Santos-Garcia, J. C. Ruiz-Morales, J. Canales-Vazquez and P. Nunez, *Boletin De La Sociedad Espanola De Ceramica Y Vidrio*, 2010, **49**, 15-22.
147. J. Deseure, Y. Bultel, L. Dessemond and E. Siebert, *Electrochim. Acta*, 2005, **50**, 2037-2046.
148. K. Q. Huang, M. Feng, J. B. Goodenough and M. Schmerling, *Journal of The Electrochemical Society*, 1996, **143**, 3630-3636.
149. T. Broux, M. Bahout, J. M. Hanlon, O. Hernandez, S. Paofai, A. Berenov and S. J. Skinner, *Journal of Materials Chemistry A*, 2014, **2**, 17015-17023.
150. Z. Q. Li, B. Wei, Z. Lu, X. Q. Huang and W. H. Su, *Solid State Ionics*, 2012, **207**, 38-43.
151. S. F. He, S. R. Le, L. L. Guan, T. Liu and K. N. Sun, *Journal of Power Sources*, 2015, **295**, 33-40.
152. K. Huang, J. Wan and J. B. Goodenough, *Journal of Materials Science*, 2001, **36**, 1093-1098.
153. D. Baek, A. Kamegawa and H. Takamura, *Solid State Ionics*, 2013, **253**, 211-216.
154. Q. A. Islam, M. W. Raja and R. N. Basu, *Journal of Alloys and Compounds*, 2014, **583**, 7-14.
155. Y. Niu, W. Zhou, J. Sunarso, F. Liang, Z. Zhu and Z. Shao, *Electrochemistry Communications*, 2011, **13**, 1340-1343.
156. Z. Yang, N. Wang, J. Xiao, H. Zhang, F. Zhang, G. Ma and Z. Zhou, *Journal of Power Sources*, 2012, **204**, 89-93.
157. K. Huang, H. Y. Lee and J. B. Goodenough, *Journal of the Electrochemical Society*, 1998, **145**, 3220-3227.
158. M. Ahmadrzaei, S. A. M. Ali, A. Muchtar, C. Y. Tan and M. R. Somalu, *Ceramics-Silikaty*, 2014, **58**, 46-49.

159. M. Al Daroukh, V. V. Vashook, H. Ullmann, F. Tietz and I. A. Raj, *Solid State Ionics*, 2003, **158**, 141-150.
160. Q. J. Zhou, T. Wei, Z. P. Li, D. M. An, X. Q. Tong, Z. H. Ji, W. B. Wang, H. Lu, L. Y. Sun, Z. Y. Zhang and K. Xu, *Journal of Alloys and Compounds*, 2015, **627**, 320-323.
161. E. P. Murray, M. J. Sever and S. A. Barnett, *Solid State Ionics*, 2002, **148**, 27-34.
162. B. Liu, X. Chen, Y. Dong, S. S. Mao and M. Cheng, *Advanced Energy Materials*, 2011, **1**, 343-346.
163. A. Mineshige, J. Izutsu, M. Nakamura, K. Nigaki, J. Abe, M. Kobune, S. Fujii and T. Yazawa, *Solid State Ionics*, 2005, **176**, 1145-1149.
164. Z. P. Shao, G. X. Xiong, Y. Cong and W. S. Yang, *Journal of Membrane Science*, 2000, **164**, 167-176.
165. Z. T. Tao, L. Bi, L. T. Yan, W. P. Sun, Z. W. Zhu, R. R. Peng and W. Liu, *Electrochemistry Communications*, 2009, **11**, 688-690.
166. R. J. Drost and W. T. Fu, *Materials Research Bulletin*, 1995, **30**, 471-478.
167. S. Vazquez, J. Basbus, A. L. Soldati, F. Napolitano, A. Serquis and L. Suescun, *Journal of Power Sources*, 2015, **274**, 318-323.
168. J. Shen, G. M. Yang, Z. B. Zhang, W. Zhou, W. Wang and Z. P. Shao, *Journal of Materials Chemistry A*, 2016, **4**, 10641-10649.
169. V. V. Kharton, F. M. Figueiredo, L. Navarro, E. N. Naumovich, A. V. Kovalevsky, A. A. Yaremchenko, A. P. Viskup, A. Carneiro, F. M. B. Marques and J. R. Frade, *Journal of Materials Science*, 2001, **36**, 1105-1117.
170. L. Almar, B. Colldeforns, L. Yedra, S. Estrade, F. Peiro, A. Morata, T. Andreua and A. Tarancon, *Journal of Materials Chemistry A*, 2013, **1**, 4531-4538.
171. K. D. Kreuer, *Solid State Ionics*, 1997, **97**, 1-15.
172. K. D. Kreuer, *Annual Review of Materials Research*, 2003, **33**, 333-359.
173. H. Iwahara, H. Uchida, K. Ono and K. Ogaki, *Journal of the Electrochemical Society*, 1988, **135**, 529-533.
174. H. G. Bohn and T. Schober, *Journal of the American Ceramic Society*, 2000, **83**, 768-772.
175. S. Ricote and N. Bonanos, *Solid State Ionics*, 2010, **181**, 694-700.
176. Z. W. Zhu, W. P. Sun, Z. Shi and W. Liu, *Journal of Alloys and Compounds*, 2016, **658**, 716-720.
177. I. Ahmed, S. G. Eriksson, E. Ahlberg, C. S. Knee, M. Karlsson, A. Matic, D. Engberg and L. Borjesson, *Solid State Ionics*, 2006, **177**, 2357-2362.
178. I. Ahmed, S. G. Eriksson, E. Ahlberg, C. S. Knee, P. Berastegui, L. G. Johansson, H. Rundlof, M. Karlsson, A. Matic, L. Borjesson and D. Engberg, *Solid State Ionics*, 2006, **177**, 1395-1403.
179. E. Fabbri, D. Pergolesi, S. Licocchia and E. Traversa, *Solid State Ionics*, 2010, **181**, 1043-1051.
180. T. Omata, T. Fuke and S. Otsuka-Yao-Matsuo, *Solid State Ionics*, 2006, **177**, 2447-2451.
181. J. F. Shin, K. Joubel, D. C. Apperley and P. R. Slater, *RSC Dalton Transactions*, 2012, **41**, 261-266.
182. W. Kwestroo, H. A. M. Vanhal and C. Langerei, *Materials Research Bulletin*, 1974, **9**, 1623-1630.
183. S. M. H. Rahman, I. Ahmed, R. Haugsrud, S. G. Eriksson and C. S. Knee, *Solid State Ionics*, 2014, **255**, 140-146.
184. S. M. H. Rahman, S. T. Norberg, C. S. Knee, J. J. Biendicho, S. Hull and S. G. Eriksson, *RSC Dalton Transactions*, 2014, **43**, 15055-15064.
185. F. Iguchi, T. Yamada, N. Sata, T. Tsurui and H. Yugami, *Solid State Ionics*, 2006, **177**, 2381-2384.
186. J. F. Shin, D. C. Apperley and P. R. Slater, *Chemistry of Materials*, 2010, **22**, 5945-5948.
187. J. F. Shin, A. Orera, D. C. Apperley and P. R. Slater, *Journal of Materials*, 2011, **21**, 874-879.

188. M. J. Scholten, J. Schoonman, J. C. Vanmilttenburg and H. A. J. Oonk, *Solid State Ionics*, 1993, **61**, 83-91.
189. G. Amoroso, P. Slater and L. Malavasi, Msci, *University of Birmingham*, 2015.
190. T. Norby and A. Magraso, *Journal of Power Sources*, 2015, **282**, 28-33.
191. K. Amezawa, H. Maekawa, Y. Tomii and N. Yamamoto, *Solid State Ionics*, 2001, **145**, 233-240.
192. J. F. Shin, L. Hussey, A. Orera and P. R. Slater, *Chemical Communications*, 2010, **46**, 4613-4615.
193. J. F. Shin and P. R. Slater, *Journal of Power Sources*, 2011, **196**, 8539-8543.
194. C. A. Hancock and P. R. Slater, *RSC Dalton Transactions*, 2011, **40**, 5599-5603.
195. A. D. Smith, J. F. Shin and P. R. Slater, *Journal of Solid State Chemistry*, 2013, **198**, 247-252.
196. J. M. Porras-Vazquez, T. F. Kemp, J. V. Hanna and P. R. Slater, *Journal of Materials Chemistry A*, 2012, **22**, 8287-8293.
197. J. M. Porras-Vazquez, T. Pike, C. A. Hancock, J. F. Marco, F. J. Berry and P. R. Slater, *Journal of Materials Chemistry A*, 2013, **1**, 11834-11841.
198. C. S. Knee, A. Magraso, T. Norby and R. I. Smith, *Journal of Materials Chemistry A*, 2009, **19**, 3238-3247.
199. A. Magraso, F. Espiell, M. Segarra and J. T. S. Irvine, *Journal of Power Sources*, 2007, **169**, 53-58.
200. L. P. Li, J. R. Wu, M. Knight and S. M. Haile, *Journal of Electrochemical Society*, 2002, **28**, 58.
201. S. J. Stokes and M. S. Islam, *Journal of Materials Chemistry*, 2010, **20**, 6258-6264.
202. T. Fukui, S. Ohara and S. Kawatsu, *Journal of Power Sources*, 1998, **71**, 164-168.
203. A. Magraso, X. Solans, J. T. S. Irvine and M. Segarra, *Ceramics International*, 2009, **35**, 1819-1827.
204. V. P. Gorelov, B. L. Kuzin, V. B. Balakireva, N. V. Sharova, G. K. Vdovin, S. M. Beresnev, Y. N. Kleshchev and V. P. Brusentsov, *Russ. Journal of The Electrochemical Society*, 2001, **37**, 505-511.
205. C. A. Hancock, J. M. Porras-Vazquez, P. J. Keenan and P. R. Slater, *RSC Dalton Transaction.*, 2015, **44**, 10559-10569.

Content of Figures

Figure 1-1 the generation of UK electricity in 2014.....	1
Figure 1-2 Birmingham University Hydrogen powered car.	2
Figure 1-3 Diagram showing the simple operation of a fuel cell Taken from Energy & Environmental science with permission from the RSC.	3
Figure 1-4 Schematic trend of the maximum Efficiency of H ₂ fuel cell at standard pressure (steam as a product = Black line), Carnot limit with 50°C exhaust temperature (blue line)	5
Figure 1-5 Types of Fuel Cells	6
Figure 1-6 Illustration of a) pure anode in contact with an electrolyte b) Composite material of anode and electrolyte in contact with an electrolyte. (red sites are the triple phase boundary points showing the meeting of O ²⁻ , e ⁻ and H ₂). Taken from Energy & Environmental science with permission from the RSC.	9
Figure 1-7 Fluorite structure XO ₂ ; cations are blue and oxide anions are red X = Zr, Ce.	13
Figure 1-8 Apatite structure (tetrahedral (XO ₄), Large sphere = M small sphere = O)	14
Figure 1-9 :- Perovskite structure showing corner-shared BO ₆ octahedra with A centred on 12-coordinate sites.....	16
Figure 1-10 SrCoO ₃ perovskite structure showing the change of structure as the temperature is increased (strontium = green, cobalt = blue, oxygen = red)	23
Figure 1-11 Structure of La ₂ NiO _{4+δ} (La = blue, Ni = Grey, O = Green)	26
Figure 2-1 Solid State – alumina crucible, lid and sample.	32
Figure 2-2 Basic labelling of axis, lengths and internal angles of a cubic unit cell.	33
Figure 2-3 14 Bravais lattices.....	34
Figure 2-4 Example of Lattice Planes with fractional intercepts and hkl values for (100), (-110) and (211).....	36
Figure 2-5 Form factors for different number electrons atoms and ion.....	38
Figure 2-6 Energy level diagram of copper	39
Figure 2-7 X-ray spectrum of copper	40
Figure 2-8 Depiction of Bragg's law from two incident beams	42
Figure 2-9 D8 Transmission and reflection geometries for X-ray diffraction.....	43
Figure 2-10 Main components of a powder XRD pattern	44
Figure 2-11 GSAS live plot view refinement profile; background (green), Calculated (red), observed (X), difference between the observed and calculated (blue) and phase (pink tick marks)	47

Figure 2-12 Raman spectroscopy energy transitions with Rayleigh and Stokes and Anti-Stokes lines.....	49
Figure 2-13 Raman microscope Renishaw 532nm optics and web camera active	51
Figure 2-14 Example TGA – Mass (black line), DTA (green line), m/z 18 H ₂ O (blue) and m/z 44 (CO ₂)	53
Figure 2-15 Van de Pauw method two measurement for 4 probe.	56
Figure 2-16 Schematic of 4 probe DC conductivity technique.....	56
Figure 2-17 Waveform and Phasor diagram for sinusoidal voltage.....	59
Figure 2-18 Waveform and phasor diagram showing the shift in phase between the voltage and the current at a known frequency ω	59
Figure 2-19 Waveform and phasor diagram showing the voltage and current in phase for a pure resistor.	60
Figure 2-20 Waveform and phasor diagram showing the voltage and current out of phase for a pure capacitor.	61
Figure 2-21 Sketched Nyquist plot for an imaginary RC circuit showing the components involved in a complex impedance plane plot	63
Figure 2-22 Nyquist plot of pure resistor and pure capacitor	64
Figure 2-23 equivalent fitting circuit for impedance plots containing separate definable semicircles.....	66
Figure 2-24 Brick layer schematic of conduction for a polycrystalline sample and equivalent circuit.	67
Figure 2-25 Impedance plot of BaSc _{0.3} Yb _{0.35} B _{0.05} Ti _{0.3} O _{3-δ} in a dry N ₂ at 350°C data fitted with a RC circuit equivalent fitting of the bulk and grain boundary responses	68
Figure 2-26 Impedance plot of CGO + BaFe _{0.8} Co _{0.1} Bi _{0.1} O _{3-δ} electrode on a CGO pellet at 900°C fitted with an equivalent circuit fitting of the bulk grain boundary responses and electrode response.....	69
Figure 2-27 Physical representation of an ASR measurement	70
Figure 2-28 fuel cell setup a) individual pellets top layer Pt current collector,	71
Figure 2-29 Schematic diagram of custom rig fuel cell set up	72
Figure 2-30 Scanning electron microscopy used for the measurements - JEOL SM-6490LV.	74
Figure 3-1 XRD patterns for Sr _{0.8} Ca _{0.2} Mn _{1-x} Si _x O _{3-δ} x = 0, 0.05, 0.075 and 0.1	80
Figure 3-2 Solid state NMR data for (a) Physical mixtures of ²⁹ SiO ₂ and Sr _{0.8} Ca _{0.2} MnO _{3-δ} –113 ppm and (b and c) the ²⁹ Si doped S Sr _{0.8} Ca _{0.2} Mn _{0.9} Si _{0.1} O _{3-δ}	82

Figure 3-3 Conductivity data for $\text{Sr}_{0.8}\text{Ca}_{0.2}\text{Mn}_{1-x}\text{Si}_x\text{O}_{3-\delta}$ $x = 0$ (black circle), 0.075 (white circle), 0.1 (white triangle) and 0.125 (white inverse triangle)	83
Figure 3-4 X-ray diffraction patterns for composite electrode, LSSO-SCMS at room temperature and fired at 1000°C for 24hrs (impurity highlighted *, red lines SCMS peak positions)	84
Figure 3-5 X-ray diffraction patterns for composite electrode, LSSO-SCMS fired at 900°C for 24hrs (red lines SCMS peak positions)	85
Figure 3-6 X-ray Diffraction patterns for composite electrode, LGSO–SCMS at room temperature and fired at RT, 900°C and 1000°C for 24hrs (impurities highlighted *, red lines SCMS peak positions).....	86
Figure 3-7 X-ray diffraction patterns for 50:50 wt% electrolyte mixture, CGO-LSSO fired at 900°C (blue lines CGO peak positions).....	88
Figure 3-8 X-ray diffraction for 50:50wt% composite electrode, CGO-SCMS fired at 900°C, (red lines SCMS peak positions and blue lines CGO peak positions)	89
Figure 3-9 ASR data plotted logR (ASR) vs 1000/T in air for composite electrodes SCMS-CGO mixed in 50:50 ● and 25:75 ○ on a LSSO electrolyte.....	91
Figure 3-10 ASR data plotted logR (ASR) vs 1000/T in air for composite electrodes SCM-CGO (50:50wt%) ● and SCMS-CGO (50:50wt%) ○ on a CGO electrolyte pellet.	92
Figure 3-11 Impedance spectra of the symmetrical cells for $\text{Sr}_{0.8}\text{Ca}_{0.2}\text{MnO}_3$ (■) and $\text{Sr}_{0.8}\text{Ca}_{0.2}\text{Mn}_{0.9}\text{Si}_{0.1}\text{O}_{3-\delta}$ (□)/CGO10 composites at 700 °C. The serial resistance was subtracted for better comparison of the spectra.....	93
Figure 3-12 Power density and cell voltage as a function of current density between 500-700°C using air and H_2	94
Figure 4-1a XRD patterns for $\text{BaCo}_{0.9-x}\text{Fe}_x\text{Bi}_{0.1}\text{O}_{3-\delta}$ $x = 0.0-0.8$, showing a hexagonal perovskite for $0 \leq x < 0.4$, a mixture of hexagonal and cubic perovskite for $0.4 \leq x < 0.6$, and a cubic perovskite for $x \geq 0.6$	103
Figure 4-2 Normalised (one formula unit) unit cell volume of $\text{BaCo}_{0.9-x}\text{Fe}_x\text{Bi}_{0.1}\text{O}_{3-\delta}$ hexagonal perovskites $x=0-0.3$ and cubic $x= 0.6-0.8$	106
Figure 4-3 High Temperature X-ray Diffraction of $\text{BaCo}_{0.4}\text{Fe}_{0.5}\text{Bi}_{0.1}\text{O}_{3-\delta}$ shown at RT and between 850-1000°C.....	107
Figure 4-4 Dilatometry data for $\text{BaCo}_{0.3}\text{Fe}_{0.6}\text{Bi}_{0.1}\text{O}_{3-\delta}$ from 35°C-800°C at 10°C min ⁻¹ in air (dashed red line – temperature profile, Solid black line is TEC profile)	109
Figure 4-5 Thermal expansion co-efficient for $\text{BaCo}_{0.9-x}\text{Fe}_x\text{Bi}_{0.1}\text{O}_{3-\delta}$ hexagonal perovskites $x=0-0.3$ and cubic 0.6-0.8 between RT-400°C in air.	110

Figure 4-6 TG profiles ($10^{\circ}\text{C min}^{-1}$ to 1000°C in N_2 protection gas) for $\text{BaCo}_{0.1}\text{Fe}_{0.8}\text{Bi}_{0.1}\text{O}_{3-\delta}$, $\text{BaCo}_{0.2}\text{Fe}_{0.7}\text{Bi}_{0.1}\text{O}_{3-\delta}$ and $\text{BaCo}_{0.3}\text{Fe}_{0.6}\text{Bi}_{0.1}\text{O}_{3-\delta}$	111
Figure 4-7 XRD pattern for $\text{BaCo}_{0.3}\text{Fe}_{0.6}\text{Bi}_{0.1}\text{O}_{3-\delta}$ before and after hydration.....	112
Figure 4-8 XRD pattern for $\text{BaCo}_{0.6}\text{Fe}_{0.3}\text{Bi}_{0.1}\text{O}_{3-\delta}$ before and after hydration.....	113
Figure 4-9 TGA-MS plot of $\text{BaCo}_{0.1}\text{Fe}_{0.8}\text{Bi}_{0.1}\text{O}_{3-\delta}$ (m/z 18 water)	114
Figure 4-10 X-ray diffraction data for $\text{BaCo}_{0.6}\text{Fe}_{0.3}\text{Bi}_{0.1}\text{O}_{3-\delta}$ and $\text{BaCo}_{0.3}\text{Fe}_{0.6}\text{Bi}_{0.1}\text{O}_{3-\delta}$ before and after a heat treatment at 800°C in 100% dry CO_2 for 24hrs. (*highlights main BaCO_3 peak impurity)	115
Figure 4-11 TG profiles ($10^{\circ}\text{C min}^{-1}$ to 1000°C in 1:1 CO_2 and N_2 mixture) for $\text{BaCo}_{0.9}\text{Bi}_{0.1}\text{O}_{3-\delta}$, $\text{BaCo}_{0.6}\text{Fe}_{0.3}\text{Bi}_{0.1}\text{O}_{3-\delta}$ and $\text{BaCo}_{0.3}\text{Fe}_{0.6}\text{Bi}_{0.1}\text{O}_{3-\delta}$	115
Figure 4-12 Conductivity data for $\text{BaCo}_{0.9-x}\text{Fe}_x\text{Bi}_{0.1}\text{O}_{3-\delta}$ $x = 0.0-0.8$	116
Figure 4-13 X-ray Diffraction patterns for composite electrode, BIZS– $\text{BaCo}_{0.9}\text{Bi}_{0.1}\text{O}_{3-\delta}$ 50:50 wt% each at room temperature and then ground/fired at 800°C and 900°C for 24hrs	117
Figure 4-14 X-ray Diffraction patterns for composite electrode, BIZS– $\text{BaCo}_{0.6}\text{Fe}_{0.3}\text{Bi}_{0.1}\text{O}_{3-\delta}$ 50:50 wt% each at room temperature and then ground/fired at 800°C and 900°C for 24hrs	118
Figure 4-15 X-ray Diffraction patterns for composite electrode, BIZS– $\text{BaCo}_{0.3}\text{Fe}_{0.6}\text{Bi}_{0.1}\text{O}_{3-\delta}$ 50:50 wt% each at room temperature and then ground/fired at 900°C for 24hrs.....	119
Figure 4-16 X-ray Diffraction patterns for composite electrode, CGO– $\text{BaCo}_{0.9}\text{Bi}_{0.1}\text{O}_{3-\delta}$ 50:50 wt% each at room temperature and then ground/fired at 800°C and 900°C for 24hrs	120
Figure 4-17 X-ray Diffraction patterns for composite electrode, CGO– $\text{BaCo}_{0.6}\text{Fe}_{0.3}\text{Bi}_{0.1}\text{O}_{3-\delta}$ 50:50 wt% each at room temperature and then ground/fired at 800°C and 900°C for 24hr	121
Figure 4-18 X-ray Diffraction patterns for composite electrode, CGO– $\text{BaCo}_{0.3}\text{Fe}_{0.6}\text{Bi}_{0.1}\text{O}_{3-\delta}$ 50:50 wt% each at room temperature and then ground/fired at 800°C and 900°C for 24hr	122
Figure 4-19 ASR data plotted $\log R$ (ASR) vs $1000/T$ in wet N_2 for electrodes $\text{BaFe}_{0.6}\text{Co}_{0.3}\text{Bi}_{0.1}\text{O}_{3-\delta}$ (100%) and $\text{BaCo}_{0.9}\text{Bi}_{0.1}\text{O}_{3-\delta}$ (100%) on a BIZS electrolyte pellet at binding temperature range of $800-1000^{\circ}\text{C}$	123
Figure 4-20 ASR data plotted $\log R$ (ASR) vs $1000/T$ in wet O_2 for electrodes $\text{BaFe}_{0.6}\text{Co}_{0.3}\text{Bi}_{0.1}\text{O}_{3-\delta}$ (100%) and $\text{BaCo}_{0.9}\text{Bi}_{0.1}\text{O}_{3-\delta}$ (100%) on a BIZS electrolyte pellet at binding temperature range of $800-1000^{\circ}\text{C}$	124
Figure 4-21 ASR data plotted $\log R$ (ASR) vs $1000/T$ in wet O_2 for composite BIZS electrodes $\text{BaFe}_{0.6}\text{Co}_{0.3}\text{Bi}_{0.1}\text{O}_{3-\delta}$ (100%/50:50wt%) and $\text{BaCo}_{0.9}\text{Bi}_{0.1}\text{O}_{3-\delta}$ (100%/50:50wt%) on a BIZS electrolyte pellet.	126

Figure 4-22 ASR data plotted logR (ASR) vs 1000/T in O ₂ for composite electrodes BIZS/BaCo _{0.9-x} Fe _x Bi _{0.1} O _{3-δ} x=0-0.3 0.6-0.8 (50:50wt%) on a BIZS electrolyte pellet.....	127
Figure 4-23 ASR data plotted logR (ASR) vs 1000/T in O ₂ for composite electrodes CGO/BaCo _{0.9-x} Fe _x Bi _{0.1} O _{3-δ} x=0-0.8 (50:50wt%) on a CGO electrolyte pellet	129
Figure 4-24 Cell voltage and power density as a function of current density between 700-500°C using air as the oxidant and H ₂ as the fuel.	130
Figure 4-25 NiO-CGO 5050 composite / CGO pellet	131
Figure 4-26 a)BIZS-BaCo _{0.3} Fe _{0.6} Bi _{0.1} O _{3-δ} 50:50wt% composite/ BIZS pellet b)CGO pellet/CGO-BaCo _{0.3} Fe _{0.6} Bi _{0.1} O _{3-δ} 50:50wt% composite	132
Figure 5-1 X-ray diffraction of Ba ₂ Sc ₂ O ₅ at temperatures of 1000°C and 1300°C (the later showing the formation of Ba ₃ Sc ₄ O ₉)	139
Figure 5-2 X-ray diffraction pattern for BaYb _{0.65-x} Sc _x B _{0.05} Ti _{0.3} O _{2.65} (x = 0.05, 0.1, 0.2, 0.3)	140
Figure 5-3 XRD patterns for BaYb _{0.6} Sc _{0.05} B _{0.05} Ti _{0.3} O ₃ , BaYb _{0.65} B _{0.05} Ti _{0.3} O ₃ BaYb _{0.55} Sc _{0.15} Ti _{0.3} O _{3-δ} BaYb _{0.45} Sc _{0.25} Ti _{0.3} O _{3-δ} and BaYb _{0.35} Sc _{0.35} Ti _{0.3} O _{3-δ} in a zoomed region of 20-50° with * denoting the impurities	141
Figure 5-4 Scanning electron microscopy images of a) BaYb _{0.6} Sc _{0.05} B _{0.05} Ti _{0.3} O _{2.65} b)BaYb _{0.35} Sc _{0.3} B _{0.05} Ti _{0.3} O _{2.65} and c) BaYb _{0.45} Sc _{0.25} Ti _{0.3} O _{2.65}	142
Figure 5-5 XRD patterns for hydrated BaYb _{0.65-x} Sc _x B _{0.05} Ti _{0.3} O _{2.65} (x= 0.05, 0.1, 0.2, 0.3)	144
Figure 5-6 X-ray diffraction data for BaYb _{0.35} Sc _{0.3} B _{0.05} Ti _{0.3} O _{2.65} and BaYb _{0.6} Sc _{0.05} B _{0.05} Ti _{0.3} O _{2.65} before and after a heat treatment to 800°C in 100% dry CO ₂ for 24hrs.	145
Figure 5-7 TG profiles (10°C min ⁻¹ to 800°C in CO ₂) for a)BaYb _{0.65} Sc _{0.05} B _{0.05} Ti _{0.3} O _{3-δ} , b)BaYb _{0.35} Sc _{0.3} B _{0.05} Ti _{0.3} O _{3-δ} , c)Ba ₂ Sc ₂ O ₅ and d)BaCe _{0.9} Y _{0.1} O _{3-δ}	146
Figure 5-8 Impedance and fitting data for BaYb _{0.6} Sc _{0.05} B _{0.05} Ti _{0.3} O _{2.65} at 350°C, 450°C and 550°C in a dry N ₂ atmosphere, showing the reduction and splitting components in the resistance over temperature.	147
Figure 5-9 Impedance data for BaYb _{0.6} Sc _{0.05} B _{0.05} Ti _{0.3} O _{2.65} at 600°C in dry and wet N ₂ atmosphere, showing the reduction in the resistance for the latter, indicative of a protonic contribution to the conductivity.....	148
Figure 5-10 Conductivity data for BaYb _{0.6} Sc _{0.05} B _{0.05} Ti _{0.3} O _{3-δ} in dry N ₂ (black Circle), wet N ₂ (white circle), and BaYb _{0.55} Sc _{0.1} B _{0.05} Ti _{0.3} O _{3-δ} dry N ₂ (black square) and wet N ₂ (white square).	149
Figure 5-11 Conductivity data for BaYb _{0.45} Sc _{0.2} B _{0.05} Ti _{0.3} O _{3-δ} in dry N ₂ (black triangle), wet N ₂ (white triangle), and BaYb _{0.35} Sc _{0.3} B _{0.05} Ti _{0.3} O _{3-δ} dry N ₂ (black diamond) and wet N ₂ (white diamond).	150

Figure 5-12 XRD patterns for $\text{BaYb}_{0.6}\text{Fe}_{0.05}\text{B}_{0.05}\text{Ti}_{0.3}\text{O}_{3-\delta}$, $\text{BaYb}_{0.55}\text{Fe}_{0.1}\text{B}_{0.05}\text{Ti}_{0.3}\text{O}_{3-\delta}$ and $\text{BaYb}_{0.6}\text{Fe}_{0.2}\text{B}_{0.05}\text{Ti}_{0.3}\text{O}_{3-\delta}$	152
Figure 5-13 Scanning electron microscopy images of a) $\text{BaYb}_{0.6}\text{Fe}_{0.05}\text{B}_{0.05}\text{Ti}_{0.3}\text{O}_{3-\delta}$ and b) $\text{BaYb}_{0.55}\text{Fe}_{0.1}\text{B}_{0.05}\text{Ti}_{0.3}\text{O}_{3-\delta}$	153
Figure 5-14 Impedance data for $\text{BaYb}_{0.6}\text{Fe}_{0.05}\text{B}_{0.05}\text{Ti}_{0.3}\text{O}_{2.65}$ at 400°C in dry and wet N_2 atmosphere, showing similar resistance for both bulk and grain components.	154
Figure 5-15 Conductivity data for $\text{BaYb}_{0.6}\text{Fe}_{0.05}\text{B}_{0.05}\text{Ti}_{0.3}\text{O}_{3-\delta}$ in dry N_2 (black circle), wet N_2 (white circle), $\text{BaYb}_{0.55}\text{Fe}_{0.1}\text{B}_{0.05}\text{Ti}_{0.3}\text{O}_{3-\delta}$ dry N_2 (black square) and wet N_2 (white square) and $\text{BaYb}_{0.45}\text{Fe}_{0.2}\text{B}_{0.05}\text{Ti}_{0.3}\text{O}_{3-\delta}$ dry N_2 (black triangle) and wet N_2 (white triangle).	155
Figure 6-1 XRD patterns for $\text{BaPr}_{0.25}\text{Y}_{0.75}\text{O}_{3-\delta}$, $\text{BaPr}_{0.25}\text{Yb}_{0.75}\text{O}_{3-\delta}$ and $\text{BaPr}_{0.25}\text{Tm}_{0.75}\text{O}_{3-\delta}$	161
Figure 6-2 XRD patterns for $\text{BaPr}_{0.25}\text{Y}_{0.5}\text{P}_{0.25}\text{O}_{3-\delta}$, $\text{BaPr}_{0.25}\text{Yb}_{0.5}\text{P}_{0.25}\text{O}_{3-\delta}$ and $\text{BaPr}_{0.25}\text{Tm}_{0.5}\text{P}_{0.25}\text{O}_{3-\delta}$	162
Figure 6-3 XRD patterns for $\text{BaY}_{0.75}\text{P}_{0.25}\text{O}_{2.75}$, $\text{BaYb}_{0.75}\text{P}_{0.25}\text{O}_{2.75}$ and $\text{BaTm}_{0.75}\text{P}_{0.25}\text{O}_{2.75}$	163
Figure 6-4 Raman spectra of BaPrO_3 , $\text{BaPr}_{0.25}\text{Y}_{0.5}\text{P}_{0.25}\text{O}_{3-\gamma}$, $\text{BaPr}_{0.25}\text{Yb}_{0.5}\text{P}_{0.25}\text{O}_{3-\gamma}$, $\text{BaPr}_{0.25}\text{Tm}_{0.5}\text{P}_{0.25}\text{O}_{3-\gamma}$ and $\text{BaTm}_{0.75}\text{P}_{0.25}\text{O}_{3-\gamma}$ with peak showing the presence of phosphate indicated.	165
Figure 6-5 Conductivity data for $\text{BaPr}_{0.25}\text{Y}_{0.5}\text{P}_{0.25}\text{O}_{3-\gamma}$ in dry N_2 (black Circle), wet N_2 (white circle), dry O_2 (black triangle) and wet O_2 (white triangle).	166
Figure 6-6 Conductivity data for $\text{BaPr}_{0.25}\text{Yb}_{0.5}\text{P}_{0.25}\text{O}_{3-\gamma}$ in dry N_2 (black Circle), wet N_2 (white circle), dry O_2 (black triangle) and wet O_2 (white triangle).	167
Figure 6-7 Conductivity data for $\text{BaPr}_{0.25}\text{Tm}_{0.5}\text{P}_{0.25}\text{O}_{3-\gamma}$ in dry N_2 (black Circle), wet N_2 (white circle), dry O_2 (black triangle) and wet O_2 (white triangle).	167
Figure 6-8 Impedance data for $\text{BaPr}_{0.25}\text{Y}_{0.5}\text{P}_{0.25}\text{O}_{3-\delta}$ at 500°C in dry and wet N_2 atmosphere, showing the reduction in the resistance for the latter, indicative of a protonic contribution to the conductivity.....	168
Figure 6-9 Conductivity data for $\text{BaYb}_{0.75}\text{P}_{0.25}\text{O}_{3-\gamma}$ in dry N_2 (black Circle), wet N_2 (white circle) and dry O_2 (black triangle).....	170
Figure 6-10 TG profiles ($10^\circ\text{C min}^{-1}$ to 1000°C in CO_2) for (a) $\text{BaPr}_{0.25}\text{Y}_{0.5}\text{P}_{0.25}\text{O}_{3-\delta}$ (b) $\text{BaPr}_{0.25}\text{Yb}_{0.5}\text{P}_{0.25}\text{O}_{3-\delta}$ and (c) $\text{BaPr}_{0.25}\text{Tm}_{0.5}\text{P}_{0.25}\text{O}_{3-\delta}$	172

Content of Tables

Table 1-1 Operating temperature, electrolyte employed, advantages and disadvantages, and applications of the various fuel cell systems.	7
Table 1-2 Explanation of the thermodynamic potential and the losses occurred to a fuel cells output voltage.....	10
Table 1-3 The thermal expansion coefficient in air of electrolyte and electrode materials.	27
Table 2-1 Seven crystal classes.....	34
Table 2-2 Unit Cell types	35
Table 2-3 Expression of d-spacing in 4 crystal classes	42
Table 2-4 Thermal analysis techniques	52
Table 2-5 Properties that are possible to be calculated by AC impedance.....	57
Table 2-6 Typical capacitance values from a corresponding response on a 1 cm ³ material	65
Table 3-1 Sr _{0.8} Ca _{0.2} Mn _{1-x} Si _x O ₃ cubic cell parameter and cell volumes	81
Table 3-2 Conductivity values for Sr _{0.8} Ca _{0.2} Mn _{1-x} Si _x O _{3-δ} (x=0, 0.075, 0.1 and 0.125) at 800°C.....	84
Table 3-3 Cell parameters for composite electrode LSSO and SCMS 50:50 mix.....	87
Table 3-4 Cell parameters for composite electrode LSGO and SCMS 50:50 mix.	87
Table 3-5 Cell parameters for composite electrode CGO and SCMS 50:50 mix.....	89
Table 3-6 Area specific resistance values for composite electrodes deposited on a La ₉ SrSi ₆ O _{26.5} electrolyte pellet at 900°C 1hr.	91
Table 3-7 Area specific resistance values for composite electrodes deposited on a CGO electrolyte pellet at 900°C 1hr.	93
Table 4-1 Thermal expansion co-efficient RT-800°C for a range of electrolytes and cathodes	98
Table 4-2 Cell parameters for BaCo _{0.9-x} Fe _x Bi _{0.1} O _{3-δ} (x=0-0.8).....	105
Table 4-3 Refined cell parameters, volumes and weight percent fractions of BaCo _{0.5} Fe _{0.4} Bi _{0.1} O _{3-δ} and BaCo _{0.4} Fe _{0.5} Bi _{0.1} O _{3-δ}	105
Table 4-4 Oxygen content for the cubic perovskites BaCo _{0.9-x} Fe _x Bi _{0.1} O _{3-δ} (x=0.6-0.8).....	106
Table 4-5 BaCo _{0.4} Fe _{0.5} Bi _{0.1} O _{3-δ} cell parameters, volumes and weight percent fraction at RT and between 850-1000°C.....	108
Table 4-6 Thermal Expansion co-efficient at RT-800°C, RT-400°C and 400-800°C for BaCo _{0.9-x} Fe _x Bi _{0.1} O _{3-δ} (x=0-0.3, 0.6-0.8).....	110
Table 4-7 Water contents for hydrated BaCo _{0.9-x} Fe _x Bi _{0.1} O _{3-δ} (x = 0.6-0.8).....	114
Table 4-8 BaCo _{0.3} Fe _{0.6} Bi _{0.1} O _{3-δ} and BaCo _{0.9} Bi _{0.1} O _{3-δ} cathodes (100%) in wet N ₂ /O ₂ on a Ba ₂ In _{1.6} Zr _{0.2} Si _{0.2} O ₅ pellet at binding temperature range of 800-1000°C.	125

Table 4-9 ASR values at 800°C and 500°C for BIZS/BaCo _{0.9-x} Fe _x Bi _{0.1} O _{3-δ} x=0-0.3 and 0.6-0.8 (50:50wt%) on a BIZS electrolyte pellet in wet O ₂	128
Table 4-10 Resistivity at 800°C and 500°C for CGO/BaCo _{0.9-x} Fe _x Bi _{0.1} O _{3-δ} x=0-0.3 and 0.6-0.8 (50:50wt%) on a CGO electrolyte pellet	128
Table 5-1 Cell parameter data for BaYb _{0.7-x} Sc _x B _{0.05} Ti _{0.3} O _{3-δ} (x= 0.05, 0.1, 0.2, 0.3).....	141
Table 5-2 % theoretical density of BaYb _{0.65-x} Sc _x B _{0.05} Ti _{0.3} O _{2.65} (x = 0.05, 0.1, 0.2, 0.3) and BaYb _{0.45} Sc _{0.25} Ti _{0.3} O _{2.65} samples (*denotes impure)	142
Table 5-3 Water contents for hydrated BaYb _{0.65-x} Sc _x B _{0.05} Ti _{0.3} O _{2.65} (x= 0.05, 0.1, 0.2, 0.3) from TGA studies.....	143
Table 5-4 % Theoretical Densities of BaYb _{0.7-x} Sc _x B _{0.05} Ti _{0.3} O _{2.65} (x= 0.05, 0.1, 0.2, 0.3)	147
Table 5-5 Fitted bulk (B) and grain boundary (GB) conductivities and capacitances for BaYb _{0.6} Sc _{0.05} B _{0.05} Ti _{0.3} O _{2.65} at 350°C, 450°C and 550°C.....	148
Table 5-6 Total conductivity data for BaYb _{0.7-x} Sc _x B _{0.05} Ti _{0.3} O _{3-δ} (x= 0.05, 0.1, 0.2, 0.3) in dry and wet N ₂ atmospheres at 500°C and 800°C	151
Table 5-7 Cell parameter data for BaYb _{0.6-z} Fe _z B _{0.05} Ti _{0.3} O _{3-δ} (z= 0.05, 0.1, 0.2)	152
Table 5-8 % Theoretical density of BaYb _{0.6-z} Fe _z B _{0.05} Ti _{0.3} O _{3-δ} z= 0.05, 0.1, and 0.2 pellets.....	153
Table 5-9 Total conductivity data for BaYb _{0.6-z} Fe _z B _{0.05} Ti _{0.3} O _{3-δ} (z= 0.05, 0.1, 0.2) in dry and wet N ₂ atmospheres at 500°C and 800°C.....	155
Table 6-1 Cell parameter data for BaPr _{0.25} (Y/Yb/Tm) _{0.5} P _{0.25} O _{3-δ} (cubic cell)	162
Table 6-2 Cell parameter data for impure Ba(Y/Yb/Tm) _{0.75} P _{0.25} O _{3-δ} (cubic cell).....	163
Table 6-3 Density of individual compositions pellets	166
Table 6-4 Total conductivity data for BaPr _{0.25} (Y/Yb/Tm) _{0.5} P _{0.25} O _{3-y} in dry and wet N ₂ atmospheres	168
Table 6-5 Total conductivity data for BaPr _{0.25} (Y/Yb/Tm) _{0.5} P _{0.25} O _{3-y} in dry and wet O ₂ atmospheres	169
Table 6-6 Total conductivity data for Ba(Yb/Tm) _{0.5} P _{0.25} O _{3-y} in dry and wet N ₂ atmospheres	170
Table 6-7 Water contents for hydrated BaPr _{0.25} (Y/Yb/Tm) _{0.5} P _{0.25} O _{3-y}	172

